AAAS

Science

SAVING RHINOS

Dehorning helps tip the balance against rhino poaching

p. 1075

5 JUNE 2025

How will global warming transform local climates? p. 1016

Nanowire implants improve vision pp. 1025 & 1041

Passive cooling in the Tropics p. 1044

ASU Science

PRIZE FOR TRANSFORMATIONAL IMPACT

Apply now to the Arizona State University and *Science* Prize for Transformational Impact!

Arizona State University and *Science* have partnered to create the **ASU–*Science* Prize for Transformational Impact**. This prize recognizes transformational research that uses innovative methods and approaches to identify problems and develop solutions with impacts on policy and decision-making.

The grand prize winner will receive a prize of **US$30,000** and their prize-winning essay will be published in *Science* online and print. A runner-up will receive **US$10,000** and have their essay published in *Science* online.

APPLY BY **AUGUST 15, 2025**

www. Science.org/ASU

Harnessing the power of cell therapy in immunology

How resetting the immune system could enable patients with lupus and other immune-mediated diseases to achieve long-lasting remission, or even a cure.

About 67 million people worldwide have an immune-mediated disease, and the number is growing. "Immune-mediated diseases are increasing around 10% every year," says Attilio Bondanza, vice president of Immunology Cell Therapy, BioPharmaceuticals at AstraZeneca. "This increase, combined with the modest remission rates of current therapies, means we need to adapt and develop radical new approaches to tackle immune-mediated diseases, especially for patients with no further options."

Attilio Bondanza

For many years, patients with immune-mediated diseases were treated with high doses of glucocorticoids and other traditional immunosuppressants, which do not address the underlying causes of disease and are associated with significant side effects. The subsequent development of more targeted therapies has improved lives for many, but despite leading to much-improved treatment outcomes including increased remission rates, they are not curative.

Emerging cell therapies, such as CAR-T cells, have the potential to reset the immune system, offering hope for complete remission—a functional cure—with a single administration for certain patients.

"Harnessing the power of the body's own immune cells to treat diseases is a potentially transformative, rapidly expanding area that could drive research and clinical care for the next decade and beyond," says Anca Askanase, professor of medicine and director of the Lupus Center at Columbia University.

Anca Askanase

A potential immune system reset

Known widely as a treatment for certain blood cancers, CAR-T cells can successfully target malignant B cells—white blood cells that make antibodies—to treat some blood cancers. These defective autoreactive B cells are also strongly involved in diseases such as lupus, multiple sclerosis, and rheumatoid arthritis, suggesting that CAR-T cells could also work for these diseases.

The goal of cell therapy in immune-mediated diseases is to restore B cells' normal function by fully depleting defective B cells, thereby resetting the immune system. Researchers at AstraZeneca are developing novel CAR-T approaches that could target these diseases' unique underlying pathophysiology.

First, a patient's own T cells are removed and engineered to express a specific chimeric antigen receptor (CAR). The cells are then reinfused into the patient. For example, researchers are investigating a CAR T-cell therapy directed to the dual targets of CD19 and B-cell maturation antigen (BCMA). By depleting CD19-expressing B cells and plasma cells that express BCMA abundantly, this approach could deliver long-lasting drug-free remission beyond that achievable with a CAR-T cell therapy aimed at a single target.

"T cells have the unique ability to penetrate into deep tissues, particularly into the bone marrow, eradicating disease-causing cells," says Bondanza. "This could potentially enable a total reset of the immune system, which in turn may have a fundamental benefit on patients' lives."

B cells aren't the only driver of immune-mediated diseases; T-cell dysfunction can trigger type 1 diabetes and inflammatory bowel disease. In healthy individuals, T cells kill pathogen-infected cells, but in those with autoimmune diseases, they erroneously attack the patient's cells. Regulatory T cells (Tregs) prevent an overactive immune response, so enhancing their activity with CAR Treg cell therapy, in which Treg cells are engineered to home in on the affected organ, may dampen or halt disease progression and prevent further organ damage.

Leading the way

"AstraZeneca's ambition is to transform the care of patients with immune-mediated disease, moving beyond symptom control and progressing to a cure," says Bondanza. "We are developing an entire pipeline of novel therapies that utilize innovative platforms, with cell therapies addressing a significant unmet need."

Across immunology, AstraZeneca is developing multiple therapies, including cell therapies, T-cell engagers, and biologics, that aim to treat patients across the full spectrum of disease severities. Within cell therapy, new approaches beyond CAR-T and CAR-Tregs are being researched, such as allogeneic (engineered cells from healthy people) and in vivo (modifying T cells within the body) technologies.

As Askanase notes, "What's most exciting about cell therapy is that this novel treatment approach to autoimmune diseases can be tailored for each patient to provide a one-time, potentially curative option, eliminating the need for life-long treatment."

IMAGES AND PHOTOS: PROVIDED BY ASTRAZENECA / ANCA ASKANASE

Veeva ID: Z4-74900 Date of Preparation: May 2025

Your bridge to successful innovation.

NEB's Customized Solutions Team is here to help, and serves as a bridge to the support and resources you need to ensure your success.

Creating the right partnership is essential when pioneering a new life science product. Every aspect of development – technical expertise, reagent optimization, manufacturing scale, turnaround time, reagent quality, and comprehensive logistical support – is vital for achieving your objectives. And in the regulated markets landscape, these challenges magnify, demanding an even more specialized approach.

Your Bridge to Successful Innovation

- Leverage NEB's 50 years of experience in enzymology and reagent manufacturing
- As an extension of your team, we prioritize a deep understanding of your objectives, work with you on an optimal solution, and help to anticipate your future needs
- Benefit from our ISO 9001- and 13485-certified processes and commitment to quality, as well as our GMP-grade* production facility, and specialized lyophilization facility for the highest quality production standards
- Access unparalleled support from our dedicated account managers, program managers, technical scientists and production teams
- We work closely with you on inventory management and global distribution through our network of NEB-owned subsidiaries, to ensure successful commercialization

NEB's Customized Solutions Team will help you access novel products, meet quality specifications, speed time to market, and streamline your supply chain, allowing you to focus more on what matters most — innovation.

Ready to start the discussion? Learn more at
www.neb.com/customizedsolutions.

** "GMP-grade" is a branding term NEB uses to describe products manufactured or finished at NEB's Rowley facility. The Rowley facility was designed to manufacture products under more rigorous infrastructure and process controls to achieve more stringent product specifications and customer requirements. Products manufactured at NEB's Rowley facility are manufactured in compliance with ISO 9001 and ISO 13485 quality management system standards. However, at this time, NEB does not manufacture or sell products known as Active Pharmaceutical Ingredients (APIs), nor does NEB manufacture its products in compliance with all of the Current Good Manufacturing Practice regulations.*

NEW ENGLAND Biolabs®

CONTENTS

5 JUNE 2025 | VOLUME 388 | ISSUE 6751

1016

After drought dried up reservoirs in Texas, officials in Austin turned to climate modelers to help plan infrastructure.

PHOTO: TONY GUTIERREZ/AP

EDITORIAL

NEWS

FEATURES

COMMENTARY

PERSPECTIVES

POLICY FORUM

Recent PhD?

Science & SciLifeLab PRIZE For Young Scientists

How about $30,000 US, having your essay published in *Science*, and being celebrated with a week of festivities in Stockholm, Sweden?

Apply now to the *Science* & SciLifeLab Prize for Young Scientists!

A global award aimed at young researchers

Every year, four early-career scientists from across the globe are awarded the *Science* & SciLifeLab Prize for Young Scientists for outstanding research they have conducted as part of their PhD.

The selected winners receive up to $30, 000 US in prize money for their accomplishments. In addition, all four winners are published in *Science* and invited by SciLifeLab to Sweden in December to participate in a unique week filled with events in honor of science. Here, they will be given the opportunity to meet with leading scientists in their field of research and create life-long connections to support their career.

Categories

The award is available in four categories:

- Cell and Molecular Biology
- Genomics, Proteomics and Systems Biology Approaches
- Ecology and Environment
- Molecular Medicine

More information

More information: scienceprize.scilifelab.se

Questions: scilifelabprize@aaas.org

Application deadline: July 15, 2025

Eligibility: applicants must have received their PhD between January 1, 2023 and December 31, 2024.

Enabled by the generous support of the Knut and Alice Wallenberg Foundation.

Knut and Alice Wallenberg Foundation

Science AAAS

SciLifeLab

BOOKS ET AL.

LETTERS

RESEARCH

HIGHLIGHTS

RESEARCH SUMMARIES

PHOTO: PAUL SOUDERS/WORLDFOTO/MINDEN PICTURES

RESEARCH ARTICLES

WORKING LIFE

ON THE COVER

The last male northern white rhino socializes with a southern white rhino. Since his death in 2018, the northern subspecies is functionally extinct after decades of illegal killing for their horns. A study from the Greater Kruger region of South Africa offers some hope for remaining rhino species, proving that dehorning operations can achieve poaching reductions under certain circumstances and in conjunction with other interventions. See page 1075. Photo: Ami Vitale

ON THE PODCAST

Farming maize in ice age Michigan, predicting the future climate of cities, and our host takes a quiz on the sounds of science

Science **serves as a forum for discussion of important issues related to the advancement of science by publishing material on which a consensus has been reached as well as including the presentation of minority or conflicting points of view. Accordingly, all articles published in *Science*—including editorials, news, commentary, and book reviews—are signed and reflect the individual views of the authors and not official points of view adopted by AAAS or the institutions with which the authors are affiliated.** *Science* (ISSN 0036-8075) is published weekly on Thursday, except last week in December, by the American Association for the Advancement of Science, 1200 New York Avenue, NW, Washington, DC 20005. Periodicals mail postage (publication No. 484460) paid at Washington, DC, and additional mailing offices. The title *Science* is a registered trademark of the AAAS. Domestic individual membership, including subscription (12 months): $165 ($74 allocated to subscription). Domestic institutional subscription (51 issues): $2865; Foreign postage extra: Air assist delivery: $135. First class, airmail, student, and emeritus rates on request. Canadian rates with GST available upon request, GST #125488122. Publications Mail Agreement Number 1069624. **Printed in the U.S.A. Change of address:** Allow 4 weeks, giving old and new addresses and 8-digit account number. **Postmaster:** Send change of address to AAAS, P.O. Box 96178, Washington, DC 20090–6178. **Single-copy sales:** $15 each plus shipping and handling available from backissues.science.org; bulk rate on request. **Authorization to reproduce** material for internal or personal use under circumstances not falling within the fair use provisions of the Copyright Act can be obtained through the Copyright Clearance Center (CCC), www.copyright.com. The identification code for *Science* is 0036-8075. *Science* is indexed in the *Reader's Guide to Periodical Literature* and in several specialized indexes.

Science AAAS

EDITOR-IN-CHIEF **Holden Thorp**, hthorp@aaas.org

EXECUTIVE EDITOR Valda Vinson

EDITORS, RESEARCH Sacha Vignieri, Jake S. Yeston **EDITOR, COMMENTARY** Lisa D. Chong

DEPUTY EXECUTIVE EDITOR Lauren Kmec

DEPUTY EDITORS Stella M. Hurtley (UK), Phillip D. Szuromi **SENIOR EDITORS** Caroline Ash (UK), Michael A. Funk, Angela Hessler, Di Jiang, Priscilla N. Kelly, Marc S. Lavine (Canada), Sarah Lempriere (UK), Mattia Maroso, Yevgeniya Nusinovich, Ian S. Osborne (UK), L. Bryan Ray, H. Jesse Smith, Keith T. Smith (UK), Jelena Stajic, Peter Stern (UK), Yury V. Suleymanov, Valerie B. Thompson, Brad Wible **ASSOCIATE EDITORS** Jack Huang, Sumin Jin, Bianca Lopez, Sarah Ross (UK), Madeleine Seale (UK), Corinne Simonti, Ekeoma Uzogara **SENIOR LETTERS EDITOR** Jennifer Sills **NEWSLETTER EDITOR** Christie Wilcox **RESEARCH & DATA ANALYST** Jessica L. Slater **LEAD CONTENT PRODUCTION EDITORS** Chris Filiatreau, Harry Jach Sr. **CONTENT PRODUCTION EDITOR** Amelia Beyna **CONTENT PRODUCTION EDITORS** Anne Abraham, Robert French, Julia Haber-Katris, Nida Masiulis, Abigail Shashikanth, Suzanne M. White **SENIOR PROGRAM ASSOCIATE** Maryrose Madrid **EDITORIAL MANAGER** Joi S. Granger **EDITORIAL ASSOCIATES** Aneera Dobbins, Lisa Johnson, Jerry Richardson, Anita Wynn **SENIOR EDITORIAL COORDINATORS** Alexander Kief, Ronmel Navas, Isabel Schnaidt, Alice Whaley (UK), Brian White **EDITORIAL COORDINATORS** Clair Goodhead (UK), Kat Kirkman, Samantha Price **ADMINISTRATIVE COORDINATOR** Karalee P. Rogers **ASI DIRECTOR, OPERATIONS** Janet Clements (UK) **ASI OFFICE MANAGER** Carly Hayward (UK) **ASI SR. OFFICE ADMINISTRATORS** Simon Brignell (UK), Jessica Waldock (UK) **COMMUNICATIONS DIRECTOR** Meagan Phelan **DEPUTY DIRECTOR** Matthew Wright **SENIOR WRITERS** Walter Beckwith, Joseph Cariz, Abigail Eisenstadt **WRITER** Mahathi Ramaswamy **SENIOR COMMUNICATIONS ASSOCIATES** Zachary Graber, Sarah Woods **COMMUNICATIONS ASSOCIATES** Kiara Brooks, Haley Riley, Mackenzie Williams

NEWS EDITOR Tim Appenzeller

NEWS MANAGING EDITOR John Travis **INTERNATIONAL EDITOR** David Malakoff **DEPUTY NEWS EDITORS** Rachel Bernstein, Shraddha Chakradhar, Martin Enserink, David Grimm, Eric Hand, Michael Price, Kelly Servick, Matt Warren (Europe) **SENIOR CORRESPONDENTS** Daniel Clery (UK), Jon Cohen, Jeffrey Mervis **ASSOCIATE EDITORS** Jeffrey Brainard, Michael Greshko, Katie Langin **NEWS REPORTERS** Adrian Cho, Jennifer Couzin-Frankel, Phie Jacobs, Jocelyn Kaiser, Rodrigo Pérez Ortega (Mexico City), Robert F. Service, Erik Stokstad, Paul Voosen, Meredith Wadman **CONSULTING EDITOR** Elizabeth Culotta **CONTRIBUTING CORRESPONDENTS** Vaishnavi Chandrashekhar, Dan Charles, Warren Cornwall, Andrew Curry (Berlin), Ann Gibbons, Sam Kean, Kai Kupferschmidt (Berlin), Andrew Lawler, Mitch Leslie, Virginia Morell, Dennis Normile (Tokyo), Cathleen O'Grady, Elisabeth Pain (Careers), Charles Piller, Sara Reardon, Richard Stone (Senior Asia Correspondent), Gretchen Vogel (Berlin), Lizzie Wade (Mexico City) **INTERN** Alexa Robles-Gil **COPY EDITORS** Julia Cole (Senior Copy Editor), Hannah Knighton, Cyra Master (Copy Chief) **ADMINISTRATIVE SUPPORT** Meagan Weiland

CREATIVE DIRECTOR Beth Rakouskas

DESIGN MANAGING EDITOR Chrystal Smith **GRAPHICS MANAGING EDITOR** Chris Bickel **PHOTOGRAPHY MANAGING EDITOR** Emily Petersen **MULTIMEDIA MANAGING PRODUCER** Kevin McLean **DIGITAL DIRECTOR** Kara Estelle-Powers **DESIGN EDITOR** Marcy Atarod **DESIGNER** Noelle Jessup **SENIOR SCIENTIFIC ILLUSTRATOR** Noelle Burgess **SCIENTIFIC ILLUSTRATORS** Austin Fisher, Kellie Holoski, Ashley Mastin **SENIOR GRAPHICS EDITOR** Monica Hersher **GRAPHICS EDITOR** Veronica Penney **SENIOR PHOTO EDITOR** Charles Borst **PHOTO EDITOR** Elizabeth Billman **SENIOR PODCAST PRODUCER** Sarah Crespi **SENIOR VIDEO PRODUCER** Meagan Cantwell **SOCIAL MEDIA STRATEGIST** Jessica Hubbard **SOCIAL MEDIA PRODUCER** Sabrina Jenkins **WEB DESIGNER** Jennie Pajerowski

CHIEF EXECUTIVE OFFICER AND EXECUTIVE PUBLISHER

Sudip Parikh

PUBLISHER, SCIENCE FAMILY OF JOURNALS Bill Moran

DIRECTOR, BUSINESS OPERATIONS & ANALYSIS Eric Knott **MANAGER, BUSINESS OPERATIONS** Jessica Tierney **MANAGER, BUSINESS ANALYSIS** Cory Lipman **BUSINESS ANALYSTS** Kurt Ennis, Maggie Clark, Isacco Fusi **BUSINESS OPERATIONS ADMINISTRATOR** Taylor Fisher **DIGITAL SPECIALIST** Marissa Zuckerman **SENIOR PRODUCTION MANAGER** Jason Hillman **SENIOR MANAGER, PUBLISHING AND CONTENT SYSTEMS** Marcus Spiegler **CONTENT OPERATIONS MANAGER** Rebecca Doshi **PUBLISHING PLATFORM MANAGER** Jessica Loayza **PUBLISHING SYSTEMS SPECIALIST, PROJECT COORDINATOR** Jacob Hedrick **SENIOR PRODUCTION SPECIALIST** Kristin Wowk **PRODUCTION SPECIALISTS** Kelsey Cartelli, Audrey Diggs **SPECIAL PROJECTS ASSOCIATE** Shantel Agnew

MARKETING DIRECTOR Sharice Collins **ASSOCIATE DIRECTOR, MARKETING** Justin Sawyers **GLOBAL MARKETING MANAGER** Allison Pritchard **ASSOCIATE DIRECTOR, MARKETING SYSTEMS & STRATEGY** Aimee Aponte **SENIOR MARKETING MANAGER** Shawana Arnold **MARKETING MANAGER** Ashley Evans **MARKETING ASSOCIATES** Hugues Beaulieu, Ashley Hylton, Lorena Chirinos Rodriguez, Jenna Voris **MARKETING ASSISTANT** Courtney Ford **SENIOR DESIGNER** Kim Huynh

DIRECTOR AND SENIOR EDITOR, CUSTOM PUBLISHING Erika Gebel Berg **ADVERTISING PRODUCTION OPERATIONS MANAGER** Deborah Tompkins **DESIGNER, CUSTOM PUBLISHING** Jeremy Huntsinger **SENIOR TRAFFIC ASSOCIATE** Christine Hall

DIRECTOR, PRODUCT MANAGEMENT Kris Bishop **PRODUCT DEVELOPMENT MANAGER** Scott Chernoff **ASSOCIATE DIRECTOR, PUBLISHING INTELLIGENCE** Rasmus Andersen **SR. PRODUCT ASSOCIATE** Robert Koepke **PRODUCT ASSOCIATES** Caroline Breul, Anne Mason

ASSOCIATE DIRECTOR, INSTITUTIONAL LICENSING MARKETING Kess Knight **ASSOCIATE DIRECTOR, INSTITUTIONAL LICENSING SALES** Ryan Rexroth **INSTITUTIONAL LICENSING MANAGER** Nazim Mohammedi, Claudia Paulsen-Young **SENIOR MANAGER, INSTITUTIONAL LICENSING OPERATIONS** Judy Lillibridge **MANAGER, RENEWAL & RETENTION** Lana Guz **SYSTEMS & OPERATIONS ANALYST** Ben Teincuff **FULFILLMENT ANALYST** Aminta Reyes

ASSOCIATE DIRECTOR, INTERNATIONAL Roger Goncalves **ASSOCIATE DIRECTOR, US ADVERTISING** Stephanie O'Connor **US MID WEST, MID ATLANTIC AND SOUTH EAST SALES MANAGER** Chris Hoag **DIRECTOR, OUTREACH AND STRATEGIC PARTNERSHIPS, ASIA** Shoupeng Liu **SALES REP, ROW** Sarah Lelarge **SALES ADMIN ASSISTANT, ROW** Victoria Glasbey **DIRECTOR OF GLOBAL COLLABORATION AND ACADEMIC PUBLISHING RELATIONS, ASIA** Xiaoying Chu **ASSOCIATE DIRECTOR, INTERNATIONAL COLLABORATION** Grace Yao **SALES MANAGER** Danny Zhao **MARKETING MANAGER** Kilo Lan **ASCA CORPORATION, JAPAN** Rie Rambelli (Tokyo), Miyuki Tani (Osaka)

DIRECTOR, COPYRIGHT, LICENSING AND SPECIAL PROJECTS Emilie David **RIGHTS AND PERMISSIONS ASSOCIATE** Elizabeth Sandler **LICENSING ASSOCIATE** Virginia Warren **RIGHTS AND LICENSING COORDINATOR** Dana James **CONTRACT SUPPORT SPECIALIST** Michael Wheeler

EDITORIAL
science_editors@aaas.org

NEWS
science_news@aaas.org

INFORMATION FOR AUTHORS
science.org/authors/
science-information-authors

REPRINTS AND PERMISSIONS
science.org/help/
reprints-and-permissions

MULTIMEDIA CONTACTS
SciencePodcast@aaas.org
ScienceVideo@aaas.org

MEDIA CONTACTS
scipak@aaas.org

PRODUCT ADVERTISING & CUSTOM PUBLISHING
advertising.science.org
science_advertising@aaas.org

CLASSIFIED ADVERTISING
advertising.science.org/
science-careers
advertise@sciencecareers.org

JOB POSTING CUSTOMER SERVICE
employers.sciencecareers.org
support@sciencecareers.org

MEMBERSHIP AND INDIVIDUAL SUBSCRIPTIONS
science.org/subscriptions

MEMBER BENEFITS
aaas.org/membership/
benefits

INSTITUTIONAL SALES AND SITE LICENSES
science.org/librarian

America is ceding the lead in creating the future

H. Holden Thorp

The renowned American management consultant and author Peter Drucker is often credited as saying that "the best way to predict the future is to create it"—a view that applies to science as much as to the business world. It implies that gaining insights and ideas that lead to new discoveries and technologies allows victory in the marketplace, ahead of the competition. As the Trump administration continues to drastically defund and dismantle basic science in America, the United States is presenting other countries with opportunities to take the lead in seeing farther ahead, anticipate where scientific and technological prowess is going, and create the future, while the United States stands on the sidelines. This is a matter not only of scientific prestige but also of economic vitality. The country will no longer be at the forefront of commercializing breakthroughs and leveraging them for maximum economic and societal benefit. Moreover, this will trigger a massive transition for the global scientific community and alter the framework that shapes how the world's economies connect and grow.

Measured by its share of published research, the United States was already falling behind before the latest cuts and attacks. For example, the percentage of papers published in *Science* with at least one corresponding author with funding from the US federal government has been declining over the past 7 years (2018 to 2024), decreasing from 54 to 44%. By contrast, the number of published papers originating from China has doubled during this time. In *Science Advances*, the number of papers published from China and the United States in 2024 was roughly the same. If this trend continues, the same will be true in a few years for *Science* and is likely to happen even sooner as the US government retreats from supporting research and China and other countries continue to increase their investments.

For now, the United States arguably remains the leader in the hot areas of artificial intelligence (AI) and quantum computing, with many of the advances coming from US-based corporate entities such as Google DeepMind and Microsoft. But commercial success in these areas grew out of basic research in computer science and solid-state physics in universities, funded by the federal government. With a bottom line to consider, for-profit businesses likely would not have started these disciplines from scratch. The recent market panic caused by the advances in AI by the Chinese company DeepSeek shows that this leadership is far from guaranteed. Moreover, applying these technologies in medicine and elsewhere will rely on still more basic research—research now threatened by sweeping cutbacks inflicted by the Trump administration.

A world where the United States is no longer leading the scientific enterprise will still benefit from science. Human creativity flourishes everywhere, after all, and other countries and cultures will have greater opportunities to shape the future in new ways. The global enterprise will adapt to the lack of American leadership, but the steep loss for the country itself is unambiguous. The United States will no longer have the same window into the technologies of the future that will allow it to shape and anticipate commercial and societal advances. This will eventually reduce the market successes and global leadership that the United States has boasted since World War II.

The United States will no longer have the same window into the technologies of the future that will allow it to shape and anticipate commercial and societal advances.

At a US Senate hearing in April on the importance of biomedical research, bipartisan support was expressed for continued investment, although whether senators in the Republican party will defy the president and rectify the cuts remains unknown. In his testimony, Sudip Parikh, the chief executive officer of the American Association for the Advancement of Science (AAAS, the publisher of *Science*), noted that the language of chemistry used to be German and that only in the past 50 years did the German language stop being a requirement for chemistry degrees in the United States. "Twenty years from now," he said, "what is going to be the language of science? Is it going to be English? I don't know that for certain." It is a sobering thought. Scientific knowledge is, fortunately, a public good, and as such, its benefits transcend international boundaries. But relinquishing its prominence in creating the future is nothing short of devastating for the United States. □

H. Holden Thorp Editor-in-Chief, *Science* journals. hthorp@aaas.org.

10.1126/science.adz3915

Celebrating Excellence *and* Impact

Since 1994, Research Corporation for Science Advancement's Cottrell Scholar program has developed outstanding early career teacher-scholars recognized by their scientific communities for the quality and innovation of their research and educational programs and their academic leadership skills. RCSA also celebrates the achievements of accomplished scientists through its annual STAR and IMPACT Awards, and through the Robert Holland Jr. Awards for Research and Leadership Excellence.

The STAR Award

Rewarding Cottrell Scholars for excellence in science teaching and research.

1. Richard Brutchey | Chemistry
University of Southern California
Cottrell Scholar 2010

2. Jenny Ross | Physics
Syracuse University
Cottrell Scholar 2010

The IMPACT Award

Honoring Cottrell Scholars for national impact in science through leadership and service.

3. Eric Hegg | Chemistry
Michigan State University
Cottrell Scholar 2002

4. Michael Strauss | Astronomy
Princeton University
Cottrell Scholar 1997

The Robert Holland Jr. Award

Welcoming senior scientists as full members of the Cottrell Scholar community for research excellence, leadership, creativity, and mentoring in the physical sciences. The award honors the late Robert Holland Jr., an engineer and corporate executive who served on RCSA's Board of Directors.

5. Kevin Hewitt | Physics
Dalhousie University

6. Angel Martí | Chemistry
Rice University

7. Enrico Ramirez-Ruiz | Astronomy
University of California, Santa Cruz

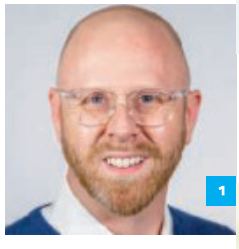

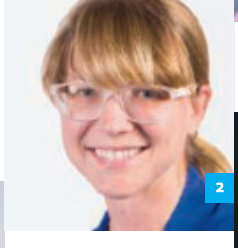

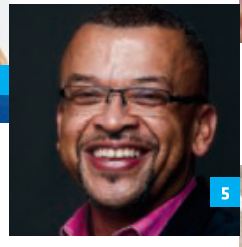

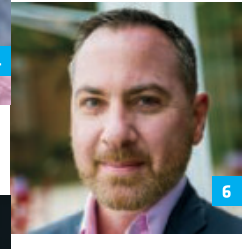

rescorp.org

RESEARCH CORPORATION
for SCIENCE ADVANCEMENT
A foundation dedicated to science since 1912.

National Academy of Sciences President Marcia McNutt is navigating a tense situation as the organization faces unprecedented contract losses and layoffs.

RESEARCH POLICY

National Academies on brink of dramatic downsizing

Venerable advisory organization hit by Trump's contract cancellations

MEREDITH WADMAN

On 24 May, the morning after a news article announced major job losses coming at the U.S. National Academies of Sciences, Engineering, and Medicine (NASEM), National Academy of Sciences President Marcia McNutt wrote an apologetic memo to employees. Her statement to *STAT* that 250 people could lose their positions by summer's end had come as news to the roughly 1100 NASEM staff. McNutt told staff "no decisions [have been] made" about the number of coming layoffs.

But there's no doubt that the 162-year-old honorary society, which produces influential reports by committees of independent experts, is headed for dramatic changes. "Our financial realities necessitate preparing for painful downsizing and reorganization," wrote McNutt, who took the helm at NASEM in 2016 following 3 years as editor-in-chief of *Science*. After 2 years of budget deficits, the private, nonprofit NASEM is now being hit with cuts to government contracts by President Donald Trump's administration.

The National Research Council (NRC), the organization's operating arm, has already been forced to lay off more than 50 people, and the next steps could soon become clearer. At a meeting on 10 and 11 June, NRC's governing board will receive the recommendations of a working group outlining the proposed reorganization.

"While it is too early to share specific outcomes, we anticipate that the NRC will emerge as a smaller organization with fewer units," McNutt wrote in a 21 May email to the chairs of NRC's many boards, the groups of expert scientists that identify research topics and frame the scope and questions of studies. "The goal of this restructuring is to eliminate redundant administrative layers, reduce indirect costs, and better align operations with our strategic priorities," she wrote.

The direction is alarming to some of NASEM's elected members, including cell biologist Randy Schekman of the University of California, Berkeley, who is a former editor-in-chief of the *Proceedings of the National Academy of Sciences*, NASEM's in-house journal. He says he fears for the future of NASEM's defining consensus reports. "I am not aware of there ever having been a crisis like this" at NASEM, he says. "It's a disaster."

The National Academy of Sciences was granted a charter by Congress in 1863 to provide the government with independent, objective advice on science and technology. Its flagship studies have addressed scores of subjects from research priorities for Alzheimer's disease treatment to shaping the next decade of solar and space physics research. Because the organization does not have congressional funding, it must raise its own money for the studies. Philanthropies fund some, but most are supported by federal agencies. NRC received $200 million in government contracts and grants in 2023, the most recent year for which the number is available. And many of those contracts have been axed by the team of cost cutters at Trump's so-called Department of Government Efficiency (DOGE).

From Trump's inauguration to 6 May, NRC lost 41 U.S. government contracts and received another eight stop-work orders, NASEM's chief operating officer, Greg Symmes, wrote in a 6 May memo to staff. "This has had an immediate impact on the program staff working on those projects." Two more contracts have been lost since then, bringing the total to 43, according to a NASEM spokesperson. "We have not yet determined how far [staff] reductions will have to go," Symmes added in a statement to *Science*.

The DOGE website lists 36 of the canceled NASEM contracts, and *Science* calculated the total cost of these losses to be more than $25 million. The list includes a $970,000 contract from the Department of Homeland Security to fund statistical research for a new office of homeland security statistics, a $250,000 contract from the Centers

PHOTO: ALLISON ROBBERT/AFP VIA GETTY IMAGES

for Disease Control and Prevention for a June workshop on preventing H5N1 bird flu transmission among farm workers and veterinarians, and a $500,000 study on drought and climate change funded by the National Oceanic and Atmospheric Administration.

In her letter to the board chairs, McNutt explains that providing bridging funds, such as from endowments, "is not a viable option" because "NRC itself has no endowment or funding reserve. While the three academies—Sciences, Engineering, and Medicine—do hold endowments, those funds are limited and highly restricted."

The presidents of those three honorific societies that together with NRC comprise NASEM—McNutt, John Anderson, and Victor Dzau—each earned more than $1 million in 2023.

> **"I am not aware of there ever having been a crisis like this [at NASEM] ... it's a disaster.**
>
> **Randy Schekman**
> University of California, Berkeley

Eleven other senior executives earned in excess of $300,000 that year, according to NASEM's tax filings.

At a time when hundreds of jobs are at risk, "It is galling that the leadership of the institution makes that kind of money," says one senior program officer with a decade of experience at the institution. Salaries for the teams that support the studies begin below $60,000. McNutt did not respond to a question asking whether reducing executives' salaries had been considered as a way to protect NRC work.

But some say the job losses are an occupational risk at an institution that consistently needs to drum up its own money. "I hired and fired lots of people over the years," says one former senior NRC staffer who asked not to be identified because of the political sensitivity of the issue. "It's the nature of being on soft money."

The recent blows follow 2 years of red ink; NASEM ran $63 million and $40 million deficits in 2022 and 2023, respectively. (The 2024 figure is not yet available.) NASEM says the shortfalls mainly reflect investment losses. But a scientist at a U.S. agency that has funded NRC studies says it has not sought federal clients as aggressively as it could. "It seems like they are in a defensive crouch and doing what they can to survive," says the scientist, who has advised NASEM boards for 30 years and who requested anonymity because they work for the government. NASEM reports can take 1.5 to 2 years to develop and cost hundreds of thousands of dollars or more. The time and expense can push clients toward more nimble competitors such as MITRE or RAND, nonprofits that advise government clients on complicated science and technology problems, the scientist adds. "Marcia McNutt's got a helluva challenge on her hands."

McNutt faces challenges that go beyond finances, including complaints that NASEM leaders are timid at a time that calls for outspokenness in defense of science. "I [have] tried to convince, unsuccessfully, Marcia McNutt ... to take a public stand," Schekman says, "and I have received no encouragement and some considerable resistance" from her. (McNutt did not respond when asked to comment on his statement.)

Members also expressed outrage when staff were ordered to purge words such as "health equity" and "marginalized populations" from complete or near-complete reports this winter. The move came soon after McNutt and Symmes wrote to staff that they were dissolving NASEM's Office of Diversity and Inclusion, citing executive orders from Trump and NASEM's obligations as a federal government contractor.

Susan Rundell Singer, a plant biologist and higher education researcher who is president of St. Olaf College and chairs the NRC Board on Science Education, hopes there will soon be more clarity on how the academy proposes to continue its research. "For 80 years the federal government and higher education have worked together to ensure we have the highest quality research and education—and we've been the envy of the world," she says. "The National Academies have played a key role [in that]. ... And that's at risk." □

With reporting by Jeffrey Mervis.

FUNDING

Final NSF budget proposal details massive cuts

Trump request favors one giant telescope and kills a gravitational wave detector **JEFFREY MERVIS**

In his "skinny budget" unveiled a month ago, President Donald Trump proposed a 57% cut to the $9 billion budget of the National Science Foundation (NSF). Now, in a more detailed budget request for fiscal year 2026, Trump explains what an agency shrunken by more than half would look like.

The request, submitted to Congress last week, would all but doom one of two proposed giant telescopes, eliminate funding for the U.S. global change research program and research on clean energy technologies, and, in a move one astrophysicist called "bonkers" on social media, close one-half of a pioneering gravitational wave observatory. The NSF budget proposal would also reduce by two-thirds the agency's investment in training the next generation of U.S. scientists and engineers and eviscerate its $1.4 billion portfolio to increase the diversity of that workforce.

"The $3.9 billion request reflects a strategic alignment of resources in a constrained fiscal environment in which NSF prioritizes investments that can have the greatest national impact," according to a statement from an agency spokesperson.

Congress would have to approve the president's budget, which would imperil many thousands of academic researchers who depend on NSF funding. Their chance of winning a grant, 26% in 2024, would plunge to 7%. The number of scientists supported by an NSF grant would contract by three-quarters.

Trump's budget would even slash many areas his administration has identified as national priorities. NSF's investment in research on advanced manufacturing, for example, would dip by 65%, microelectronics research by 54%, and support for biotechnology by 30%. Research on artificial intelligence and quantum information science are the only priority areas not ravaged, with AI getting a 3% boost and QIS holding steady.

Although massive layoffs were rumored, NSF's 1550-person workforce would shrink by only 15% from its 2024 tally, the document says. However, the number of academic scientists who take leave from their institutions to work at NSF as "rotators" for up to 4 years would drop from 300 to 70.

The budget provides only top-level numbers for each of NSF's eight parent directorates. The Engineering and STEM Education directorates would

suffer the deepest cuts, some 75%; while the Technology, Innovation, and Partnerships and the Geosciences directorates would shrink by 44%. But the budget omits detailed descriptions of the funding for the 37 divisions within those directorates. An NSF plan *Science* previously revealed would eliminate those divisions and instead focus the agency on Trump's handful of priority areas.

The agency also plans to jettison specific facilities, including one detector in the Laser Interferometer Gravitational-Wave Observatory (LIGO), now operating from twin locations in Louisiana and Washington state. Scientists note the two exquisitely sensitive detectors are designed to work in concert to spot minute ripples in space and rule out local events. "We need two LIGO sites to prove sources are astrophysical and not, like, a rabbit hopping nearby," Ohio State University astronomer Laura Lopez noted on social media. And when combined with information from international counterparts, the pair can pinpoint a wave's celestial source.

In February, NSF's oversight board recommended the agency spend $1.6 billion on only one of the two optical telescopes that have been vying for funds. Now the 2026 budget request identifies a loser in that competition, the Thirty Meter Telescope (TMT) planned for Hawaii. NSF says it won't spend any more money on the TMT. "We are disappointed that the NSF's current budget request does not include TMT," says its executive director, Harvard University astronomer Robert Kirshner.

Instead, NSF has agreed to assess, but did not commit to pay for, the final design review for the TMT's rival, the 25-meter Giant Magellan Telescope in Chile. The budget also says that passing that review "does not guarantee that a project will be approved for construction." □

THEY SAID IT

Devastating.

Duke University's Barton Haynes, responding to a decision by the National Institute of Allergy and Infectious Diseases to dramatically pare back U.S. HIV vaccine research by not renewing funding for two consortia, one of which he leads.

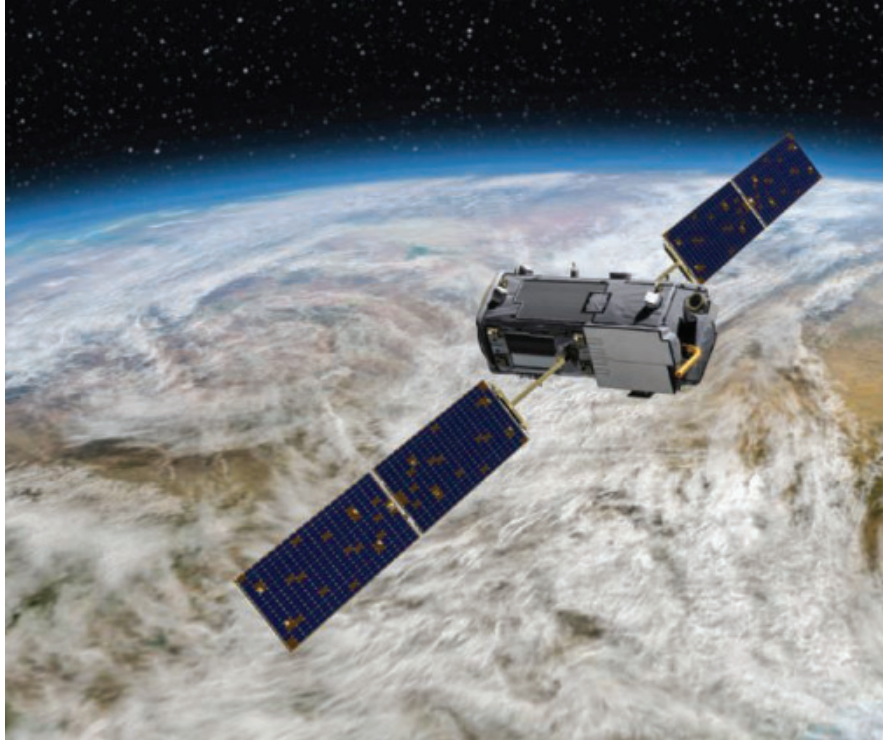

PHOTO: NASA/JPL

SPACE SCIENCE

Budget proposal would kill dozens of active and planned NASA spacecraft

Proposal comes as White House pulls its nominee to lead NASA

PAUL VOOSEN

President Donald Trump's administration wants to curtail science at NASA, prematurely ending a host of active missions in space and dropping plans for future probes. The budget proposal, released last week, emphasizes human exploration and missions that would land "the first human ever, an American, on Mars." But it calls for cutting NASA's science spending in half, to $3.9 billion, and would end more than 40 "lower priority" missions for a "leaner, more focused Science program."

If approved by the U.S. Congress, the plans would effectively end NASA's long-standing role as the world leader in space science, says Alan Stern, a planetary scientist at the Southwest Research Institute and former NASA science chief. "This is a tragic mistake for the new administration," he says, adding that the proposal would undermine the country's pipeline of future scientific talent and waste billions of dollars already spent on the missions.

A day after the budget release, the White House also abruptly pulled its nominee for NASA administrator, Jared Isaacman, a billionaire and commercial astronaut, just ahead of a Senate confirmation vote, leaving the agency without a leader to defend it. Reportedly, Isaacman's donations to Democratic lawmakers undermined his position with Trump, even though he had previously disclosed them. Isaacman had also expressed support for a full NASA science budget and was an ally of Elon Musk, whose standing at the White House has frayed in recent weeks.

The request would kill off several active climate science missions, including two Orbiting Carbon Observatories (OCOs) that map atmospheric carbon abundance around the planet. OCO-2, a standalone spacecraft, launched in 2014, and OCO-3 is mounted on the International Space Station. The missions investigate variations in the natural carbon cycle and have proved capable of tracing human carbon emissions.

More than 40 missions would be canceled in a NASA budget proposal, including the Orbiting Carbon Observatory-2.

The budget proposal would also end the Earth-facing instruments on the Deep Space Climate Observatory and kill the space station's Sage III instrument, which measures ozone, water vapor, and other gases in the atmosphere. And it would terminate the aging Terra, Aqua, and Aura satellites, each of which has operated for more than 2 decades, providing unprecedented insight into climate change with steady, well-calibrated instruments.

Beyond Earth, the proposal would cut short the Juno mission to Jupiter, which has revealed the gas giant's interior structure and provided close-up views of its large moons. It would end New Horizons, a probe that has imaged Pluto and is now pushing into the Kuiper belt, a region of cold, icy objects that is deeper than scientists once thought. It would terminate the OSIRIS-APEX mission, which is reusing a healthy spacecraft that collected samples from an asteroid to visit the near-Earth asteroid Apophis. And it would turn off several spacecraft orbiting Mars, including Mars Odyssey and Maven.

The budget plan would also shut down nearly every major science mission the agency has not yet begun to build. It would end the Atmosphere Observing System, a multibillion-dollar series of satellites meant to study how pollution is changing clouds and storms—one of the main sources of uncertainty for future climate change. And it would terminate the Surface Biology and Geology mission, which would loft an instrument into space capable of dividing reflected light into more than 400 channels by wavelength. The relative intensities can be used to prospect for critical minerals and track forest and farm health. "It's deeply unfortunate they don't understand the greater value of an instrument like that," says Anne Nolin, a remote-sensing scientist at the University of Nevada, Reno.

In the planetary science division, the administration would cancel the troubled $7 billion Mars Sample Return, a series of missions to collect rock samples from Mars and return them to Earth, because it foresees human missions doing the job more quickly. It would also end two missions NASA has planned for Venus. One, called DAVINCI, would send an armored sphere parachuting through the venusian atmosphere to divine its elemental composition and sniff for evidence of recent volcanic activity on the surface. The other, Veritas, would use a radar to peer through the planet's thick clouds and chart surface topography, revealing whether tectonic plates are active on its surface.

In the heliophysics division, the budget proposal would end plans for the Geospace Dynamics Constellation, a swarm of six satellites that would measure interactions between the Sun and Earth's magnetosphere. In astrophysics, work would continue on the Roman Space Telescope, a survey telescope as big as the current Hubble Space Telescope, but its development funding would be squeezed from $400 million to $156 million, potentially undermining plans to finish the spacecraft.

Also surviving in the request are missions that have just recently launched or are well into construction, including Dragonfly, an ambitious rotorcraft that will explore Saturn's large moon, Titan; and NISAR, a joint radar mission with India, launching this month, which would measure minute changes in the shape of Earth's surface.

Stern, for one, is ready to take the fight for NASA's future to Congress. "I believe these cuts will not stand," he says. "I'm ready to take up that battle. And I know I'm in good company." □

BUDGET

WHAT ELSE IS TRUMP PROPOSING?

Documents released on 30 May provided new details about the White House's proposals to make deep cuts to research spending in the 2026 fiscal year that begins on 1 October. Most of the revelations concern NASA and the National Science Foundation (see stories, pp. 1009 and 1010), but other plans also came into focus.

The Centers for Disease Control and Prevention (CDC) would see a 53% cut, to $4.3 billion, and its staff would be reduced by 43% to 7571, as most functions related to noninfectious diseases are abolished or rehoused in a new Administration for a Healthy America. "For too long, CDC has grown beyond … core functions" such as disease surveillance, the request states. Infectious disease work also takes a hit: A $1.5 billion program aimed at preventing viral hepatitis, sexually transmitted infections, and tuberculosis is reduced to $300 million to support a new grant program "that allows states to have more flexibility" in spending such money.

Department of State funding for global health programs would drop by 62%, to $3.8 billion. Funding for the President's Emergency Plan for AIDS Relief, one of the world's largest anti-HIV programs, would fall 30%, to $2.9 billion, as part of a plan to phase it out. Funding for the President's Malaria Initiative would be reduced by 45%, to $424 million, and ended for Gavi, the Vaccine Alliance and the Global Fund to Fight AIDS, Tuberculosis and Malaria, which this year received $300 million and $1.7 billion, respectively.

The National Institutes of Health's budget would fall 40% to $27.5 billion, and its 27 institutes and centers would be consolidated into just eight or eliminated altogether. (On 30 May an appeals judge upheld a lower court ruling that blocked the reorganization plan, although that ruling could be reversed.)

Funding for the **Department of Energy's (DOE's) Office of Science** would drop 14% to $7.1 billion. The request essentially eliminates climate research as part of a plan to cut DOE's biological and environmental research programs by 56% to $395 million. Funding for applied research in DOE's Office of Energy Efficiency and Renewable Energy would fall 74% to $888 million. *—Adrian Cho, Jon Cohen, Sara Reardon, and Meredith Wadman*

IN OTHER NEWS

MPOX OUTBREAK HITS SIERRA LEONE

An explosive mpox outbreak has overwhelmed health systems in Sierra Leone and raised fears of wider spread in the region. The small West African country, population about 9 million, has seen more than 3000 cases since January and accounted for more than half of all new mpox cases in Africa over the past few weeks.

Sierra Leone only has 60 beds in special treatment centers where mpox patients can be isolated, says Yap Boum, deputy lead of a team set up by the World Health Organization and the Africa Centres for Disease Control and Prevention to deal with mpox outbreaks on the continent. Vaccine doses are in short supply as well.

The virus belongs to clade IIb, a variant that circulated for several years in Nigeria before suddenly causing a global outbreak in 2022, primarily among men who have sex with men. But it appears to behave more like another variant, clade Ib, which has caused outbreaks in the Democratic Republic of the Congo and its neighbor Burundi the past year. Cases seem evenly split between men and women, and doctors are seeing many patients with severe disease, including lesions all over their body, not just the genitals. "We are still a bit puzzled by what is going on," Boum says.

But some researchers say the new outbreak shows clade Ib and IIb may be more similar than previously believed, and that local factors may determine how these strains spread and the severity of the disease they cause. "Just because it's happened one way in one place, doesn't mean it's going to happen that same way in another place," says Anne Rimoin, an mpox researcher at the University of California, Los Angeles.

University of Manitoba virologist Jason Kindrachuk, who co-authored a 1 June preprint about the Sierra Leone outbreak, fears it could spread to neighboring countries. "We could see very rapid geographic expansion of IIb if we don't really try and get things under control quickly," he warns.
—Kai Kupferschmidt

The U.S. National Institutes of Health–funded PHOENIx study aims to prevent transmission of tuberculosis, which is especially common among miners in South Africa.

PHOTO: ALFREDO CALIZ/PANOS PICTURES/REDUX

INFECTIOUS DISEASES

NIH funding policy deals new blow to HIV trial networks

Halt to foreign "subawards" disrupts studies and compromises ethical obligations to trial volunteers **SARA REARDON**

In 2019, the National Institutes of Health (NIH) launched an ambitious global study to see whether people could avoid getting the tuberculosis-causing mycobacterium from an infected household member by preemptively taking a drug normally used to treat TB. The network running the project, called Advancing Clinical Therapeutics Globally for HIV/AIDS and Other Infections (ACTG), has already spent nearly $70 million of NIH's money to enroll 5832 people from 31 sites in 13 countries where TB is prevalent.

But the study, known as PHOENIx, is now facing a dire threat to its success—NIH itself. The agency's controversial new policy on foreign funding, in combination with White House executive orders freezing or canceling federal grants and contracts to Harvard University and South Africa, has begun to shutter or dramatically curtail work at as many as one-third of ACTG sites, including 22 contributing data to PHOENIx.

ACTG coordinates dozens of trials related to HIV, coinfections such as TB that often accompany it, and related complications such as heart disease. It's one of four NIH-backed HIV clinical trial networks with global sites relying on "subawards" from a U.S. grantee. In a 1 May policy directive, NIH halted such subawards, saying it will instead require foreign collaborators' funds to be awarded and tracked separately.

The agency, however, still has not described how foreign partners of U.S. groups can get such grants, only saying the process will be in place by the end of September. Nor has it explained to global networks such as ACTG how their foreign partners, many of whom had expected new

subawards payments from NIH by 1 June, can keep their trial sites running, both to preserve good science and fulfill ethical obligations to their volunteer trial participants. "We're told that there'll be a new system put in place, but we don't have it, and until then, we have to figure out how to manage a very large number of sites and number of participants," says Amita Gupta of Johns Hopkins University, one of the global chairs of PHOENIx.

Another blow to HIV trial networks came in April, when President Donald Trump's administration shut down all NIH money going to Harvard, home to centers that manage patient data—including on safety issues—for ACTG and other networks. Worried that hundreds of millions of dollars and countless hours of work devoted to trials will now go to waste, ACTG leaders say they have written a letter to NIH Director Jayanta "Jay" Bhattacharya asking for help on the subaward policy. They've noted the ethical concerns if foreign trial sites have to close, but have not had an opportunity to meet with the agency's senior leadership. NIH also didn't respond to *Science*'s queries on the pending cash crunch for ACTG sites or similar situations elsewhere.

Clinical trial organizers say they are shuffling money to ensure all participants in ongoing studies can complete their courses of experimental treatment or at least be monitored for potential health problems resulting from those treatments. But to find that money, ACTG and its members have already had to forgo other research activities, halt trial enrollment, lay off dozens of employees, shrink ongoing trials, and cancel at least six HIV-related trials that were scheduled to start this year. "We are doing everything we can so something bad doesn't happen," such as sites kicking participants out of a study prematurely, says incoming ACTG Vice Chair Joseph Eron of the University of North Carolina at Chapel Hill.

Two-thirds of ACTG's research sites are safe for now because their subawards were renewed before May, but the remainder will run out of money this week. For South African researchers, the NIH policy and a February executive order blocking U.S. research money to the country are "a double whammy," says Linda-Gail Bekker, an HIV/AIDS researcher at the University of Cape Town.

To pay for monitoring and treating clinical trial participants at its threatened foreign sites, ACTG will tap its central, approximately $34 million NIH grant, which normally supports activities such as laboratory analysis and new trial design. For example, this central grant could help make up the shortfall for two ongoing ACTG trial sites in Thailand affected by the subaward policy, says Khuanchai Supparatpinyo, an infectious disease researcher at one of these sites, Chiang Mai University. "Although the funding limitation may affect our overall scientific research capacity, I would say that it will not affect our patients' safety," he says.

Bekker has already had to stop five studies testing ways to suppress HIV's replication in an infected person because of the executive order's funding freeze. She notes that trial participants sign onto the NIH-backed studies of experimental interventions with the understanding that the researchers would complete the work. "They put their bodies on the line and now you actually aren't able to answer the question that was intended," she says. NIH has indicated it will still provide some funds to South Africa for trial participants' safety, but has not made it clear how researchers can apply for them.

As the NIH foreign subaward policy threatens to close trial sites outside of South Africa, PHOENIx leaders are still trying to find ways to complete the study. "[NIH has] come up with a policy that's making it really difficult to maintain the integrity of the trial, and we're trying our very best," Gupta says. "But if we can't keep staff and the lights on, then we're going to have some real waste and that will just be a total tragedy." □

IN FOCUS

IMAGE: SCHMIDT *ET AL.*/NJIT/NSO/AURA/NSF

Sun's dancing plasma snapped

Astronomers have captured the clearest images to date of the Sun's outer atmosphere, known as the corona, showing plasma structures dancing and twisting in exquisite detail. Normally, turbulence in Earth's atmosphere causes telescope images of this region to come out blurry. But in a *Nature Astronomy* paper published last week, scientists report using an adaptive optics system—which they liken to a "pumped-up" version of a camera's autofocus—to remove this blur. The resulting videos reveal how solar prominences—large, bright arches extending outward from the Sun's surface—are shaped by the star's magnetic field, while also documenting the "coronal rain" of plasma that falls back toward the Sun's surface as it cools. The new system could help crack enduring mysteries about the corona, such as why it is so much hotter than the Sun's surface. —*Phie Jacobs*

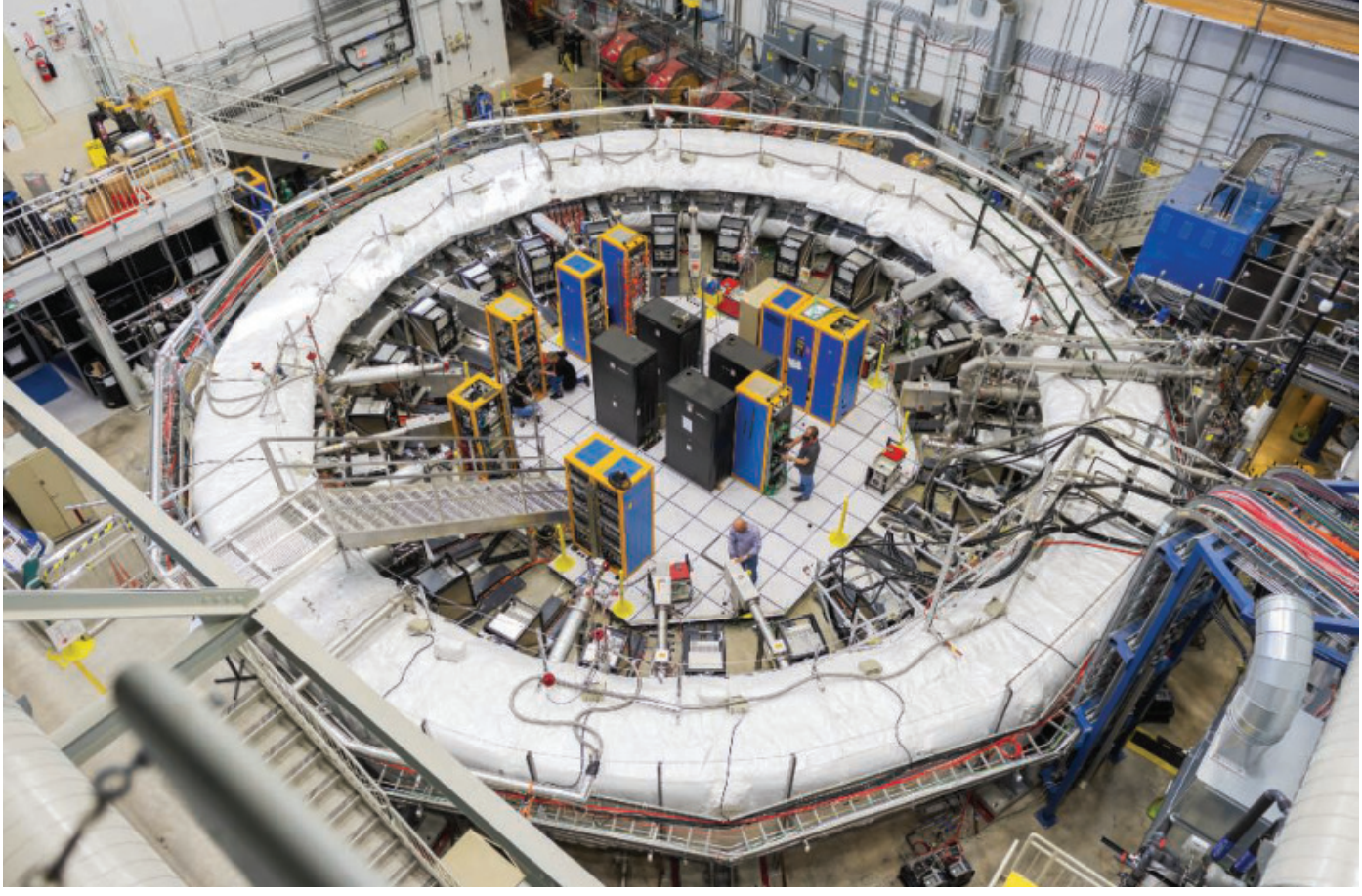

PHOTO: RYAN POSTEL/FERMI NATIONAL ACCELERATOR LABORATORY

PARTICLE PHYSICS

Physicists' best hint of something new vanishes

Long-running experiment concludes muon is no more magnetic than theory predicts **ADRIAN CHO**

More than 1 trillion muons were loaded into this magnetic ring, in batches of 5000.

A famous particle physics experiment has ended not with a bang, but a whimper. For nearly a quarter-century, physicists with the Muon g-2 experiment had reported that a subatomic particle called the muon was more magnetic than predicted by the standard model, the well-tested theory that describes fundamental particles and their interactions. The discrepancy suggested new particles and forces might lurk on the horizon. However, this week the Muon g-2 collaboration presented its final results at Fermi National Accelerator Laboratory (Fermilab) and dashed those hopes: The muon's magnetism exactly matches the latest theoretical results, released a week earlier. The discrepancy vanished not because experimenters previously erred, but because the theoretical estimate changed.

"In the end, the g-2 experimental value is entirely consistent with the standard model," says Aida El-Khadra, a theorist at the University of Illinois Urbana-Champaign. "I can't say I'm not a little sad." However, Sally Dawson, a theorist at Brookhaven National Laboratory, says the new results show how theorists and experimenters can independently determine a particle's property to mind-boggling precision. "It's a triumph."

The muon is a short-lived, heavier cousin of the electron, and is magnetized like a little compass needle. To measure its magnetic strength, physicists fed muons moving at near–light-speed into a 14-meter-wide ring-shaped magnet with an exquisitely uniform field, which causes the particles to run laps around the ring and twirl as they go.

The simplest analysis suggests a lone muon should twirl exactly as fast as it orbits the ring, so its magnetic pole always points in the direction it's going. But quantum theory predicts that "virtual" particles popping in and out of the vacuum of empty space around the muon will boost its magnetism by about 0.1%, an adjustment denoted by "g-2" in physicists' equations. The extra magnetism causes the muon to twirl slightly faster than it orbits, roughly 30 times every 29 laps. Experimenters can precisely measure that precession—and, hence, the muon's magnetization—by studying electrons emitted as the muons decay.

The Muon g-2 experiment first ran at Brookhaven from 1997 to 2001 and found the muon was more magnetic than predicted by 8.6 parts per billion. The tantalizing but not conclusive difference led scientists to lug the ring 5000 kilometers by barge and truck from New York state to Fermilab, in Illinois, in 2013, so they could continue the measurements. The team released a result in 2021 that confirmed the Brookhaven result and another in 2023 that was twice as precise.

Now, the team has upped its precision by another factor of two, measuring the muon's magnetism with a precision of 148 parts per trillion, 9% better than hoped. "Fifteen years ago we wrote down an ambitious goal," says David Hertzog, a longtime col-

laborator at the University of Washington. "And this team beat that goal."

But that measurement no longer disagrees with the prediction. In 2020, a team called the Muon g-2 Theory Initiative published an "official" standard model prediction that disagreed with the experimental result at the time. However, last week, just in time for the latest experimental reading, the initiative released a new value that now agrees with the measurements, old and new.

To predict the muon's magnetism, theorists must account for all the possible ways virtual standard model particles can affect the muon. Calculations involving particles called quarks are particularly thorny because they interact through the strong nuclear force, which is nearly intractable mathematically. In principle, researchers can use data from high-energy particle colliders to deduce those contributions exactly. But the data needed for one particular contribution aren't entirely consistent—a problem worsened last year when physicists with an experiment called CMD-3 in Russia published data that disagreed even more with previous data.

Meanwhile, theorists have been improving a computational technique that simplifies strong-force calculations by mathematically breaking up continuous space and time into a "lattice" of discrete points. After decades of development, multiple groups have produced lattice estimates for the particular quark contribution that are consistent and sufficiently precise, says El-Khadra, who leads the theory initiative. So the theorists replaced the data-driven value with the one from the lattice groups, which changed the standard model prediction.

The move is a vindication for one leading lattice theory group, called the Budapest-Marseille-Wuppertal (BMW) collaboration, which in 2020 had already suggested the data-driven approach was wrong. "I'm very happy that the other lattice groups are confirming our results," says Zoltan Fodor, a theorist at Pennsylvania State University and leader of the BMW group.

One group of experimenters isn't ready to move on. Physicists at the Japan Proton Accelerator Research Complex plan to perform their own g-2 measurement with a much smaller ring and fewer muons. "Ours is the only experiment that can test the Brookhaven-Fermilab result," says project leader Tsutomu Mibe, a physicist with Japan's High Energy Accelerator Research Organization.

But that experiment will be less precise, predicts Lee Roberts, a physicist at Boston University, so the Fermilab result is "the end of the road." A member of the Muon g-2 collaboration from the start, Roberts, who is 78, adds, "I never imagined I would spend the rest of my life on the same experiment. When you've got a good horse, ride it." □

ARCHAEOLOGY

Pre-Columbian Great Lakes farmers transformed the land

Innovative techniques yielded corn, beans, and squash for 600 years before European contact

ANDREW LAWLER

With brutal winters and poor soil, Michigan's Upper Peninsula seems an unlikely place to grow crops. But researchers working with the region's local Menominee tribe have uncovered evidence that Indigenous peoples in the area built a vast, sophisticated agricultural network that yielded prolific quantities of corn, beans, and squash for 6 centuries before Europeans arrived.

"The extent of these systems is quite amazing," says archaeologist Susan Kooiman at Michigan State University, who wasn't involved with the work, which appears today in *Science* (p. 1082). "This really challenges our preconceived notions about agriculture in the northern Great Lakes region." Kooiman adds that the fields' scale and sophistication surpass anything seen before in the pre-Columbian eastern United States.

The work centered on the Sixty Islands site, an area just across the border from Wisconsin long associated with the Menominee people. "This special place tells us where we've come from and where we're going," says David Grignon, the tribe's historic preservation officer and study co-author. The Menominee partnered with Dartmouth College environmental archaeologist Madeleine McLeester and colleagues to survey the site with drone-based lidar, which uses lasers to map hidden surface features.

The researchers were stunned to find an intricate system of fields made up of long, low ridges spanning nearly 100 hectares. Excavating confirmed that farmers used compost and likely gathered rich soil from nearby wetlands to improve the land's fertility. Radiocarbon dates from charcoal showed these activities took place between 1000 and 1600 C.E.

"The agriculture here is so much bigger and denser than what we see anywhere else in eastern North America," McLeester says. With no sign of nearby large population centers, "these results blew our minds."

She notes such ridges, between 10 to 35 centimeters high, function as raised beds, retaining moisture and heat that provide for a slightly longer and more productive growing season than conventional fields. "There were no beasts of burden, so this was all done by hand," McLeester says.

Diseases brought by Europeans devastated the communities who farmed these lands. After, forests grew and hid its agricultural legacy.

The ridges were of variable lengths and orientations, suggesting they were created by different groups rather than the result of a master plan. "This shows that you can have really significant changes to the landscape without chiefs or kings," notes Michael Adler, an archaeologist at Southern Methodist University.

The ridges were in use during the Mississippian culture, which between 600 and 1400 C.E. produced the only pre-Columbian urban areas north of the Rio Grande. Although its heartland was around Cahokia, in today's East St. Louis, Illinois, its influence reached at least as far as Aztalan, a large Mississippi-style settlement 300 kilometers south of Sixty Islands in today's southern Wisconsin. Kooiman speculates that the ridges reflect the influence of these mound builders, and that the fields may have produced food to trade with the copper-producing areas around Lake Superior.

Alder hopes lidar will be used to search for more traces of agriculture across the wooded areas of the Great Lakes as well as New York state and New England. Kooiman agrees. "We haven't looked carefully enough and assumed that only complex societies could make these kinds of dramatic landscape changes." She also notes that the Dartmouth-Menominee partnership is an important model for future studies. "Such collaboration is the future of American archaeology." □

FEATURES

HAZY FUTURES

Projecting the local impacts of global warming is a stubborn challenge. But cities need answers fast

A wastewater treatment plant isn't top on everyone's sightseeing itinerary. But on a cloudless, breezy day in April, Agmed Weber, operations manager for the Walnut Creek plant—which handles more than half of the sewage here in Texas's booming capital city—is an enthusiastic tour guide. He marvels at the foresight of those who built the jumbo plant a half-century ago, when Austin was a third of its current size. "They were really thinking about the future," he says. Weber feels a similar pressure—to prepare for not only continued population growth, but also a hotter future. Austin is "in a tight space where we need to think ahead," he says.

The plant is dominated by vast outdoor pools in which microbes chew through waste until it is clean enough to return to rivers. But in one corner sit two large tanks and a series of purple pipes that route some of the treated wastewater back to the city to water lawns or flush toilets. Based on a climate study that predicts more severe droughts in Austin's future, the city is planning, by 2050, to increase the amount of reused wastewater by more than 10 times, as part of a $1 billion expansion of the plant. "That program is going to grow exponentially," Weber says.

Like many cities around the world, Austin is now facing questions about how to build and adapt for a changing climate. A growing number of these cities—as well as insurance companies, home builders, and farmers—are turning to climate modelers for answers. But despite decades of effort, forecasting how global warming will play out on a local scale remains a stubborn challenge, riven with uncertainty. There is little agreement on how best to convert climate models, which simulate the entire world at coarse resolutions, into the detailed local

PAUL VOOSEN in Austin, Texas

PHOTO: TONY GUTIERREZ/AP

In 2011, a record drought dried up reservoirs in central Texas, raising fears that global warming will further stress local water supplies.

forecasts of temperature and rainfall that planners crave. Different methods lead to drastically different projections, especially in terms of rainfall—even when using the same climate model. "It really is a mess right now," says Alex Hall, a climate scientist at the University of California, Los Angeles.

The problem has become more pronounced with the discovery that global climate models, good at the big picture, often miss local impacts that are already painfully evident. For example, despite nailing the overall pace and intensity of global warming, models did not predict the more frequent heat waves that are plaguing Europe. In order to make local forecasts, modelers must not only do the global-to-local conversion, but also adjust for these model biases. Tiffany Shaw, a climate dynamicist at the University of Chicago, calls this "the other climate crisis." "The cat's going to get out of the bag, and the question will be, what value does this information have?"

While scientists fret about the limitations of their models, others are not as cautious. Dozens of firms have sprung up selling climate risk products, often promising unrealistic levels of detail, down to a city block. "It's unfortunately closer to a Wild West scenario right now," says David Lafferty, a climate scientist at Cornell University. "There is a real need to evaluate those products."

But there is little time. City by city, county by county, decisions must be made about the capacity and resilience of infrastructure in a fast-approaching future that humanity has never experienced. Deep in the heart of Texas, reservoirs need to be built and pipes need to be laid.

LOCATED IN THE DRY Texas Hill Country, Austin has always depended on the Colorado River for its water. Not *that* Colorado River, but rather the

Texas Colorado River, which slashes nearly 1400 kilometers through the state before emptying into the Gulf of Mexico. The Colorado was a source of life, but also of hardship when it flooded or dried up. Finally, in the late 1950s, the state built a series of dams, creating reservoirs. One sits astride Austin's downtown: a long placid lake lined with boardwalks, running trails, and the reflections of newly built high-rises.

The reservoirs made Austin more resilient but not impregnably so. From 2008 to 2016, the city suffered its worst drought since the 1950s. Reservoir levels dropped by two-thirds. Residents faced severe water-use restrictions, and farmers downstream lost billions of dollars' worth of crops. It was a scary time, says Marisa Flores Gonzalez, who leads water resources planning at Austin Water, the city's utility. "When you're in the middle of a drought that's very severe, you don't know where the bottom is."

Prompted by that drought, Flores Gonzalez and her colleagues wondered how much lower the bottoms might be in a warmer future. "We are a land of extremes," she says. "We have to be prepared." At the state level, Texas does not factor climate change into assessments of future drought risk, a policy that may reflect the dominance of climate-skeptical Republicans in its government. But Austin, the state's leading Democratic stronghold, is under no such restriction.

Flores Gonzalez had studied the Texas landscape from an early age. As a teen, she helped her father with his small business, which used geographic information systems (GIS) tools to help energy and water utilities plan infrastructure. In college at the University of Texas (UT) at Austin, she first pursued an English degree. "I was going to be the next great Mexican American writer," she says. Then the 2008 recession hit, and she switched to geography. "I knew utilities. I knew GIS. And so I adjusted my plans."

She joined Austin Water just as the city kicked off a study of its future water supply, an effort it calls Water Forward. The scientists who contributed to the first report followed standard practice at the time. They took the outputs from 20 different global climate models (using only the most severe greenhouse gas emissions scenario—one now seen as implausible). They took temperature and rain measurements from local weather stations and adjusted them based on the projected climate change signal. Then they used those forecasts to estimate the key factor for water infrastructure: future flows in the Colorado near Austin.

In some ways, the projections that ended up in the 2018 report weren't surprising: Austin would have more dry days, and on days when it did rain, it would rain more, reflecting the ability of warmer air to hold more water. Overall, annual flows on the Colorado in the last 2 decades of the century would be 30% lower than today's.

But a few outliers among the 20 models suggested that, because of extreme rainstorms, annual flows in some years could end up seven times today's annual average—an Amazonian prediction that didn't sit right with Flores Gonzalez and made her question the whole modeling process. Austin was preparing to be drier. But should it really prepare to be wetter, too?

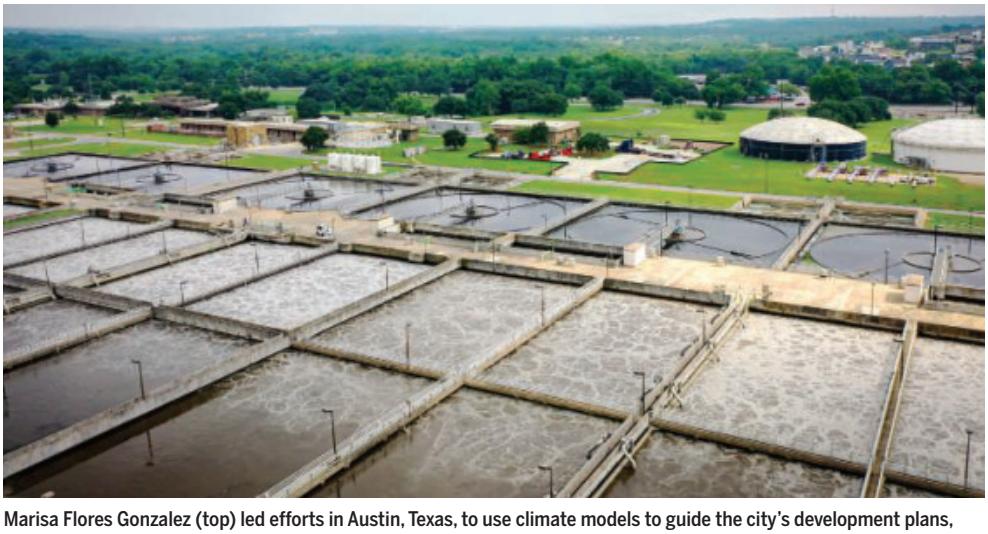

Marisa Flores Gonzalez (top) led efforts in Austin, Texas, to use climate models to guide the city's development plans, which include boosting the reuse of treated water from its Walnut Creek sewage plant (bottom).

PHOTOS: AUSTIN WATER

WHEN YOU HEAR the phrase "climate model," it's tempting to think researchers have created a silicon simulacrum of the planet, down to the finest detail. But because of computational constraints, most climate models simulate the planet coarsely, dividing the atmosphere and oceans up into gridlike boxes 100 kilometers wide or more. Using the equations of fluid dynamics, the models calculate how the atmosphere evolves as energy and moisture flow from box to box in discrete time steps.

Big picture, the models get a lot right: They've precisely charted the nearly 1.5°C rise in temperatures the world has experienced since the 1800s, along with accelerated warming in the Arctic and over the continents. "The basic physics is sound," says Timothy Palmer, a climate

Unwelcome surprises

Climate models are good at the big picture of global warming, but at a regional level they have blind spots. With decades of observations in hand, researchers can now identify local climate trends the models failed to predict.

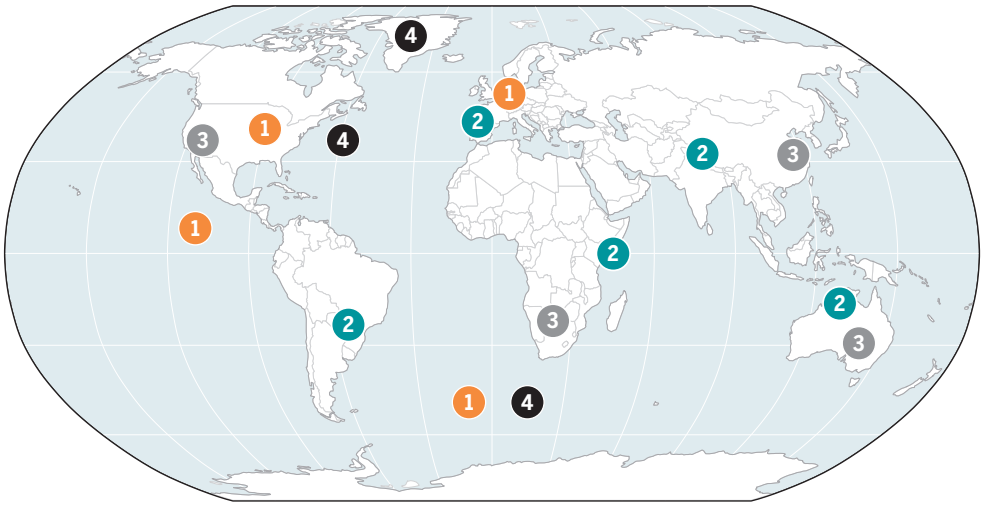

1 Temperature
Europe has faced unexpected summer heat, whereas the Southern Ocean; eastern, tropical Pacific Ocean; and U.S. Midwest have stayed cooler than predicted.

2 Rainfall
Models fail to capture rising rainfall in South America and Australia and drying in East Africa, Europe, and northern India.

3 Humidity
Because warmer air can hold more moisture, models predict rising humidity in many arid places. But such changes have not occurred in the U.S. Southwest and elsewhere.

4 Winds
Unforeseen shifts in wind patterns have led to more stalled, sunny weather over Greenland. They have also strengthened the jet stream over the Atlantic Ocean and intensified storm tracks over the Southern Ocean.

scientist at the University of Oxford. But they do have stubborn biases, particularly when it comes to how winds and moisture flow around the planet. Those biases often emerge not from the equations of fluid dynamics, but rather the empirical codes used to handle processes, such as cloud formation, that the models can't simulate directly.

Until recently, Shaw says, "we were making predictions of worlds we couldn't see." But with the warming so strong now, and with several decades of observations in hand, climate scientists can now identify model flaws by comparing their predictions with what has transpired in the real world.

Last year, Shaw co-led a workshop that confronted the problem head on, leading to a paper this year in *Science Advances* that ran through a laundry list of the models' failures. Not only did they fail to predict heat waves in Europe, but they also missed a cooling in the eastern tropical Pacific Ocean. They overlooked the strengthening of the North Atlantic jet stream in winter, which increases rain and snow in Northern Europe, and they also missed the more frequent occurrence of stalled high-pressure systems over Greenland, which bring sunny days and rapid ice melt. They failed to capture a cooling in the Southern Ocean, and they predicted that arid regions would get moister when they didn't. "I really think this is a time of reflection and maturation," Shaw says.

GIVEN THE MODELS' limitations, many climate scientists eschew regional projections and think the even harder task of making hyperlocal predictions is a fool's errand.

But a whole field nevertheless arose to do just that. Like investigators in a crime procedural show who magnify a telling detail in a photo, somehow increasing its pixel density in the process, these approaches aim to wring local detail from a coarse global picture.

One way to do this "downscaling and bias correction," as it is known, is by taking the output from a global climate model and feeding it into another model that covers a smaller area at high resolution. Such models can capture the details of storms and the way mountains affect weather, but because they still rely on input from the global models, they inherit biases that must be accounted for. And they are computationally expensive to run: A supercomputer that can run a global model would not have the power to simulate Texas alone at a resolution of 10 kilometers.

A more common—and computationally cheaper—method was pioneered several decades ago by Andy Wood, a hydrologist at the National Center for Atmospheric Research. He took daily, local records of temperature and precipitation, averaging them together to match the grid size of a global climate model and its monthly cadence. He could then compare the historical records with the climate model to gauge the magnitude of the model's bias. Finally, after adjusting the local records based on the model's forecast for the region, he undid the averaging imposed at the start to create new high-resolution climate projections.

By now, these techniques have proliferated into a whole cottage industry of ever more complex statistical matching. But the complexity hasn't brought certainty. Even when the same climate model is used for the exact same region, the adjustments can produce widely varying results, as Wood and others laid out in a study in *Environmental Research Letters* (*ERL*) in April. For example, one method predicts the Pacific Northwest should expect 90 millimeters of summer rain by 2100; under another, that projection drops in half. For other parts of the United States, like the Rocky Mountain West, the choice of method can mean the difference between expecting more rain than the present—or less.

The adjustments can also wipe out any trends predicted by a climate model. Last year, Auroop Ganguly, a climate scientist at Northeastern University, and his colleagues applied a widely used downscaling and bias correction method to two different outputs: real climate model data and random noise. To their shock, the results were statistically indistinguishable. Every lesson from the model was lost, they found in a study published in *ERL*. "All the science that goes into building these earth system models was rendered meaningless,"

> **"We still have no real confidence to determine that one downscaling method is better than another.**
>
> **Andy Wood**
> National Center for Atmospheric Research

CREDITS: (GRAPHIC) V. PENNEY/*SCIENCE*; (DATA) T. SHAW *ET AL.*, *FRONTIERS IN CLIMATE*, **6**, 1391634 (2024)

Ganguly says. Adaptation planners and scientists in developing countries use the technique, so its shortcomings could have practical consequences. "The implications are really serious," Ganguly says.

Wood has grown frustrated as downscaling methods have gotten more elaborate. "We still have no real confidence to determine that one downscaling method is better than another" at projecting future climate, he says. "At some point it becomes unpalatable. It, to some extent, destroys confidence in the results."

He also wonders whether the projections from global models, however coarse and unreliable, are good enough for practical purposes. "It may get you to the same decision for your infrastructure as if you went through that increasingly unpalatable process," he says.

THE FIRST Austin Water Forward report was a tremendous learning experience for Flores Gonzalez, who now comfortably drops climate science jargon like "CMIP"—the acronym for the Coupled Model Intercomparison Project, of course. When city officials began planning a second report in 2018, they wanted the best possible projections. They created an advisory group to provide real-time peer review of the process. And this time the city hired climate scientists at UT, including Zong-Liang Yang and his graduate student at the time, Sabiha Tabassum.

Yang and Tabassum made several changes at the start. First, they used projections for high-, medium-, and low-emission futures, representing a broader spread in possibility. Second, knowing the different biases that existed, they didn't treat every climate model as equally valid. Rather, they sifted through 35 climate models and found the ones that best captured the Texas climate. This filtering led them to five models, from South Korea, Australia, and Europe. "We have high confidence they are giving the right results for the right reasons," Yang says.

All too often, local climate projections skip this step, says Douglas Maraun, a climate scientist at the University of Graz. "The key aspect is model evaluation." Often researchers use the model they are most comfortable with, whatever it says—or they use a global suite of data that has already been downscaled. Such global data sets are particularly problematic, as rarely does one model handle everywhere in the world well, says John Nielsen-Gammon, the state's climatologist at Texas A&M University. "The users of downscaled information typi-

Zooming into the future

Global climate models (GCMs), which divide the planet up into coarse grid cells, can project the world's fate under global warming. But applying these results at the scale of a city or farm is a persistent challenge.

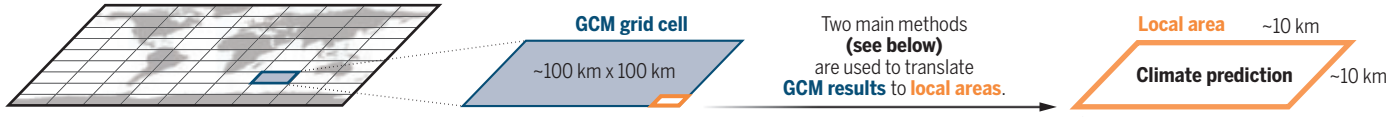

For example, a GCM might predict average monthly rainfall for a **grid cell*** decades into the future.

But even a 100-kilometer grid cell is too coarse to make predictions that local officials want.

Both are fraught with problems.

Statistical downscaling

By comparing GCM results for the past with weather station measurements, the model results can be adapted to a local region.

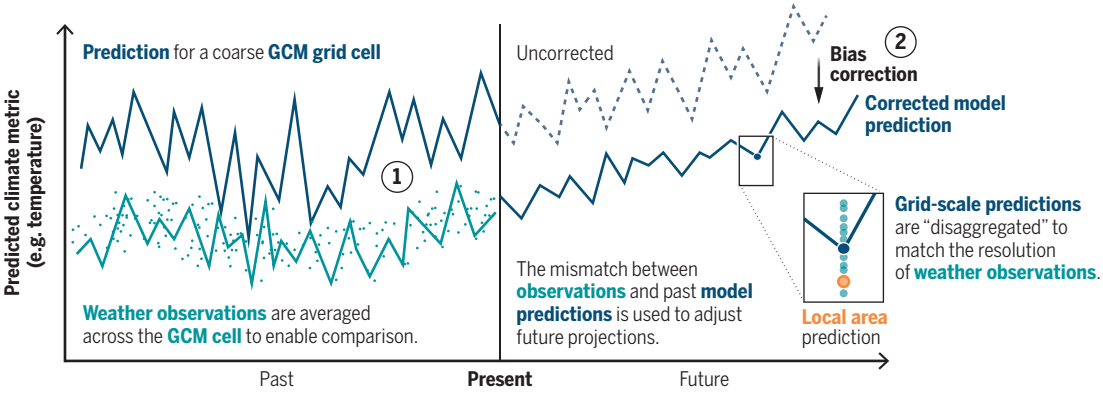

WEAKNESSES

1. Assumes correlations between historic weather and GCM do not change in the future
2. Different statistical methods produce different results.

Regional climate models

Researchers can also obtain local predictions by feeding GCM results into a high-resolution regional climate model (RCM).

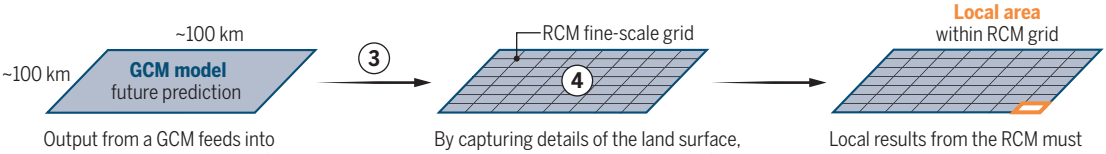

Output from a GCM feeds into the smaller grid cells of an RCM.

By capturing details of the land surface, such as mountains and lakes, the RCM can make more accurate projections.

Local results from the RCM must still be bias corrected using historical observations.

WEAKNESSES

3. Inherits GCM's biases
4. Requires supercomputer, making it infeasible for many users

GRAPHIC: M. HERSHER/*SCIENCE*

cally do not know what the strengths or weaknesses are."

The UT team converted the models' output into a regional forecast using standard downscaling and bias correction methods. But because the models tracked the region so well, Yang says, the corrections were relatively minor. After that, the data were converted into Colorado River flow, the numbers that mattered for Austin.

The results looked more plausible than before. The number of dry days increased, while rain grew concentrated into more severe storms. "But those extreme flows were less prevalent in this round than the last one," Tabassum says. After integrating these projections with others, such as population growth, the team found that, in half of the scenarios considered, the city would begin to run out of water in 2070.

The new Water Forward report, approved by the Austin city council late last year, includes strategies to forestall that future. The city should drastically expand its use of reclaimed water in its distinctive purple pipes. It should encourage its residents to use less water. It should explore storing water in a dedicated underground aquifer for use during drought; it should add a backup reservoir, an existing lake previously used by a power utility; and it should study the possibility of desalinating groundwater. Finally, the report said, the city should prepare for true emergency scenarios where treated water from its sewage plant would be fed back into a reservoir and reused as drinking water.

In short, it said: The future is drier—and riskier—but still livable.

THE NEXT TIME AUSTIN—or any other city—sets out to forecast its climate future, it may have better tools. Last year, the National Oceanic and Atmospheric Administration funded a project co-led by Benjamin Kirtman, an atmospheric scientist at the University of Miami, to pit different downscaling techniques against each other, applying them to different climate models and seeing how the results diverge. "Do this over and over again and you can ultimately assess how well they work," he says. His ultimate aim is to help develop the underpinnings of a climate projection service for wide use by local governments.

Later this year, Berkeley Earth, a California climate nonprofit previously known for its focus on historical climate records, will debut another approach, which it calls its Climate Model Synthesis. The project will take 40 global climate models and, for each region in the world, find the ones that best match historical observations. It will then use a machine-learning algorithm informed by Berkeley Earth's high-resolution temperature record to downscale the results. The end result should be local, reasonably accurate projections that reflect "the breadth of uncertainty and expertise represented by the models," says Robert Rohde, Berkeley Earth's chief scientist.

Another route is to forgo downscaling and bias correction and instead build global climate models at superhigh resolutions. That's the drive at Destination Earth, an EU initiative costing more than €300 million that has now run prototype global models at a 5-kilometer resolution, using some of the world's most powerful supercomputers. "The idea is to operationalize climate projections for the first time" by regularly updating these projects, says Irina Sandu, its director. "It's creating a globally consistent map of downscaled information."

But even with all its computing power, the team has only been able to complete projections out to 2040. And running the models multiple times to capture the spread of possibilities is prohibitively expensive. That's why Sandu and others believe they will need to take advantage of the promising ability of artificial intelligence (AI) to emulate climate models and repeat their runs quickly—an approach that is already catching on for ordinary weather forecasting, with the European Centre for Medium-Range Weather Forecasts (ECMWF), the world's leading forecaster, pioneering it.

ECMWF and Google, among others, have teams looking at how to use such advanced AI to entirely replace the downscaling done by high-resolution regional climate models. After training on a climate model, Google's AI substitute proved particularly good at capturing compound extremes such as high heat and winds. "It allows us to really sample all the possible states of the atmosphere," says Ignacio Lopez-Gomez, who led a Google study published in April in the *Proceedings of the National Academy of Sciences*. And the limited computation needed to run it could make its power widely available.

EARLY ONE MORNING back in downtown Austin, Boyce Freitag descended into an underground concrete cistern the size of a large rowhouse. From a balcony, he looked onto the dark pool below. Light from a hole in the ceiling illuminated the grimy patina of the cistern's walls. "Hope spiders don't give you the skeevies," he says. Originally built for a defunct power plant, the cistern found a purpose again last decade when Austin built its new central library next door. "This is where the magic happens," adds Freitag, the library's building manager.

PHOTO: JOSH HANER/*THE NEW YORK TIMES* VIA REDUX

Although good at projecting global trends, climate models have missed regional phenomena, such as an uptick in clear-sky weather over Greenland that has exacerbated ice melt.

The cistern collects rainwater from neighborhood storm drains, which is then pumped to the gleaming library to flush toilets. It's just one example of where the city is going, Flores Gonzalez says. After the first Water Forward report, the city rolled out leak-detecting smart water meters to nearly every resident. And now new, large commercial buildings will be required to incorporate water reuse into their plans from the start.

Austin Water's collaboration with the UT researchers will continue. Flores Gonzalez takes pride in their analysis of Austin's future, but they still have more to do: They want to better understand just how much river flow could increase in future years when a warmer atmosphere delivers exceptional rainfall, for example. But Austin knows enough to act, she says. "The next 10 years are going to be some of the most important years in Austin Water's history."

The adaptation can't come soon enough. Several years ago, the city once again plunged into drought. And its bottom is still unknown. □

PERSPECTIVES

ECOLOGY

How migrating marine megafauna tracks with conservation

Area-based conservation is not sufficient to protect the ocean's most highly mobile species

Leah R. Gerber[1] *and* **Katrina Davis**[2]

Humpback whales can migrate for thousands of miles to different areas for breeding, calving, and feeding.

Despite growing global commitments to protect ocean biodiversity, conservation falls short in safeguarding the species most vital to ocean health. On page 1086 of this issue, Sequeira *et al.* (*1*) report an extensive dataset representing 15,000 tracked marine megafauna and show that less than 8% of the area used by tracked individuals overlaps with designated marine protected areas. By identifying specific, predictable areas that remain largely outside existing conservation frameworks, the authors propose important marine megafauna areas. As policy-makers rally behind ambitious targets, including the 30×30 goal—to protect 30% of the ocean by 2030—and the United Nations High Seas Treaty, the findings of Sequeira *et al.* offer an empirical foundation to align conservation efforts with the movements and needs of highly migratory marine species.

Sequeira *et al.* systematically combined data from many disparate sources covering 11 million geopositions from nearly 16,000 animals across 121 species to get a global picture of the ocean space used by highly mobile marine megafauna—from whales to sharks to seabirds—revealing that 66% of the area they occupy predominantly functions as critical migratory corridors or residence areas. The data synthesis points to the tremendous potential of marine animal tracking data to inform conservation planning on an unprecedented scale. The study also highlights a persistent gap between data collection and its applications in policy. The authors adopted a retrospective approach, mapping species movements to infer conservation priorities, particularly through marine protected areas, where human activities are managed or restricted to conserve marine ecosystems, biodiversity, and cultural resources. This strategy reflects a broader trend in conser-

PHOTO: PAUL SOUDERS/WORLDFOTO/MINDEN PICTURES

vation science in which efforts often begin with gathering data rather than posing management-driven questions. As the world faces substantial biodiversity challenges, future work should build on clearly defined conservation goals that are informed by rigorous science that links management actions to conservation outcomes. This could involve, for example, designing networks of marine protected areas or other interventions that protect species during life-history stages that are most critical to the growth rates of populations and long-term viability of the species (*2, 3*). Furthermore, aligning conservation goals to the technical, political, or economic feasibility of available management actions (*4*) can help prioritize and focus data collection to design interventions that most effectively address those objectives.

Although the focus of Sequeira *et al.* on marine protected areas is understandable given the prominence of this management strategy in policy-making, this emphasis can unintentionally oversimplify the diverse threats facing marine megafauna. Marine protected areas are a vital part of the conservation toolkit, but as Sequeira *et al.* indicate, they are not a panacea—especially for wide-ranging species that regularly traverse multiple government jurisdictions, such as gray whales, which migrate through regions governed by three countries (*5*). Effective conservation must account for the timing, location, and nature of interactions between these animals and threats such as bycatch, ship strikes, ocean noise, plastic pollution, and whaling (*6*). These problems are often addressed in fragmented ways that fail to capture the cumulative impacts that marine species face throughout their migratory journeys.

One illustrative example is whaling—one of the few ocean threats regulated at the global level. Although still a controversial topic, whaling now contributes relatively little to overall human-caused mortality compared to other, less-regulated threats. Yet, most public discourse on whale conservation focuses on whaling activities. By framing whaling within a broader context of cumulative impacts, the conservation dialogue shifts to where the real problems are occurring, thereby focusing efforts on solutions that will maximize conservation impacts. Such an approach is equally relevant for other marine species that migrate over long distances, such as sea turtles, seabirds, and pelagic sharks.

The goal of the 30×30 initiative has galvanized international momentum, yet its impact depends on clearly articulated outcomes. Rather than asking what percentage of habitat should be protected, the community might instead ask what level or kind of protection is needed to reduce extinction risk or to maintain the ecological roles of marine megafauna and which life stages or activities (e.g., migration or residency areas) should be targeted. Conservation goals should be grounded in these kinds of a priori predictions and measurable outcomes.

To realize such results, conservation planning must evolve to integrate diverse datasets and assess the relative importance of different threats for each species or group—as well as incorporate information on how likely management actions are to achieve targeted changes (*7*). This approach would enable more strategic allocation of resources (*8*) and allow conservation efforts to focus on the most pressing drivers of decline. The important marine megafauna areas framework introduced by Sequeira *et al.* is a major step toward identifying key spatial overlaps between different species and human activities, also opening the door for more comprehensive analyses.

Mobility and migration data remain one of the neglected traits of macroecological studies, with a few exceptions that have been limited to the terrestrial realm. Yet, those terrestrial examples have provided key insights into the effects of human activities on animal performance (*9*), ecological processes (*9*), and biodiversity trends (*10*). The role of mobility and migration in the marine realm is likely more important for the ecology and evolution of species than on land, because movement is energetically less costly through water than through air (*11*). Connecting information on the functional and life-history traits of marine species with the rich tracking dataset from Sequeira *et al.* provides a timely opportunity to investigate how marine megafauna are responding to anthropogenic threats.

Beyond identifying marine regions of high biodiversity or movement, determining how species interact with environmental and human threats should help identify feasible management actions. For example, how frequently do migratory species encounter bycatch hotspots, and which mitigation measures are most effective? Other questions surround the effectiveness of mitigation measures and their expected economic or sociopolitical costs. Another concern is the impacts of noise pollution and how those compare to, and intersect with, the effects of fisheries on marine megafauna. Adopting a threat-based framework (*12*) rooted in systematic decision-making not only informs where marine protected areas might be most critical but also informs complementary interventions—such as modifying fishing gear or implementing vessel speed reductions—that extend beyond protected zones.

Transparency around the intentions and outcomes of large-scale data initiatives is crucial. Long-term monitoring has often paved the way for unanticipated discoveries. However, without clearly defined goals prior to accessing such a rich resource, there is a risk of becoming sidetracked by exploratory analyses that may lead to less robust or spurious findings. Substantial investment has gone into global marine animal tracking, and understanding what conservation gains have been or could be achieved is key. By ensuring that future efforts are targeted at areas or threats that cost-effectively improve species outcomes, rich datasets can be leveraged for tangible species protection, in addition to describing movement patterns.

The findings of Sequeira *et al.* provide a forward-looking change in marine conservation. Data must serve decision-making, not just documentation. Conservation strategies should be rooted in clearly defined goals, informed by threats, and measured by their past or expected success in reducing harm to vulnerable species. Although the important marine megafauna areas framework offers a compelling spatial lens, its value will be maximized when drawing upon knowledge of individual species' traits and life histories (*13, 14*) and combining this knowledge with a diverse suite of management tools that reflect the complexity of governing marine ecosystems (*15*).

The future success of marine megafauna conservation will depend on implementing targeted, scalable strategies that transcend political boundaries and address multiple stressors. With the work of Sequeira *et al.* as a foundation, it is time to embrace outcome-oriented, evidence-based conservation—not just to meet targets, but to make a measurable difference for the ocean and its most iconic species. □

REFERENCES AND NOTES

1. A. M. M. Sequeira *et al.*, *Science* **388**, 1086 (2025).
2. D. T. Crouse, L. B. Crowder, H. Caswell, *Ecology* **68**, 1412 (1987).
3. P. W. J. Baxter, M. A. McCarthy, H. P. Possingham, P. W. Menkhorst, N. McLean, *Conserv. Biol.* **20**, 893 (2006).
4. L. R. Gerber, K. D. Hyrenbach, M. A. Zacharias, *Science* **307**, 525 (2005).
5. S. K. Hooker, L. R. Gerber, *Bioscience* **54**, 27 (2004).
6. M. C. Bottrill *et al.*, *Trends Ecol. Evol.* **23**, 649 (2008).
7. L. R. Gerber *et al.*, *Science* **362**, 284 (2018).
8. M. A. Tucker *et al.*, *Science* **359**, 466 (2018).
9. W. Jetz, D. S. Wilcove, A. P. Dobson, *PLOS Biol.* **5**, e157 (2007).
10. J. H. Steele, *Nature* **313**, 355 (1985).
11. L. Mair *et al.*, *Nat. Ecol. Evol.* **5**, 836 (2021).
12. R. S. Beltran *et al.*, *J. Exp. Biol.* **228** (suppl. 1), JEB247981 (2025).
13. C. C. P. Cosset, J. J. Gilroy, D. P. Edwards, *Conserv. Biol.* **33**, 66 (2019).
14. S. A. Levin, J. Lubchenco, *Bioscience* **58**, 27 (2008).
15. M. Di Marco *et al.*, *Conserv. Biol.* **30**, 189 (2016).

ACKNOWLEDGMENTS

This work took place while L.R.G. was a visiting fellow at the Oxford Martin School and Wadham College at the University of Oxford.

10.1126/science.ady4423

[1]Center for Biodiversity Outcomes and School of Life Sciences, Arizona State University, Tempe, AZ, USA. [2]Department of Biology, University of Oxford, Oxford, UK.
Email: leah.gerber@asu.edu

BATTERIES

Keeping in contact with lithium

Sodium in the lithium anode promotes fast discharge in a solid-state battery **Dominic Spencer-Jolly**

Solid-state lithium batteries are considered an attractive option for powering electric vehicles because of substantial improvements in their energy storage capacity and improved safety. However, the interface between the lithium metal anode and the solid electrolyte is structurally unstable, which causes deterioration at the point of contact at the interface and ultimately battery failure, even at moderate rates of discharge. Preventing this contact loss during operation often requires applying an impractically high compressive force to the battery cell (a high stack pressure). On page 1062 of this issue, Yoon *et al.* (*1*) report that adding electrochemically inactive sodium to the lithium metal anode improves the interfacial contact, even under a low stack pressure. This could unlock a large-scale solid-state battery capable of the fast discharge rates required for the acceleration of electric vehicles.

A thin layer of lithium is plated onto the anode during charging of a solid-state battery. By contrast, when a solid-state battery is discharged, lithium atoms are removed from the surface of the anode and transported as lithium ions across the solid electrolyte. Each stripped atom creates a vacancy in the lithium metal anode at the interface with the solid electrolyte. To maintain interfacial contact, these vacancies must diffuse through the anode away from the interface at a rate that is faster than formation of new vacancies; otherwise, vacancies accumulate at the interface and create empty pockets known as interfacial voids (*2*). These voids reduce the interfacial contact area and cause current to focus at small areas during charging, which increases the local rate of lithium plating. This can trigger dendrite growth—the formation of microscopic filaments of lithium metal that penetrate through the solid electrolyte, causing a short circuit—even when the rate of charging is relatively low (*3*).

The maximum discharge rate of a solid-state battery is thus determined by the rate of vacancy diffusion in the lithium anode. Fast diffusion of vacancies enables a high rate of discharge without the formation of interfacial voids. To achieve this, a compressive force is often applied to a battery. A high stack pressure induces creep (time-dependent deformation under a constant stress) in a lithium anode. This causes lithium to fill any vacancies along the solid electrolyte interface, preventing interfacial voids from forming. However, stack pressures of 5 to 10 MPa are often necessary to enable modest discharge rates on the order of 1 mA·cm^{-2} (*3*, *4*). Although this is feasible for small laboratory-scale battery cells, it is impractically high for large-scale commercial batteries.

Yoon *et al.* demonstrate a means to mitigate contact loss at the anode–solid electrolyte interface without requiring high stack pressure. Adding 5 to 20% of electrochemically inactive sodium metal to the lithium anode prevented the emergence of interfacial voids. Instead of vacancies accumulating to form voids, sodium metal dynamically accumulated at the interface (see the figure). Because sodium has a lower yield strength (stress before permanent deformation) than that of lithium, the sodium domains deformed and elongated at the solid electrolyte interface to suppress void formation. The authors refer to this dynamic accretion of sodium as "interfacial morphogenesis" owing to its similarity to biological morphogenesis processes by which cells self-assemble into functional tissues.

Interfacial morphogenesis observed by Yoon *et al.* hindered dendrite growth in a solid-state battery. Accumulated electronically conductive sodium metal at the interface distributed the current evenly across the interface at subsequent charging. This promoted homogeneous lithium plating and thus prevented the initiation of dendrite growth. The authors also demonstrated long-term cycling (repeated charging and discharging) of battery cells under relatively low stack pressures (2.5 MPa and lower). The finding is a substantial step toward developing a high-performance solid-state battery that can operate under commercially relevant stack pressure.

The findings of Yoon *et al.* complement a previous study that modified the surface of the solid electrolyte with an interlayer to mediate homogeneous stripping and plating of lithium layers (*5*). These two approaches (interfacial morphogenesis and interlayers) offer new pathways to overcoming instability at the anode-solid electrolyte interface and cycling of batteries under low stack pressures. However, contact loss at the cathode-solid electrolyte interface is equally important. A high stack pressure is also required for this interface to achieve long-term cycling stability (*6*, *7*). Ultimately, preventing contact losses at both electrode-electrolyte interfaces without stack pressure will be a major step toward realizing commercially viable solid-state lithium batteries. □

Interfacial morphogenesis in a solid-state battery

Lithium atoms are stripped from an anode during discharge, creating empty pockets at the anode-electrolyte interface. Adding sodium to a lithium metal anode suppresses the formation of voids and helps maintain interfacial contact. Sodium domains can also hinder dendrite growth and promote uniform lithium plating during charging.

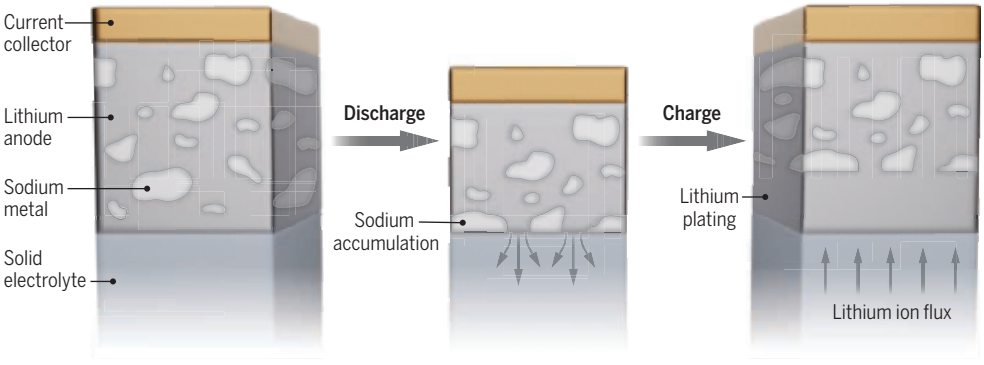

GRAPHIC: N. BURGESS/*SCIENCE*

REFERENCES AND NOTES

1. S. G. Yoon *et al.*, *Science* **388**, 1062 (2025).
2. T. Krauskopf, F. H. Richter, W. G. Zeier, J. Janek, *Chem. Rev.* **120**, 7745 (2020).
3. J. Kasemchainan *et al.*, *Nat. Mater.* **18**, 1105 (2019).
4. M. J. Wang, R. Choudhury, J. Sakamoto, *Joule* **3**, 2165 (2019).
5. Y. G. Lee *et al.*, *Nat. Energy* **5**, 299 (2020).
6. R. Koerver *et al.*, *Chem. Mater.* **29**, 5574 (2017).
7. S. Puls *et al.*, *Nat. Energy* **9**, 1310 (2024).

ACKNOWLEDGMENTS

D.S.-J. acknowledges support from the Royal Society (grant RGS\R2\242573).

10.1126/science.ady3208

School of Metallurgy and Materials, University of Birmingham, Birmingham, UK.
Email: d.h.spencer-jolly@bham.ac.uk

BIOMEDICAL SCIENCE

Nanowires replace lost retinal cells

Tellurium nanowire networks could open up new avenues for artificial vision

Eduardo Fernández[1,2,3,4]

Diseases caused by retinal degeneration are major causes of irreversible vision loss worldwide (*1*). These disorders are characterized by the progressive loss of photoreceptor cells (rods and cones) in the retina, the light-sensitive layer at the back of the eye. However, the other neurons in the retina, including bipolar, amacrine, horizontal, and retinal ganglion cells, often remain largely functional, preserving the connection to the visual cortex via the optic nerve. Retinal prostheses aim to provide a useful visual sense by artificially stimulating these surviving retinal neurons (*2*), but most systems face challenges that include a need for an external power supply and limited stimulation of retinal neurons. On page 1041 of this issue, Wang *et al.* (*3*) present a retinal prosthesis composed of tellurium nanowire networks (TeNWNs), which addresses some of these limitations while also responding to a broader range of the electromagnetic spectrum than rods and cones.

Vision impairment represents a substantial global health challenge. Although clinical approaches based on gene therapy and stem cell therapy, as well as several innovative therapeutics, are becoming available (*4*–*6*), there is no treatment for many causes of blindness. The number of individuals experiencing blindness and visual impairment owing to aging and pathologies such as retinal degenerative diseases is expected to rise (*1*). Therefore, numerous research groups worldwide are exploring alternative strategies for improving visual function in these patients (*2*, *7*), with varying degrees of success (*8*).

Visual prostheses aim to restore some degree of sight by using implanted electrode arrays—commonly made from platinum, platinum-iridium alloys, gold, titanium nitride, or iridium oxide—to electrically stimulate surviving neurons along the visual pathway, thereby generating visual percepts known as phosphenes (*9*). Because blindness is usually of retinal origin, many approaches have focused on the retina as a site for stimulation. These devices typically bypass the damaged or degenerated photoreceptor cells and target surviving neurons within the retina, primarily bipolar cells (subretinal implants) or retinal ganglion cells (epiretinal implants) (*10*). Usually, a camera mounted on glasses captures the surrounding visual scene and uses radio signals to transmit the information to the implant. Nevertheless, despite initial promising results, the performance of retinal implants has fallen short of expectations, ultimately leading to their withdrawal from the market (*11*). The reasons are complex and include limited resolution, difficulties in user adaptation, and challenges in marketing. Furthermore, the surgery needed to implant these prostheses is intricate, and the devices face challenges related to their long-term biocompatibility (interactions with the eye tissues), reliability, and stability (*2*).

To overcome the limitations of existing retinal prostheses, advanced materials, including several types of nanoparticles, carbon nanotubes, graphene, quantum dots, and organic semiconductors, have been proposed (*12*, *13*). Wang *et al.* used TeNWNs to build a subretinal prosthesis for the conversion of incident light into efficient photocurrents. These nanowires range from approximately 10 nm to several hundred nanometers in diameter, with lengths from hundreds of nanometers up to tens of micrometers. Their optoelectronic properties result in substantial photovoltaic conversion, which generates electrical currents in response to both visible and infrared light (see the images). This ability is potentially advantageous for vision restoration because near-infrared light has deeper tissue penetration and higher safety thresholds than visible light (*14*).

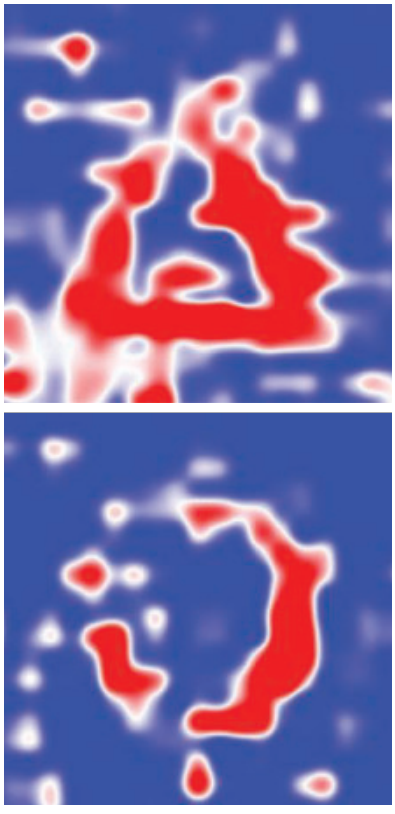

Tellurium nanowire networks generate a voltage response (red) to a triangular (top) and circular (bottom) laser pattern.

IMAGES: WANG *ET AL.*

To evaluate the safety and efficacy of this approach for transmitting light signals and eliciting visual behaviors, Wang *et al.* implanted TeNWNs in the subretinal space of mice and nonhuman primates. This narrow anatomical space is located beneath the retina, between the photoreceptor layer and the retinal pigment epithelium. The implants were maintained for up to 60 days in mice and up to 112 days in nonhuman primates and showed good biocompatibility during this time, although longer-term biocompatibility studies are required. The authors observed robust retinal ganglion cell responses in blind animals with TeNWN implants when stimulated with a customized laser projection system using visible and near-infrared light, and these responses propagated to the areas of the brain that process visual information. Additionally, these animals showed an improved ability to localize light sources and perform simple pattern recognition tasks compared with nonimplanted control animals.

The technology developed by Wang *et al.* shows promise as an effective approach for restoring vision by replacing damaged photoreceptors with TeNWNs, eliminating the need for additional power supply modules. Furthermore, it enables the addition of infrared photosensitivity without apparently disrupting normal vision. Nevertheless, further research is necessary before it can be used clinically. For example, the proposed approach preserves some of the signal-processing capabilities of the retina, but changes in the retinal network during continuing degeneration may affect this processing, potentially leading to a decline in the implant's effectiveness over time (*10*). Moreover, despite the ability of TeNWNs to generate large photocurrents, laser irradiation is still necessary to activate them. Thus, achieving sufficient sensitivity for function in normal daylight without external devices remains a challenge. In addition, implanting TeNWNs involves creating a local retinal detachment followed by a small retinal incision to insert the device into the subretinal space. Performing this procedure in fragile, diseased retinas poses a substantial challenge owing to the risk of retinal detachment, fibrosis, and scarring.

Despite achieving regulatory milestones and demonstrating

some functional benefits, visual prosthetic devices available now do not yet provide a sufficient level of visual improvement to consistently outweigh the associated costs, surgical risks, and intensive rehabilitation required for widespread patient acceptance and market success. Therefore, the long-term success of these technologies depends on developing cost-effective solutions and ensuring their availability to a broader range of patients. As the field evolves, establishing rigorous, standardized criteria for device indications, patient selection, and the optimal timing of implantation for each individual will be fundamental. It will also be important to consider the ethical implications surrounding these technologies, especially their use, accessibility, long-term consequences, and safety (*15*). The ability of these devices to detect light outside the human visible spectrum also warrants consideration. However, translating this information into meaningful and usable visual percepts, rather than just abstract patterns or signals, remains a formidable challenge.

The methodology developed by Wang *et al.* offers the potential for developing a new generation of devices capable of converting light into neural stimulation signals and restoring limited but useful vision to many blind individuals. However, considering previous negative experiences with other retinal prosthesis approaches, it is necessary to avoid creating unrealistic expectations that could adversely affect the advancement of these technologies. □

REFERENCES AND NOTES

1. M. J. Burton *et al.*, *Lancet Glob. Health* **9**, e489 (2021).
2. K. A. Ramirez, L. E. Drew-Bear, M. Vega-Garces, H. Betancourt-Belandria, J. F. Arevalo, *Int. J. Retina Vitreous* **9**, 73 (2023).
3. S. Wang *et al.*, *Science* **388**, eadu2987 (2025).
4. M. E. McClements, M. E. A. A. Elsayed, L. Major, C. M. de la Camara, R. E. MacLaren, *Mol. Diagn. Ther.* **28**, 575 (2024).
5. M. Carleton, N. W. Oesch, *Front. Cell. Neurosci.* **18**, 1502473 (2024).
6. W. S. Tan *et al.*, *Nat. Protoc.* 10.1038/s41596-025-01142-y (2025).
7. J. Tang *et al.*, *Nat. Mach. Intell.* **7**, 627 (2025).
8. E. Fernandez, J. A. Robles, *PLOS Biol.* **22**, e3002896 (2024).
9. E. Fernandez, *Bioelectron. Med.* **4**, 12 (2018).
10. D. Palanker, *Cold Spring Harb. Perspect. Med.* **13**, a041525 (2023).
11. E. Strickland, M. Harris, *IEEE Spectr.* **59**, 24 (2022).
12. G. Lanzani *et al.*, *Nat. Rev. Bioeng.* **2**, 829 (2024).
13. J. Nie *et al.*, *ACS Nano* **19**, 11823 (2025).
14. Q. Zhu *et al.*, *Int. J. Med. Sci.* **18**, 109 (2021).
15. R. Yuste *et al.*, *Nature* **551**, 159 (2017).

ACKNOWLEDGMENTS

The author acknowledges support by grants PDC2022-133952-100 and PID2022-1416060B-100 from the Spanish "Ministerio de Ciencia, Innovación y Universidades," by grant CIPROM/2023/25 from the Generalitat Valenciana, and by INTENSE Dutch Neurotechnology Consortium from Netherlands.

10.1126/science.ady4439

[1]Bioengineering Institute and Cátedra Bidons Egara, University Miguel Hernández, Elche, Spain. [2]CIBER Research Center on Bioengineering, Biomaterials and Nanomedicine (CIBER BBN), Madrid, Spain. [3]John Moran Eye Center, University of Utah, Salt Lake City, UT, USA. [4]Radboud University, Donders Centre for Neuroscience, Nijmegen, Netherlands.
Email: e.fernandez@umh.es

NEUROSCIENCE

The complex role of brain cilia in feeding control

Variants in a ciliary receptor are associated with obesity

Anushweta Asthana *and* **Peter K. Jackson**

Obesity is a complex polygenic disease that stems from misfunctions in cellular signaling pathways that govern energy balance, appetite control, and inflammation. Genome-wide association studies (GWASs) for obesity-related genes have identified a growing list of mutations in genes that encode G protein–coupled receptors (GPCRs), a large family of cell surface receptor proteins that detect many metabolites and hormones to regulate physiology. Several of these GPCRs localize to primary cilia, which are tiny microtubule-based cell membrane protrusions. On page 1042 of this issue, Xun *et al.* report obesity-associated alleles of G protein–coupled receptor 45 (GPR45) in mice. They found that GPR45 is localized to primary cilia in neurons within a key brain feeding control center, the paraventricular nucleus of the hypothalamus (*1*). GPR45 thus joins a complex brigade of neural GPCRs that regulate feeding and is poised to become part of the armamentarium of druggable receptors now actively helping patients control obesity.

Primary cilia are found in most tissues, including the brain and many endocrine glands. They act as antennae that amplify the signaling of highly localized GPCRs, thus propagating sensory, hormonal, and metabolite signals to many tissues that mediate metabolism (*2*). Inherited mutations in components of the ciliary machinery contribute to obesity, diabetes, and multitissue ciliopathies, notably in Bardet-Biedl syndrome, an inherited disorder that presents with high body-mass index (BMI) and diabetes (*3*). Similarly, mice bearing a mutation in the *Tub* gene (tubby mice) have disrupted GPCR trafficking to cilia and obesity (*4*). However, many molecular details of how ciliary GPCRs regulate feeding control and energy expenditure remain unclear. Notably, cilia integrate opposing orexigenic (or obesogenic) and anorexigenic signals, suggesting that they do not simply mediate "on" and "off" signals but fine-tune metabolic messaging. Mutations in cilial components disrupt the balance of these feeding controls.

Hyperphagia (excessive eating) is linked to genetic or pathophysiological defects in hypothalamic feeding centers, including the paraventricular nucleus, which is located at the base of the brain around the third ventricle. This region borders the blood-brain barrier, which receives circulating endocrine signals that make contact with hypothalamic neurons to control food intake (*5*). After a meal, metabolites, including glucose and fatty acids, and endocrine signals released from the gut and pancreatic islets [e.g., peptide YY (PYY) 3-36 and insulin] accumulate in serum and then in cerebrospinal fluid. In humans, these signals typically require around 20 min to reach the brain and activate anorexigenic signals, corresponding to "feeling full" after a meal.

Multiple ciliary GPCRs work in a coordinated fashion to promote satiety and suppress overfeeding. These include the ciliary melanocortin-4-receptor (MC4R), which responds to anorexigenic melanocortins produced in the brain, and neuropeptide Y receptor type 2 (NPY2R), which responds to PYY 3-36 produced in pancreatic islets

and the gut. After feeding, brain-derived melanocortins activate the MC4R, which then activates the G protein $G_{\alpha s}$ (GNAS). GNAS stimulates adenylate cyclase 3 (ADCY3), a ciliary enzyme that catalyzes production of cyclic adenosine monophosphate (cAMP). Ciliary cAMP propagates downstream signals, which ultimately modulate neurons to control feeding behavior. Mutations in the genes encoding MC4R, GNAS, and ADYC3 are among the most common genetic variants linked to obesity *(6, 7)*. In patients with Bardet-Biedl syndrome or in tubby mice, ciliary GPCRs in hypothalamic neurons fail to localize to cilia and thus do not activate neuronal signaling pathways that usually block feeding (*4*). Many patients with rare genetic lesions in ciliary components also exhibit hyperphagic obesity.

To identify additional genes involved in feeding and metabolism, Xun *et al.* performed a chemical mutagenesis genetic screen in mice (*1*). Notably, they identified two obesity-associated missense alleles of the gene encoding GPR45 (*Gpr45*), which mapped to amino acid substitutions Ser to Pro at residue 214 and Tyr to Cys at residue 287. Further mouse experiments established that obesity was caused by overfeeding. Mice with genetic deletion of *Gpr45* (*Gpr45*$^{-/-}$ mice) were also obese and hyperphagic. The authors observed that GPR45 is highly expressed within the hypothalamus. They also found that the obesity-associated missense mutations in *Gpr45* prevented ciliary localization of the receptor and that GPR45 transport to primary cilia requires the tubby-related protein 3 (TULP3), the central controller of GPCR trafficking. To understand how GPR45 modulates signaling, the authors showed that GPR45 expression increases the amount of ciliary GNAS in mice and in cultured cells. In cells, GPR45-dependent translocation of GNAS from the cytoplasm to cilia also increased the amount of ciliary cAMP. Crossbreeding the *Gpr45*$^{-/-}$ mouse line with a line bearing a loss-of-function variant of *Adcy3* did not enhance obesity, suggesting that the two regulators are not independent and thus work in concert.

The GPR45-ADCY3 circuit is coregulated with other receptor signaling pathways, notably the MC4R-ADCY3 pathway. Xun *et al.* found that overexpression of GPR45 in cell culture was sufficient to activate ciliary MC4R, suggesting a link between these pathways. Nonetheless, MC4R agonists were still able to suppress feeding in *Gpr45*$^{-/-}$ mice, suggesting that a strong agonist can bypass coupling between the receptors. Further work is needed to understand the cross-talk among these and other obesity-related receptors. The endogenous ligand of GPR45 is unknown, but identifying this molecule could facilitate the development of GPR45 agonists as obesity therapeutics.

Nonciliary GPCRs, including the leptin receptor (LEPR), also localize to the hypothalamus and other tissues to control both feeding and metabolism. The amount of leptin released increases in proportion to stored fat mass to limit obesity (*8*). The hormone glucagon-like peptide-1 (GLP-1) is also a key regulator of obesity: GLP-1 receptor (GLP1R) agonists are now a central therapy for diabetes and obesity worldwide (*9*). GLP-1 is released from the gut after feeding and binds to GLP1R in the gut, pancreas, and brain, which stimulates food movement, insulin secretion, and anorexigenic signals, respectively. How GLP1R and other GPCRs coordinate feeding is unclear. Moreover, additional receptors and ligands that affect feeding are still being identified. A human GWAS study linked missense mutations in the gene encoding G protein–coupled receptor 75 (*GPR75*) to reduced BMI (*10*). GPR75 deletion confers reduced food intake in mice; this receptor is normally selectively ciliary in neurons (*11*). The GPR75 ligand or ligands remain unknown. Another study found that after exercise, glycolytic production of lactate drives the synthesis of a circulating lactate-phenylalanine conjugate, a potent appetite-suppressing signal (*12*). Here, it is the receptor that remains unknown. Receptors for serotonin, dopamine, and somatostatin also populate cilia in the hypothalamus and may affect feeding (*2*).

The emerging model is that the hypothalamus integrates input from nutrient sensors, smell and taste sensing, and hormone signals from fat, pancreas, and gut to regulate feeding control and energy expenditure. How these various systems are coordinated remains unclear, but disruptions in cilia appear to affect multiple GPCRs and tip the balance toward hyperphagia and obesity. Understanding the molecular mechanisms for cross-talk among GPR45, GPR75, MC4R, LEPR, NPY2R, and lactate-phenylalanine, as well as fatty acid and glucose sensing, will be critical to advance both discovery biology and engineering of targeted therapeutics. As understanding of this repertoire of signals progresses, developing bifunctional or multifunctional molecules that target multiple satiety GPCRs may extend the range and efficacy of presently available GLP1R drugs. For example, adding GPR45 agonist or GPR75 antagonist activity to these GLP1R agonists may create improved therapies. Dual agonists combining GLP1R with other GPCRs have already shown improved efficacy in obesity.

Inherited mutations in components of the ciliary machinery contribute to obesity, diabetes, and multitissue ciliopathies...

The original target and therapeutic hypothesis for GLP1R agonists was to accelerate insulin secretion from pancreatic β cells to treat diabetes. Findings suggest that ciliary GPCR signaling also directly stimulates insulin secretion from β cells and drives adipocyte stem cell differentiation to create new healthy fat cells (*13–15*), which is critical to limit inflammation and diabetes. Thus, the same ciliary gene lesions that affect feeding may also cause reduced insulin secretion and adipose tissue defects, both key drivers of diabetes. By creating therapeutics for relevant ciliary GPCRs, antiobesity effects could potentially be combined with important antidiabetic improvements, providing essential therapies for metabolic disease. □

REFERENCES AND NOTES

1. Y. Xun *et al.*, *Science* **388**, eadp3989 (2025).
2. K. I. Hilgendorf, C. T. Johnson, P. K. Jackson, *Curr. Opin. Cell Biol.* **39**, 84 (2016).
3. C. Vaisse, J. F. Reiter, N. F. Berbari, *Cold Spring Harb. Perspect. Biol.* **9**, a028217 (2017).
4. A. V. Loktev, P. K. Jackson, *Cell Rep.* **5**, 1316 (2013).
5. R. Haddad-Tóvolli, N. R. V. Dragano, A. F. S. Ramalho, L. A. Velloso, *Front. Neurosci.* **11**, 224 (2017).
6. J. E. Siljee *et al.*, *Nat. Genet.* **50**, 180 (2018).
7. E. Mendes de Oliveira *et al.*, *N. Engl. J. Med.* **385**, 1581 (2021).
8. N. Perakakis, O. M. Farr, C. S. Mantzoros, *J. Am. Coll. Cardiol.* **77**, 745 (2021).
9. Z. Zheng *et al.*, *Signal Transduct. Target. Ther.* **9**, 234 (2024).
10. P. Akbari *et al.*, *Science* **373**, eabf8683 (2021).
11. Y. Jiang, Y. Xun, Z. Zhang, *J. Clin. Invest.* **134**, e182121 (2024).
12. V. L. Li *et al.*, *Nature* **606**, 785 (2022).
13. C.-T. Wu *et al.*, *Genes Dev.* **35**, 1243 (2021).
14. J. W. Hughes *et al.*, *Proc. Natl. Acad. Sci. U.S.A.* **117**, 8912 (2020).
15. K. I. Hilgendorf *et al.*, *Cell* **179**, 1289 (2019).

ACKNOWLEDGMENTS

P.K.J. acknowledges support from National Institutes of Health grants R01GM121565 and R01 DK127665 and from Stanford Diabetes Research Center (SDRC) grant P30 DK116074. A.A. acknowledges support from National Institutes of Health grant NIA T32 AG000266. We thank R. E. Turn and M. O. Azizzanjani for providing feedback.

10.1126/science.ady6368

[1]Baxter Laboratory for Stem Cell Biology, Department of Microbiology and Immunology, Department of Pathology, Stanford University School of Medicine, Stanford, CA, USA. Email: pjackson@stanford.edu

POLICY FORUM

CRITICAL MINERALS

A global minerals trust could prevent inefficient and inequitable protectionist policies

Critical mineral supply and demand require global coordination to reduce market volatility and conflict risk

Saleem H. Ali[1,2,3], Daniel M. Franks[2], Jose A. Puppim de Oliveira[4,5,6], Kaveh Madani[3], Owen Gaffney[7,8], Eva Anggraini[9], Leonard Wantchekon[10,11], Xianlai Zeng[12]

The global transition to sustainable energy and infrastructure faces a critical challenge: ensuring equitable access to essential minerals while also providing fair and stable income for mineral suppliers and mitigating the serious risk of resource conflicts. As demand for critical energy transition minerals [defined by the United Nations (UN) as those necessary for renewable energy technologies] surges, their uneven distribution risks heightening geopolitical tensions and the potential for supply chain disruptions. With critical minerals likely to generate considerable discussion at the meeting of G7 countries this month, we propose a Global Minerals Trust to address these challenges, incentivize cooperative resource management for the green transition, and disincentivize the formation of cartels. The Trust would serve as a neutral steward or broker ensuring fair prices for both mineral suppliers and consumers, discouraging a rush toward inefficient new mines, and supporting developing countries with technical assistance to sustainably expand mineral industries.

Under normal trade practices, firms seeking to sell and buy minerals can negotiate ad hoc bilateral deals. But the need for the trust arises because countries with resource supply and those with resource demands may have geopolitical differences that prevent normal trade practices of comparative advantage from being realized. Buyers' and sellers' freedom to engage one another is constrained, for example, by nations imposing export regulations, sanctions, or tariffs. The current trust deficit between the United States and China is emblematic of tensions around mineral supply chains. The geographical concentration of these minerals and their processing in China and a handful of countries has raised concerns about supply security and potential resource nationalism. Geopolitical tensions over access to minerals in locations such as Greenland and Ukraine have led to bilateral dealmaking that might not be anchored in constraints of economic geology or market efficiency. If optimally efficient options are foreclosed by geopolitical constraints, resulting deals will focus on poorer ore bodies that can require more energy and cause more environmental and societal harms to exploit. Environmental and social impacts of mining have led to localized conflicts, which can also constrain supply.

By contrast, a trust is a resource-sharing mechanism, subject to collective governance and coordination rather than an ad hoc bilaterally driven approach, to hold assets for the fair use of beneficiaries who might otherwise feel compelled to compete over them. Trusts can work best where commodities are nonperishable, traceable, and tradable, and thus can be highly appropriate for minerals. The Trust mechanism serves the purpose of an exchange for buyers and sellers that can enable sovereign entities to sell and purchase in a competitive market, while promoting fair access to minerals for broader humankind. This approach offers several benefits to mineral-producing nations, including stable and predictable demand for their mineral resources and access to a global market with fair pricing mechanisms.

The Trust also serves the cause of resource justice concerns by helping to provide a transparently managed trading platform for commodities needed for the green transition. Where producing countries also have demonstrable domestic demand for existing downstream industries for these resources, they would of course have the right to prioritize retention of the minerals for their own use. Exceptions can also be made for downstream products being developed for domestic vertical integration of green technology that would ultimately reach global markets.

Some constituents may interpret the Trust as an erosion of some national decision-making power, yet there is ample precedent for commodity flows being monitored and regulated for global environmental benefits, as exemplified by International Tropical Timber Agreements. Mineral laws in most countries already recognize state property rights, a form of collective citizen ownership rather than individual property rights. Individual benefit can still ensue from collective ownership by the state. The Trust extends the same logic of state ownership with a planetary mandate but ensuring that benefits accrue to the citizens from where the resource is extracted. Sovereignty is most directly enshrined in ownership of the resource itself and the ability to benefit from its use and sale. This would not change; there would simply be assurance of supply. Mediating trade through a trust would avoid constraints of bilateral tensions between nations.

Countries opting into the Trust retain the rights to develop particular projects, which are subject to national laws and permitting decisions and would be developed either by private or public entities. Initially the sale of minerals through the Trust could be limited to existing mines, refineries, and recycling facilities. However, with pooled development, funding new projects could also be motivated by the Trust in ways similar to how countries like Japan have undertaken the Japan Organization for Metals and Energy Security at a national level.

NATURAL RESOURCE TRUSTS

The Trust draws inspiration from the concept of a "common heritage of humankind" (*1*), which has been invoked for minerals within international waters under the UN Convention on the Law of the Sea but remains consistent with the concept of Permanent Sovereignty Over Natural Resources as enshrined in UN General Assembly (resolutions from 1962 and the World Charter for Nature in 1982 (*2*). The Trust also resonates with the emerging governance concept of a "planetary commons" that has recently been considered by the Earth Commission (*3*).

Conceptualizations of a "planetary trust" date back to the work of international law scholar Edith Brown Weiss. A planetary trust, in her view, would consider humanity as a trustee for nature, responsible for sustainable use of resources as well as to improve physical and systems efficiency involved in resource extraction. Later, Weiss's ideas were considered in rulings by the International Court of Justice pertaining to natural resource usage and environmental decline. At the national level, India has noted language related to a trust in its National Minerals Policy: "natural resources, including minerals, are a shared inheritance where the State is a trustee on behalf of the people" (Clause 10, p. 11) (*4*).

Ecological economists in Vermont used this idea to move the state legislature to form a Common Assets Trust that would manage resources such as groundwater and timber to ensure overall sustainable

outcomes and financial dividends for state citizens from their use (*5*). This remains an active area for policy innovation at the local level for benefit sharing of natural assets. Although financial benefits of a minerals trust would accrue to the source country, the material infrastructure benefits of green technologies would accrue to the planet at large.

The Trust's architecture builds on the work of Nobel laureate Elinor Ostrom, who identified principles for creating trust among diverse groups with competing interests in order to sustainably manage common pool resources (*6*). The Earth Systems Governance project over the past two decades has suggested that new institutions such as resource trusts could lead toward "Earth Systems Law" that considers inherent interdependence between national and international law on

Molten copper flows into molds at a smelting plant in Wuzhou, China. Both mined and recycled metals used in green technologies could be managed through a trust.

PHOTO: HE HUAWEN/VCG VIA GETTY IMAGES

key planetary issues. The notion of "subsidiarity" which underpins the sovereignty sharing arrangements of the European Union (EU) and recognizes the value of environmental directives across borders is a prototype of such a system (*7*).

Another way to conceptualize natural resource trusts is through the notion of a "Commonwealth." This concept, with roots in resource distribution and equity, has been explored in the context of mineral resources (*8*). The United Kingdom has also explored ways of better cooperation on mineral supply through the proposal of a Critical Minerals Markets Information System. Such a program could facilitate the informational management of a Minerals Trust. Sharing geological data to ensure that mining is targeted toward the most environmentally and economically efficient sites, as well as support for developing countries in these mechanisms, could be features of the Trust's management platform.

Through the Trust mechanism, countries are simply providing assurance to have this resource available, with the support of a reliable capital accounting system, for sale at a fair market price for a planetary need of the global commons. This concept could also help operationalize the idea for a nationally determined contribution (NDC) framework for energy transition minerals that has also been proposed to emulate the decarbonization NDC under the climate change convention (*9*). Countries contributing minerals for sale through the Trust could also receive additional development incentives, such as fair access to the mineral-based products made from their minerals. They could also negotiate the NDC in accordance with their own domestic needs for specific infrastructure to maintain resource sovereignty.

In many ways, a planetary trust for minerals would be similar to an asset protection trust whereby an asset-holder would assign their assets to a third-party trustee to manage but would still be able to reap the benefits from any financial transactions from their rent or sale. Assets in such a trust are also insulated from potential national financial crises and creditors. The beneficiaries are the mineral producers (state or private mining companies), and the trustees are the countries that both produce the minerals and create the green technologies that need access to those minerals. The functioning of the minerals market could certainly include recycled materials and aspire to a circular economy, including the option to lease metals and thereby have inherent incentives for product reuse and takeback. However, in many industries requiring a new metallic constituent that was previously not in use, such as for lithium, recycling simply won't be viable for at least two or more decades, as there are few stocks of the manufactured products available for such circularity to come to immediate fruition.

OPERATIONAL DYNAMICS OF THE TRUST

Currently, mineral sales are ad hoc transactions that are undertaken through corporate transactions of purchase and sale but subject to import and export regulation. A trust would streamline these transactions by providing a level playing field of transactional regulations agreed to by the trustees. Green technology producers would pay the commodity market price, which itself will likely get more stabilized owing to the stockpile that is built into the architecture of the trust. Trustees would ensure that the necessary minerals are sold to green technology producers through a fair and transparent process. Existing international organizations could manage the trust's key technical decision points. For example, such decisions could consider quotas for mineral producers that are linked to demonstrable needs for green technologies, or which technology creators are eligible for using materials needed for approved green technologies. Industry organizations and key environmental and social vigilance institutions could also play a role in the decision-making process through various governance committees of the trusteeship. In particular, the International Renewable Energy Agency and the Climate Technology Centre Network could have key roles in this mechanism. Intellectual property on mineral processing technologies as well as on the demand-side uses would be protected unless voluntarily shared through open-source licensing such as the idea of a "Green Knowledge Commons" that may also disincentivize cartel formation. Another protection against cartels is that, unlike oil, minerals have the advantage of being more durable and recyclable and hence less suitable for a cartel, more suitable for a trust arrangement.

A stockpile mechanism in the trust could facilitate future reuse and recycling by creating a leasing mechanism for metals that have short-term usage. The World Bank has shown interest in such a leasing mechanism for batteries through their "Climate Smart Mining" initiative (*10*). It is worth noting that in 1975, there was an attempt by the UN Conference on Trade and Development to create a mineral trading platform for the tin industry that could also have a stockpile. However, this system did not flourish because it was not a trust co-managed by both producing and consuming countries and had rigid production and pricing requirements rather than the adaptive system of a mineral trust, whereby prices would be determined by the market and excess production could be stored in a stockpile. Inspired by the 12th-century Hanseatic trading leagues, The European Coal and Steel Community proposed by one of the intellectual progenitors of the EU in the 1960s, Jean Monet, followed a similar logic of supply assurance and helped to build diplomatic trust as well between erstwhile antagonists.

A fundamental feature of the trust idea is that countries fairly benefit from their resources. Producers would simply not be allowed to constrain supply for political ends because of the planetary imperative at stake for these specific uses. If they violate the terms, they would not be able to be part of the trust and hence lose the preferred downstream access to suppliers. The trustees are producers and consumers, and joining as a consumer would mean you agree to buy through the trust as well. Although exceptions could be made for environmental constraints of supply reduction, independent audit mechanisms could be in place to ensure compliance with the terms of the trust. These would be similar to technical audit protocols undertaken through organizations such

as the International Atomic Energy Agency (IAEA). In a sense, this would be analogous to an international riparian agreement committing to downstream water flow but a better deal for the upstream producer because they would get full payment for material flow.

Other uses of the metals in question could be managed independently outside the trust as long as the green transition needs are prioritized for sale through the trust. So, for example, Indonesia, which is the world's largest nickel producer, could still go on earning profits from selling metal outside the trust but would just not constrain supply for green transition projects as part of its NDC. The trust would simply prevent weaponization of mineral trade barriers such as export bans or unilateral tariffs that have even hampered the operations of the World Trade Organization (WTO), and prevent the misuse of allowable exceptions within the WTO's rules (Article XX of the General Agreement on Tariffs and Trade) and various International Commodity Agreements (*11*). There would also be no price targets set, which has led to dysfunction of various commodity agreements.

Green technology producers benefiting from the Mineral Trust could also be required to support and invest in technology development in critical energy transition mineral suppliers, particularly developing countries, to make them future green technology producers. Mineral-producing developing countries could negotiate fair prices to buy back any technologies manufactured from their minerals affordably to support their own transition. This would allow those countries to add value to mineral production, making them not only raw material suppliers, but also add value to the minerals by upgrading locally the value chain and ensure more equitable access to mineral-based renewable energy technologies, improving the mineral security of developing countries (*12*). Most consequentially for planetary sustainability, the minerals trust would prevent redundancies in resource extraction and energy usage for processing and encourage a circular economy.

NEXT STEPS

Initially, the Minerals Trust could be developed through an alliance of a few key producing and consuming countries through ad hoc agreements. However, to have global impact, a multilateral arrangement is important to ensure that some of the negative externalities of resource nationalism do not take root. A key attractive feature of the trust will be its goal to ensure that green technologies are available for solving global commons issues such as climate change. At the same time, the economic security offered by reliable supply chains would be attractive to even those constituents who are not convinced by environmental arguments. In the long term, the mandate for the trust could also come from the UN Security Council to ensure a higher bar of accountability for trustees. The Council has already engaged in climate change matters (*13*), but this engagement should be expanded to infrastructure and mineral security. Such an elevation would move mineral security from its current transactional domain between nations to a multilateral matter of diplomacy with planetary implications.

Errant mineral development of low-grade ores or developments in ecologically and socially vulnerable regions can ultimately be protected only if the world's major producing and consuming countries sign on to this arrangement. Fortunately, we now have excellent means of tracking mineral supply from mines to markets, using a range of analytical tools developed in the field of "forensic geology" as well as much closer regulatory monitoring of mineral trade, particularly from recycled sources.

A parallel case in point pertains to the uranium supply for energy and defense being decoupled and closely monitored by the IAEA (*14*). Although the defense industry's demand may still lead to errant decisions on suboptimal resource extraction, the sheer scale and scope of demand for consumer products for the green transition is far more than what might be needed by the defense sector. For example, the Government Accountability Office in the United States estimates that Defense department demand for rare earth minerals is 0.1% of what is needed for civilian uses for the green transition (*15*). Yet, the discourse on "critical minerals" has become highly securitized with presumptions about defense demands that are in fact miniscule compared with commercial and civilian needs for the green energy transition. With more transparent sharing of data on demand and supply, some of the anxiety that characterizes current debates on "friendshoring" of mineral supply could also be better managed.

The UN Secretary General's panel on critical energy transition minerals completed its mandate to suggest interventions to assure mineral supply in September 2024 at the Summit for the Future. Its recommendations are being handled by specialized UN agencies and the UN Working Group on Transforming the Extractive Industries for Sustainable Development. The idea for a trust could be considered within this process. Meanwhile, efforts to develop regional partnerships on mineral sourcing outside the UN's purview, such as the United States's Mineral Security Partnership, which are currently exclusionary by design could prototype the formulation of a minerals trust.

The UN Economic Commission for Europe has recently proposed a World Resource Bank to support critical minerals projects, and the G20 implemented an Agricultural Market Information System in 2011. Such initiatives offer examples of cooperative arrangements for planetary stewardship. Ultimately, the minerals trust, if governed through an agreement between cooperating states, could provide a win-win opportunity for price stabilization, supply assurance, and market confidence on key technologies that are essential for a more sustainable future. □

REFERENCES AND NOTES

1. P. Taylor, "The concept of the common heritage of mankind" in *Research Handbook on Fundamental Concepts of Environmental Law* (Edward Elgar Publishing, 2022), pp. 252.
2. M. Bungenberg, S. Hobe, Eds., *Permanent Sovereignty Over Natural Resources* (Springer, 2015).
3. J. Rockström *et al.*, *Proc. Natl. Acad. Sci. U.S.A.* **121**, e2301531121 (2024).
4. E. Brown Weiss, *Environ. Policy Law* **50**, 449 (2021).
5. J. Farley, R. Costanza, G. Flomenhoft, D. Kirk, *Ecol. Econ.* **109**, 71 (2015).
6. E. Ostrom, *Am. Econ. Rev.* **100**, 641 (2010).
7. F. Biermann, *Earth System Governance: World Politics in the Anthropocene* (MIT Press, 2014).
8. G. Flomenhoft, "An inquiry into the economic commonwealth of mineral resources: Does ownership matter?" thesis, Sustainable Minerals Institute, The University of Queensland (2020).
9. J. M. Klinger, G. K. Murphy, C. Wolk, *Nat. Energy* **9**, 1452 (2024).
10. I. M. Jiskani, Q. Cai, W. Zhou, S. A. Ali Shah, *Resour. Policy* **71**, 102007 (2021).
11. B. M. Hoekman, P. C. Mavroidis, D. R. Nelson, *World Econ.* **46**, 1163 (2023).
12. D. M. Franks, J. Keenan, D. Hailu, *Nat. Sustain.* **6**, 21 (2023).
13. Security Council Report. The UN Security Council and Climate Change (2021); https://www.securitycouncilreport.org/atf/cf/%7B65BFCF9B-6D27-4E9C-8CD3-CF6E4FF96FF9%7D/climate_security_2021.pdf.
14. A. Brown, A. Glaser, *Sci. Glob. Secur.* **24**, 131 (2016).
15. US Government Accountability Office, *Critical Materials: Action Needed to Implement Requirements That Reduce Supply Chain Risks* (2024); https://www.gao.gov/products/gao-24-107176.

ACKNOWLEDGMENTS

M. Jastrzebiec-Pyszynski (European Parliamentary Research Service), E. Brown Weiss (Georgetown University Law School), A. Hool (ESM Foundation, Switzerland), H. Tulsidas (UN Economic Commission for Europe), and O. Ostensson provided valuable guidance for this paper. M. Aczel (UNU-INWEH) also provided valuable guidance in final revisions. The Rockefeller Foundation, through its support of the Bellagio alumni network of which S.H.A. is a member, helped to support the formulation of this idea. J.A.P.d.O. acknowledges support from Brazil FAPESP grant 2022/14558-2 (CEPID).

10.1126/science.adv9841

[1]Department of Geography and Spatial Sciences, University of Delaware, Newark, DE, USA. [2]University of Queensland, Global Centre for Mineral Security, Sustainable Minerals Institute, St. Lucia QLD, Australia. [3]United Nations University, Institute for Water, Environment and Health (UNU-INWEH), Richmond Hill, ON, Canada. [4]Getulio Vargas Foundation (FGV EAESP), São Paulo, Brazil. [5]Global Development Institute, The University of Manchester, Manchester, UK. [6]Institute for Global Public Policy, Fudan University, Shanghai, China. [7]Earth4All, Winterthur, Switzerland. [8]Copernicus Institute of Sustainable Development, Utrecht University, Utrecht, Netherlands. [9]IPB University, Department of Resource and Environmental Economics, Bogor, Indonesia. [10]Princeton University School of Public and International Affairs, Princeton, NJ, USA. [11]African School of Economics, Abuja, Nigeria. [12]State Key Laboratory of Iron and Steel Industry Environmental Protection, School of Environment, Tsinghua University, Beijing, China. Email: saleem@udel.edu

Understanding how and why wet dogs shake has serious engineering implications.

PHOTO: SASASTOCK VIA SHUTTERSTOCK

SCIENCE AND SOCIETY

In defense of silly science

A biologist pushes back against attacks on curiosity-driven research

Christopher Kemp

Carly Anne York
Basic Books, 2025. 288 pp.

THE SALMON CANNON AND THE LEVITATING FROG | In 1975, Wisconsin Democratic senator William Proxmire began presenting prizes, which he called the Golden Fleece Awards, to people he believed were guilty of squandering public funds. Scientists quickly became some of his favorite targets. Sometimes, the scientists Proxmire targeted subsequently lost funding, prestige, and even their positions at research institutions. Their work was fodder for late-night comedy: A-Hooga! Glowing rabbits! Zing! Worms in space!

A few years ago, when Carly Anne York was a graduate student studying squid biomechanics, someone asked her what her research was actually for. She had no answer. It was what she calls "silly science." She wondered whether it was even worthy of a Golden Fleece Award. But, as York writes in *The Salmon Cannon and the Levitating Frog*, a lot of science that seems frivolous at first is later proven to be powerfully useful. Discovery is a crooked road.

This is an important moment in history to make an earnest argument for the value of curiosity-driven scientific discovery. York's book appears on shelves as Elon Musk's Department of Government Efficiency, or DOGE, ransacks the National Institutes of Health and the Centers for Disease Control and Prevention and defunds valuable research everywhere. And people are cheering as they do it, even as they wait for the arrival of new cancer therapies and novel treatments for Parkinson's disease—even as they are diagnosed with chronic illnesses themselves.

York's book reminds readers that curiosity-driven science is sacred. It gave us scientists such as Archimedes, Copernicus, and Isaac Newton. It powered the Enlightenment. It gave us Einstein, a rumpled young patent clerk dreaming absentmindedly about the shape of the Universe. Viewed through a curving tunnel of space-time, the forefathers of modern science all seem DOGEable now. To some watchers, Isaac Newton sat beneath an apple tree dozing all day.

York deftly and fizzily recounts examples of science that at first glance seemed silly but, when developed, became incredibly valuable. She writes, for example, that in 1668, the first bone graft surgery used part of a dog skull to patch a hole in a wounded soldier's skull. Now, because of equal parts serendipity and curiosity, we use coral as a matrix for bone grafts instead. Readers learn that studying the bumpy tubercles that line the edge of a humpback whale fin has led to new, more efficient designs for wind turbine blades. Scientists studying the distinctive waggle dance that honey bees use to communicate the location of pollen sources to other bees have helped develop algorithms for moving digital information through complex networks. Robotics experts who have built miniature robots modeled on cockroaches have given us devices we can use to search the rubble of collapsed buildings for survivors. And on.

There is, in places, an unevenness to the book, which seems pitched to a young adult level of reading comprehension. (York has previously written two science books for children.) At times, she is almost too bubbly for me, an unrepentant grump. I cringed at sentences such as, "Everyone knows the honeybee waggle dance: You put your left wing in, you put your left wing out, you put your left wing in, and you waggle all about…." Cornell University's famed ornithology department is "a place where people knew their sparrows from their starlings." A male jumping spider has "a few tricks up his sleeves."

What is more, some of the silly science that York includes really does not seem all that silly. I am thinking here of Sir Alexander Fleming's 1928 discovery of penicillin, which required lottery-winning levels of good fortune but also relied on the presence of quick minds to understand what luck had brought them. Other examples—many of them—definitely are silly, and they have not led to any meaningful real-world utility. Even so, perhaps they will.

This is the central vital point of York's book. In an unseen future that we are hurtling toward, research on the strange physics that allows 50,000 California blackworms to tangle into intertwined worm balls could lead to a range of novel real-world applications—for instance, smart bandages that adjust to their wounds. But we must let the discoveries unfurl the way they always have—unpredictably, slowly, haphazardly. They will not develop at all if we allow autocrats to defund curiosity-driven research before it even bears fruit. □

10.1126/science.adx8621

The reviewer is at the Department of Translational Neuroscience, Michigan State University, Grand Rapids, MI, USA, and is the author of *Dark and Magical Places: The Neuroscience of Navigation* (Norton, 2022). Email: cjkemp@gmail.com

ECONOMICS

Values remain a mystery to many economists

The field ignores moral plurality at its peril **George F. DeMartino**

The Price of Our Values
Augustin Landier and David Thesmar
University of Chicago Press, 2025. 232 pp.

In 1987, the economist and philosopher Amartya Sen published *On Ethics and Economics*, in which he argued that "the nature of modern economics has been substantially impoverished by the distance that has grown between economics and ethics" (*1*). A central theme that emerged here and in Sen's later work was that economists make a fundamental error in treating individuals and the world they inhabit as morally simple, where one normative value—such as utility maximization—could serve as the moral compass to govern all human aspirations. Sen countered with a conception of individuals and the social world that featured moral pluralism. He urged economists to see that a society organizing its practices, laws, and institutions according to the dictates of any one ethical principle, be it utilitarianism, egalitarianism, libertarianism, or some other framework, would not be a world in which complex human beings would care to live. Amen to that.

Sen's urging largely failed to move tin-eared economists to take moral complexity seriously, which is why there is still an urgent need for a book like *The Price of Our Values* by economists Augustin Landier and David Thesmar. This new book rises to the Senian challenge, exploring how moral pluralism undermines all sorts of economic shibboleths that too often prevent the economics profession from meeting the needs of those it seeks to serve.

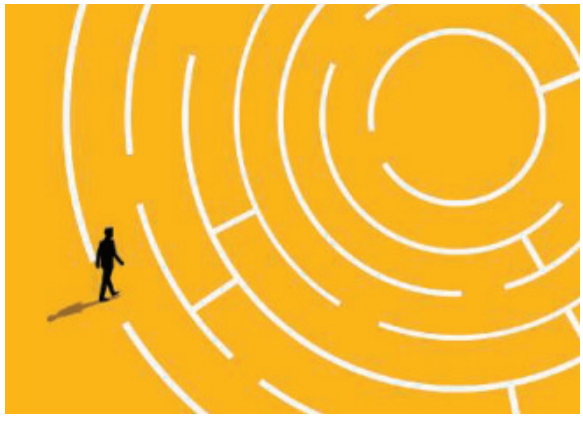

Our principles affect our decision-making to a greater degree than most economists account for.

The book's title might be taken to foreshadow yet another defense of the hardheaded cost-benefit analysis that many economists view as the uniquely appropriate means to guide policy formation. ("You want equality, well you'd better be prepared to pay for it," one imagines them admonishing.) But Landier and Thesmar are up to something else—something far more important. Their research demonstrates that the real people who populate the world hold distinct moral values. They are hardly the one-dimensional self-interested "pleasure machines" that the influential 19th-century economist Francis Edgeworth claimed them to be (*2*).

For Landier and Thesmar, moral pluralism is not a problem to be fixed but rather an essential feature of the human condition that economists had better reckon with as they intervene in matters of public policy. Drawing on the research of social psychologist Jonathan Haidt, they emphasize six central human values: "compassion, liberty, loyalty to the in-group, fairness, authority, and sanctity." They note, correctly, that "we all care about all of these moral values to some extent, but the relative weights we place on each of them vary quite a bit."

This is beyond inconvenient for the standard approach to economics, where what I think of as "moral geometry" seeks "efficiency" above all other values when confronting daunting social questions, such as whether it is acceptable to harm one group in order to benefit another. Moral geometry reduces complex moral problems to simple math problems and then assumes that once one solves the math problem, one has something useful to say about the moral issue. Noneconomists can be forgiven for thinking that there is something fundamentally wrong with a profession that proceeds in that way. In this book, they can learn just why that approach is so troubling.

Throughout the book, Landier and Thesmar report on the findings of their own and others' surveys from France, Germany, and the US that elicit the values that drive individuals in hypothetical but relevant thought experiments. One survey, for example, elicited people's responses to benevolent "nudges" that sought to induce them to do something that was in their own best interest. An example of this would be locking up sugary items in grocery stores while providing consumers with a code they can use to easily open the locked cabinet. In this case, the benefit to the consumer is potentially substantial, while the cost to access the goods is trivial. And yet, in the US, more than 80% of survey respondents rejected this proposal. The authors hypothesize that resistance to innocuous, benevolent nudges like this one might lie in the importance individuals place on the value of autonomy. In this case—as in many others reported in the book—the standard economic assumption that actors will always maximize utility fails to accord with competing principles that people bring to social interactions and to how they expect to be treated by society's institutions.

The Price of Our Values is a short book that manages to range across many of the issues where traditional economists' moral judgments fail society most egregiously. Chapters explore altruism, freedom, community, justice, corporate governance, and other pressing topics. The authors draw on the foundational work of sociologists, such as Émile Durkheim, who recognize the ways in which the purely "transactional" nature of markets that economists value so highly yields the tragedy of anomie, where individuals suffer a loss of connection and purpose.

Throughout the book, Landier and Thesmar focus readers' attention on social identities that are alternatively nourished or threatened by institutions such as the markets that economists have long viewed as uncontroversial means for acquiring more of what we want. By the end, the nonexpert reader is likely to be wary of the simple-minded economist touting efficiency as the solution to society's most pressing problems. Economists, meanwhile, will have learned that there is good reason to take seriously the complexity and plurality of the moral landscape in our quest to promote social betterment—not as it is defined by us, but as it is defined by those we seek to serve. □

REFERENCES AND NOTES

1. A. Sen, *On Ethics and Economics* (Basil Blackwell, 1987).
2. F. Y. Edgeworth, *Mathematical Psychics* (C. Kegan Paul & Co., 1881).

10.1126/science.adx5991

The reviewer is at the Josef Korbel School of International Studies, University of Denver, Denver, CO, USA. Email: george.demartino@du.edu

The Landsat 9 satellite launched in 2021, and NASA has committed to launch its successor by 2031.

PHOTO: USSF 30TH SPACE WING/CHRIS OKULA/NASA

Independent oversight crucial to Landsat Next

Since the launch of the satellite Landsat-1 in 1972, eight Landsat Earth observation missions have provided an unbroken record that has been used to document and understand global change, Earth's resources, and terrestrial processes (*1*). Despite longstanding funding challenges (*2*, *3*), the US Sustainable Land Imaging Program committed in September 2016 (*4*) to extend the Landsat record into the next decade, leading to the scheduled launch of the Landsat Next mission in 2030 or 2031 (*5*). On 11 March, the NASA Transition Authorization Act of 2025 was introduced, which directs NASA to assess how the private sector could contribute to Landsat missions (*6*). Private sector investment could alleviate the program's financial challenges but should not be undertaken without strong oversight in place.

The Act outlines the government's vision for ensuring data quality, continuity, open access, and long-term archiving. It includes a directive for NASA to assess aspects of the Landsat missions that could be provided by the private sector, such as ground system operations and provision of commercial satellite data (*6*). Although the previous commercialization of Landsat in the mid-1980s was not successful (*7*), industry has become established in delivering Earth observation systems, and partnerships between space agencies and commercial entities could reduce costs. For example, to incorporate new science and improved ancillary data, the US Geological Survey (USGS) used commercial cloud processing software to reprocess the Landsat archive (*8*).

However, the success of the Landsat program depends on independent scientific oversight. Feedback has been paramount to responsibly managing the acquired data and addressing design issues, including functional sensor performance specifications, data delivery and formats that affect users, and interoperability with other planned and in-orbit Earth observation systems (*9*).

If NASA plans to provide Landsat continuity through a government and industry partnership, then independent oversight remains critical. To date, oversight has been provided by a National Geospatial Advisory Subcommittee and by the Landsat Science Team (LST) (*7*, *10*). LST members, who are selected by USGS and NASA on the basis of competitive scientific proposals, include scientists and engineers drawn from academia and US federal science and mission agency employees, as well as members of non-US institutions who ensure an international perspective and transparency (*9*).

Landsat provides US $3.4 billion in annual benefits (*11*), eclipsing mission costs (*12*). Qualified oversight will ensure that these benefits, and the objective evidence that Landsat provides for understanding Earth, will continue.

David P. Roy[1], Michael A. Wulder[2], Curtis Woodcock[3]

[1]Center for Global Change and Earth Observations, and Department of Geography, Environment, & Spatial Sciences, Michigan State University, East Lansing, MI, USA. [2]Canadian Forest Service (Pacific Forestry Center), Natural Resources Canada, Victoria, BC, Canada. [3]Department of Earth and Environment and Center for Remote Sensing, Boston University, Boston, MA, USA. Email: roydavi1@msu.edu

REFERENCES AND NOTES

1. M. A. Wulder *et al.*, *Remote Sens. Environ.* **280**, 113195 (2022).
2. M. M. Waldrop, *Science* **215**, 1600 (1982).
3. E. Marshall, *Science* **246**, 321 (1989).
4. US Geological Survey, "MOU – Sustainable land imaging research, development, and operations" (USGS, 2016).
5. US Geological Survey, "Landsat Next" (USGS, 2025).
6. NASA, NASA Transition Authorization Act of 2025, https://www.commerce.senate.gov/services/files/0B3F390C-72B0-4C41-B1BE-F5C8A886992C.
7. Landsat Legacy Project Team, "Landsat's enduring legacy: Pioneering global land observations from space" (American Society for Photogrammetry and Remote Sensing, 2017); https://doi.org/10.14358/ASPRS.1.57083.101.7.
8. C. J. Crawford *et al.*, *Sci. Remote Sens.* **8**, 100103 (2023).
9. D. P. Roy *et al.*, *Remote Sens. Environ.* **145**, 154 (2014).
10. Z. Wu *et al.*, *Remote Sens. Environ.* **231**, 111214 (2019).
11. C. L. Straub, S. R. Koontz, J. B. Loomis, "Economic valuation of Landsat imagery" (US Geological Survey, Open-File Report 2019–1112, 2019); https://pubs.usgs.gov/of/2019/1112/ofr20191112.pdf.
12. National Academies of Sciences, Engineering, and Medicine, *Thriving on Our Changing Planet: A Midterm Assessment of Progress Toward Implementation of the Decadal Survey* (National Academies Press, 2024); https://doi.org/10.17226/27743.

10.1126/science.adx5773

Ecological risks of biodegradable plastics

The current draft of the global plastics treaty suggests that biodegradable plastics have the potential to end plastic pollution (*1*). This perception, combined with ever-rising consumer demand, has fueled biodegradable plastic production, which reached 2.47 million tonnes in 2024 and is projected to hit 5.73 million tonnes by 2029 (*2*). However, the widespread adoption of biodegradable plastics could pose ecological risks that must be addressed.

The weathering of biodegradable plastics releases vast amounts of diverse oligomers, complex chemical mixtures, into the environment (*3*). These oligomers share characteristics with persistent organic pollutants (*4*), raising concerns about their potential adverse impacts on ecosystems. Oligomers exhibit higher bioavailability than larger solid plastic particles, posing greater exposure risks to wildlife and humans (*5*).

More than 9000 chemicals of the 16,000 "plastic chemicals" listed by the Norwegian Research Council lack publicly available information and remain unregulated by global initiatives, including the Stockholm Convention (*6*). When released from biodegradable plastics, chemicals such as terephthalic acid and bisphenol A have been shown to induce genetic, reproductive, and immunotoxic effects in organisms by disrupting cellular mitochondrial metabolism (*3*, *7*).

The risks of biodegradable plastics are amplified by the plastisphere, microbial communities that colonize plastic surfaces (*8*). Oligomers such as lactic acid that are released from polylactic acid biodegradable plastics can facilitate the growth of microbes such as *Actinobacteriota* within the plastisphere (*9*). The integration of these oligomers into microbial metabolic processes may exacerbate plastic-associated greenhouse gas emissions (*10*). In addition, rising temperatures amid climate change may further complicate the already elusive impacts of biodegradable plastic oligomers on biodiversity.

Mitigating the potential risks posed by weathered biodegradable plastics requires coordinated actions among research communities, industries, and policy-makers to advance a circular biodegradable plastic economy. Key strategies include identifying the sources and degradation pathways of toxic biodegradable plastic-derived oligomers (*10*), developing biodegradable plastics with controlled and complete degradation capabilities, and redesigning biodegradable plastic structures to enable monomer recovery or replace hazardous oligomers with safer, bio-based alternatives (*11*, *12*). These actions can minimize the potential adverse impacts of biodegradable plastics on wildlife and human health.

Xiaoli Zhao[1], Xiaowei Wu[2], Qi Wang[3], Fengchang Wu[1]

[1]State Key Laboratory of Environmental Criteria and Risk Assessment, Chinese Research Academy of Environmental Sciences, Beijing, China. [2]Jiangsu Key Laboratory of Atmospheric Environment Monitoring and Pollution Control, School of Environmental Science and Engineering, Nanjing University of Information Science and Technology, Nanjing, China. [3]National Key Laboratory of Advanced Polymer Materials, Polymer Research Institute, Sichuan University, Chengdu, China. Email: wufengchang@vip.skleg.cn

REFERENCES AND NOTES

1. United Nations Environment Programme, "Zero Draft of the plastics treaty (UNEP/PP/INC.3/4)" (UNEP, 2023); https://wedocs.unep.org/bitstream/handle/20.500.11822/43239/ZERODRAFT.pdf.
2. European Bioplastics, "Bioplastic market development update 2024" (European Bioplastics, 2024); https://www.european-bioplastics.org/bioplastics-market-development-update-2024/.
3. M. Wang *et al.*, *Nat. Nanotechnol.* **18**, 403 (2023).
4. T. Dey *et al.*, *Science.* **378**, 841 (2022).
5. Y. K. Lee., *Water Res.* **271**, 122867 (2025).
6. N. Jones, *Nature* 10.1038/d41586-024-00805-2 (2024).
7. E. Fabbri, "Chemical characterization and toxicity evaluation of bioplastics leachates in early larval stages and adult mussels, *Mytilus galloprovincialis*," paper presented at ESCPB 2022: European Society for Comparative Physiology and Biochemistry, Naples, Italy, 28–32 August 2022; https://easychair.org/smart-program/ESCPB2022/2022-08-31.html#talk:201967.
8. X. X. Su *et al.*, *Nat. Commun.* **13**, 1 (2022).
9. Y. Z. Sun *et al.*, mSystems **7**, 1 (2022).
10. J. Shi *et al.*, *Adv. Sci.* **12**, 2409585 (2024).
11. M. Guicherd *et al.*, *Nature* **631**, 884 (2024).
12. S. Kakadellis, G. Rosetto, *Science* **373**, 49 (2021).

10.1126/science.adw9060

Africa's epidemic of low-quality medicines

Between July and October 2023, about 70 Gambian children under the age of 5 died after drinking cough syrup containing high levels of ethylene glycol and diethylene glycol, both of which are toxic to humans (*1*). These tragic deaths exemplify the dangers of medicines that fail to meet quality specifications and standards, as well as those that deliberately misrepresent their identity, composition, or source (*2*). To prevent the distribution of substandard and falsified (SF) medicines, the quality of all medicines should be regulated, which will require coordinated leadership and extensive data collection.

SF medicines jeopardize the health of millions of people, particularly those in vulnerable populations (*3*), and can lead to treatment failures, increased mortality, and the development of drug-resistant pathogens (*4*). For example, SF antimicrobials, including antibacterials, have a poorly understood but potentially negative effect on antimicrobial resistance (*5*). About 10% of antimicrobials in low- and middle-income countries may be SF (*6*), and in sub-Saharan Africa, local prevalence rates could exceed 50% (*7*). The lack of coordination among international, national, and local regulatory bodies hampers effective control and monitoring.

The African Medicines Agency (AMA), established by the African Union through a treaty in 2021 (*8*), could provide a solution. An effective AMA could serve as a catalyst for coordinating surveillance, guiding policy-making, and integrating SF countermeasures into broader health initiatives. The AMA could also facilitate a robust consensus on standards for serialization, track and trace technology, and quality control, which could deter counterfeiters and encourage best practices (*9*). To establish a stronger evidence base on SF prevalence rates, which could better inform policy and regulatory interventions, the AMA could incentivize and foster research partnerships and collaborations between African universities and research centers. The AMA could then enrich this evidence base by nurturing regional scientific expertise. By facilitating effective quality control and streamlining data collection, the AMA could help to protect millions of African lives from this silent epidemic.

Heather Hamill[1], Fanqi Zeng[1], Simon Mariwah[2]

[1]Department of Sociology, University of Oxford, Oxford, UK. [2]Department of Geography and Regional Planning, University of Cape Coast, Cape Coast, Ghana.
Email: fanqi.zeng@sociology.ox.ac.uk

REFERENCES AND NOTES

1. V. Khare, "Maiden Pharmaceuticals: Fury in The Gambia over India cough syrup deaths," *BBC*, 20 August 2023.
2. World Health Organization, "Definitions of substandard and falsified (SF) medical products" (WHO, 2017).
3. P. N. Newton, M. D. Green, F. M. Fernández, *Trends Pharmacol. Sci.* **31**, 99 (2010).
4. P. N. Newton, A. Dondorp, M. Green, M. Mayxay, N. J. White, *Lancet* **362**, 169 (2003).
5. S. Cavany *et al.*, *Nat. Commun.* **14**, 223 (2023).
6. World Health Organization, "A study on public health and socioeconomic impact of substandard and falsified medical products" (WHO, 2017).
7. S. Ozawa *et al.*, *JAMA Netw. Open.* **1**, e181662 (2018).
8. African Union, "Treaty for the establishment of the African Medicines Agency" (AMA, 2021).
9. N. Wairagkar *et al.*, *PLOS Glob. Public Health* **5**, e0004276 (2025).

10.1126/science.adw8919

RESEARCH

IN *SCIENCE* JOURNALS

Edited by **Michael Funk**

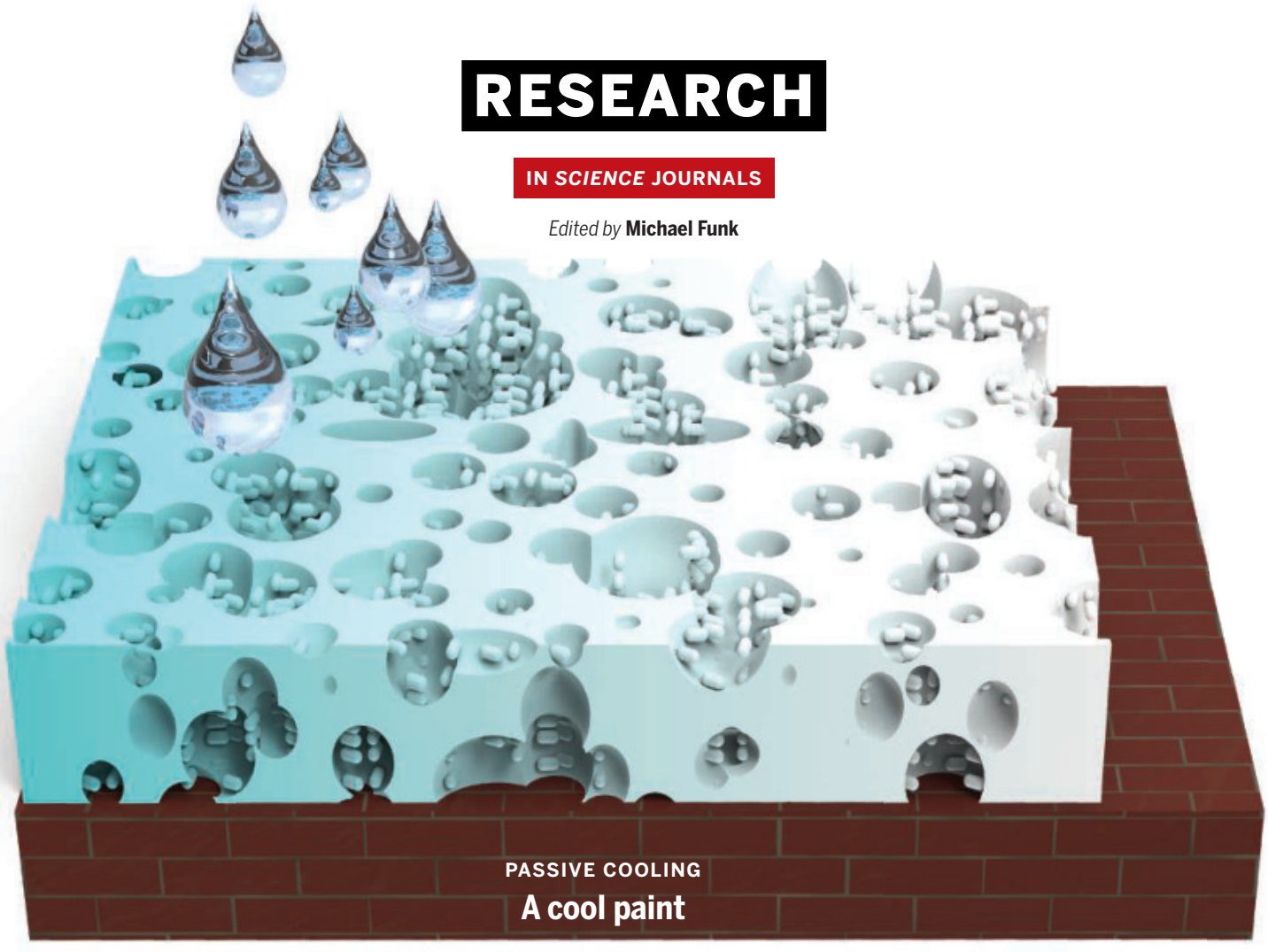

PASSIVE COOLING

A cool paint

The top and exterior of buildings can be used to passively cool, but this requires materials with the right properties to do so effectively. Fei *et al*. designed a paint that cools both radiatively and through evaporation and that appears to keep buildings relatively cool even in humid environments. Although radiative cooling is effective at reducing temperature, it requires the material to be sky-facing. Designing a paint that also cools through evaporation allows the material to be effective when applied to the sides of the buildings as well. —Brent Grocholski *Science* p. 1044, 10.1126/science.adt3372

Conceptual drawing of combined evaporative-radiative cooling paint.

ILLUSTRATION: FEI *ET AL.*

CONSERVATION

A sad solution

Despite much effort and money spent over decades, rhinoceros populations continue to decline because of the market for their horns based on unsubstantiated health claims in some countries. Over time, rhinoceros poaching has become a multimillion-dollar illegal trade, often controlled by multinational criminal organizations. In the face of this crisis, there are many local heroes who dedicate their lives to protecting the few remaining rhinoceroses using an array of approaches, from increased ranger presence to tracking dogs, at a cost of millions of dollars per year. Kuiper *et al*. looked at the effectiveness of these approaches and found that only one, removal of the poacher's reward through dehorning, significantly reduced rhinoceros loss. —Sacha Vignieri

Science p. 1075, 10.1126/science.ado7490

SOLID STATE PHYSICS

Measuring the quantum metric

The quantum metric, the real part of the complex-valued quantum geometric tensor, has a bearing on the electronic properties of solids, including transport. Although the quantum metric has been measured directly in artificial systems, determining the full tensor in solids has proven tricky. Kim *et al*. extracted this quantity using photoemission measurements in black phosphorus. The researchers expect that their methodology can be extended to other materials with related band structures. —Jelena Stajic

Science p. 1050, 10.1126/science.ado6049

SYNTHETIC CHEMISTRY

Insects transform carbon rings

The insertion of oxygen atoms into carbon belt and ring molecules was achieved after feeding the substrates to tobacco cutworm (*Spodoptera litura*). Usami *et al*. explored whether insects could process a carbon nanoring, methylene-bridged [6]cycloparaphenylene, through a xenobiotic pathway. Of those tested, only *S. litura* survived, and examination of its excretions showed that it converted this molecule to an unusual oxylene derivative in 10% yield. For [n]cycloparaphenylenes, oxygen atoms were inserted into the bonds between phenyl groups. —Phil Szuromi

Science p. 1055, 10.1126/science.adp9384

ARCHAEOLOGY

The Menominee, maize, and precolonial "Michigan"

Between 1000 and 1600 CE, maize was intensively grown by Indigenous peoples in the Americas. However, it was originally a tropical to subtropical plant, and most of its production was believed to have occurred in similar environments. McLeester *et al*. used a suite of approaches, including remote spatial measurements and excavation, to explore a Menominee site in the Upper Peninsula of Michigan, revealing evidence of extensive maize agriculture and associated cultural complexity even at the most northern extent of its viability. —Sacha Vignieri

Science p. 1082, 10.1126/science.ads1643

BIOCHEMICAL CYCLES

An integrated couple

Anthropogenic activities have greatly perturbed both the carbon and nitrogen cycles, with clear ecological consequences. Successful management to minimize these impacts is vital to preserving the sustainability of environmental networks and human society. Focusing on China, Xu *et al*. developed an integrated model for quantifying carbon and nitrogen fluxes and their interactions. By managing them together in an integrated manner, large reductions of carbon and nitrogen could be achieved at lower abatement costs and greater societal benefits than if they were treated separately. —Jesse Smith

Science p. 1098, 10.1126/science.ads4105

VACCINES

Prolonged protection

Lipid nanoparticle messenger RNA (LNP-mRNA) vaccines induce robust immune responses and provide protection against infectious diseases. However, this immunity can be short-lived, resulting in the need for frequent booster vaccinations. Aunins *et al.* investigated how adjuvanting LNP-mRNA vaccines with mRNA encoding the cytokine interleukin-12 influences CD8 T cell responses in mice. These vaccines enhanced antigen-specific CD8 T cell responses, augmented CD8 T cell memory, and provided greater protection after challenge with *Listeria monocytogenes* and in a melanoma model. This work demonstrates that cytokine-adjuvanted LNP-mRNA vaccines represent a strategy to tailor the magnitude of the immune response to vaccination. —Hannah Isles

Sci. Immunol. (2025) 10.1126/sciimmunol.ads1328

GENE THERAPY

Targeted treatment for inflammation

Osteoarthritis (OA) in the knee joint is typically accompanied by elevations in inflammatory signaling in the intra-articular space. Protein and small-molecule therapies delivered to the intra-articular space are cleared rapidly from the joint, so new strategies to enrich therapeutics for long-term treatment are needed. De La Vega *et al*. have taken a step toward a safe gene therapy for patients with OA in a first-in-human, single-center, phase 1 clinical trial to test the safety of intra-articular delivery of an adeno-associated virus expressing interleukin 1 receptor antagonist (IL-1Ra), an endogenous inhibitor of the proinflammatory cytokine IL-1. In a dose-escalation trial in nine participants, the authors observed that a single intra-articular injection of the gene product led to an increase in IL-1Ra in the synovial fluid that remained elevated for up to a year. There were no serious adverse events related to the gene delivery. These data support the progression to larger-scale trials of this gene therapy to further explore the potential for its long-term therapeutic benefit for OA. —Molly Ogle

Sci. Transl. Med. (2025) 10.1126/scitranslmed.adu9804

IN OTHER JOURNALS

Edited by **Corinne Simonti** *and* **Jesse Smith**

MICROBIOLOGY

Bacteria versus amoeba

Soil-dwelling bacteria are frequently preyed upon by amoebal predators. The plant pathogen *Pseudomonas syringae* can infect virtually all economically relevant crop species, and some strains can sense and kill their microbial predators. Zhang *et al*. studied how *P. syringae* combats the social amoeba *Polysphondylium pallidum* using a bacterial "chemical radar system." *P. syringae* secretes the lipopeptide syringafactin, which is deacylated by the amoeba. The bacterial sensor protein Chemical Radar Regulator (CraR) senses these peptides and activates a process that generates the amebicide pyrofactin. This system, which is widespread in *P. syringae*, allows for the successful infection of plants, and analogous systems may be present in other microorganisms. —Stella M. Hurtley

Cell (2025) 10.1016/j.cell.2025.02.033

PHYSIOLOGY

Is sleep need adjustable?

Inadequate sleep is often associated with poor health. Noting that average sleep duration varies among countries and cultures, Ou *et al.* explored whether this is associated with different health outcomes. The authors used historical data from 71 countries in addition to their own data from people in 20 countries. Although correlational and self-reported, the data showed interesting trends. Overall, health appeared not to be poorer in countries where average sleep amounts were shorter. In all countries, people tended to get less sleep than the optimal amount for that country. However, better health wasn't associated with achieving a specific duration of sleep. Rather, it was associated with sleep patterns that were close to the perceived ideal in that culture. —L. Bryan Ray

Proc. Natl. Acad. Sci. U.S.A. (2025) 10.1073/pnas.2419269122

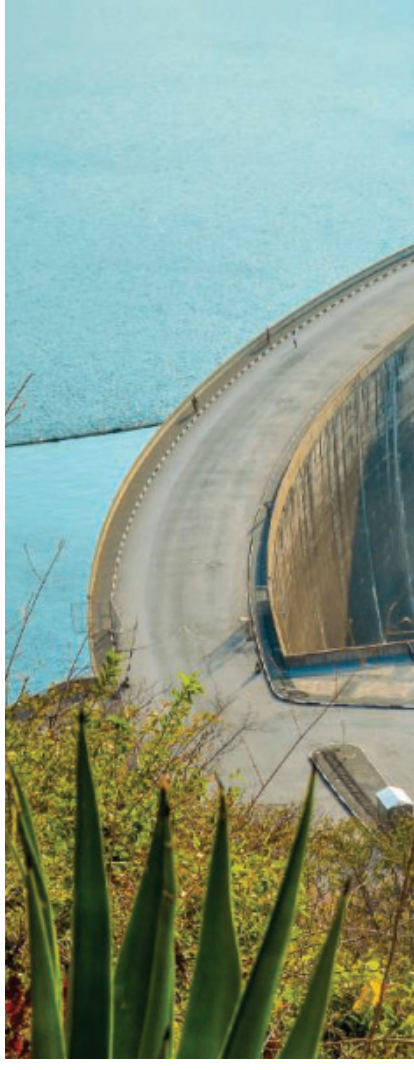

PHOTO: IMPALA PHOTO/ISTOCK PHOTO

DISTURBANCE ECOLOGY

Competition beneath the bark

In western North America, indigenous bark beetles are a major source of mortality in conifer forests. Douglas-fir beetles (*Dendroctonus pseudotsugae*) often show large population increases (irruptions) after tree-damaging fires, which are increasing in size and frequency. Mitchell *et al.* found that competition with woodboring beetles, which also

WATER STORAGE

Poles on the move

Human activities have been conducted at such immense scales that they literally have affected how the world turns. Valencic *et al.* discuss one dimension of that impact: movement of the poles due to water impoundment. Using data on how the construction of dams has altered the distribution of terrestrial surface water in reservoirs, the authors calculated the path of true north polar wander from 1835 to 2011 CE. A dramatic change in the direction and rate of polar wander around 1950 reflects a shift from dominantly North American impoundment to greater storage in East Asia, Africa, and the rest of the world, providing a stark reminder of our growing footprint on the environment. —Jesse Smith

Geophys. Res. Lett. (2025) 10.1029/2025GL115468

The Kariba dam on the Zambezi River has created the world's largest artificial lake.

colonize fire-injured trees, may limit Douglas-fir beetle irruptions after fire. After three large wildfires in British Columbia, Canada, in 2017, both types of beetles attacked the same host trees. Douglas-fir beetle populations grew rapidly only in stands where less than half of trees were occupied by woodboring beetles. These complex interactions suggest that managing for beetle diversity may reduce Douglas fir (*Pseudotsuga menziesii*) mortality after fires. —Bianca Lopez

Ecol. Appl. (2025) 10.1002/eap.70024

ECONOMICS

Diversity gives direction to research

The transition of 76 all-male US universities to coeducation between 1960 and 1990 increased gender-related research publications from those universities by 44%. Truffa and Wong estimate that 6% of this growth in research on female subjects and gender differences, seen 3 to 6 years after the onset of coeducation, was due to a shift in the gender composition of the faculty. Incumbent faculty, predominately male, who predated the coeducational transition increased the gender-related share of their publications by 27%. This suggests that interactions with more diverse peers and students inspired new directions in research. —Brad Wible

Amer. Econ. Rev. (2025) https://www.aeaweb.org/articles?id=10.1257/aer.20221561

HUMAN GENOMICS

Comparing human mutation rates

It is well known that specific genetic variants and mutation patterns differ between human populations, but a study by Garcia-Salinas *et al.* provides evidence that the rate at which new mutations occur in offspring can also differ. The authors analyzed data from a cohort of about 10,000 trios consisting of a child and both parents who had undergone whole-genome sequencing. The overall cohort was ancestrally diverse, but each set of parents shared a continental-level genetic ancestry, enabling the authors to compare the rates of de novo mutations between people of different ancestral backgrounds. Concerningly, parental smoking appeared to be an independent risk factor for increased de novo mutations in offspring. —Yevgeniya Nusinovich

Nat. Commun. (2025) 10.1038/s41467-025-59750-x

PHYSICS

Going under threshold

The original discovery of the *J/y* meson, a particle consisting of a charm quark and an antiquark, provided important evidence for the quark model of particle physics. More recently, creating this meson in collisions of photons with nuclei has been used to discern the inner structure of the bound proton. This is most effective for photon energies below the threshold value needed in collisions with free protons. Pybus *et al.* succeeded in producing the *J/y* meson at such subthreshold photon energies using deuterium, helium, and carbon nuclei. The meson production was in excess of theoretical predictions, but a full understanding awaits future measurements with improved statistics. —Jelena Stajic

Phys. Rev. Lett. (2025) 10.1103/PhysRevLett.134.201903

RESEARCH ARTICLE SUMMARY

HUMAN DEVELOPMENT

Gastruloids enable modeling of the earliest stages of human cardiac and hepatic vascularization

Oscar J. Abilez†* Huaxiao Yang†, Yuan Guan, Mengcheng Shen, Zehra Yildirim, Yan Zhuge, Ravichandra Venkateshappa, Shane R. Zhao, Angello H. Gomez, Marcel El-Mokahal, Logan Dunkenberger, Yoshikazu Ono, Masafumi Shibata, Peter N. Nwokoye, Lei Tian, Kitchener D. Wilson, Evan H. Lyall, Fangjun Jia, Hung Ta Wo, Gao Zhou, Bryan Aldana, Ioannis Karakikes, Detlef Obal, Gary Peltz, Christopher K. Zarins, Joseph C. Wu*

Full article and list of author affiliations: https://doi.org/10.1126/science.adu9375

INTRODUCTION: Human pluripotent stem cells (hPSCs), including human embryonic stem cells and human induced pluripotent stem cells, can differentiate into various cell types of the body, such as cardiomyocytes, hepatocytes, and individual types of vascular cells. Furthermore, hPSCs can be used to create organoids, which are self-organizing three-dimensional (3D) structures that mimic key structural and functional characteristics of their in vivo organ counterparts. Several approaches to create organoids with a vascular system have been pursued to (i) avoid necrosis in the center of organoids where oxygen tension is low; (ii) achieve larger organoid growth for improving fidelity in modeling development, modeling diseases, and discovering new drugs; and (iii) increase the viability of implanted organoids used as regenerative therapies. However, codifferentiating the key cell types of an organoid along with a de novo vasculature comprising robust branching, hierarchical organization, and lumina formation has not been fully achieved.

RATIONALE: Although model organisms have provided insight into the earliest stages of organ vascularization, we know very little about this process in humans because of ethical restrictions and the technical difficulty of obtaining human embryos at early developmental stages. However, hPSCs have been shown to model key aspects of development, including primitive streak formation, gastrulation, germ layer formation, and individual organ-specific cell type creation. Moreover, geometric micropatterning of hPSCs has enabled reproducible and scalable modeling of these developmental processes. With this basis, we developed an in vitro model to mimic the earliest developmental stages of cardiac and hepatic organoid vascularization, which corresponds to the first 3 weeks of in vivo human development and Carnegie Stages 9 and 10.

RESULTS: Using four hPSC fluorescent reporter systems and spatially micropatterned hPSCs, we produced cardiac vascularized organoids (cVOs) in a scalable and reproducible fashion. Notably, we used the four reporter systems to characterize gastruloid, progenitor, and cardiovascular cell type formation in situ in developing cVOs. We identified a growth factor and small molecule cocktail that when added to micropatterned hPSCs generated a spatially organized, branched, and lumenized vascular network within a multilineage cVO comprising endocardial, myocardial, epicardial, and neuronal cell types. Single-cell transcriptomics, high-resolution 3D microscopy, and multiple functional analyses showed that cVOs were structurally and functionally similar to that of a 6.5–postconception week human embryonic heart at Carnegie Stages 19 and 20; however, our comparison also revealed differences that warrant future investigation. Additionally, we found that NOTCH and bone morphogenetic protein (BMP) signaling were required for vascularization in cVOs, with BMP inhibition having a more negative effect on vascular formation than NOTCH. To demonstrate the broader utility of our vascularization strategy, we used the same vascular-inducing cocktail to produce hepatic vascularized organoids (hVOs), which also comprised a spatially organized, branched, and lumenized vascular network integrated with multilineage hepatic cell types.

CONCLUSION: Our in vitro model represents a technical advance for addressing questions regarding de novo organ vascularization. Furthermore, our results suggest that a conserved developmental program is involved in creating the vasculature within different organ systems. □

*Corresponding author. Email: ojabilez@stanford.edu (O.J.A.); joewu@stanford.edu (J.C.W.) †These authors contributed equally to this work. Cite this article as O. J. Abilez *et al.*, *Science* **388**, eadu9375 (2025). DOI: 10.1126/science.adu9375

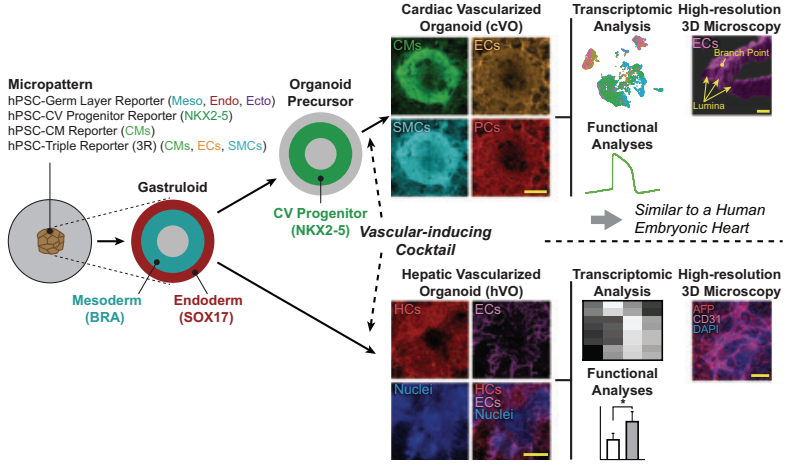

Micropatterning of four hPSC reporter lines enabled gastruloid, cardiovascular, progenitor, and cVO formation. The identification of a vascular-inducing cocktail of growth factors enabled generation of a spatially organized, branched, and lumenized vascular network within a multilineage cVO. Transcriptomics, high-resolution 3D microscopy, and functional analyses showed that cVOs are similar to a human embryonic heart. The same vascular-inducing cocktail was then used to produce hVOs. CMs, cardiomyocytes; ECs, endothelial cells; SMCs, smooth muscle cells; PCs, pericytes; HCs, hepatocytes.

RESEARCH ARTICLE SUMMARY

PHYSIOLOGY

Is taurine an aging biomarker?

Maria Emilia Fernandez, Michel Bernier, Nathan L. Price, Simonetta Camandola, Miguel A. Aon, Kelli Vaughan, Julie A. Mattison, Joshua D. Preston, Dean P. Jones, Toshiko Tanaka, Qu Tian, Marta González-Freire, Luigi Ferrucci, Rafael de Cabo*

Full article and list of author affiliations: https://doi.org/10.1126/science.adl2116

INTRODUCTION: Taurine (2-aminoethane-sulfonic acid), a conditionally essential amino acid involved in multiple important biological functions, has been extensively studied as a biomarker and therapeutic molecule for diverse disease states. Because age is the primary risk factor for the development of many of these conditions, the potential of taurine to serve as a biomarker or modulator of aging has also been the focus of numerous research efforts. Several studies have found that circulating taurine concentrations decrease with age, including a recent report that further demonstrated that supplementation with taurine improves multiple age-related phenotypes and extends life span in model organisms. This study has sparked renewed interest in taurine as a potential biomarker, driver, and therapeutic target for aging. However, the question of how circulating taurine concentrations change with age is still a matter of debate because other studies have found no change or increased taurine concentrations with age.

RATIONALE: Several aspects of study design can increase variability and contribute to the discrepancies observed in previous reports, including (i) evaluation of circulating taurine changes across limited age ranges, (ii) reliance on cross-sectional data, and (iii) "pooled data" (e.g., when data from both sexes, divergent age ranges, or various health statuses are combined for analysis). To examine this, we performed longitudinal and cross-sectional assessments of circulating taurine concentrations in healthy human subjects and two commonly used animal models (nonhuman primates and mice) of both sexes over a broad age range to evaluate the age-related changes in taurine concentrations. Additionally, we assessed how these concentrations are associated with functional measures of health status (gross motor function and body weight) at different life stages.

RESULTS: Measurement of taurine concentration was performed on longitudinally collected plasma of human subjects (26 to 100 years old) from the Baltimore Longitudinal Study of Aging (BLSA), longitudinally collected serum from rhesus monkeys (3 to 32 years old), and C57BL/6J mice (9 to 27 months old) from the Study of Longitudinal Aging in Mice (SLAM). Taurine concentrations exhibited a sex-specific increase with age in all cohorts except male mice, in which taurine remained unchanged. These longitudinal analyses also revealed that the interindividual variability contributes more to the differences in taurine concentrations than age. Similar age-related changes in taurine concentrations were observed in two cross-sectional studies of geographically distinct human populations. The relation between taurine and muscle strength or body weight was inconsistent within and across cohorts.

CONCLUSION: First, circulating taurine does not decline with age (concentrations increase or remain unchanged) in healthy individuals of three mammalian species across the adult life span. Second, the interindividual variability in circulating taurine is generally greater than the longitudinal change across the life span, which limits its utility as a biomarker of aging. Third, the associations between circulating taurine concentrations and functional measures of health status are context dependent (i.e., age, species, or cohort)—a result that does not support the notion that a reduction in circulating taurine promotes the aging phenotype. On the basis of these findings, we conclude that low circulating taurine concentrations are unlikely to serve as a good biomarker of aging. □

*Corresponding author. Email: decabora@grc.nia.nih.gov Cite this article as M. E. Fernandez *et al.*, *Science* **388**, eadl2116 (2025). DOI: 10.1126/science.adl2116

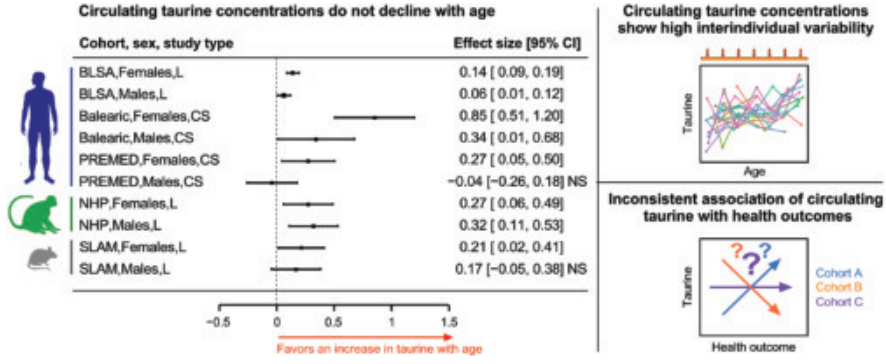

Age-related changes in circulating taurine concentrations and their association with health outcomes. (Left) Circulating taurine does not decline with age in healthy human subjects, nonhuman primates, and mice of both sexes when evaluated longitudinally (L) or cross-sectionally (CS) across the adult life span. (Top right) Longitudinal studies reveal that taurine concentrations show high interindividual variability. (Bottom right) Taurine shows inconsistent associations with health outcomes. Balearic, Balearic Islands Study of Aging; PREMED, Predictive Medicine Research; NHP, nonhuman primate; 95% CI, 95% confidence interval; NS, not significant.

RESEARCH ARTICLE SUMMARY

STRUCTURAL BIOLOGY

Structural insights into chromatin remodeling by ISWI during active ATP hydrolysis

Youyang Sia†, Han Pan†, Kangjing Chen, Zhucheng Chen*

Full article and list of author affiliations: https://doi.org/10.1126/science.adu5654

INTRODUCTION: DNA wraps around histone octamers to form nucleosomes, chromatin's basic units. Adenosine triphosphate (ATP)–dependent chromatin remodelers—switch/sucrose nonfermentable (SWI/SNF); imitation switch (ISWI); chromodomain, helicase, DNA binding (CHD); and inositol requiring 80 (INO80)—reposition nucleosomes to regulate chromatin structure and function. SWI/SNF creates accessible chromatin, whereas ISWI senses linker DNA length and spaces nucleosomes evenly. These enzymes share highly conserved motor domains, which are at the heart of the chromatin remodeling reaction. Recent cryo–electron microscopy (EM) studies revealed staggered DNA translocations of the nucleosome, with a ½-bp rather than full 1-bp DNA bulge at the site bound by the motor. When and how the other strand is translocated remains unknown. Moreover, to prevent excessive chromatin remodeling, the translocation activity is negatively regulated, the mechanism of which remains enigmatic.

RATIONALE: The previous studies were presumably constrained by the absence of actual translocation so that only three states of the remodeling reaction are captured. By using ATP to sustain the translocation reaction, we enabled the motor to traverse all potential stages of the remodeling cycle. To catch the actions in various states, we collected datasets with different concentrations of ATP and determined nine high-resolution cryo-EM structures of ISWI bound to the nucleosome during active translocation.

RESULTS: The structures of the canonical ATP- and adenosine diphosphate (ADP)–bound states were determined at resolutions of 2.3 to 2.6 Å, which provide clear views of the motor domains and the interaction with the DNA. In particular, we found that motifs V and VI relay the signal from the bound nucleotides to the nucleosome, underlying the DNA bulge and translocation upon ATP hydrolysis. In the ADP* state, we observed the full 1-bp DNA distortion. The tracking strand movement results in a loss of the DNA-histone contact at SHL2.5. The complexes in the unbound apo and apo* states adopt conformations similar to that of the ADP and ADP* states, respectively. In the ADP^{+} and ADP^{*+} states, we identified a C-terminal positive element (PosC) and an arginine-tyrosine anchor motif (RYA), both of which promote the ISWI activity. In the ADP^{S} state, the motor adopts a globally open conformation, but the DNA slips back to a relaxed state, suggesting that the energy of ATP hydrolysis is dissipated without being converted to DNA translocation. In the ADP^{B} state, we identified a newly formed regulatory element, the Brake helix. Brake binds to the Gating helix, which is induced to extend more, resulting in abnormal opening of the enzyme and ISWI inhibition. This mechanism of Brake-mediated inhibition is important for linker DNA sensitivity of ISWI.

CONCLUSION: Together, these findings lead to a multistate remodeling model that includes an inner core of the remodeling cycle and an outer regulatory layer. The proposed inner cycle provides a unifying mechanism of DNA translocation for chromatin remodeling. The outer regulation layer is ISWI specific, shedding light on the mechanism of linker DNA sensing by ISWI. □

*Corresponding author. Email: zhucheng_chen@tsinghua.edu.cn †These authors contributed equally to this work. **Cite this article as Y. Sia *et al.*, *Science* 388, eadu5654 (2025) DOI: 10.1126/science.adu5654**

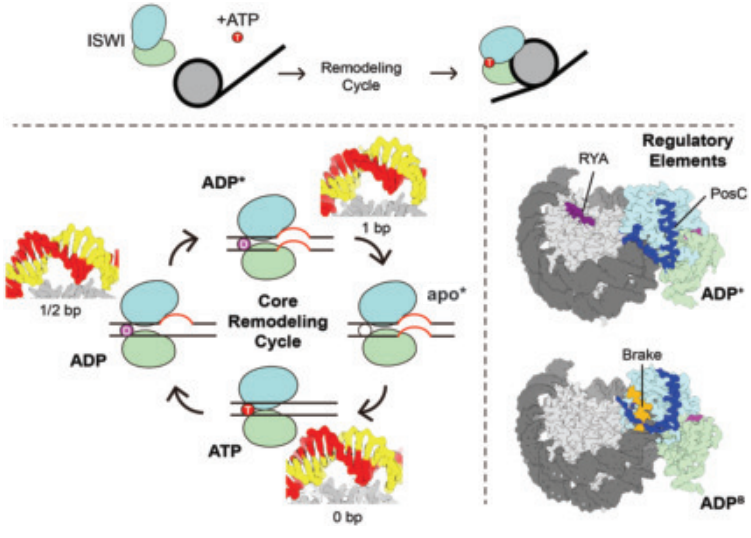

Mechanism of chromatin remodeling by ISWI. Chromatin remodeler ISWI slides nucleosomes to generate regularly spaced nucleosome arrays. By using electron microscopy, we caught the actions of ISWI in actively translocating the nucleosome and determined the structures of the complex in the ADP, ATP, ADP*, apo, apo*, ADP^{+}, ADP^{*+}, ADP^{S}, and ADP^{B} states at resolutions ranging from 2.3 to 3.0 Å. The structures reveal the conformational changes of ISWI and the altered interactions with the nucleosome in different states. These findings lead to a multistate model of ISWI action, providing a comprehensive mechanism of DNA translocation and regulation underpinning chromatin remodeling.

RESEARCH ARTICLE SUMMARY

NEUROTECHNOLOGY

Tellurium nanowire retinal nanoprosthesis improves vision in models of blindness

Shuiyuan Wang†*, Chengyong Jiang†, Yiye Yu†, Zhenhan Zhang†, Ruge Quhe†, Ruyi Yang, Yufei Tian, Xindong Chen, Wenqiang Fan, Yinge Niu, Biao Yan, Chunhui Jiang, Yang Wang, Zhen Wang, Chunsen Liu, Weida Hu*, Jiayi Zhang*, Peng Zhou*

Full article and list of author affiliations: https://doi.org/10.1126/science.adu2987

INTRODUCTION: In nature, there are animals, such as snakes, that assess their environment more accurately by sensing both infrared radiation and the visible-light spectrum. The human eye lacks photoreceptors responsive to the infrared spectrum, and infrared light with a longer wavelength and lower energy cannot trigger visual signals. In patients with severe eye diseases (e.g., macular degeneration), infrared vision could, in principle, aid vision in low light and darkness. Developing technologies that use a wider spectrum of light, including infrared, could provide notable benefits.

RATIONALE: Present designs for broad-spectrum retinal protheses use nanoparticles or photodiodes to convert infrared into visible light or heat to stimulate retinal cells. Because they require injections or bulky auxiliary devices, there are safety and practicality issues for potential application to humans. Creation of a safe, easy-to-implant retinal prosthesis that enables the processing of both visible and infrared light may restore vision loss and enhance natural vision. We designed a next-generation retinal nanoprosthesis based on tellurium nanowire networks that intrinsically converts broadband light—including visible to infrared light—with efficient photovoltaic conversion, yielding giant with photocurrents under zero-electric bias and without the need for extra auxiliary equipment. We then achieved safe and simple implantation in the subretinal space of mice and *Macaca fascicularis*.

RESULTS: Through theoretical calculations, we show spontaneous giant and wide-spectrum photocurrents of tellurium nanowire networks to be correlated with the asymmetry of nanowire lattice internal defects and external interfacial effects. Through a combination of narrow bandgaps, strong absorption, and engineered asymmetries, tellurium optoelectronic nanodevices showed record-high photocurrents and the widest spectrum of responsive photosensitivity wavelengths compared with reported techniques for the restoration of photosensitivity in blindness, covering the visible to near-infrared–II range. Preimplantation tests confirmed the stability of the nanoprosthesis's optoelectronic properties and its precise response to light patterns. In blind mice, the implanted nanoprosthesis replaced damaged photoreceptors and triggered responses in both the optic nerve and visual cortex. Implanted mice showed better light-induced pupil reactions and improvement in light-associated learning behaviors (such as water reward–based visual-cue associative learning and choice-box tasks) when compared with untreated mice and when using light intensities nearly 80 times weaker than the clinical safety threshold. The biocompatibility and efficacy of the proposed nanoprosthesis was further demonstrated in nonhuman primates (*Macaca fascicularis*), where the nanoprosthesis was tightly bound to the retina in the subretinal space and generated robust retina-derived responses to visible and infrared light.

CONCLUSION: Our study provides biologically feasible parameters for a retinal prosthesis using designed tellurium nanowire networks.

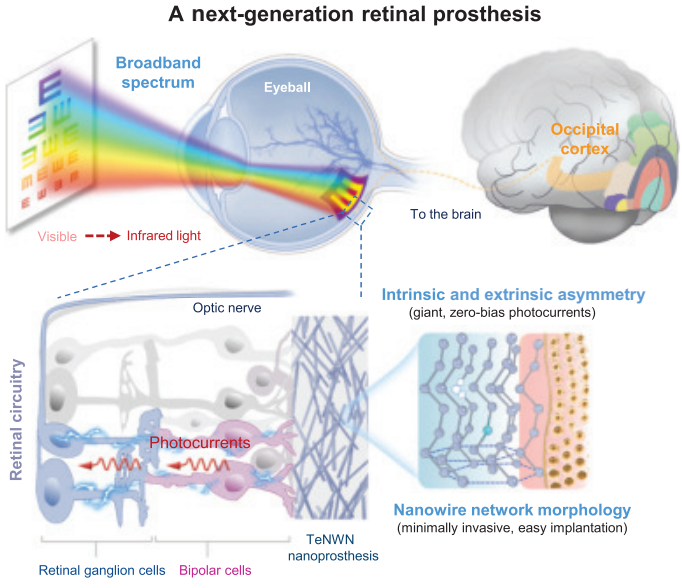

A next-generation nanoprosthesis that restores and enhances vision. Tellurium possess broad-spectrum optical absorption from visible to infrared light (top left). A subretinal-implanted tellurium nanoprosthesis replaces degenerated photoreceptors and generates photocurrents to activate residual retinal circuitry (bottom left) and the occipital cortex (top right). Giant, spontaneous, bias-free photocurrents and minimally invasive easy implantation is achieved by asymmetry engineering and nanowire network morphology (bottom right). Together, these properties make tellurium nanowire networks (TeNWNs) the next generation of visual prosthesis technology.

These nanowires naturally convert light into photocurrent signals with zero electrical bias and can cover the visible to infrared spectrum. The tested nanoprosthesis generates strong photocurrents to activate the remaining retinal circuitry in a dysfunctional eye, works through a simple subretinal implantation procedure, and avoids bulky intra- and extraocular components. In blind mice, this retinal nanoprosthesis restored the brain's response to light and improved vision-based behaviors at clinically safe light levels. Nonhuman primates implanted with this nanoprosthesis gained infrared vision without impairment of normal vision. This successful animal study paves the way for future human trials, showcasing the potential of this prosthesis to restore visible vision and expand augmented infrared perception for blind humans and offer a safer, more effective, and wider-spectrum solution than existing technologies. □

*Corresponding author. Email: sy_wang@fudan.edu.cn (S.W.); wdhu@mail.sitp.ac.cn (W.H.); jiayizhang@fudan.edu.cn (J.Z.); pengzhou@fudan.edu.cn (P.Z.) †These authors contributed equally to this work. **Cite this article as S. Wang *et al.*, *Science* 388, eadu2987 (2025). DOI: 10.1126/science.adu2987**

RESEARCH ARTICLE SUMMARY

CELL BIOLOGY

GPR45 modulates Gα$_s$ at primary cilia of the paraventricular hypothalamus to control food intake

Yu Xun†, Yiao Jiang†, Baijie Xu, Miao Tang, Sara Ludwig, Kazuhiro Nakamura, Saikat Mukhopadhyay, Chen Liu, Bruce Beutler, Zhao Zhang*

Full article and list of author affiliations: https://doi.org/10.1126/science.adp3989

INTRODUCTION: The discovery of *obese* mice and the positional cloning of the *obese* gene *leptin* have substantially increased our understanding of the endocrine control of energy balance. Secreted by adipose tissue, leptin primarily acts on its receptor in the arcuate nucleus of the hypothalamus (ARH) to transduce signals that either promote or suppress appetite through melanocortin-4 receptor (MC4R) neurons in the paraventricular nucleus of the hypothalamus (PVH). This leptin-melanocortin signaling pathway centrally regulates energy homeostasis, and its dysfunction causes obesity in both mice and humans.

RATIONALE: To accelerate the discovery of genes involved in energy balance, we performed a forward genetic screen using random mutagenesis in mice, followed by automated meiotic mapping. This approach identified multiple genes associated with primary cilia—small hairlike structures extending from the surface of most neurons. Genetic disorders that disrupt ciliary function frequently cause obesity. Both MC4R and its downstream signaling mediator adenylyl cyclase 3 (ADCY3) are localized to neuronal cilia, and their mislocalization from cilia leads to obesity. However, the mechanisms by which melanocortin signaling functions within cilia and how ciliary dysfunction contributes to obesity are not well understood.

RESULTS: Our genetic screen identified two obesity-associated alleles, *expansive* and *extensive*, which result from distinct missense mutations in an orphan G protein–coupled receptor (GPCR), *Gpr45*. Knockout of *Gpr45* in mice led to obesity, confirming that both mutations cause a loss of function. Mice lacking *Gpr45* consumed more food, and pair-feeding them the same amount as control mice rescued the obesity phenotype. *Gpr45* mRNA was highly expressed in the PVH, and its loss in PVH or MC4R-expressing neurons led to obesity. We found that the GPR45 protein was exclusively localized to primary cilia in both cultured cells and PVH neurons, with its ciliary localization mediated by TUB-like protein 3 (TULP3), a key adaptor for ciliary trafficking. Overexpression of GPR45 caused the accumulation of the stimulatory G protein subunit Gα$_s$ in cilia, where it is normally present at low levels. In contrast, *Gpr45* knockout mice exhibited reduced ciliary Gα$_s$ levels in the PVH. Furthermore, the Gα$_s$ transported by GPR45 was active in stimulating ADCY3, thereby increasing localized cyclic adenosine monophosphate (cAMP) levels in the cilia, which are distinct from the cytoplasmic cAMP pool. Most MC4R cilia in the PVH also showed GPR45 presence, while coexpression of GPR45 with MC4R enhanced Gα$_s$ translocation and ciliary cAMP production. GPR45 and ADCY3 are likely working in the same signaling pathway to regulate feeding, as loss of *Gpr45* did not further increase obesity in *Adcy3*-deficient mice. Moreover, both *expansive* and *extensive* mutations disrupted the ciliary localization of GPR45 and impaired its ability to transport Gα$_s$ and increase ciliary cAMP levels.

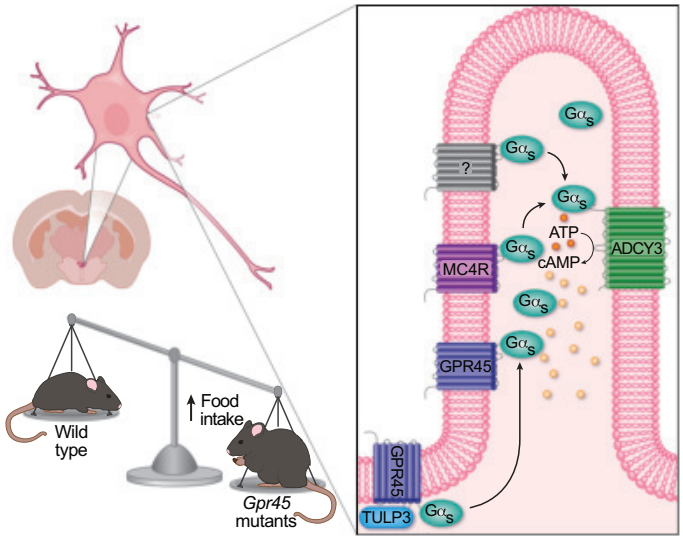

GPR45 transports Gα$_s$ into primary cilia to regulate food intake. In wild-type mice, GPR45 relies on TULP3 to transport Gα$_s$ into the primary cilia of PVH neurons. Within the cilia, Gα$_s$ supports MC4R and possibly other Gα$_s$-coupled GPCRs to activate ADCY3, leading to the production of cAMP from adenosine triphosphate (ATP), which signals to suppress appetite. In *Gpr45* mutant mice, owing to missense mutations that prevent its ciliary localization or complete knockout, this process is disrupted. As a result, ciliary signaling is impaired, leading to increased food intake and obesity.

CONCLUSION: This study identifies GPR45 as a critical ciliary GPCR that regulates food intake by modulating ciliary Gα$_s$ signaling in the PVH. Differing from typical GPCRs, GPR45 transports Gα$_s$ into cilia to be used by other Gα$_s$-coupled GPCRs, such as MC4R. GPR45 functions as a gatekeeper for ciliary Gα$_s$ to sustain a localized cAMP pool essential for ciliary melanocortin signaling. Dysregulated cilia or ciliary targeting of key leptin-melanocortin members disrupts such a GPR45-maintained ciliary cAMP pool and thus causes obesity. Given that the human GPR45 protein shows high sequence similarity to its mouse counterpart and GPCRs are highly druggable, these findings have potential therapeutic implications for developing anti-obesity medications. □

*Corresponding author. Email: zhao.zhang@utsouthwestern.edu †These authors contributed equally to this work. **Cite this article as Y. Xun *et al.*, *Science* 388, eadp3989 (2025). DOI: 10.1126/science.adp3989**

RESEARCH ARTICLE SUMMARY

NEUROSCIENCE

In vivo multiplex imaging of dynamic neurochemical networks with designed far-red dopamine sensors

Yu Zheng†, Ruyi Cai†, Kui Wang‡, Junwei Zhang‡, Yizhou Zhuo, Hui Dong, Yuqi Zhang, Yifan Wang, Fei Deng, En Ji, Yiwen Cui, Shilin Fang, Xinxin Zhang, Haiyun Huang, Kecheng Zhang, Jinxu Wang, Guochuan Li, Xiaolei Miao, Zhenghua Wang, Yuqing Yang, Shaochuang Li, Jonathan B. Grimm, Kai Johnsson, Eric R. Schreiter, Luke D. Lavis, Zhixing Chen, Yu Mu, Yulong Li*

Full article and list of author affiliations: https://doi.org/10.1126/science.adt7705

INTRODUCTION: Neurochemical signals, including neurotransmitters, neuromodulators, and intracellular signaling molecules, are dynamically modulated within networks that mediate various brain functions and contribute to neurological disorders. Dopamine (DA), one of the most important neuromodulators, interacts intricately with other neuromodulators such as acetylcholine (ACh) and endocannabinoids (eCBs), along with intracellular signals such as cyclic adenosine 5′-monophosphate (cAMP) and Ca^{2+}. Decoding these networks is crucial for understanding neural mechanisms underlying behaviors and related disorders. However, current genetically encoded sensors are limited to the green and red spectra, hindering real-time simultaneous detection of multiple neurochemical signals. There is an urgent need to expand the spectral range of neuromodulator sensors to include far-red and near-infrared (NIR) wavelengths (i.e., those >650 nm).

RATIONALE: By utilizing G protein–coupled receptors (GPCRs) and circularly permutated fluorescent proteins (cpFPs), we and others have developed a series of green and red GPCR activation–based (GRAB) sensors, enabling the detection of neuromodulators in vivo with high spatiotemporal resolution. However, expanding this strategy with far-red/NIR proteins presents challenges because of the suboptimal properties of existing far-red/NIR fluorescent proteins. The combination of protein tags with rhodamine derivatives offers a promising alternative approach, providing a broad spectral range and high brightness. We integrated the cpHaloTag–chemical dye approach with the GRAB strategy, resulting in the creation of HaloDA1.0, the first single protein–based far-red chemigenetic sensor for neuromodulators. Capitalizing on its far-red wavelength, HaloDA1.0 provides opportunities for monitoring three neurochemicals simultaneously by combining with existing green and red sensors.

RESULTS: HaloDA1.0 demonstrated robust sensitivity, high specificity, subsecond response kinetics, and compatibility with a variety of far-red chemical dyes. Combining HaloDA1.0 with two other neuromodulator sensors in acute mouse brain slices, we achieved simultaneous imaging of three key neuromodulators, DA, ACh, and eCB, after electrical stimulation and pharmacological interventions. In zebrafish larvae, HaloDA1.0 enabled three-color imaging of DA, ATP, and Ca^{2+}, revealing coordinated activation patterns during electrical shocks and acute seizure attacks. Our in vivo dye screening further established HaloDA1.0's effective performance in living mice with a silicon-rhodamine dye. This enabled dual-color recording alongside optogenetic manipulations. Furthermore, we achieved simultaneous multicolor recording of spontaneous and behaviorally associated DA, ACh, and cAMP signals in the nucleus accumbens, unveiling distinct regulatory patterns and providing a comprehensive perspective of concurrent regulation of intracellular cAMP signaling.

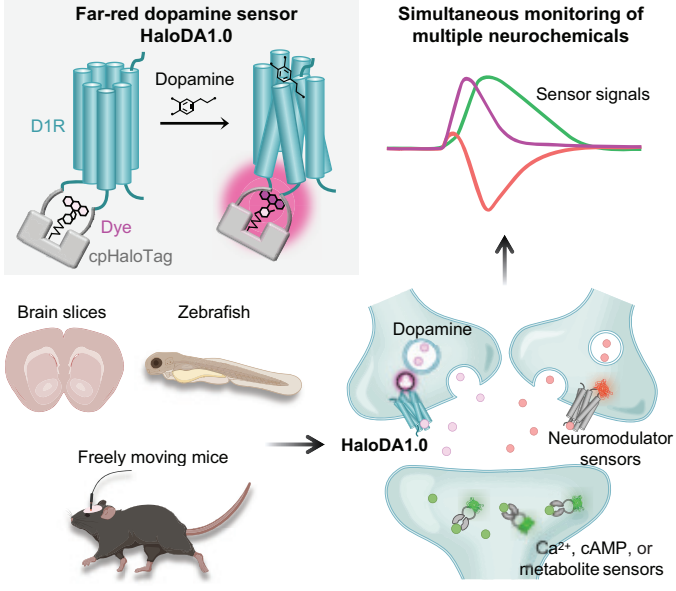

Development and applications of a far-red dopamine sensor for simultaneous monitoring of multiple neurochemicals. This sensor functions by modulating the equilibrium of the lactone form (L) and zwitterionic form (Z) of chemical dyes. Combining the far-red sensor with green and red sensors enables simultaneous monitoring of three neuromodulators or both neuromodulators and intracellular signals in various biological systems. Some schematics were created using BioRender.com.

CONCLUSION: To monitor multiple neurochemicals simultaneously, we developed the chemigenetic far-red DA sensor HaloDA1.0, enabling sensitive DA detection both in vitro and in vivo. This sensor demonstrates significant advantages for monitoring multiple neurochemical signals across diverse biological systems, including cultured neurons, acute mouse brain slices, zebrafish, and living mice. This strategy enhances our understanding of the complex interactions among various neurochemical signals, paving the way for deeper insights into neural circuit function and improved comprehension of neurological and psychiatric disorders. □

*Corresponding author. Email: yulongli@pku.edu.cn †These authors contributed equally to this work. ‡These authors contributed equally to this work. Cite this article as Y. Zheng *et al.*, *Science* 388, eadt7705 (2025). DOI: 10.1126/science.adt7705

PASSIVE COOLING

Passive cooling paint enabled by rational design of thermal-optical and mass transfer properties

Jipeng Fei[1], Xuan Zhang[2], Di Han[1], Yue Lei[3], Fei Xie[4], Kai Zhou[5], See-Wee Koh[1], Junyu Ge[1], Hao Zhou[1], Xingli Wang[6], Xinghui Wu[1], Jun-Yan Tan[1], Yuheng Gu[1], Yongping Long[1], Zhi Hui Koh[1], Su Wang[7], Panwei Du[8], Tangwei Mi[9], Bing-Feng Ng[1], Lili Cai[5], Chi Feng[10], Qiaoqiang Gan[3,11], Hong Li[1,6]*

Integrating radiative and evaporative cooling shows promise for enhancing passive cooling, but durable self-curing integrated cooling paints remain underdeveloped. We designed a modified cementitious structure with advanced thermal-optical and mass transfer properties, boosting cooling power while ensuring durability, mechanical strength, and broad adhesion. The paint achieves 88 to 92% solar reflectance (depending on wetting), 95% atmospheric window emittance, ~30% water retention, and self-replenishing properties, maintaining stable optical performance even when wet. Field tests in tropical Singapore demonstrated superior cooling performance compared with commercial white paints. Pilot-scale demonstrations highlighted consistent electricity savings under varying weather conditions, supported by theoretical modeling. By leveraging sustainable water evaporation and thermal radiation, this paint offers a practical and long-term solution for mitigating the urban heat island effect.

Passive cooling is gaining ever-increasing attention as a sustainable strategy to reduce CO_2 emissions from space cooling, a major contributor to global warming. Radiative passive cooling, which dissipates heat through the atmospheric window, is effective in dry climates with clear skies and has been adopted in commercial cooling paints (e.g., Nippon Solareflect), one of the most important passive cooling products (*1*). However, the efficacy of radiative cooling diminishes in humid regions, such as Singapore, where high relative humidity (RH) and cloud cover limit the cooling power to ~20 W/m^2 (*2*). Furthermore, having a directional cooling mechanism, radiative cooling shows substantially reduced efficiency on building facades due to restricted radiation angles to the sky. In densely built areas, where cooling demand is high owing to the urban heat island (UHI) effect, the limited application area of radiative cooling paint further reduces its usefulness. Thus, a more effective cooling paint design is desirable to enhance cooling beyond radiative cooling's limits, particularly in humid climates [Fig. 1A; detailed discussion in supplementary text section 1 of (*3*)] (*4*).

Evaporative cooling, exploiting water's high latent heat (~2256 J/g), provides a nondirectional cooling mechanism, overcoming the limitations of radiative cooling (*5*, *6*). Although they are an excellent platform for evaporative cooling, multilayer hydrogel systems in previous work suffer from swelling, poor adhesion, and structural degradation during hydration-dehydration cycles, restricting their long-term reliability (*7*, *8*). Our recent optofluidic metagel designs have improved the cooling performance of hydrogels by integrating multiple cooling strategies, yet the limited scalability and poor strength remain challenges (*9*). A paintable optofluidic cooler is desirable yet difficult to realize, as it must balance evaporative cooling, solar reflection, and radiative cooling while ensuring strong adhesion, durability, and ease of application (fig. S1A).

A cementitious matrix with a porous calcium silicate hydrate (C-S-H) network offers a promising solution, as it forms a robust and interconnected porous structure that enables water transport without swelling or detachment (*10*). Cement's durability, cost-effectiveness, tunable porosity, and spontaneous hydration–based volumetric curing make it an ideal candidate to embed evaporative cooling for scalable application (*11*, *12*). In this study, we developed a cement-based integrated cooling paint with a rationally designed nanoparticle-modified C-S-H porous network that ensures high solar reflectance, minimal optical variation upon transition between hydrated and dehydrated states, and high thermal emittance, showing unprecedented cooling performance in a pilot demonstration.

Optical performance of cement cooling paint (CCP)

Scanning electron microscopy (Fig. 1B and fig. S1, B and C) reveals that CCP has a homogeneous, interconnected porous structure (~1 μm pore diameter), with barium sulfate ($BaSO_4$) nanoparticles (~400 nm) firmly bonded to a C-S-H matrix. Simulations confirm strong Mie scattering from nanoparticles (300 to 1500 nm), covering ~90% of solar energy [Fig. 1B, inset; section 2 of (*3*)]. In comparison to titanium dioxide (TiO_2), $BaSO_4$ exhibits negligible ultraviolet light absorbance, reducing solar heating by ~4 to 7% (*13*, *14*). Additionally, CCP's porous structure enhances solar reflectance due to Mie scattering at C-S-H/air boundaries, given the refractive index mismatch (Fig. 1C) (*15*). Consequently, CCP achieves ~93% solar reflectance in dry state (Fig. 1D).

Upon wetting, reduced refractive index mismatch at pore boundaries weakens scattering, lowering reflectance (*13*). However, in the 300- to 1300-nm non–water absorptive range, CCP retains high reflectance (Fig. 1D), in contrast to reported reversible porous structures (*15*). High-resolution imaging confirms that nanoparticles remain attached to the porous matrix, stabilizing optical performance by maintaining comparable scattering in wet and dry states (fig. S1C and Fig. 1E). Increased nanoparticle coverage further minimizes reflectance drop in wet state (Fig. 1E, inset, and fig. S1D). Bare C-S-H matrix exhibits obvious reflectance loss owing to the weakened boundary scattering, whereas nanoparticle-coated pores sustain strong scattering by preventing direct C-S-H/water contact. As confirmed in Fig. 1F and fig. S1E, reflectance loss ($R_{dry} - R_{wet}$) decreases with higher $BaSO_4$ content. CCP-30, optimized by nanoparticle incorporation, exhibits <2% solar reflectance variation from ultraviolet light to 1300 nm while maintaining good mechanical strength (movie S1). The optimized nanoparticle and pore dimensions efficiently scatter near-infrared light while preserving a margin on visible light reflection, keeping high solar reflection yet mitigating visual discomfort. Although reflectance declines from 1300 nm to 2500 nm because of reduced pore scattering and water's intrinsic near-infrared light absorption, this accounts for only ~2% of total solar irradiance (Fig. 1F and fig. S2A). Consequently, CCP-30 shows only ~4% overall

[1]School of Mechanical and Aerospace Engineering, Nanyang Technological University, Singapore. [2]Department of Energy and Power Engineering, School of Mechanical Engineering, Beijing Institute of Technology, Beijing, China. [3]Division of Physical Science and Engineering, King Abdullah University of Science and Technology, Thuwal, Saudi Arabia. [4]Changchun Institute of Optics, Fine Mechanics and Physics, Chinese Academy of Sciences, Ji Lin, China. [5]Department of Mechanical Science and Engineering, University of Illinois at Urbana–Champaign, Urbana, IL, USA. [6]International Research Laboratory (IRL) 3288, CNRS International–Nanyang Technological University–Thales Research Alliance (CINTRA CNRS/NTU/THALES), Singapore. [7]Pan-United Concrete Pte Ltd, Singapore. [8]School of Civil and Environmental Engineering, Nanyang Technological University, Singapore. [9]School of Science and Engineering, University of Dundee, Dundee, UK. [10]School of Architecture and Urban Planning, Chongqing University, Chongqing, China. [11]Center for Renewable Energy and Storage Technologies (CREST), King Abdullah University of Science and Technology, Thuwal, Saudi Arabia. ***Corresponding author. Email: ehongli@ntu.edu.sg**

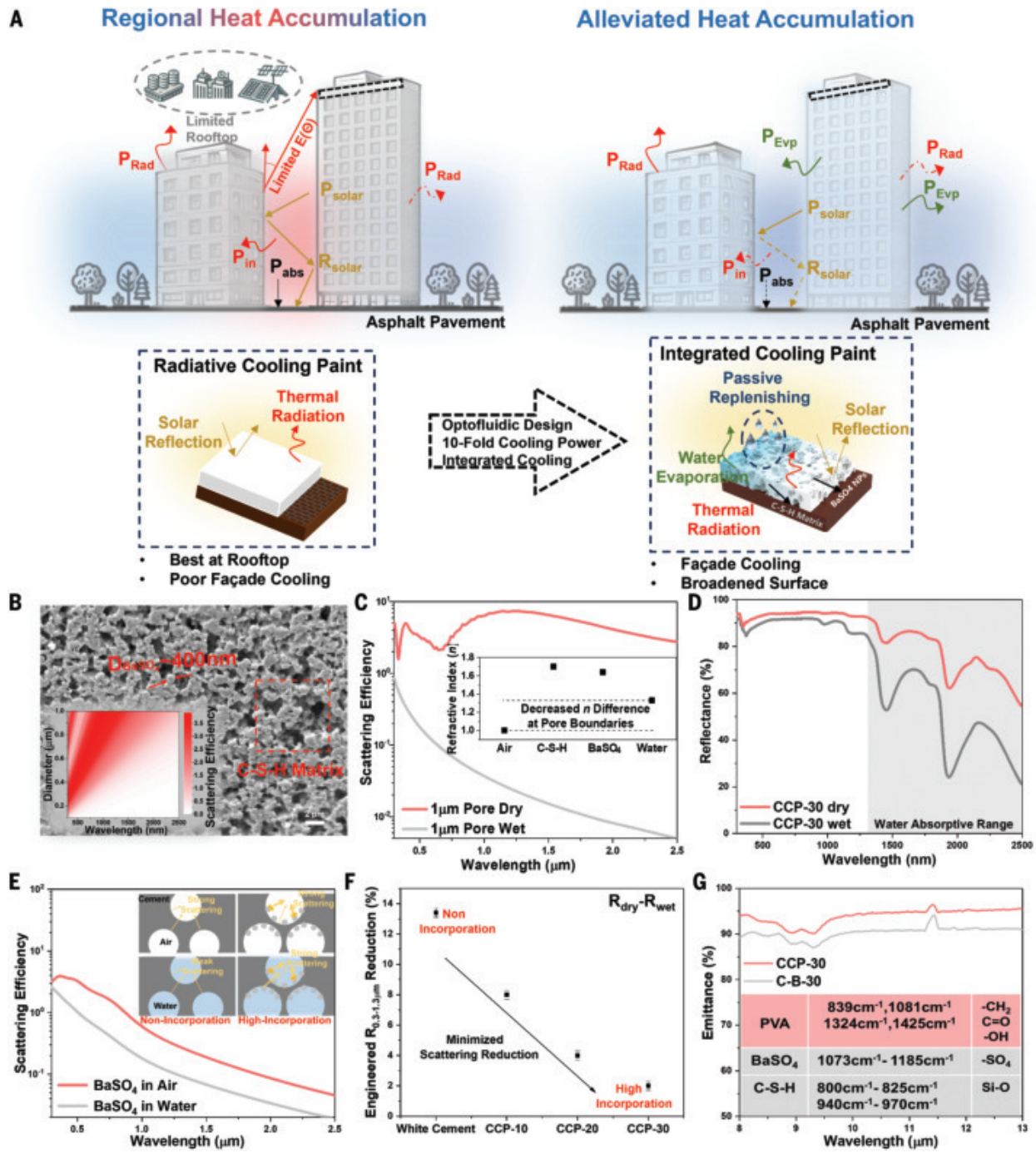

Fig. 1. Concept and optical performance of CCP-30. (**A**) Comparison of radiative cooling paint versus integrated cooling paint for buildings. P, power; R, reflection; Rad, radiation; Abs, absorption; Evp, evaporation; P_{in}, incident heat. (**B**) SEM image of C-S-H porous structure and surficial bonded nanoparticles. (Inset) Scattering efficiency simulation. (**C**) Scattering efficiency change of porous structure ($D = 1$ μm) under wet and dry states. (Inset) Refraction index difference among paint matrix ($BaSO_4$, C-S-H gel), water, and air. (**D**) Solar reflectance spectrum of CCP-30 under dry and wet states. (**E**) Scattering efficiency change of nanoparticle (D = ~400 nm) under wet and dry states. (Inset) Schematic illustration of synergic scattering effect by pore boundaries and nanoparticles under different states. "High-incorporation" means more nanoparticles. (**F**) Reflectance reduction of different samples in non–water absorptive range upon wetting. Error bars represent standard deviation of multiple measurements. (**G**) Emissivity spectra within the atmospheric window. (Inset) Bond type and vibration range.

reflectance variation across the solar spectrum upon wet-dry transitions (fig. S2B). Meanwhile, CCP-30 exhibits around 95% long-wavelength infrared emittance thanks to the intrinsic vibrations of chemical bonds (Fig. 1G, inset), which is higher than the sample without polyvinyl alcohol (PVA) additive, C-B-30 (Fig. 1G and fig. S3A) (*16*–*18*). Notably, CCP-30, with its compact internal structure (fig. S3, B and C), has high strength to ensure mechanical robustness (*19*, *20*).

Structural and mechanical design of CCP

CCP-30 forms through the hydration of cement powder, generating a C-S-H gel that enhances strength and durability (*21*). The water-to-cement (W/C) ratio, typically between 0.4 and 1, balances mechanical strength and workability (*22*). Although increasing the W/C ratio improves nanoparticle dispersion and optical performance, it also affects capillary porosity (50 nm < d < 10 μm), as water molecules create pores upon

evaporation (*23*–*25*). However, excessive water (e.g., W/C ratio = 2) results in weak, chalky structures owing to poor C-S-H connectivity (fig. S4A). Thus, CCP-30, having optimal W/C ratio, exhibits excellent strength [minimal weight loss even under severe abrasion (fig. S4B)] while maintaining sufficient porosity. Weak structures in pure cement samples arise from inadequate C-S-H particle compaction during hydration, as confirmed by the obvious boundaries of hydrated C-S-H (Fig. 2A and fig. S5). Added $BaSO_4$ nanoparticles mitigate this issue by forming weak hydrogen bonds with water (fig. S6), reducing free water content (Fig. 2A) and enhancing powder compaction. CCP-30 slurry achieves an effective W/C ratio range of 0.38 to 0.47, yielding a compact structure with workability comparable to that of standard mortar paint [fig. S7; section 3 of (*3*)] (*26*). Its viscoelastic properties allow adjustable thickness (up to 2.28 mm) in a single vertical painting, facilitating water storage and aesthetic applications.

Early hydration cracks (Fig. 2B, C-B-30) and weak surfaces (fig. S4B, C-B-30) indicate that nanoparticles alone do not ensure robustness. Fast water loss upon paint installation induces capillary pressure-driven plastic shrinkage (Fig. 2C, C-B-30) (*27*). To address this shrinkage, ~2 wt % PVA and LiCl were incorporated (Fig. 2B, CCP-30), creating a stronger hydrogen bonding network and hygroscopic effect to retain moisture, minimizing plastic shrinkage (Fig. 2C, CCP-30). PVA chains provide ample oxygen sites for interaction with silicate and calcium hydroxyl, effectively enhancing robustness by forming a network-like film to bridge cracks inside the C-S-H matrix (*28*, *29*).

C-B-30's weak surface suggests a lower C-S-H density due to incomplete hydration (*10*). Raman spectrum confirms the presence of C-S-H matrix in both samples, yet distinct peaks around 1500 cm^{-1} suggest the reduced hydration degree in C-B-30 [Fig. 2D; section 4 of (*3*)] (*21*, *30*, *31*). The polymeric network and hygroscopic salt in CCP-30 facilitate prolonged hydration, improving C-S-H interconnection. PVA acts as an internal water reservoir, ensuring continuous hydration, whereas C-B-30 lacks adequate water, leading to weak structures (Fig. 2E) (*29*). The initial curing time of CCP-30 (2 to 3 hours, C191-08 Vicat Needle Method) aligns with that of commercial paints and is followed by continuous slower hydration that improves robustness. As a result of the extended curing process, the C-S-H matrix in CCP-30 exhibits a more homogeneous crystalline

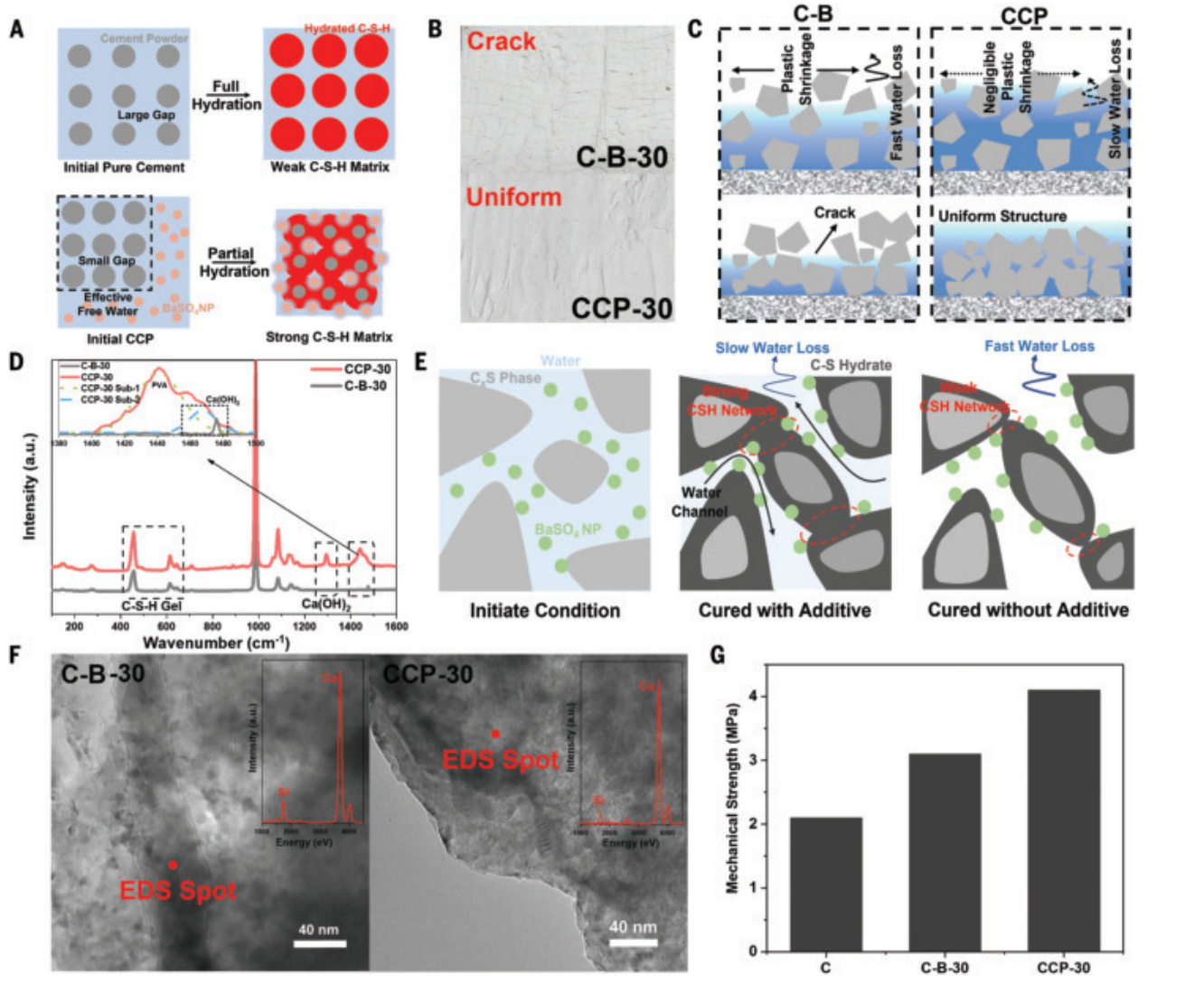

Fig. 2. Mechanical performance. (**A**) Schematic illustration showing that a lower W/C ratio resulted in compact cement powder distribution within CCP-30. (**B**) Optical images showing contrastive surficial morphology between C-B-30 and CCP-30. (**C**) Mechanism illustration of distinct water evaporation–induced structural difference. (**D**) Raman spectra of C-B-30 and CCP-30. (Inset) Enlarged view. a.u., arbitrary units. (**E**) Mechanism illustration of additive-induced distinct water evaporation (light gray, original cement particle; dark gray, C-S-H hydrate phase). (**F**) TEM images and related spotting EDS elemental spectra. (**G**) Mechanical strength comparison at day 7. Sample "C" is pure cement.

structure than that of C-B-30. Transmission electron microscopy (TEM) and energy-dispersive x-ray spectroscopy (EDS) reveal distinct matrix uniformity and Ca/Si ratios, confirming enhanced hydration in CCP-30 [Fig. 2F; section 5 of (*3*)]. With securely bonded nanoparticles and evenly dispersed PVA and LiCl [figs. S8 and S9; section 5 of (*3*)], CCP-30 shows an interconnected porous structure and exceptional robustness (Fig. 2G) during the spontaneous hydration process.

Fluidic design of CCP

With its interconnected porous structure, CCP-30 replenishes water passively with rain and water vapor (Fig. 3A). Its hydrophilic surface enables fast capillary accumulation (fig. S10, A to C, and movie S1). The nonswelling porous framework and slow water accumulation by hygroscopic salt (fig. S11), with minimized absorption-induced heating, endow CCP-30 with the capability of replenishing water from air. CCP-30 can capture ~16 wt % water vapor for sustainable evaporative cooling (fig. S10D). Notably, its low salt concentration prevents leaching upon heavy rain (fig. S10E). CCP-30 has superior surface fluidic properties, preventing droplet formation and condensation under extreme conditions, suggesting possible water replenishment through dew (fig. S10F).

Micro-CT (computed tomography) imaging (Fig. 3B) reveals a diffusible porous network with reduced closed-pore formations in CCP-30, contributing to balanced water cycling and mechanical stability. The better interconnection is attributed to the partially confined interparticle hydration through polymer wrapping outside C-S-H (*29*). Differential scanning calorimetry (DSC) indicates more efficient evaporative behavior at ambient temperatures, which is further verified by thermogravimetric analysis (TGA) (Fig. 3C and fig. S12) (*9*).

To evaluate the impact of CCP-30 on neighboring buildings, black absorbers were placed in front of CCP-30 and HR-RC (a highly reflective $BaSO_4$-based radiative cooling paint) under direct sunlight [Fig. 3D; section 6 of (*3*)] (*9*, *32*, *33*). Infrared imaging shows that CCP-30 maintains ~5°C lower temperatures than HR-RC (Fig. 3E and fig. S13), with the black absorber in front of CCP-30 surfaces being 8°C

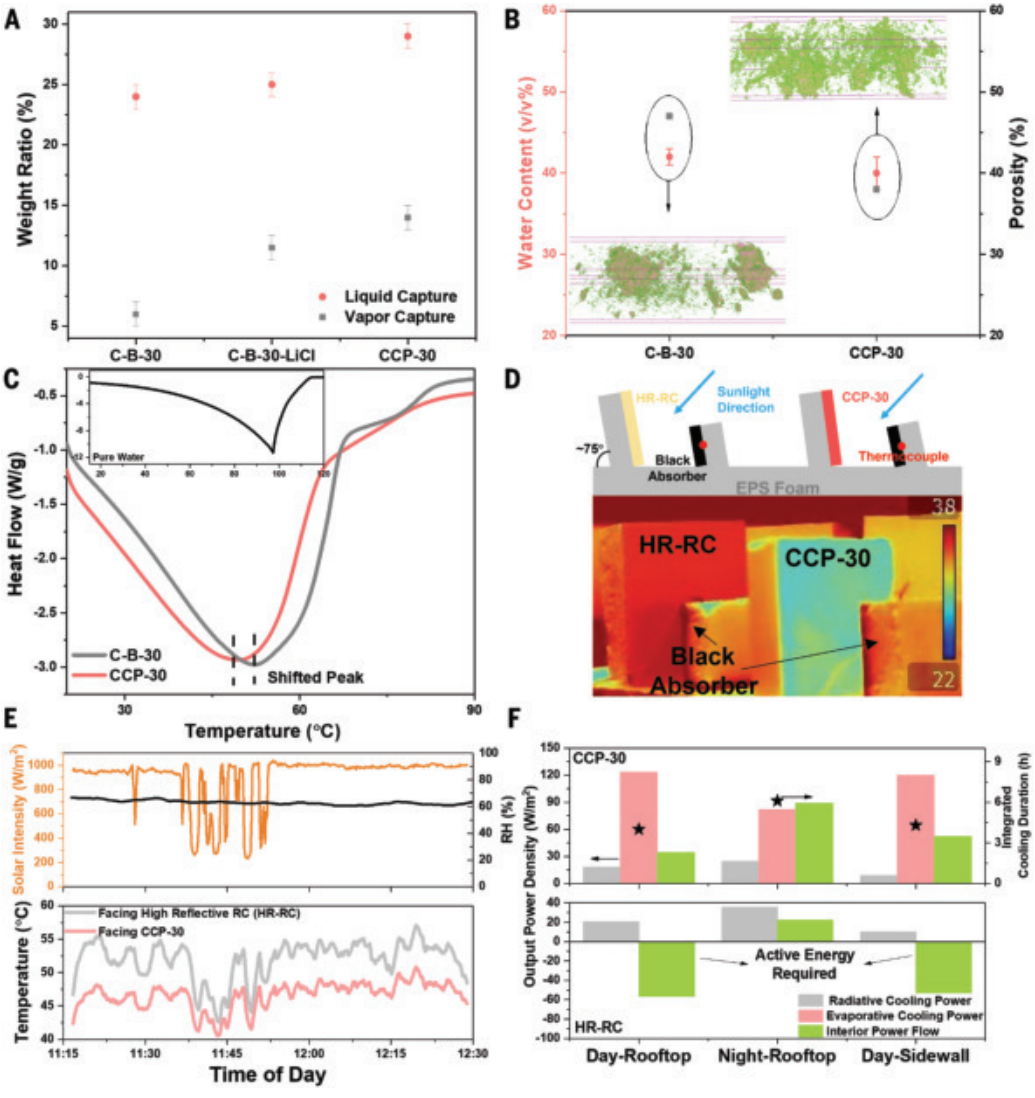

Fig. 3. Fluidic property and cooling mechanism. (**A**) Water uptake comparison. Error bars represent standard deviation of multiple measurements. (**B**) Porous network evaluation through water absorption and micro-CT scan. Error bars represent standard deviation of three measured samples. (**C**) DSC characterization of water evaporation behaviors. (Inset) Pure water evaporation profile. (**D**) Schematic (top) and heat mapping (bottom; measured at 11:30 a.m.) of the setup, where samples were stabilized under direct sunlight for 30 min. (**E**) Weather conditions (top) and black absorbers' temperature (bottom). (**F**) Cooling potential comparison based on typical Singapore climates at different facings. The negative interior power flow represents that active power is required to maintain the boundary condition.

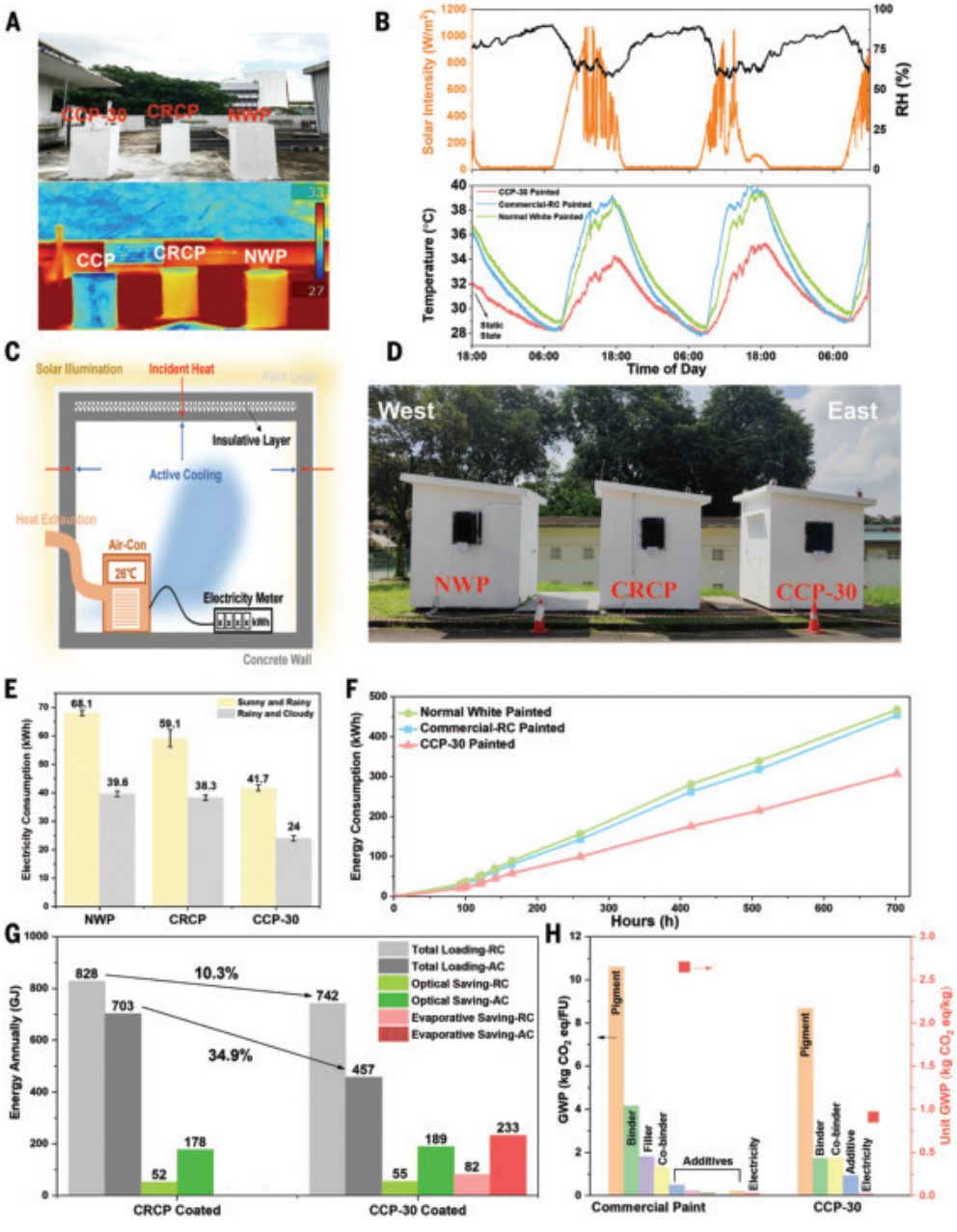

Fig. 4. Field tests. (**A**) Optical (top) and infrared (bottom) images of the three demo houses coated with different paints. (**B**) Three-day cooling performance test of different paints on demo houses (12 to 15 May 2023; top); air temperature during the test is provided in fig. S18D. (**C** and **D**) Electricity savings test in a livable house (3 m by 3 m by 4 m), where independent electricity meters and air-conditioning systems (EuropAce, EPAC 12C) were installed. (**E**) Two sets of 3-day (sunny and rainy, 11 to 14 August 2023; rainy and cloudy, 15 to 18 August 2023) electricity consumption in different weather. Room temperature was set at 26°C on the air-conditioning systems. Daily weather profiles can be found at www.weather.gov.sg/climate-historical-daily [search: "Jurong (West)"]. (**F**) Month-long electricity consumption (18 August to 16 September 2023). (**G**) Year-round energy saving simulation of a typical four-story house under Singapore climate. RC, rooftop coated; AC, all-facade coated. (**H**) Carbon footprint analysis through life-cycle assessment. Daily weather profiles can be found at www.weather.gov.sg/climate-historical-daily [search: "Jurong (West)"].

cooler. This reduction in heat flux indicates that CCP-30 dissipates heat through evaporative cooling rather than solely by reflecting solar irradiance like HR-RC, effectively mitigating the UHI effect.

The cooling performance of CCP-30 and HR-RC in tropical Singapore was evaluated through quasi-static thermal assessment [Fig. 3F and fig. S14; section 7 of (*3*)] (*9*). Maintaining an interior temperature of 26°C, CCP-30 demonstrated up to 140 W/m^2 cooling power, outperforming HR-RC by a factor of 3 to 10, depending on orientation. This effectiveness is further confirmed by interior power flow measurements, showing CCP-30's superior cooling capability and adaptability.

Evaluation on decoupled passive methods under adiabatic boundary conditions was conducted to better understand the working principles of integrated cooling (fig. S15), which outperforms radiative cooling at lower humidity, achieving higher output power and lower surface temperatures, which is especially effective for facades. In contrast to radiative cooling that has limited cooling at high humidity and certain orientations, evaporative cooling maintains consistent cooling with varying orientations [section 8 of (*3*)]. A further extension to a one-dimensional near-static model was built for evaluating the potential of integrated cooling from both material and climatic aspects, aiming to provide insights for the design of integrated cooling products beyond paint [figs. S16 and S17; section 7 of (*3*)].

Outdoor cooling performance and environmental impact

A long-term surface-level cooling experiment was conducted (fig. S18A), comparing CCP-30 with a commercial radiative cooler [commercial RC paint (CRCP): Nippon Solareflect Si], whose optical characteristics are shown in fig. S13 (*9*, *32*). The results demonstrate that capillary absorption provides more effective cooling (up to 7°C) than moisture capture (up to 3°C) owing to greater water replenishment. During intermittent rainfall, evaporative cooling was enhanced by water staying on the CRCP surface. High humidity further constrained evaporative cooling, whereas heavy rainfall led to similar temperatures on both samples. Besides, it is important to balance moisture capture and salt leaching upon frequent rainfall for sustainable cooling as well as to consider the design strategy for several typical climates [fig. S18, B and C; discussion in section 9 of (*3*)].

We assessed indoor temperature reduction and electricity savings to quantify the cooling paint's effectiveness. A test was conducted on three identical houses (50 cm by 40 cm by 70 cm) made of industrial concrete blocks (10 cm thick) coated with different paints, including CCP-30, CRCP, and normal white paint (NWP) (Fig. 4, A and B, and figs. S13 and S18D). As a result of the high heat capacity and low thermal conductivity of concrete, delayed temperature peaks were

observed with respect to that of solar irradiance. The CCP-30–coated house maintained the lowest indoor temperature throughout the test, remaining >4.5°C cooler than the others. The lower sidewall temperature of CCP-30 was attributed to its evaporative cooling (infrared image in Fig. 4A, taken at 2:30 p.m., 13 May 2023). Despite similar optical properties among the paints, CCP-30 demonstrated superior cooling thanks to its integrated cooling.

To quantify energy savings, we applied NWP, CRCP, and CCP-30 to habitable concrete houses equipped with air conditioning and electricity meters (Fig. 4, C and D). Over the course of two 3-day experiments (Fig. 4E), CCP-30 demonstrated energy savings of between 30 and 40% in comparison to the other paints during alternating sunny and rainy days. During continuous rainy and cloudy days, CCP-30 maintained ~40% energy savings over other paints. The similar electricity consumption of NWP- and CRCP-painted houses indicates minimal contribution of radiative cooling on rainy or cloudy days. The substantial energy savings of CCP-30 were attributed to evaporative cooling, even with high humidity. A comparison (fig. S19) clearly showed that CCP-30 exhibited the lowest energy consumption and the least sensitivity to weather fluctuations. A month-long test (Fig. 4F) confirmed electricity savings of up to 40% compared with commercial paints, with a difference of ~6% between NWP and CRCP. The electricity consumption difference (~170 kWh) suggests an additional ~243 W cooling power from CCP-30 by effectively mitigating the peak of solar heating, shaving the temperature peak on the wall. Scalable simulation through EnergyPlus revealed a consistent energy savings difference (~34%) with experimental results, where ~68,333.3 kWh electricity could be saved annually upon full installation of CCP-30 on a four-story house [Fig. 4G; section 10 of (*3*)]. Additionally, life-cycle analysis reveals an ~28% lower functional-unit (FU) and ~65% lower unit-mass carbon footprint of CCP-30 than NWP, indicating substantial environmental benefits [Fig. 4H and fig. S20; section 11 of (*3*)].

According to design criteria, applicability-related features were evaluated in terms of cost-effectiveness, scalability, and ease of installation [figs. S21 and S22A and movie S2; discussion in sections 12 to 14 of (*3*)]. Made from cementitious material and inorganic pigments, CCP-30 costs 10 to 30 times less than commercial alternatives [section 15 of (*3*)]. Unlike conventional resin-based paints, CCP-30 cures volumetrically with water, maintaining its thickness and requiring fewer coats, which substantially reduces labor costs. Its optimized rheology allows a single-layer application of 1-mm thickness, ensuring durability and ease of use [fig. S22, B and C; section 16 of (*3*)]. The paint demonstrates superior adhesion, robustness, and weather resistance, maintaining optical stability and resisting color degradation over time [figs. S23 and S24, A to E; sections 17 and 18 of (*3*)]. Compared to CRCP and NWP, CCP-30 enhances energy savings by 5 to 10% annually thanks to its superior optical stability (fig. S24, E and F). Its matte surface reduces glare while maintaining high reflectivity, and its mold-resistant and cleanable surface hinders dust accumulation [figs. S24, G to I, S25, and S26; section 18 of (*3*)]. It also poses no corrosion risk to reinforced concrete [fig. S27; section 19 of (*3*)].

In summary, a paintable integrated passive cooler (CCP-30) has been developed by combining radiative and evaporative cooling through a rational thermal-optical and mass transfer design. Sustainable evaporative cooling is enabled by self–water replenishment through rainwater and atmospheric moisture harvesting, stored in a hydroscopic porous network. CCP-30 achieves up to 10 times higher cooling power than commercial cooling paints in tropical climates. In pilot-scale tests, it consistently achieves electricity savings of 30 to 40% compared with radiative cooling, cutting carbon emissions proportionally. As a water-based cementitious paint, CCP-30 offers high mechanical strength, weather resistance, fast curing, and cost-effectiveness. Its self-curing mechanism and strong adhesion, offering ease of application, make it suitable for various surfaces. This work demonstrates an innovative passive cooling solution with practical viability for global decarbonization.

REFERENCES AND NOTES

1. A. G. Papatsounis, P. N. Botsaris, S. Katsavounis, *Energies* **15**, 1117 (2022).
2. D. Han, B. F. Ng, M. P. Wan, *Sol. Energy Mater. Sol. Cells* **206**, 110270 (2020).
3. Materials and methods and supplementary text sections are available in the supplementary materials.
4. D. Zhao *et al.*, *Appl. Phys. Rev.* **6**, 021306 (2019).
5. Y. Yang, G. Cui, C. Q. Lan, *Renew. Sustain. Energy Rev.* **113**, 109230 (2019).
6. T. Rahman *et al.*, *Road Mater. Pavement Des.* **24**, 1103–1129 (2023).
7. J. Li *et al.*, *Sci. Adv.* **8**, eabq0411 (2022).
8. C. Feng *et al.*, *Nano Energy* **85**, 105971 (2021).
9. J. Fei *et al.*, *Nano Lett.* **24**, 623–631 (2024).
10. J. W. Bullard *et al.*, *Cement Concr. Res.* **41**, 1208–1223 (2011).
11. S. Goto, D. M. Roy, *Cement Concr. Res.* **11**, 575–579 (1981).
12. F. B. P. da Costa, L. M. Haselbach, L. C. P. da Silva Filho, *Constr. Build. Mater.* **268**, 121084 (2021).
13. J. Fei *et al.*, *Adv. Funct. Mater.* **32**, 2203582 (2022).
14. C. Tian, *Sci. Rep.* **10**, 7999 (2020).
15. J. Mandal *et al.*, *Joule* **3**, 3088–3099 (2019).
16. A. Kharazmi *et al.*, *Beilstein J. Nanotechnol.* **6**, 529–536 (2015).
17. Á. B. Sifontes *et al.*, *J. Nanomater.* **2015**, 510376 (2015).
18. E. Bernard, Y. Yan, B. Lothenbach, *Cement Concr. Res.* **143**, 106393 (2021).
19. M. Mirzababaei, A. Arulrajah, M. Ouston, *Procedia Eng.* **189**, 25–32 (2017).
20. D. Cao *et al.*, *Constr. Build. Mater.* **390**, 131775 (2023).
21. F. Liu, Z. Sun, C. Qi, *J. Mater. Civ. Eng.* **27**, 04014223 (2015).
22. S. Singh, P. Munjal, N. Thammishetti, *J. Build. Eng.* **4**, 94–100 (2015).
23. P. Navi, C. Pignat, *Adv. Cement Base. Mater.* **4**, 58–67 (1996).
24. H. Dong, P. Gao, G. Ye, *Mater. Struct.* **50**, 154 (2017).
25. M. Arandigoyen, J. I. Alvarez, *Appl. Surf. Sci.* **252**, 8077–8085 (2006).
26. G. Lu, K. Wang, *ACI Mater. J.* **107**, 12–19 (2010).
27. D. Snoeck, L. Pel, N. De Belie, *Cement Concr. Compos.* **93**, 54–62 (2018).
28. D. Hou, J. Yu, P. Wang, *Compos. B Eng.* **162**, 433–444 (2019).
29. J. Fan, G. Li, S. Deng, Z. Wang, *Appl. Sci.* **9**, 2178 (2019).
30. M. Tarrida, M. Madon, B. Le Rolland, P. Colombet, *Adv. Cement Base. Mater.* **2**, 15–20 (1995).
31. Z. Zhang, J. Du, M. Shi, *Materials* **15**, 2660 (2022).
32. D. Han *et al.*, *Sol. Energy Mater. Sol. Cells* **240**, 111723 (2022).
33. D. Han, J. Fei, H. Li, B. F. Ng, *Build. Environ.* **221**, 109281 (2022).

ACKNOWLEDGMENTS

The Office of Development and Facilities Management (ODFM) of Nanyang Technological University provided the house testbed for energy savings evaluation. The authors acknowledge the Facility for Analysis, Characterizations, Testing and Simulation (FACTS), Nanyang Technological University Singapore, for use of electron microscopes and other facilities. **Funding:** This work was supported by the Singapore Ministry of Education Tier 1 (RG153/23) and Tier 2 (MOE-T2EP50123-0016) Programs, GAP fund (NGF-2023-14-014) from NTUitive, Nanyang Technological University. B.-F.N. acknowledges support from the Singapore National Research Foundation (NRF2021-NRF-ANR001). **Author contributions:** J.P.F. and H.L. conceived of the idea. J.P.F. conducted material development and experimental investigations. X.Z., D.H., Y.L., Q.Q.G., H.Z., B.-F.N., and C.F. conducted theoretical modeling and analysis. F.X., K.Z., S.-W.K., J.Y.G., X.L.W., X.H.W., J.-Y.T., Y.H.G., Y.P.L., Z.H.K., and L.L.C. helped with field tests and material characterizations. S.W., P.W.D., and T.W.M. provided instructions and help on material development and validation. H.L. supported and supervised the project. All authors commented on and revised the manuscript. **Competing interests:** J.P.F. and H.L. have filed a Patent Cooperation Treaty (PCT) patent published by the Intellectual Property Office of Singapore under publication no. WO 2024/063701 A1 related to this work. The authors declare that they have no other competing interests. **Data and materials availability:** All materials and methods, including code and coding parameters, are included in the manuscript and supplementary materials.

SUPPLEMENTARY MATERIALS

science.org/doi/10.1126/science.adt3372
Materials and Methods; Supplementary Text; Figs. S1 to S27; Tables S1 to S6; References (*34*–*60*); Movies S1 to S4

Submitted 24 September 2024; accepted 2 April 2025

10.1126/science.adt3372

SOLID STATE PHYSICS

Direct measurement of the quantum metric tensor in solids

Sunje Kim[1,2,3]†, Yoonah Chung[4]†, Yuting Qian[1,2,3]†, Soobin Park[4], Chris Jozwiak[5], Eli Rotenberg[5], Aaron Bostwick[5], Keun Su Kim[4]*, Bohm-Jung Yang[1,2,3]*

The quantum metric tensor is a central geometric quantity in modern physics that is defined as the distance between nearby quantum states. Despite numerous studies highlighting its relevance to fundamental physical phenomena in solids, measuring the complete quantum metric tensors in real solid-state materials is challenging. In this work, we report a direct measurement of the full quantum metric tensors of Bloch electrons in solids using black phosphorus as a representative material. We extracted the momentum space distribution of the pseudospin texture of the valence band from the polarization dependence of angle-resolved photoemission spectroscopy measurement. Our approach is poised to advance our understanding of quantum geometric responses in a wide class of crystalline systems.

The quantum geometric tensor (QGT) can delineate the geometric attributes inherent in quantum states (*1*, *2*). Recent investigations underscore the central contribution of the QGT in describing a broad spectrum of electronic (*3*, *4*) and optical (*5*–*7*) properties observed in solid systems. The QGT is expressed by the complex-valued tensor Q_{ij} (i and j represent indices for spatial coordinates) whose real and imaginary parts are the quantum metric and the Berry curvature, respectively (*8*). The Berry curvature can be interpreted as the fictitious magnetic field induced by the topological monopole (*9*), which fundamentally modifies the electron's equation of motion (*10*); various quantized and topological electronic transport phenomena, including quantum anomalous Hall effect (*11*–*13*), quantized Faraday and Kerr rotation (*14*), and the Fermi arc in the topological semimetal (*15*), have been attributed to the Berry curvature effects. The momentum space distribution of the Berry curvature has been measured in various solid systems by estimating the local orbital angular momentum by using the circular dichroism angle-resolved photoemission spectroscopy (CD-ARPES) signal (*16*–*20*).

On the other hand, the quantum metric, which is the real part of the QGT, has been spotlighted recently as an important geometric quantity explaining various fundamental physical phenomena. Defined as the distance between two different quantum states (*21*), the quantum metric has been shown to quantify the spread of the Wannier function in real space (*22*) and to describe the electric quadrupole moment of the localized wave packet (*23*, *24*). Moreover, the quantum metric was shown to influence electronic transport property and superconductivity critically. For example, quantum metric affects the nonlinear Hall effect in a space-time inversion symmetric system characterized by zero Berry curvature (*25*, *26*). Additionally, superconductivity was shown to be induced in the energetically flat band owing to the nontrivial quantum metric (*27*–*29*). Lastly, with increasing attention to this quantity, a myriad of physical phenomena originating from the quantum metric in solids has been found, including the anomalous Landau level of flat bands (*30*–*32*), excitonic Lamb shift (*33*), and geometric orbital susceptibility (*34*, *35*).

Direct measurements of the quantum metric have focused on simple artificial two-level systems (*36*–*38*). An indirect measurement of a portion of the quantum metric in solids was achieved only recently using CD-ARPES experiments (*20*). However, that approach cannot be extended to extract the complete quantum metric tensor G_{ij}, which has three independent components, G_{xx}, G_{xy}, and G_{yy} in two dimensions, contrary to the Berry curvature tensor F_{ij} with only one independent component F_{xy} because of its antisymmetric nature. It is thus essential to design an effective methodology for the direct measurement of the full quantum metric tensor in solid-state systems.

In this work, we report the experimental measurement of the complete quantum metric tensor of the Bloch electronic states in solids. Our investigation centers on the pseudospin measurement through polarization-dependent ARPES experiments on bulk black phosphorus (BP) whose low-energy band structure is well-described by an effective two-band Hamiltonian. The two quantum states of the two-band Hamiltonian are equivalently described by a pseudospin, which can be represented by a vector on the Bloch sphere (Fig. 1, A and B). The measurement of the pseudospin enables the direct determination of the complete quantum metric tensor for the two quantum states near the Fermi level, which governs the electric transport and optical properties of the materials in a low-energy regime (*3*–*5*, *25*, *26*).

More explicitly, BP, characterized by a puckered honeycomb lattice structure (Fig. 2A), possesses space-time inversion symmetry and weak spin-orbit coupling. The symmetry inherent in the system results in the pseudospin Hamiltonian residing along a great circle of the Bloch sphere. This characteristic allows the pseudospin to be precisely determined by a rotation angle (θ) along the great circle, which can be directly measured by the polarization dependence of ARPES intensity taken from BP owing to its simple band structure (*39*–*42*). Considering that the symmetry of this system forces the Berry curvature to be uniformly zero across the entire Brillouin zone, the quantum metric tensor serves as a complete specification of the full QGT, thereby governing the geometric characteristics of the quantum state. Our research is poised to reveal a central role of quantum geometry in the experimental exploration of physical phenomena dictated by the quantum metric tensor in solid-state systems.

Measuring the complete quantum geometric tensor in solids

Before presenting our ARPES experimental results, we first explain the central idea for measuring the complete QGT in solids with Fig. 1. The QGT $Q^n_{ij}(k)$ of the nondegenerate cell-periodic Bloch state $|u_n(\boldsymbol{k})\rangle$ with the crystal momentum $\boldsymbol{k}$ and the band index n is given by

$$Q^n_{ij}(\boldsymbol{k}) = \left\langle \partial_{k_i} u_n(\boldsymbol{k}) \middle| \left[1 - P_n(\boldsymbol{k})\right] \middle| \partial_{k_j} u_n(\boldsymbol{k}) \right\rangle \tag{1}$$

where $\partial_{k_i} = \partial / \partial k_i$ is the differential operator on the momentum k_i, and $P_n(\boldsymbol{k}) = |u_n(\boldsymbol{k})\rangle\langle u_n(\boldsymbol{k})|$ is the projection operator onto $|u_n(\boldsymbol{k})\rangle$. Given the complex-valued tensor $Q^n_{ij}(\boldsymbol{k})$, its real and imaginary parts give rise to the quantum metric $G^n_{ij}(\boldsymbol{k})$ and the Berry curvature $F^n_{ij}(\boldsymbol{k})$ of $|u_n(\boldsymbol{k})\rangle$ as

$$G^n_{ij}(\boldsymbol{k}) = \mathrm{Re}\left[Q^n_{ij}(\boldsymbol{k})\right] \tag{2}$$

$$F^n_{ij}(\boldsymbol{k}) = -2\mathrm{Im}\left[Q^n_{ij}(\boldsymbol{k})\right] \tag{3}$$

For the exact calculation of $G^n_{ij}(\boldsymbol{k})$ and $F^n_{ij}(\boldsymbol{k})$, each component of $|u_n(\boldsymbol{k})\rangle$ should be precisely determined, which requires a huge effort in real solid systems because of the large dimension of $|u_n(\boldsymbol{k})\rangle$. However,

[1]Department of Physics and Astronomy, Seoul National University, Seoul, Republic of Korea. [2]Center for Theoretical Physics (CTP), Seoul National University, Seoul, Republic of Korea. [3]Institute of Applied Physics, Seoul National University, Seoul, Republic of Korea. [4]Department of Physics, Yonsei University, Seoul, Republic of Korea. [5]Advanced Light Source, E. O. Lawrence Berkeley National Laboratory, Berkeley, CA, USA. *Corresponding author. Email: keunsukim@yonsei.ac.kr (K.S.K.); bjyang@snu.ac.kr (B.-J.Y.) †These authors contributed equally to this work.

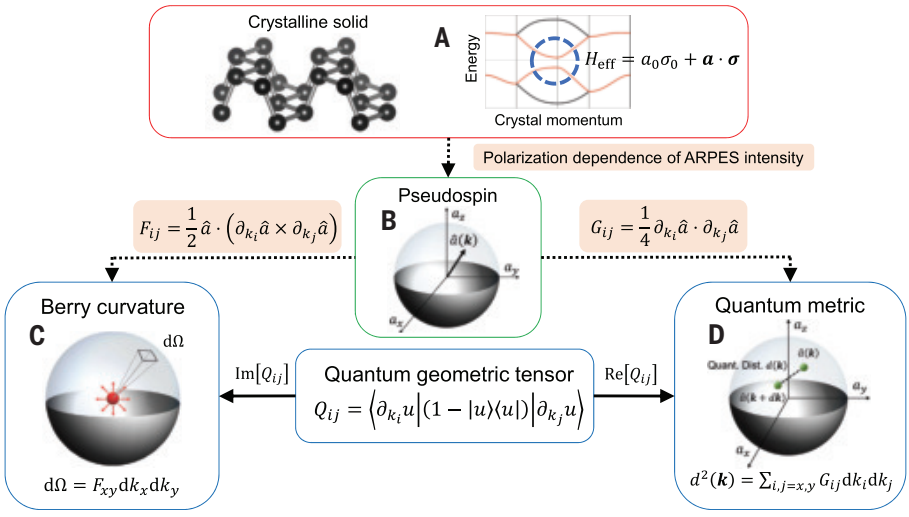

Fig. 1. Strategy for measuring the complete quantum geometric tensor in solids using the pseudospin. (**A**) The low-energy band structure of BP where the red and black lines are the energy bands. The two bands near the Fermi level (the red lines in the blue dashed circle) can be described by a 2×2 effective Hamiltonian $H_{\text{eff}} = a_0\sigma_0 + a\cdot\sigma$, where a_0 is a real number, σ_0 is the 2×2 identity matrix, $\boldsymbol{a}$ is a three-component real-valued vector, and $\boldsymbol{\sigma} = (\sigma_x, \sigma_y, \sigma_z)$ is a vector of Pauli matrices. Here, the lower-energy eigenstate $|u_{\text{eff}}\rangle$ of H_{eff} describes the topmost occupied state, which we call the pseudospin spinor state. (**B**) The Bloch vector $\hat{a} = \boldsymbol{a}/|\boldsymbol{a}|$ on the Bloch sphere corresponding to the pseudospin spinor state $|u_{\text{eff}}\rangle$. The quantum geometric tensor of the pseudospin spinor can be calculated by using $\hat{a}$ as $F_{ij} = \frac{1}{2}\hat{a}\cdot\left(\partial_{k_i}\hat{a}\times\partial_{k_j}\hat{a}\right)$, $G_{ij} = \frac{1}{4}\partial_{k_i}\hat{a}\cdot\partial_{k_j}\hat{a}$. For the experimental measurement of the pseudospin spinor in the momentum space, we used the polarization dependence of ARPES intensity. (**C** and **D**) Schematic description for the Berry curvature F_{ij}, which is the fictitious magnetic flux from a Weyl point, and the quantum metric G_{ij}, which describes the distance between two infinitesimally separated quantum states. In two dimensions, the Berry curvature is a scalar quantity with a single component F_{xy}. By contrast, the quantum metric is a tensor object with three independent components (G_{xx}, G_{yy}, G_{xy}), which makes it difficult to measure completely in experiments. Re, real; Im, imaginary; Ω, Berry curvature.

if the low-energy band structure near the Fermi level can be well-described by two quantum states energetically separated from other bands (Fig. 1A), then $|u_n(\boldsymbol{k})\rangle$ can be approximately described by an eigenstate $\left|u_{n,\text{eff}}(\boldsymbol{k})\right\rangle$ of a 2×2 effective Hamiltonian $H_{\text{eff}}(\boldsymbol{k})$ given by

$$H_{\text{eff}}(\boldsymbol{k}) = a_0(\boldsymbol{k})\sigma_0 + \boldsymbol{a}(\boldsymbol{k})\cdot\sigma \tag{4}$$

where a_0 is a real number, σ_0 is the 2×2 identity matrix, $\boldsymbol{a}$ is the three-component real-valued vector, and $\boldsymbol{\sigma} = (\sigma_x, \sigma_y, \sigma_z)$ is a vector of Pauli matrices. Because the two-component state $\left|u_{n,\text{eff}}(\boldsymbol{k})\right\rangle$, called the pseudospin spinor state (*43*), well approximates $|u_n(\boldsymbol{k})\rangle$, $G^n_{ij}(\boldsymbol{k})$ and $F^n_{ij}(\boldsymbol{k})$ can be computed by using $\left|u_{n,\text{eff}}(\boldsymbol{k})\right\rangle$ instead of $|u_n(\boldsymbol{k})\rangle$. Also, equivalently, we can express the QGT using the Bloch vector $\hat{a} \equiv \boldsymbol{a}/|\boldsymbol{a}|$ (Fig. 1B). Given that the Bloch vector $\hat{a}(\boldsymbol{k})$ includes all the information of the pseudospin spinor state, $G^n_{ij}(\boldsymbol{k})$ and $F^n_{ij}(\boldsymbol{k})$ can be expressed in terms of $\hat{a}(\boldsymbol{k})$ (Fig. 1, C and D) as (*44*)

$$G^n_{ij}(\boldsymbol{k}) = \frac{1}{4}\partial_{k_i}\hat{a}(\boldsymbol{k})\cdot\partial_{k_j}\hat{a}(\boldsymbol{k}) \tag{5}$$

$$F^n_{ij}(\boldsymbol{k}) = \frac{1}{2}\hat{a}(\boldsymbol{k})\cdot\left[\partial_{k_i}\hat{a}(\boldsymbol{k})\times\partial_{k_j}\hat{a}(\boldsymbol{k})\right] \tag{6}$$

In bulk BP, because of the space-time inversion symmetry with weak spin-orbit coupling, the Bloch vector always lies on a great circle on the Bloch sphere (*45*) and, thus, can be determined by the rotation angle $\theta(\boldsymbol{k})$ along the great circle. After choosing the basis in a way that the great circle is placed on the $z = 0$ plane of the Bloch sphere, the pseudospin can be expressed in terms of $\theta(\boldsymbol{k})$ as

$$\hat{a}(\boldsymbol{k}) = [-\cos\theta(\boldsymbol{k}), \sin\theta(\boldsymbol{k}), 0] \tag{7}$$

The corresponding pseudospin spinor state $\left|u_{n,\text{eff}}(\boldsymbol{k})\right\rangle$, which is the lower energy eigenstate of the effective Hamiltonian in Eq. 4, is given by

$$\left|u_{n,\text{eff}}(\boldsymbol{k})\right\rangle = \frac{C(\boldsymbol{k})}{\sqrt{2}}\begin{bmatrix} e^{i\theta(\boldsymbol{k})} \\ 1 \end{bmatrix} \tag{8}$$

where $C(k)$ is the U(1) phase factor. Note that the pseudospin spinor state can be interpreted as a superposition of two states localized at two sublattices with a phase difference. Let us suppose that the tight-binding basis $|\text{A}\rangle = (0,1)^{\text{T}}$ [resp. $|\text{B}\rangle = (1,0)^{\text{T}}$] is the electron's state localized at a sublattice site A (resp. B). Then $\left|u_{n,\text{eff}}(\boldsymbol{k})\right\rangle$ in Eq. 8 can be interpreted as a linear combination of the states $|\text{B}\rangle$ and $|\text{A}\rangle$ with the phase difference $e^{i\theta(\boldsymbol{k})}$. In the case of the BP, the phase difference between the sublattice sites A and B in Fig. 2A in one sublayer is approximately given by $e^{i\theta(\boldsymbol{k})}$, where $\theta(\boldsymbol{k})$ is the pseudospin rotation angle of the BP (*45*). In Fig. 2B, we illustrate the pseudospin spinor states for $\theta = 0, \pi$ by showing the relative phase difference between the sublattice site A and B. The quantum metric tensor $G^n_{ij}(\boldsymbol{k})$ and the Berry curvature $F^n_{ij}(\boldsymbol{k})$ can also be calculated using $\theta(\boldsymbol{k})$ as

$$G^n_{ij}(\boldsymbol{k}) = \frac{1}{4}\partial_{k_i}\theta(\boldsymbol{k})\partial_{k_j}\theta(\boldsymbol{k}) \tag{9}$$

$$F^n_{ij}(\boldsymbol{k}) = 0 \tag{10}$$

where the Berry curvature is identically zero owing to the spinless space-time inversion symmetry (*46*). Therefore, the measurement of $\theta(\boldsymbol{k})$ can give the complete determination of the full QGT in the momentum space.

The rotation angle $\theta(\boldsymbol{k})$ is precisely measurable through the polarization dependence of the ARPES intensity. More specifically, we used four kinds of polarizations of the incident light: linear horizontal (LH), linear vertical (LV), left-handed circular (LC), and right-handed circular (RC) polarizations (Fig. 2A). By using the ARPES intensities I_{LH}, I_{LV}, I_{LC}, and I_{RC}, for each polarization, we defined the linear dichroism (LD) APRES signal $p_{\text{L}} = (I_{\text{LH}} - I_{\text{LV}})/(I_{\text{LV}} + I_{\text{LH}})$ and the CD-APRES signal $p_{\text{C}} = (I_{\text{RC}} - I_{\text{LC}})/(I_{\text{RC}} + I_{\text{LC}})$. Then, approximating the final state as multiple plane wave functions (*39*, *42*), these signals are related to the pseudospin by

$$p_{\text{L}} = \cos\theta, \quad p_{\text{C}} = \sin\theta \tag{11}$$

which give us complete information to determine θ (*39*–*42*). Moreover, to exclude any possible issue related to the final state effect, we have also developed a general symmetry-based method to extract the pseudospin from the ARPES signal without approximating the form of the final state, which gives

$$\cos\theta = 1 - 2\frac{\left|M_{\text{LV}}(k_x, k_y)\right|^2}{\left|M_{\text{LV}}(k_x, 0)\right|^2} \tag{12}$$

where M_{LV} is the dipole matrix element for the LV-polarized light. For a more detailed explanation of the theoretical analysis leading to Eq. 12, see (*45*).

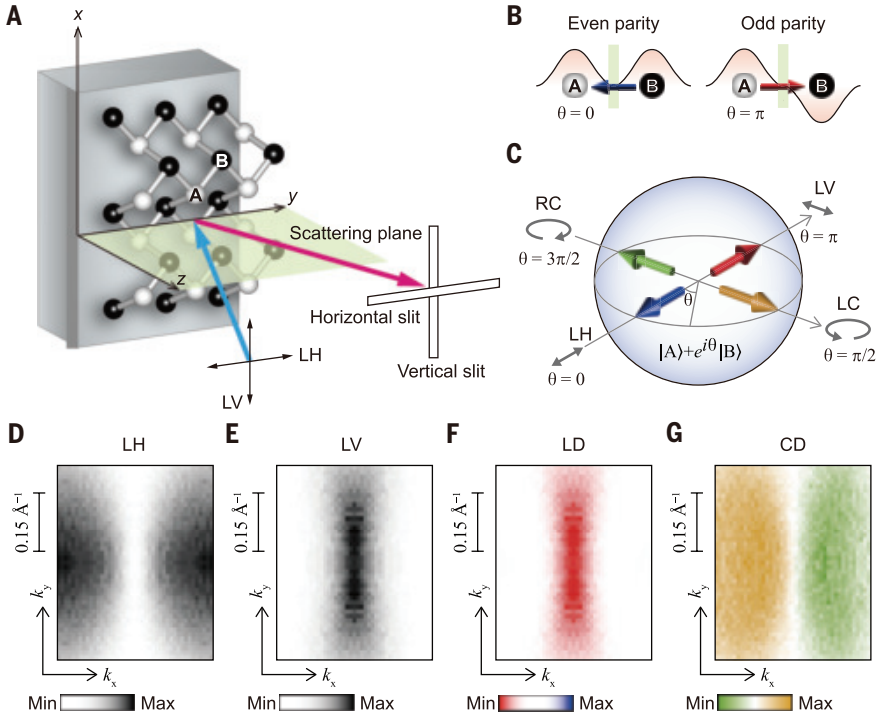

Fig. 2. Measurement of the pseudospin texture by ARPES. (**A**) Schematic illustration for experimental geometry, sample orientation, and scattering plane. The cyan and magenta arrows indicate incoming photon and outgoing photoelectron, respectively; the scattering plane shown in light green is parallel to the glide mirror plane of BP. The white and black balls are phosphorus atoms of BP in A and B sublattices, respectively. (**B**) Relative phase of wave functions in the two sublattices for the pseudospin $\theta = 0$ of even parity (blue arrow pointing to the left) and the $\theta = \pi$ of odd parity (red arrow pointing to the right). (**C**) Bloch sphere for wave functions in A and B sublattices. The four representative pseudospins characterized by $\theta = 0,\ \pi/2,\ \pi,\ 3\pi/2$ are indicated by blue, yellow, red, and green arrows, respectively. The double-head or curved arrows show polarization conditions required to excite the blue, red, yellow, green pseudospin states, respectively. (**D** and **E**) ARPES intensity of BP taken with LH (D) and LV polarization (E) at a temperature of 6 K. Each energy distribution curve at k_x and k_y is fit to determine the energy position, and the ARPES intensity at the energy position is plotted as a function of k_x and k_y. (**F**) LD-ARPES intensity map taken by subtracting the intensity in (E) from that in (D). Before this subtraction, the two maps in (D) and (E) are normalized based on their maximum intensity in constant-energy maps at 0.54 to 0.63 eV (fig. S4). (**G**) CD-ARPES intensity pattern taken by subtracting the map taken by RC polarization from that taken by LC polarization.

Measurement of the pseudospin texture in BP

We measured the QGT by utilizing the pseudospin texture in bulk BP. The bulk BP has an insulating band structure with a band gap of 0.335 eV at the Z point, i.e., $(k_x, k_y, k_z) = (0, 0, \pi)$, of the Brillouin zone with the primitive unit cell (*47*). As the two energy bands near the Fermi level are mainly composed of the p_z orbitals (*47*, *48*), the corresponding two-band tight-binding model based on the p_z orbitals correctly predicts the electronic and optical properties of the material consistent with ab initio calculational results (*48*). It was recently shown that BP exhibits a bipolar pseudospin texture, wherein electron and hole states near the Z point possess opposite net pseudospin polarizations, presenting potential applications in pseudospintronics (*38*). In this system, the highest occupied and the lowest unoccupied bands can be energetically inverted by applying an external electric field (*49*, *50*) or doping on the surface (*51*). The band inversion process accompanies topological gap-closing points that exhibit the winding pseudospin texture around them (*52*).

The intriguing property of BP is that the pseudospin physics is well defined across a broad momentum space region. For example, in monolayer BP, although the unit cell contains four phosphorus atoms, thus the minimal tight-binding Hamiltonian has a 4×4 matrix form, the Hamiltonian takes a block-diagonal form composed of 2×2 matrices over the entire Brillouin zone owing to the crystalline symmetry (*53*), which allows pseudospin description based on a 2×2 block Hamiltonian. In the case of the bulk BP with eight phosphorus atoms in a unit cell, similar block-diagonalization occurs across the entire $k_z = 0$ plane when the hopping parameters between layers are small (*45*). The minor change of the energy band and the quantum states along the k_z direction (fig. S2) signifies the weak interaction between layers in bulk BP, thereby maintaining well-defined pseudospin characteristics over a substantial Brillouin zone region, where the band structure has predominantly p_z orbital characters.

ARPES is an adequate experimental means to extract and quantify the net pseudospin polarization of BP because the pseudospin polarization can be correlated with the photon polarization dependency of ARPES intensity in the case of elemental crystals with little contribution of final-state effects (*45*). If the scattering plane is aligned along the yz plane (see Fig. 2A, where x and y axes are along the armchair and zigzag directions of BP, respectively), then quantum interference between two sublattices results in the ARPES selection rule reflecting their relative phases, that is, pseudospin. Linear horizontal (LH)–polarized light excites the pseudospin states of $\theta = 0$ (see Eq. 8) with even parity; linear vertical (LV)–polarized light suppresses the pseudospin states of $\theta = 0$. By contrast, LV-polarized light excites the pseudospin states of $\theta = \pi$ with odd parity (Fig. 2, B and C). Based on the rule of correlation between photon polarizations and sublattice interference, the pseudospin polarization of $\theta = \pm\pi/2$ corresponding to the yellow and green pseudospin in Fig. 2C is excited most strongly for the left circularly (LC)– and right circularly (RC)–polarized light, respectively. For more detailed information on this selection rule, see (*45*).

Figure 2, D to G, shows the distribution of ARPES intensity in the electronic structure of BP, collected by curve fitting to energy distribution curves taken as a function of k_x and k_y (see fig. S4 for the fuller set of raw ARPES data). The ARPES intensity pattern taken by LH-polarized light in Fig. 2D shows a clear suppression around the zigzag axis azt $k_x = 0$. Away from this $k_x = 0$ line, the intensity is much stronger. By contrast, ARPES data taken with LV-polarized light in Fig. 2E show exactly opposite tendencies: stronger intensity can be found at the $k_x = 0$ line, and the intensity is much weaker away from the $k_x = 0$ line. By subtracting the data in Fig. 2E from that in Fig. 2D after intensity normalization, the LD-ARPES intensity pattern is presented in Fig. 2F, where the pseudospins $\theta = 0$ and $\theta = \pi$ are shown in blue and red, respectively, as defined in Fig. 2C. Electronic states in the vicinity of the $k_x = 0$ line are strongly polarized to the pseudospin $\theta = \pi$. In a similar way, one can obtain information on the pseudospin polarization to $\theta = \pi/2$ (yellow) and $3\pi/2$ (green) by subtracting those taken by LC- and RC-polarized light (CD-ARPES), as shown in Fig. 2G. The CD-ARPES intensity pattern shows that half the Brillouin zone on the left is polarized to $\theta = \pi/2$, whereas the other half is polarized to $\theta = 3\pi/2$, which is therefore antisymmetric with respect to the $k_x = 0$ line. The LD-ARPES and CD-ARPES intensity patterns do not depend on the photon energy and scattering geometry (see figs. S5 and S6), indicating that they reflect information on initial states with little contribution from final-state

effects. Therefore, we could obtain the full pseudospin texture that can be used to extract the quantum metric tensor.

Comparison of the measured pseudospin distribution with theory

We compared the pseudospin texture measured from the polarization dependence of ARPES intensity as in Fig. 2 with theory. To accurately extract the quantum metric tensor of bulk BP, we performed density functional theory (DFT) calculations. We first optimized our experimental crystal structure with the optB88-vdW as van der Waals density functional (*54*). The relaxed lattice structure has $a = 4.441$ Å, $b = 3.346$ Å, and $c = 10.719$ Å , shown in Fig. 3, A and B, associated with the Brillouin zone of the primitive cell in Fig. 3C. With this optimized structure, we conducted electronic band structure calculations with the HSE06 hybrid functional (*55*). This approach overcame the limitations of local density and generalized gradient approximations, accurately predicting a 0.33-eV gap at Z point represented in Fig. 3C, consistent with the experimentally observed narrow gap range around 0.335 eV (*39*, *47*). Including spin-orbit coupling (SOC) in the calculations revealed negligible changes in the band structure. Consequently, we neglected SOC in following calculations. To calculate the pseudospin of BP near the band gap, we constructed the tight-binding model, which faithfully describes the Bloch state as well as the energy band near the Fermi level (*45*).

In Fig. 3D, we present the pseudospin rotation angle, $\theta_{TB}(\boldsymbol{k})$, derived from a tight-binding (TB) model (*45*). Notably, as depicted in Fig. 3D, $\theta_{TB}(\boldsymbol{k})$ is an odd function for k_x around $\theta_{TB} = \pi$ and an even function for k_y. This observation can be attributed to the different symmetry representations of the glide mirror symmetry, G_x, and the mirror symmetry, M_y (*45*). The measured pseudospin angle $\theta^{PW}_{exp}(\boldsymbol{k})$ and $\theta^{GFS}_{exp}(\boldsymbol{k})$ deduced from the ARPES experiment in Fig. 2 with the plane wave (PW) approximation and general final state (GFS) approach (*45*), respectively, are illustrated in Fig. 3, E and F. A comparative analysis of $\theta_{TB}(\boldsymbol{k})$, $\theta^{PW}_{exp}(\boldsymbol{k})$, and $\theta^{GFS}_{exp}(\boldsymbol{k})$ in Fig. 3, D to F, reveals a similarity in their values and symmetries. To compute the derivatives of the pseudospin in order to obtain the quantum metric tensor through Eq. 9, we fit seventh-order polynomials around the Z point, considering the symmetries of BP to obtain smooth functions for each $\theta^{PW}_{exp}(\boldsymbol{k})$ and $\theta^{GFS}_{exp}(\boldsymbol{k})$. We note that this fitting procedure remains impartial to the theoretical model and serves to mitigate potential experimental errors associated with each dataset, which could otherwise exert adverse effects on the derivative of $\theta^{PW}_{exp}(\boldsymbol{k})$ and $\theta^{GFS}_{exp}(\boldsymbol{k})$.

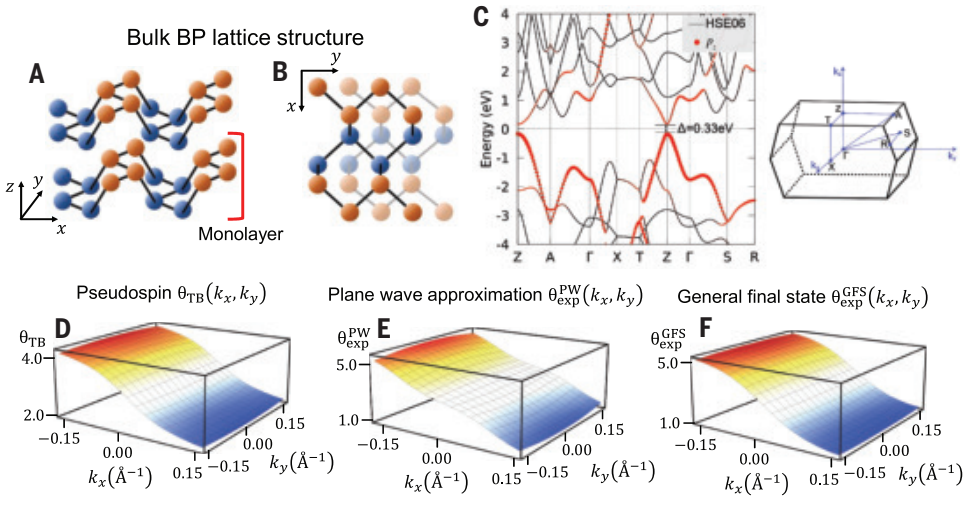

Fig. 3. Momentum space distribution of the pseudospin: theory versus experiment. (**A** and **B**) Side and top views, respectively, of the lattice structure of the bulk BP Phosphorus atoms in different sublayers are marked with different colors. Bulk BP is formed by vertical stacking of monolayers after a half lattice vector displacement in the *y* direction. The blurred balls in (B) represent their location in the lower layer. (**C**) The energy band structure obtained by DFT calculations plotted along the high symmetry direction of the Brillouin zone shown in the right panel (*45*). The two bands near the band gap at the Z point are mainly contributed by p_z orbitals represented by red dots. Δ, direct band gap of BP. (**D**) The pseudospin textures $\theta_{TB}(k_x, k_y)$ near the Z point, obtained by using the Wannier Hamiltonian (*45*). (**E** and **F**) The pseudospin angles calculated from the polarization-dependent ARPES signal based on Eqs. 11 and 12, respectively. Polynomial fits of the pseudospin angles using a symmetric seventh-order polynomial are illustrated, which are used to calculate the quantum metric tensor by using Eq. 9 (*45*).

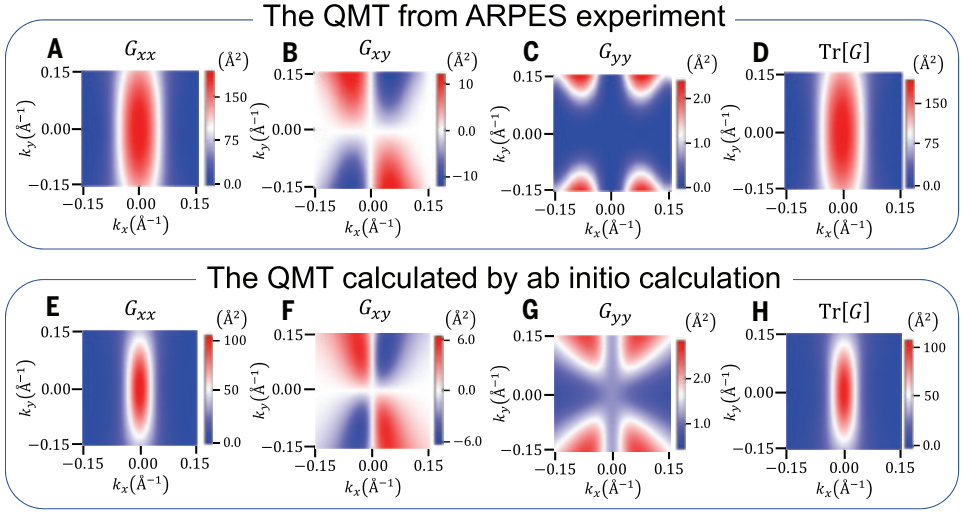

Fig. 4. The momentum space distribution of the quantum metric tensor: theory versus experiment. (**A** to **D**) The experimentally measured components of the quantum metric tensor (QMT) and its trace, $\mathrm{Tr}[G] = G_{xx} + G_{yy}$, of the highest valence band near the Γ point. To extract the QMT from experiments, the polynomial fit of the experimental pseudospin data in Fig. 3F was used, which was determined by considering a general final state (*45*). (**E** to **H**) The components of the quantum metric tensor and its trace for the highest valence band in Fig. 3C, which are directly calculated from DFT calculations (*45*).

Determination of the quantum metric tensor using the pseudospin

By utilizing the fitted pseudospin angle $\theta^{GFS}_{exp}(\boldsymbol{k})$ and the relationship between the pseudospin and the quantum metric tensor established in Eq. 9, we calculated the quantum metric tensor associated with the highest valence band of bulk BP. The results are depicted in Fig. 4, A to D. Consistent with the weak interlayer interaction along the *z* direction, we observed minimal changes in both energy and quantum states along the k_z direction (see fig. S2). Consequently, we restricted our quantum metric tensor calculations to the k_x-k_y plane with $k_z = \pi$. In

this case, the quantum metric tensor is characterized by three independent elements, namely G_{xx}, G_{xy}, and G_{yy}. Additionally, we compute the trace of the quantum metric tensor, $\mathrm{Tr}[G] = G_{xx} + G_{yy}$, which remains invariant for the rotation of the orthogonal coordinates around the k_z axis. Although $\theta^{\mathrm{PW}}_{\mathrm{exp}}(\boldsymbol{k})$ exhibit similar distribution as that of $\theta^{\mathrm{GFS}}_{\mathrm{exp}}(\boldsymbol{k})$, the quantum metric tensor derived from $\theta^{\mathrm{PW}}_{\mathrm{exp}}(\boldsymbol{k})$ deviates from the one derived from $\theta^{\mathrm{GFS}}_{\mathrm{exp}}(\boldsymbol{k})$ owing to the limitation of the plane wave approximation (fig. S12).

From the results presented in Fig. 4, A to D, it is evident that the magnitudes of each component decrease in the order of G_{xx}, G_{xy}, and G_{yy}. To elucidate the reason for this ordering, note that, as shown in Fig. 3F, the pseudospin exhibits a pronounced slope along the k_x direction, whereas its inclination along the k_x direction is comparatively smaller. Considering that G_{ij} is determined by the product of two gradients of the pseudospin angle along k_i and k_j directions (see Eq. 9), the overall value of G_{ij} decreases with an increase in the number of y indices. Additionally, a difference was observed between the minimal anisotropy in the energy dispersion of the highest occupied band along the k_x and k_y directions, illustrated in Fig. 3C and fig. S1, and the significant anisotropy in G_{xx} and G_{yy}, illustrated in Fig. 4, A and C, which is consistent with the fact that the energy band dispersion is not sufficient to determine the complete quantum metric tensor.

In Fig. 4, E to H, we present the quantum metric tensor for the highest valence band, directly calculated by DFT (*45*). A comparative analysis with the quantum metric tensor measured from the ARPES experiment revealed similarities in the texture and overall values. However, it is noteworthy that the discrepancy associated with G_{xx} is larger than that of G_{xy} and G_{yy}. This discrepancy arises from the fact that, near the origin, the x-directional slope of $\theta^{\mathrm{GFS}}_{\mathrm{exp}}$ is steeper than that of θ_{TB}. Consequently, G_{xx} from $\theta^{\mathrm{GFS}}_{\mathrm{exp}}$ becomes larger than that from θ_{TB}. On the other hand, the y-directional slopes of $\theta^{\mathrm{GFS}}_{\mathrm{exp}}$ and θ_{TB} are nearly the same, which can be confirmed from the minor discrepancy in G_{yy} (see Eq. 9).

Discussion and outlook

Our approach for estimating the QGT through pseudospin measurements broadly applies to diverse solid systems: It can be applied to any material whose low-energy band structure can be described by an effective 2×2 Hamiltonian. Although the extension to multiband systems is generally challenging, we expect that our method can still be used if the low-energy band structure of multiband systems can be characterized by some pseudospin degrees of freedom with few interband coupling parameters (*56*). The method we developed for QGT measurement establishes a foundational framework for investigating newly described physical phenomena in solids stemming from the QGT.

REFERENCES AND NOTES

1. M. V Berry, in *Geometric Phases in Physics* (World Scientific Publishing, 1989), pp. 7–28.
2. M. V. Berry, *Proc. R. Soc. London Ser. A* **392**, 45–57 (1984).
3. P. Törmä, S. Peotta, B. A. Bernevig, *Nat. Rev. Phys.* **4**, 528–542 (2022).
4. R. L. Klees, J. C. Cuevas, W. Belzig, G. Rastelli, *Phys. Rev. B* **103**, 014516 (2021).
5. J. Ahn, G. Y. Guo, N. Nagaosa, A. Vishwanath, *Nat. Phys.* **18**, 290–295 (2022).
6. G. E. Topp, C. J. Eckhardt, D. M. Kennes, M. A. Sentef, P. Törmä, *Phys. Rev. B* **104**, 064306 (2021).
7. N. Nagaosa, T. Morimoto, *Adv. Mater.* **29**, 1603345 (2017).
8. Y. Q. Ma, S. Chen, H. Fan, W. M. Liu, *Phys. Rev. B Condens. Matter Mater. Phys.* **81**, 245129 (2010).
9. N. P. Armitage, E. J. Mele, A. Vishwanath, *Rev. Mod. Phys.* **90**, 015001 (2018).
10. N. Nagaosa, J. Sinova, S. Onoda, A. H. MacDonald, N. P. Ong, *Rev. Mod. Phys.* **82**, 1539–1592 (2010).
11. R. Yu *et al.*, *Science* **329**, 61–64 (2010).
12. C. Z. Chang *et al.*, *Science* **340**, 167–170 (2013).
13. J. G. Checkelsky *et al.*, *Nat. Phys.* **10**, 731–736 (2014).
14. L. Wu *et al.*, *Science* **354**, 1124–1127 (2016).
15. S. Y. Xu *et al.*, *Science* **347**, 294–298 (2015).
16. S. Cho *et al.*, *Phys. Rev. Lett.* **121**, 186401 (2018).
17. M. Schüler *et al.*, *Sci. Adv.* **6**, eaay2730 (2020).
18. S. Cho *et al.*, *Sci. Rep.* **11**, 1684 (2021).
19. M. Ünzelmann *et al.*, *Nat. Commun.* **12**, 3650 (2021).
20. M. Kang *et al.*, *Nat. Phys.* **21**, 110–117 (2025).
21. J. P. Provost, G. Vallee, *Commun. Math. Phys.* **76**, 289–301 (1980).
22. N. Marzari, D. Vanderbilt, *Phys. Rev. B Condens. Matter* **56**, 12847–12865 (1997).
23. Y. Gao, D. Xiao, *Phys. Rev. Lett.* **122**, 227402 (2019).
24. M. F. Lapa, T. L. Hughes, *Phys. Rev. B* **99**, 121111(R) (2019).
25. A. Gao *et al.*, *Science* **381**, 181–186 (2023).
26. N. Wang *et al.*, *Nature* **621**, 487–492 (2023).
27. H. Tian *et al.*, *Nature* **614**, 440–444 (2023).
28. F. Xie, Z. Song, B. Lian, B. A. Bernevig, *Phys. Rev. Lett.* **124**, 167002 (2020).
29. L. Liang *et al.*, *Phys. Rev. B* **95**, 024515 (2017).
30. J. W. Rhim, K. Kim, B. J. Yang, *Nature* **584**, 59–63 (2020).
31. Y. Hwang, J. W. Rhim, B. J. Yang, *Nat. Commun.* **12**, 6433 (2021).
32. J. Jung, H. Lim, B. J. Yang, *Phys. Rev. B* **109**, 035134 (2024).
33. A. Srivastava, A. Imamoğlu, *Phys. Rev. Lett.* **115**, 166802 (2015).
34. Y. Gao, S. A. Yang, Q. Niu, *Phys. Rev. B Condens. Matter Mater. Phys.* **91**, 214405 (2015).
35. F. Piéchon, A. Raoux, J. N. Fuchs, G. Montambaux, *Phys. Rev. B* **94**, 134423 (2016).
36. X. Tan *et al.*, *Phys. Rev. Lett.* **122**, 210401 (2019).
37. M. Yu *et al.*, *Natl. Sci. Rev.* **7**, 254–260 (2020).
38. A. Gianfrate *et al.*, *Nature* **578**, 381–385 (2020).
39. S. W. Jung *et al.*, *Nat. Mater.* **19**, 277–281 (2020).
40. M. Mucha-Kruczyński *et al.*, *Phys. Rev. B Condens. Matter Mater. Phys.* **77**, 195403 (2008).
41. Y. Liu, G. Bian, T. Miller, T. C. Chiang, *Phys. Rev. Lett.* **107**, 166803 (2011).
42. C. Hwang *et al.*, *Phys. Rev. B Condens. Matter Mater. Phys.* **84**, 125422 (2011).
43. D. Pesin, A. H. MacDonald, *Nat. Mater.* **11**, 409–416 (2012).
44. Y. Hwang, J. Jung, J. W. Rhim, B. J. Yang, *Phys. Rev. B* **103**, L241102 (2021).
45. Additional analyses are available as supplementary materials.
46. D. Xiao, M. C. Chang, Q. Niu, *Rev. Mod. Phys.* **82**, 1959–2007 (2010).
47. A. Morita, *Appl. Phys., A Solids Surf.* **39**, 227–242 (1986).
48. A. N. Rudenko, S. Yuan, M. I. Katsnelson, *Phys. Rev. B Condens. Matter Mater. Phys.* **92**, 085419 (2015).
49. S. S. Baik, K. S. Kim, Y. Yi, H. J. Choi, *Nano Lett.* **15**, 7788–7793 (2015).
50. Q. Liu, X. Zhang, L. B. Abdalla, A. Fazzio, A. Zunger, *Nano Lett.* **15**, 1222–1228 (2015).
51. J. Kim *et al.*, *Science* **349**, 723–726 (2015).
52. J. Kim *et al.*, *Phys. Rev. Lett.* **119**, 226801 (2017).
53. M. Ezawa, *New J. Phys.* **16**, 115004 (2014).
54. J. Klimeš, D. R. Bowler, A. Michaelides, *J. Phys. Condens. Matter* **22**, 022201 (2010).
55. A. V. Krukau, O. A. Vydrov, A. F. Izmaylov, G. E. Scuseria, *J. Chem. Phys.* **125**, 224106 (2006).
56. B. Bradlyn *et al.*, *Science* **353**, aaf5037 (2016).
57. S. Kim *et al.*, Direct measurement of the quantum metric tensor in solids, Dryad (2025); https://doi.org/10.5061/dryad.jwstqjqmq.
58. yutqian, yutqian/v2qgt: v1.0.0-alpha, Zenodo (2025); https://doi.org/10.5281/zenodo.14915109.

ACKNOWLEDGMENTS

We thank S. H. Ryu, M. Huh, and Y. Kim for help with ARPES experiments. **Funding:** The Samsung Science and Technology Foundation under project no. SSTF-BA2002-06 (S.K., Y.Q., B.-J.Y.); National Research Foundation of Korea (NRF) funded by the Korean government (MSIT), grant no. RS-2021-NR060087 (S.K., Y.Q., B.-J.Y.); Global Research Development Center (GRDC) Cooperative Hub Program through the NRF funded by the MSIT, grant no. RS-2023- 00258359 (S.K., Y.Q., B.-J.Y.); Global-LAMP program of the NRF funded by the Ministry of Education, grant no. RS-2023-00301976 (S.K., Y.Q., B.-J.Y.); NRF funded by the MSIT, grant nos. NRF-2021R1A3B1077156, NRF-RS-2024-00416976, NRF-RS-2022-00143178, and NRF-2022M3H3A106307411 (Y.C., S.P., K.S.K.); Yonsei Signature Research Cluster Program, grant no. 2024-22-0163 (K.S.K.). This research used resources of the Advanced Light Source, which is a Department of Energy Office of Science User Facility under the contract no. DE-AC02-05CH11231. **Author contributions:** Conceptualization: S.K., K.S.K., B.-J.Y.; Methodology: S.K., Y.C., Y.Q., C.Z., E.R., A.B., K.S.K., B.-J.Y.; Investigation: S.K., Y.C., Y.Q., S.P., K.S.K., B.-J.Y.; Visualization: S.K., Y.C., Y.Q., K.S.K., B.-J.Y.; Funding acquisition: K.S.K., B.-J.Y.; Project administration: K.S.K., B.-J.Y.; Supervision: K.S.K., B.-J.Y.; Writing – original draft: S.K., Y.C., K.S.K., B.-J.Y.; Writing – review & editing: S.K., Y.C., Y.Q., K.S.K., B.-J.Y. **Competing interests:** The authors declare that they have no competing interests. **Data and materials availability:** The data and materials that support the findings of this study are available on Dryad (*57*). The DFT code to calculate the quantum metric tensor is available on the GitHub repository (*58*).

SUPPLEMENTARY MATERIALS

science.org/doi/10.1126/science.ado6049
Materials and Methods; Supplementary Text; Figs. S1 to S12; Table S1; References (*59*–*67*)

Submitted 10 February 2024; resubmitted 12 August 2024; accepted 2 April 2025

10.1126/science.ado6049

SYNTHETIC CHEMISTRY

In-insect synthesis of oxygen-doped molecular nanocarbons

Atsushi Usami[1,2]*†, Hideya Kono[3]†, Vic Austen[3]†, Quan Manh Phung[2,3], Hiroki Shudo[3], Tomoki Kato[3], Hayato Yamada[3,4], Akiko Yagi[2,3], Kazuma Amaike[5], Kazuhiro J. Fujimoto[2,3]*, Takeshi Yanai[2,3]*, Kenichiro Itami[2,5,6]*

Many functional molecules and materials have been produced with organic chemistry or with in vitro enzymatic approaches. Individual organisms, such as insects, have the potential to serve as natural reaction platforms in which high densities of multiple enzymes can perform new and complex reactions. We report an "in-insect" unnatural product synthesis that takes advantage of their xenobiotic metabolism. We selectively transform belt- and ring-shaped molecular nanocarbons into otherwise difficult-to-prepare derivatives in which oxygen atoms are inserted into aromatic rings. Cytochrome P450 variants are most likely the enzymes responsible for this reaction. Molecular dynamics simulations and quantum chemical calculations indicated a possible mode of substrate incorporation into the enzyme and an unconventional mechanism of direct oxygen insertion into carbon–carbon bonds.

Natural products found in organisms are often difficult to synthesize through conventional organic chemistry or with in vitro enzymatic approaches (*1*–*3*). One factor that adds to this challenge is that organisms can adapt to changing environments and perform complex reactions efficiently and accurately on new substrates. For example, insects have developed highly effective detoxification systems and control mechanisms against xenobiotics such as plant secondary metabolites and pesticides (*4*). However, research has thus far primarily focused on the composition and reactivity of enzymes participating in biological reactions, rather than actively exploiting these pathways for the production of unnatural functional molecules through xenobiotic metabolism.

The aim of this study was to use the xenobiotic metabolism of insects directly for creating new functional organic materials. We now report an "in-insect" unnatural product synthesis in which biotransformation using insect xenobiotic metabolism can selectively functionalize specific molecular nanocarbons, to yield otherwise difficult-to-make and functional molecular nanocarbons (*5*). Many types of molecular nanocarbons (Fig. 1A), such as C_{60} and other fullerenes (*6*), cycloparaphenylenes (CPPs) (*7*–*11*), carbon nanobelts (*12*–*19*), methylene-bridged CPPs (*20*, *21*), warped nanographenes (*22*–*24*), and cyclocarbons (*25*, *26*), have been reported, but aside from C_{60} they are generally not used in organic synthesis as reactants because of the difficulties in the selective functionalization of these molecules. For example, given the existence of oxygen-derivatized carbon frameworks in graphene oxide (*27*), it should be possible to introduce oxygen atoms into molecular nanocarbons. We show that in-insect synthesis provides numerous opportunities as an enabling technology for the preparation of new molecular nanocarbons.

[1]Institute for Advanced Research, Nagoya University, Chikusa, Nagoya, Japan. [2]Institute of Transformative Bio-Molecules (WPI-ITbM), Nagoya University, Chikusa, Nagoya, Japan. [3]Department of Chemistry, Graduate School of Science, Nagoya University, Chikusa, Nagoya, Japan. [4]Integrated Research Consortium on Chemical Sciences, Nagoya University, Chikusa, Nagoya, Japan. [5]Molecule Creation Laboratory, Pioneering Research Institute, RIKEN, Wako, Saitama, Japan. [6]Center for Sustainable Resource Science, RIKEN, Wako, Saitama, Japan. ***Corresponding authors. Email: usami.atsushi.y5@f.mail.nagoya-u.ac.jp (A.U.); fujimotok@chem.nagoya-u.ac.jp (K.J.F.); yanait@chem.nagoya-u.ac.jp (T.Y.); kenichiro.itami@riken.jp (K.I.)** †These authors contributed equally to this work.

In-insect transformation of methylene-bridged [6]cycloparaphenylene

We selected methylene-bridged [*6*]cycloparaphenylene ([6]MCPP) as the initial molecular nanocarbon substrate because of its rigid and belt-like structure (*20*, *21*), distinct cell internalization properties (*28*), and commercial availability (*29*). We fed [6]MCPP to several different insects, but most did not survive as a result of the inherent toxicity of [6]MCPP. For example, *Bombyx mori* (domestic silkworm) exhibits no tolerance to [6]MCPP and did not survive at any concentration tested.

We found that the tobacco cutworm *Spodoptera litura* (Lepidoptera, Noctuidae) was suitable for the in-insect functionalization of [6]MCPP. *S. litura* is a polyphagous pest that feeds on more than 120 plant species (*30*). *S. litura* has a biological life cycle of 35 to 40 days, and a simple xenobiotic metabolism test (biotransformation) using the oral administration of plant secondary metabolites and pesticides has been established (*31*). Moreover, recent genomic studies have reported that *S. litura* possesses approximately twice as many detoxifying enzymes—such as cytochrome P450 (CYPs), carboxylesterase, and glutathione-*S*-transferase—as the monophagous species *B. mori*, a known lepidopteran model insect (*32*).

Groups of 50 larvae were fed an artificial diet containing [6]MCPP (200 nmol/larva), boiled kidney beans, and agar for 2 days (*33*) (Fig. 1B). An artificial diet without [6]MCPP was administered for an additional day to completely excrete [6]MCPP from the body. Fresh frass was collected every 12 hours for 3 days and immersed in CH_2Cl_2, followed by extraction. In this crude extract, we identified the presence of one [6]MCPP derivative in addition to the remaining unreacted [6]MCPP. The sole product formed was found to be an oxygen adduct by MALDI-TOF mass spectrometry and thus we named this product [6]MCPP-oxylene.

Through purification by gel permeation chromatography and preparative thin-layer chromatography, [6]MCPP-oxylene was isolated in 9.9 ± 0.4% yield, and [6]MCPP was recovered in 71.1 ± 18.3% yield. The selectivity (substrate specificity) of this biotransformation is high as [6]MCPP-oxylene remained the sole product even when the reaction scale was increased 50-fold. Dioxylene products were not observed under any of the conditions we tested. The feeding activity of *S. litura* was reduced when the concentration of [6]MCPP exceeded 400 nmol/larva. Therefore, [6]MCPP concentration of 200 nmol/larva appeared to be optimal for this biotransformation and the upper limit at which there was no feeding inhibition of larvae [see supplementary materials (SM) for details].

Structural characterization of [6]MCPP-oxylene

Initially, we assumed that [6]MCPP-oxylene was a typical C–H bond hydroxylation product at either the aromatic or benzylic C–H bond of [6]MCPP. We measured the ^{1}H-NMR spectra of [6]MCPP-oxylene at 400 and 600 MHz in acetone-d_6 at 25°C. However, six singlets of aromatic hydrogen atoms and eight doublets of geminal hydrogen atoms were observed (Fig. 1C), which were not consistent with aromatic or benzyl C–H bond hydroxylation products (Fig. 1B). The structure of [6]MCPP-oxylene was revealed by single-crystal x-ray crystallography (Fig. 1D), in which the oxygen atom was inserted by cleaving the C_{phenyl}–C_{phenyl} bond on the opposite side of the methylene moiety in the five-membered ring. The highly symmetric belt structure of [6]MCPP (*20*) was noticeably altered into an oval shape in [6]MCPP-oxylene, exhibiting a short diameter of 7.47 Å and a long diameter of 9.67 Å. In the solid state, [6]MCPP-oxylene aligned and stacked to fill the interior of the ring structure, with one molecule tilted at approximately 90° relative to the other (see SM for details).

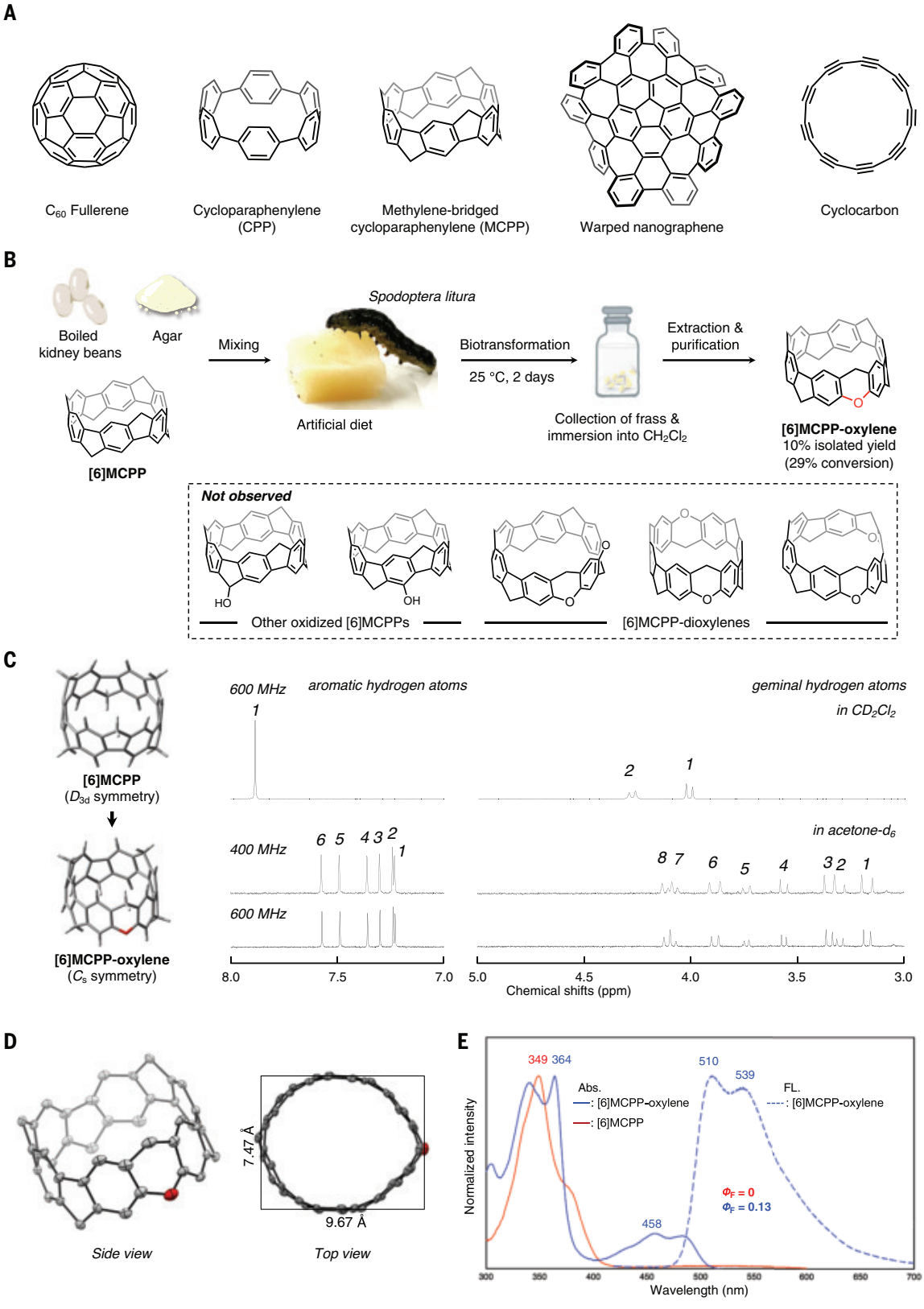

Fig. 1. In-insect transformation of molecular nanocarbons by *Spodoptera litura*. (**A**) Representative molecular nanocarbons. (**B**) Scheme of the biotransformation. Reaction conditions: The artificial diet consisted of boiled kidney beans, agar, water, and molecular nanocarbons. The insects are the fourth- and fifth-instar larvae of *S. litura*. Frass was collected and immersed in a solvent, and the product was purified from the frass extract. (**C**) ^{1}H NMR spectra of [6]MCPP (600 MHz, CD_2Cl_2) and [6]MCPP-oxylene (600 and 400 MHz, acetone-d_6). (**D**) Oak Ridge thermal ellipsoid plot (ORTEP) drawing [6]MCPP-oxylene with thermal ellipsoids set to 50% probability. Hydrogen atoms and solvent molecules are omitted for clarity. (**E**) Ultraviolet-visible absorption (solid lines) and fluorescence (dashed line) spectra of the toluene solutions of [6]MCPP and [6]MCPP-oxylene. The fluorescence spectra were measured upon excitation at 360 nm for [6]MCPP-oxylene.

The optimized structure of [6]MCPP-oxylene exhibited C_s symmetry, which agrees well with its ^{1}H-NMR spectrum.

The influence of oxygen-doping on the optical properties of the [6]MCPP framework can be observed in the ultraviolet-visible absorption and fluorescence spectra of [6]MCPP-oxylene versus [6]MCPP (Fig. 1E). The major absorption band of [6]MCPP-oxylene was observed at a maximum absorption wavelength (λ_{max}) of 364 nm, which was bathochromically shifted compared with that of [6]MCPP (349 nm). Although [6]MCPP shows a weak absorption band within the 450- to 600-nm wavelength region, [6]MCPP-oxylene showed a maximum absorption wavelength of 458 nm and absorption bands in the 400- to 500-nm range. No fluorescence was observed for [6]MCPP, but [6]MCPP-oxylene fluoresced at 510 and 539 nm with a fluorescence quantum yield (Φ_F) of 0.13 at room temperature in toluene. This simple alteration in the structure but extensive change in properties of [6]MCPP underscores the power of the one-cycle in-insect transformation.

Identification of responsible enzymes

In addition to the product generated, the pathway and mechanism of [6]MCPP-oxylene formation are of fundamental interest. To verify whether the oxygen-doping of [6]MCPP was derived from intestinal bacteria, enzymes within the body, or both, biotransformation was conducted using intestinal bacteria as the target. However, we found that bacteria were not involved in biotransformation (see SM for details).

The effects of [6]MCPP feeding on individual insects were comprehensively analyzed using RNA sequencing to identify enriched Kyoto Encyclopedia of Genes and Genomes (KEGG) and differentially expressed gene (DEG) pathways. The enriched KEGG analysis is shown in detail in the SM. The signaling pathway with the highest rich factor was the "intestinal immune network for IgA production" with the lowest DEG number, suggesting that a few related genes in the pathway showed large expression changes. This analysis suggested that the accelerated neutralizing function of [6]MCPP could be attributed to its recognition as a xenobiotic or toxin.

The number of expressed genes that increased (red) or decreased (blue) upon feeding [6]MCPP is shown in Fig. 2A. In particular, an increase in the gene expression of metabolism-related pathways was observed. Based on the biotransformation pathway (Fig. 1B), which involved the insertion of the single oxygen atom into [6]MCPP, we focused on five CYP variants [X1, X2, X3, X4, and X5; cytochrome P450 6B2-like isoforms X1 (RefSeq ID; XP_022824880), X2 (XP_022824881), X3 (XP_022824882), X4 (XP_022824884), and X5 (XP_022824885)] that were suggested to be involved in xenobiotic metabolism (*32*, *34*). These CYP variants exhibited different levels of gene expression associated with [6]MCPP-feeding, as determined by quantitative reverse transcription-polymerase chain reaction (qRT-PCR) (Fig. 2B).

These results suggested that at least three CYP variants, CYP X2, X3, and X4, were involved in biotransformation of [6]MCPP (*32*). We then used an RNA interference technique (*35*), in which a small interfering RNA (siRNA) targeting these CYP variants was injected into the hemolymph of *S. litura* larvae (Fig. 2C). The siRNA used in this study was designed to knock down the expression levels of five CYP genes, rather than targeting a specific CYP gene. We examined the expression levels of three CYP variants that were predominantly up-regulated by [6]MCPP feeding and the production of [6]MCPP-oxylene. The levels of gene expression for each CYP in *S. litura* fed [6]MCPP after siRNA injection were 20 to 80% lower than those in injected with siRNA against green fluorescent protein (GFP) as a control, with substantial differences in CYP X2 and CYP X3 (Fig. 2D). The siRNA injection decreased the production yield of [6]MCPP-oxylene to 4.4 ± 1.9% (Fig. 2E). Therefore, these CYP variants are key enzymes in the biotransformation process.

These CYP variants are microsomal cytochrome P450s that bind to the membrane through their N-terminal transmembrane hydrophobic segment, and thus direct purification and functional evaluation of these proteins from insects is challenging owing to the high technical demand. Therefore, CYP X2 and CYP X3, which showed high expression of CYP variants in the in-insect synthesis, were deleted from their transmembrane sites (fig. S14) and their codons were optimized for expression in *Escherichia coli*. In addition, NADPH P450 reductase (CPR), an essential redox partner for the catalytic activity of CYPs (*36*), was prepared in the same manner.

The optimized genes were transferred into plasmids either singly (CYP X2-ctm, CYP X3-ctm, and CPR-ctm) or in tandem (CYP X2t and CYP X3t) for coexpression of CYP X2-ctm with CPR-ctm and CYP X3-ctm with CPR-ctm, respectively. The constructed plasmids were transformed into *E. coli* C41(DE3) cells (*37*), and used for whole-cell biotransformation as biocatalysts, as shown in Fig. 2F (see SM for details). The biotransformation of [6]MCPP using *E. coli* expressing only CYP X2-ctm, CYP X3-ctm, and CPR-ctm did not yield [6]MCPP-oxylene. By contrast, when CYP-ctm variants were coexpressed with CPR-ctm, [6]MCPP-oxylene was produced in 4.0 ± 0.4% yield (CYP X2t) and 4.0 ± 0.6% yield (CYP X3t), respectively (Fig. 2G and fig. S15). These results support CYP X2 and CYP X3 being the key enzymes involved in the biotransformation of [6]MCPP. The microbe-assisted biotransformation efficiency is less than that of individual insects in which multiple P450 species and other oxidases functioned synergistically.

In-insect transformation of cycloparaphenylenes

Having established the in-insect oxygen-doping of [6]MCPP, we hypothesized that the *S. litura* mediated reaction can be extended to carbon nanorings, [*n*]cycloparaphenylene ([*n*]CPP) (*7*–*11*). Thus, eight carbon nanorings of different ring sizes ([5]CPP to [12]CPP) were used as starting materials and biotransformed by *S. litura* larvae. Notably, the biotransformation of CPPs by *S. litura* larvae is a size-selective reaction that proceeds exclusively with [6]CPP (Fig. 3A; for details see SM). Other CPPs were unreacted and recovered in 52 to 77% yield from frass extracts as shown in fig. S17.

In the reaction of [6]CPP under otherwise identical conditions, oxygen-doped [6]CPP ([6]CPP-oxylene) was similarly isolated in 5.8 ± 0.9% yield together with unreacted [6]CPP (50.0 ± 17.0%) from the frass extract. The structure of [6]CPP-oxylene, in which a single oxygen atom was inserted into a C_{phenyl}–C_{phenyl} bond of the CPP framework, was confirmed by single-crystal x-ray crystallography analysis. Similar to the case of [6]MCPP-oxylene, the symmetry of the molecules changed from D_{3d} symmetric ([6]CPP) to C_2 symmetric ([6]CPP-oxylene) (Fig. 3B; for details see SM).

[6]CPP-oxylene had a weak absorption band at 400 to 500 nm, whereas [6]CPP showed a maximum absorption wavelength at 414 nm and absorption bands at 360 to 480 nm (Fig. 3C). This oxygen-doping assisted emerging fluorescence properties. Although [6]CPP was nonfluorescent, [6]CPP-oxylene exhibited an emission band centered at 524 nm with a quantum efficiency (Φ_F) of 0.26 at room temperature in toluene.

The gene expression levels of the CYP variants exhibited slight variations compared with the biotransformation of [6]MCPP, with only CYP X2 showing a substantial difference (Fig. 3D). This difference in the expression levels of CYP variants suggested that [6]CPP was more conformationally flexible than [6]MCPP, thereby affecting its binding stability to CYPs. In the microbe-assisted biotransformation of [6]CPP, [6]CPP-oxylene was only detected in 1.9 ± 0.4% of (CYP X2t, Fig. 3E, and fig. S16). These results support CYP X2 being the enzyme involved in the biotransformation of [6]CPP.

Substrate binding to CYP variants

We performed a two-step calculation of the binding affinity between [6]MCPP and the CYP variants to understand the mode of substrate incorporation into the CYP variants and the mechanism of oxygen insertion. For the calculation, CYP X3 was selected because its expression was the most up-regulated during the biotransformation of [6]MCPP. As the first

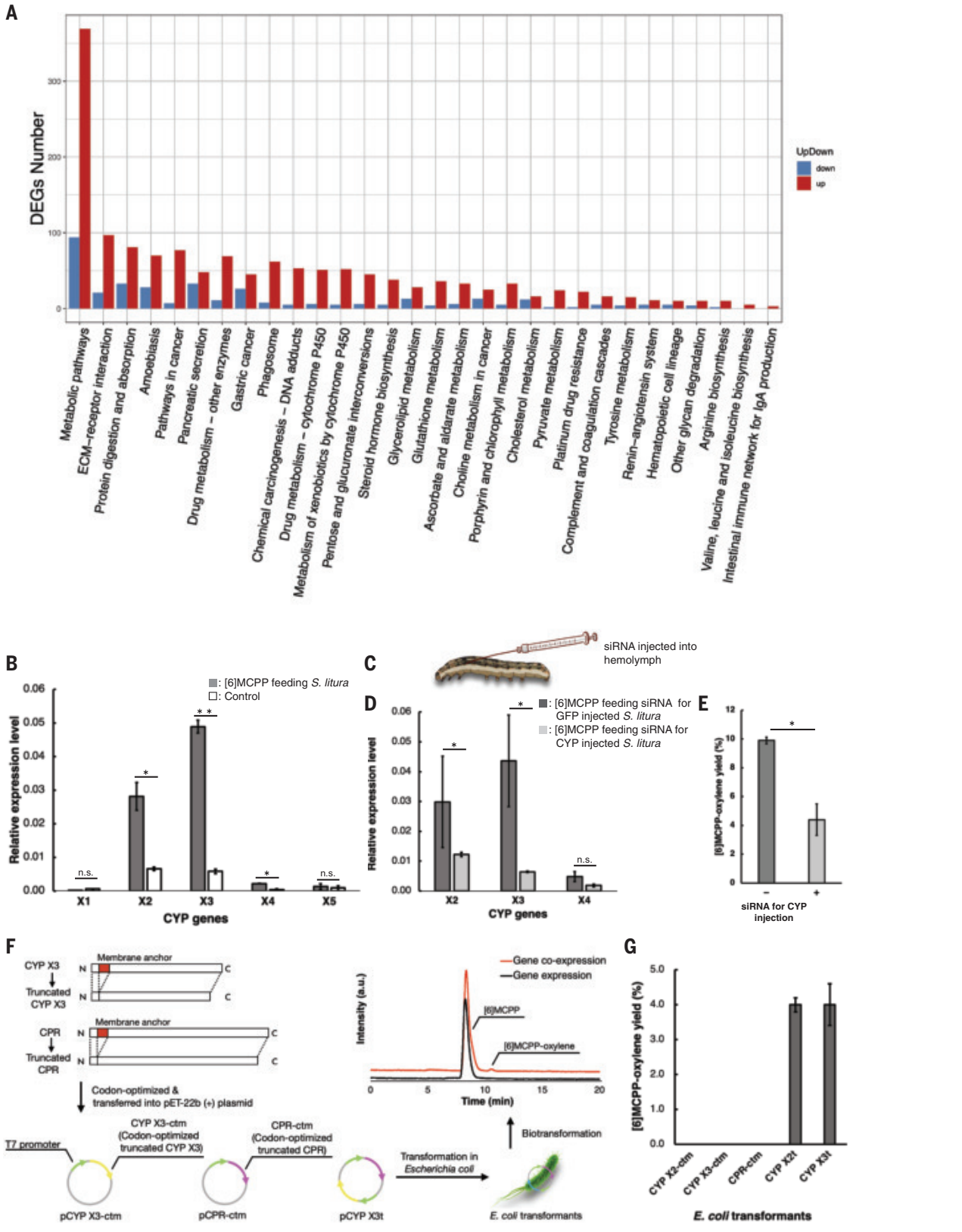

Fig. 2. Insight of in-insect synthesis of [6]MCPP-oxylene by *Spodoptera litura*. (**A**) Differentially expressed genes (DEGs) analysis of [6]MCPP-feeding *S. litura*. Up-regulation, red; Down-regulation, blue. (**B**) qRT-PCR of five CYP genes in the midgut of *S. litura* fed [6]MCPP. The reference gene is EF-1α. (**C**) Injection of siRNA into the hemolymph. (**D**) qRT-PCR of three CYP genes in the midgut of siRNA-injected *S. litura* fed [6]MCPP. (**E**) Biotransformation of [6]MCPP by siRNA for GFP or CYP injected *S. litura*. (−), *S. litura* with siRNA for GFP injected.; (+), *S. litura* with siRNA for CYP injected. (**F**) Scheme of microbe-assisted biotransformation. (**G**) Microbe-assisted biotransformation of [6]MCPP. Statistically significant differences are indicated with their respective *P*-values (*$P < 0.05$, **$P < 0.01$, Welch's *t*-test). Columns and bars indicate means and standard error of the mean (SEM) from three independent experiments.

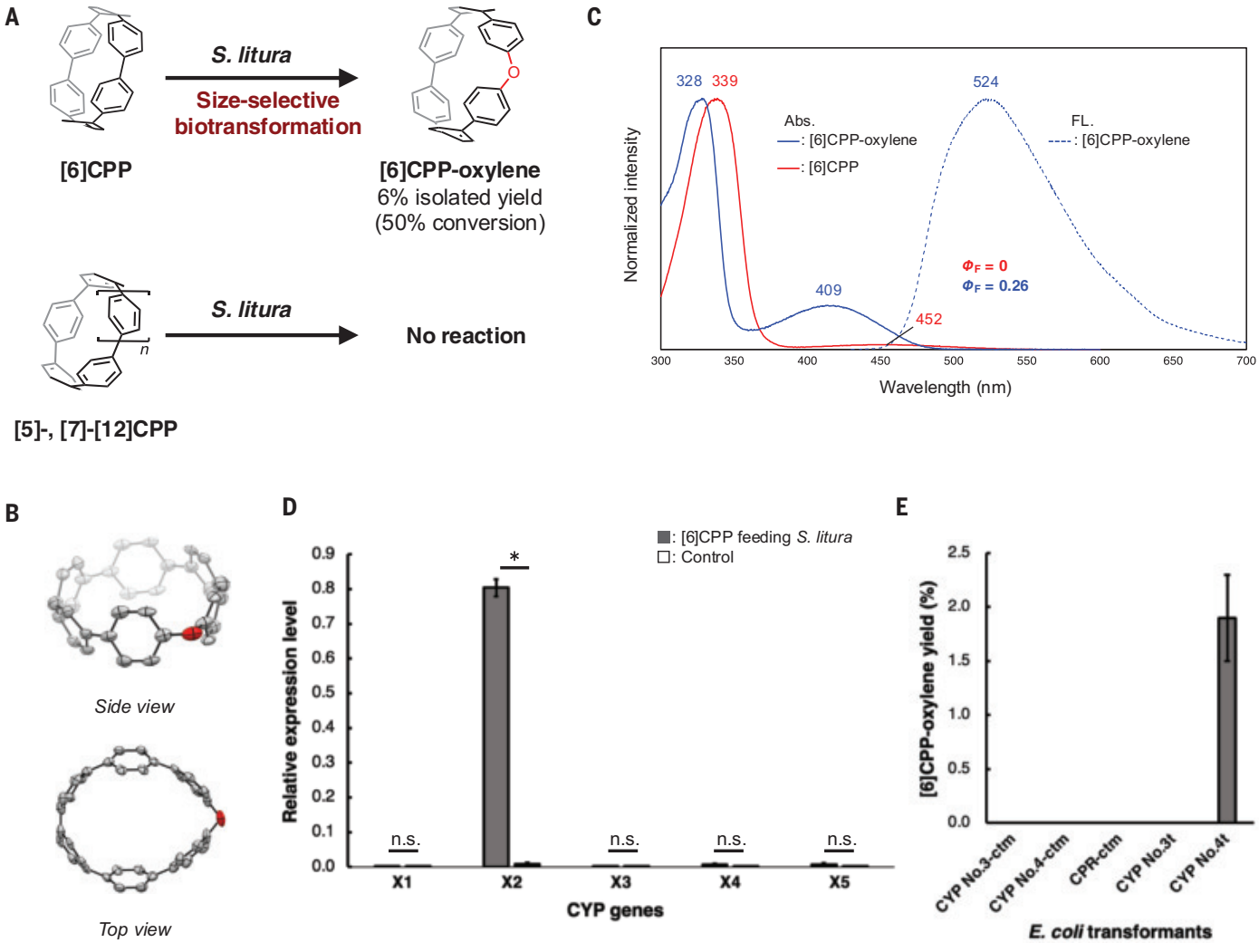

Fig. 3. In-insect transformation of [6]cycloparaphenylene ([6]CPP). (**A**) In-insect synthesis of [6]CPP-oxylene. (**B**) Oak Ridge thermal ellipsoid plot (ORTEP) drawing [6]CPP-oxylene with thermal ellipsoids set to 50% probability. Hydrogen atoms and solvent molecules are omitted for clarity. (**C**) Ultraviolet-visible absorption (solid lines) and fluorescence (dashed line) spectra of the toluene solutions of [6]CPP and [6]CPP-oxylene. The fluorescence spectra were measured upon excitation at 410 nm for [6]CPP-oxylene. (**D**) qRT-PCR of five CYP genes in the midgut of *S. litura* fed [6]CPP. The reference gene is EF-1α. (**E**) Microbe-assisted biotransformation of [6]CPP. Statistically significant differences are indicated with their respective *P*-values ($P < 0.05$, Welch's *t*-test). Columns and bars indicate means and SEM from three independent experiments.

step, docking simulations (*38*) were performed to explore the conformation of [6]MCPP binding to CYP X3. Given that the three-dimensional (3D) structure of CYP X3 has not been experimentally determined, the structure predicted by AlphaFold2 (*39*) was used in the simulations.

Placement of the heme cofactor at the active site of CYP was determined by superposition with a structurally homologous enzyme, human CYP3A4 [PDB ID: 4I3Q (*40*)]. The results of the docking simulations yielded insights into the arrangement of [6]MCPP within CYP X3. As the second step, molecular dynamics (MD) simulations were conducted on the obtained [6]MCPP-CYP X3 complex structure (movie S1). As illustrated in Fig. 4A, the results demonstrated the sustained stability of [6]MCPP within CYP X3 throughout an extended simulation period of 1 μs. Comparable computational analyses confirmed the presence of CPPs within the CYP variants (CYP X2; movies S2 for [6]MCPP and S3 for [6]CPP). These computational findings strongly imply the involvement of [6]MCPP-oxylene and [6]CPP-oxylene formation catalyzed by CYP450.

Although our calculations successfully demonstrated the binding of [6]MCPP to CYP X3, this interaction was hindered by the wide spatial separation between the center of [6]MCPP and the active site, namely heme. In the last MD snapshot, the distance between the center of mass of [6]MCPP and the iron atom of heme was 14.2 Å, and the nearest neighbor distance from the carbon of [6]MCPP to heme iron was 10.5 Å. Considering the available structural space within CYP X3 (Fig. 4A), we attempted to incorporate an additional [6]MCPP molecule into CYP X3.

Docking and MD simulations confirmed the ability of CYP X3 to accommodate two [6]MCPP molecules stably (Fig. 4B and movie S4). The time evolution of the distance between the [6]MCPP center and heme iron during the MD simulation exhibited an average distance of 10.8 Å with standard deviation of 0.42 Å, and the distance for the last MD snapshot was 10.8 Å. The nearest-neighbor distance between the [6]MCPP carbon and heme iron was 6.6 Å. These results substantiated the stable binding of the two [6]MCPP molecules to CYP X3.

Furthermore, our findings demonstrate that the [6]MCPP-heme distance was reduced when two [6]MCPP molecules were introduced, compared with the scenario with only one [6]MCPP molecule. Similar observations were made for the incorporation of two CPP molecules within CYP X2 (movie S5 for two [6]MCPPs and movie S6 for two [6]CPPs). Thus, our analysis provides substantial evidence supporting

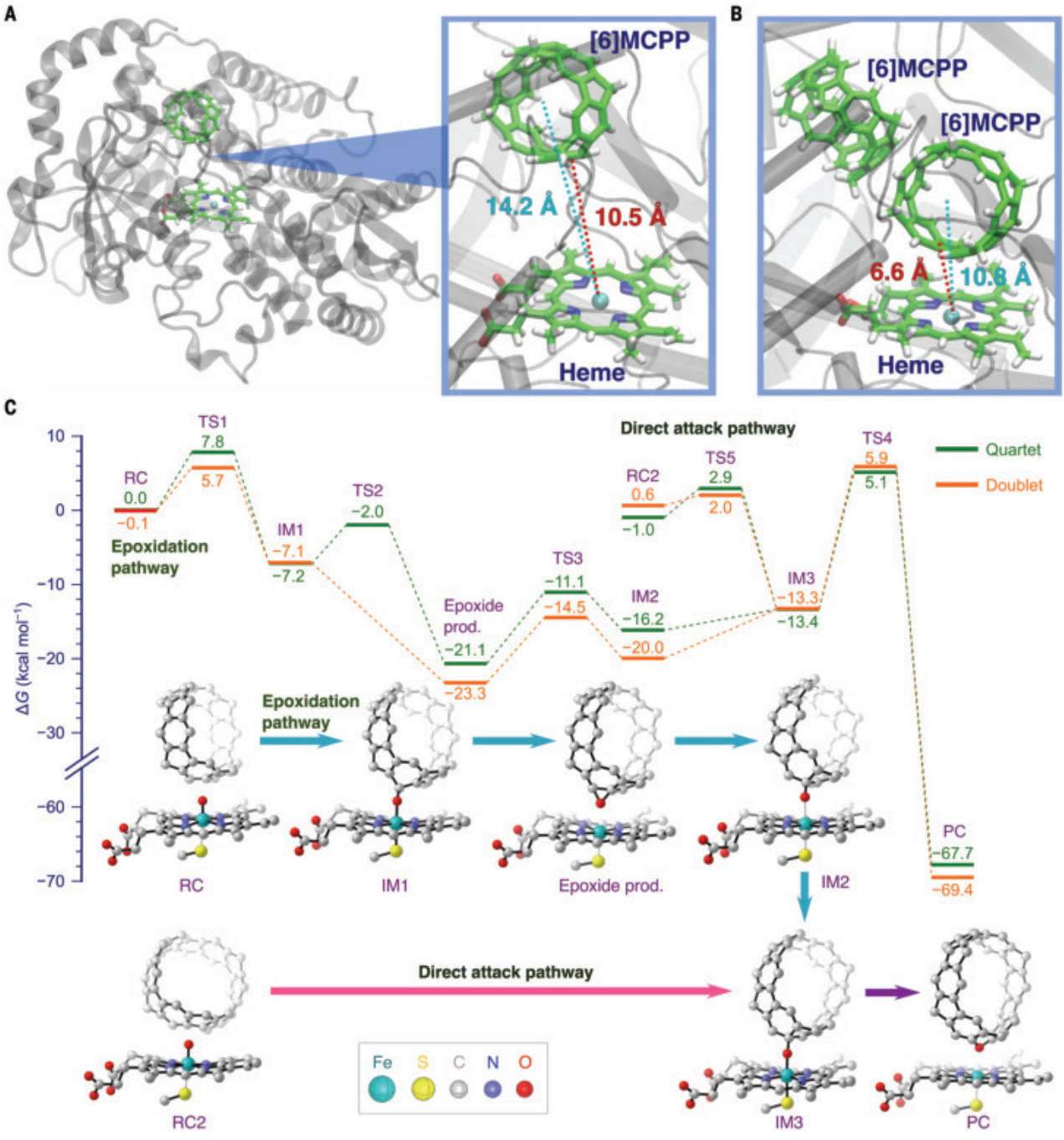

Fig. 4. Substrate binding to CYP variants and mechanism of oxygen-doping. (**A**) The binding structure of a [6]MCPP molecule to CYP X3 obtained after 1 μs of MD simulation. (**B**) Binding structure of the two [6]MCPPs to CYP X3 after 1 μs of MD simulation. The distance between the [6]MCPP molecular center and Fe atom is shown in blue, and the nearest-neighbor distance between the [6]MCPP molecule and Fe atom is shown in red. (**C**) Calculated free energy profiles at 298 K for the conversion of [6]MCPP to [6]MCPP-oxylene catalyzed by Cpd I. Two spin states—quartet and doublet—are considered. Two pathways are proposed: the epoxidation pathway (blue arrows) and the direct pathway (pink arrow). The energy values are expressed in kcal mol^{-1}.

the role of CYP450 in the formation of [6]MCPP-oxylene. These MD simulations are based on classical mechanics and do not elucidate the chemical reaction processes involving the recombination of covalent bonds between atoms.

Mechanism of oxygen-doping of [6]MCPP

We explored the reaction mechanism for the conversion of [6]MCPP to [6]MCPP-oxylene, catalyzed by the active species of P450 reaction cycles, Compound I (Cpd I), using density functional theory calculations (see SM for computational details). Our analysis considered two near-degenerate spin states: a quartet and a doublet (*41*), and we analyzed two pathways: epoxidation and direct attack (Fig. 4C).

The epoxidation pathway involved the formation of an intermediate (IM1) and an epoxide product, followed by the formation of two intermediates (IM2 and IM3). The insertion of oxygen into the five-membered ring formed the product. This step was rate-determining, with activation

free energies from IM2 to TS4 of 25.9 and 21.3 kcal mol^{-1} for the doublet and quartet states, respectively. In the direct attack pathway, IM3 was formed from a slightly different reactant complex (RC2). The subsequent transformation of IM3 to [6]MCPP-oxylene mirrored the epoxidation pathway. We believe that the direct attack pathway is favored over the epoxidation pathway because it involves fewer elementary reactions and has lower activation free energy than the reactant complex. Compared with the epoxide product, the oxylene product was considerably more stable (by > 45 kcal mol^{-1}), indicating that it was the thermodynamic product of the conversion process.

We also considered the feasibility of two competing reactions: hydroxylation at either the benzylic or aromatic C–H bonds of [6]MCPP. Both products were thermally less stable than the oxylene product by 14.7 and 8.3 kcal mol^{-1}, respectively. In addition, for the C–H hydroxylation to be feasible, a linear Fe–O–H arrangement would be required. Because of the orientation of [6]MCPP relative to Cpd I in the active site, benzylic C–H hydroxylation can be expected to be less probable. The formation of the phenol product could theoretically proceed through the nonenzymatic ring opening of the epoxide through protonation, as previously described (*42*). However, MD simulations indicated that [6]MCPP was stable in the active site, suggesting that the epoxide conversion into phenol was less likely to occur under the studied conditions.

We also theoretically explored the formation of [6]MCPP-dioxylene products by peroxidation (fig. S33). Among three possible dioxylene products, the pseudo-meta position was the most stable state with a strain energy (ΔH) of 17.4 kcal mol^{-1}. However, even when the reaction scale was increased 50-fold, only [6]MCPP-oxylene was obtained as the product. Thus, these experimental and computational studies revealed that [6]MCPP-oxylene was produced by utilizing a distinctive biological pathway.

Finally, the reaction mechanism of the Cpd I-catalyzed conversion of [6]CPP to [6]CPP-oxylene was investigated in manner similar to that of the conversion of [6]MCPP. The pathways proposed for this reaction (figs. S26 and S27) closely mirrored the pathways of [6]MCPP. The rate-determining step, exhibiting an activation free energy of ~20 kcal mol^{-1}, was still the insertion of oxygen into the [6]CPP ring.

Conclusions

This study provides insight into the production of single oxygen-doped molecular nanocarbons and the biocatalytic utilization of non-natural molecules. The in-insect synthesis of functional molecular nanocarbons not only offers a new toolbox and opportunity in nanocarbon science, but also represents major possibilities for biocatalysts in a range of unnatural product syntheses. Although biotransformation reactions present a scientific challenge in the form of high substrate specificity, as demonstrated in this study, we envision that a broader range of molecular nanocarbons can be nonclassically functionalized by utilizing genome-editing technologies to design CYP variants with extended enzyme pockets or mutations in their binding sites. Coupled with the remarkable recent progress in directed evolution technology and artificial metalloenzymes, the concept of in-insect synthesis offers a distinct and alternative option for molecule synthesis, enhancing our ability to discover, develop, and apply unnatural molecules in science and technology, expanding our chemical repertoire.

REFERENCES AND NOTES

1. A. M. Blanco *et al.*, *Med. Biochem.* **442**, 165–181 (2017).
2. P. K. Robinson, *Essays Biochem.* **59**, 1–41 (2015).
3. A. Alissandratos, *Biophys. Rev.* **12**, 175–182 (2020).
4. L. Gao, H. Qiao, P. Wei, B. Moussian, Y. Wang, *Arch. Insect Biochem. Physiol.* **109**, e21869 (2022).
5. I. A. Stepek, M. Nagase, A. Yagi, K. Itami, *Tetrahedron* **123**, 132907 (2022).
6. L. T. Scott *et al.*, *Science* **295**, 1500–1503 (2002).
7. R. Jasti, J. Bhattacharjee, J. B. Neaton, C. R. Bertozzi, *J. Am. Chem. Soc.* **130**, 17646–17647 (2008).
8. H. Takaba, H. Omachi, Y. Yamamoto, J. Bouffard, K. Itami, *Angew. Chem. Int. Ed.* **48**, 6112–6116 (2009).
9. S. Yamago, Y. Watanabe, T. Iwamoto, *Angew. Chem. Int. Ed.* **49**, 757–759 (2010).
10. E. J. Leonhardt, R. Jasti, *Nat. Rev. Chem.* **3**, 672–686 (2019).
11. Y. Segawa, A. Yagi, K. Matsui, K. Itami, *Angew. Chem. Int. Ed.* **55**, 5136–5158 (2016).
12. G. Povie, Y. Segawa, T. Nishihara, Y. Miyauchi, K. Itami, *Science* **356**, 172–175 (2017).
13. K. Y. Cheung *et al.*, *Chem* **5**, 838–847 (2019).
14. K. Y. Cheung, K. Watanabe, Y. Segawa, K. Itami, *Nat. Chem.* **13**, 255–259 (2021).
15. Y. Han, S. Dong, J. Shao, W. Fan, C. Chi, *Angew. Chem. Int. Ed.* **60**, 2658–2662 (2021).
16. W. Fan *et al.*, *J. Am. Chem. Soc.* **143**, 15924–15929 (2021).
17. M. Krzeszewski, H. Ito, K. Itami, *J. Am. Chem. Soc.* **144**, 862–871 (2022).
18. Y. Segawa *et al.*, *Nat. Synth.* **1**, 535–541 (2022).
19. W. Fan *et al.*, *Nat. Synth.* **2**, 880–887 (2023).
20. Y. Li, Y. Segawa, A. Yagi, K. Itami, *J. Am. Chem. Soc.* **142**, 12850–12856 (2020).
21. H. Kono *et al.*, *J. Am. Chem. Soc.* **145**, 8939–8946 (2023).
22. K. Kawasumi, Q. Zhang, Y. Segawa, L. T. Scott, K. Itami, *Nat. Chem.* **5**, 739–744 (2013).
23. H.-A. Lin *et al.*, *Angew. Chem. Int. Ed.* **57**, 2874–2878 (2018).
24. K. Kato *et al.*, *J. Am. Chem. Soc.* **143**, 5465–5469 (2021).
25. K. Kaiser *et al.*, *Science* **365**, 1299–1301 (2019).
26. Y. Gao *et al.*, *Nature* **623**, 977–981 (2023).
27. C. Kostaras, C. Pavlou, C. Galiotis, K. G. Dassios, *Carbon* **221**, 118909 (2024).
28. K. Günther *et al.*, *Angew. Chem. Int. Ed.* **64**, e202414645 (2025).
29. TCI Chemicals, "Methylene-bridged [6]CPP" (TCI, 2025); https://www.tcichemicals.com/assets/brochure-pdfs/Brochure_FF122_E.pdf
30. N. Ferry, M. G. Edwards, J. A. Gatehouse, A. M. R. Gatehouse, *Curr. Opin. Biotechnol.* **15**, 155–161 (2004).
31. M. Miyazawa, H. Takechi, *Nat. Prod. Commun.* **2**, 435–443 (2007).
32. T. Cheng *et al.*, *Nat. Ecol. Evol.* **1**, 1747–1756 (2017).
33. S. Marumoto, Y. Okuno, Y. Hagiwara, M. Miyazawa, *J. Oleo Sci.* **67**, 1253–1257 (2018).
34. R. Nauen, C. T. Zimmer, J. Vontas, *Curr. Opin. Insect Sci.* **43**, 78–84 (2021).
35. R.-L. Wang *et al.*, *J. Insect Physiol.* **75**, 54–62 (2015).
36. L. Shi *et al.*, *Pestic. Biochem. Physiol.* **173**, 104775 (2021).
37. K. Uchida, T. Akashi, T. Aoki, *Plant Biotechnol. (Tsukuba)* **32**, 205–213 (2015).
38. J. Eberhardt, D. Santos-Martins, A. F. Tillack, S. Forli, *J. Chem. Inf. Model.* **61**, 3891–3898 (2021).
39. J. Jumper *et al.*, *Nature* **596**, 583–589 (2021).
40. I. F. Sevrioukova, T. L. Poulos, *J. Med. Chem.* **56**, 3733–3741 (2013).
41. Q. M. Phung, K. Pierloot, *J. Chem. Theory Comput.* **15**, 3033–3043 (2019).
42. S. P. de Visser, S. Shaik, *J. Am. Chem. Soc.* **125**, 7413–7424 (2003).
43. A. Usami *et al.*, In-insect synthesis of oxygen-doped molecular nanocarbons, Zenodo (2025); https://doi.org/10.5281/zenodo.15081113

ACKNOWLEDGMENTS

We thank M. Yoshimura (Kyoto University) and D. Imoto (Nagoya University) for fruitful comments. We also thank A. Ohashi for their technical assistance. I. Takahashi (Nagoya University) is acknowledged for creating Figures 2C and 2F. **Funding:** K.I. and A.U. thank JSPS KAKENHI (grant numbers 19H05463 to K.I., and 22K14782 to A.U.); JST ACT-X (grant number JPMJAX22B3), Foundation of Public Interest of Tatematsu, the Sasakawa Scientific Research Grant, the Nakajima Foundation, the Naito Science & Engineering Foundation, and the the Iwatani Naoji Foundation (to A.U.); JSPS Promotion of Joint International Research (grant number 22K21346 to A.Y., K.J.F., and T.Y.); MEXT Promotion of Development of a Joint Usage/Research System Project CURE (grant number JPMXP1323015482 to K.J.F. and T.Y.,); and RIKEN CPR project (to K.I.) for financial support. H.K., V.A., H.S., and T.K. thank the Nagoya University Graduate Program of Transformative Chem-Bio Research (WISE Program) supported by MEXT. H.K., H.S. and T.K. thank the JSPS fellowship for young scientists. H.K. thanks the THERS Interdisciplinary Frontier Next Generation Researcher Scholarship supported by MEXT. V.A. thanks the Sato Yo International Scholarship Foundation. H.S. thanks the Nagoya University Interdisciplinary Frontier Fellowship. Computations were performed using the resources of the Research Center for Computational Science, Okazaki, Japan (Project Number 23-IMS-C087 and 24-IMS-C082). **Author contributions:** A.U. and K.I. conceived the concept of in-insect synthesis. K.I. directed the project. A.U. performed all the in-insect synthesis. A.U., H.K., H.Y., and K.A. performed and analyzed biological experiments. A.U., H.K., H.S., T.K., A.Y., and K.I. performed and analyzed synthesis, structure determination, and photophysical property experiments. V.A., Q.M.P., K.J.F., and T.Y. conducted computational studies. All authors analyzed and checked the data. A.U., V.A., K.J.F. and K.I. wrote the manuscript with feedback from other authors. All authors have given approval to the final version of the manuscript. **Competing interests:** The authors declare no competing interests. No patents were filed. **Data and materials availability:** Materials and methods, experimental procedures, photophysical studies, NMR spectra, and computational details are available in the SM and Zenodo (*43*). Crystallographic data for the structure of [6]MCPP-oxylene and [6]CPP-oxylene are available from the Cambridge Crystallographic Data Centre under reference number 2346752 and 2346751.

SUPPLEMENTARY MATERIALS

science.org/doi/10.1126/science.adp9384
Materials and Methods; Figs. S1 to S35; Tables S1 to S31; References (*44*–*82*); Movies S1 to S6

Submitted 18 April 2024; resubmitted 21 February 2025; accepted 7 April 2025
10.1126/science.adp9384

BATTERIES

Interface morphogenesis with a deformable secondary phase in solid-state lithium batteries

Sun Geun Yoon[1], Bairav S. Vishnugopi[2], Douglas Lars Nelson[3], Adrian Xiao Bin Yong[4,5], Yingjin Wang[6], Stephanie Elizabeth Sandoval[1,3], Talia A. Thomas[1], Kelsey Anne Cavallaro[3], Pavel Shevchenko[7], Elif Pınar Alsaç[1], Congcheng Wang[1], Aditya Singla[2], Julia R. Greer[6], Elif Ertekin[5,8], Partha P. Mukherjee[2], Matthew T. McDowell[1,3]*

The complex morphological evolution of lithium metal at the solid-state electrolyte interface limits performance of solid-state batteries, leading to inhomogeneous reactions and contact loss. Inspired by biological morphogenesis, we developed an interfacial self-regulation concept in which a deformable secondary phase dynamically aggregates at the interface in response to local electro-chemo-mechanical stimuli, enhancing contact. The stripping of a lithium electrode that contains 5 to 20 mole % electrochemically inactive sodium domains causes spontaneous sodium accumulation across the interface, with the sodium deforming to attain intimate electrical contact without blocking lithium transport. This process, characterized with operando x-ray tomography and electron microscopy, mitigates voiding and improves cycling at low stack pressures. The counterintuitive strategy of adding electrochemically inactive alkali metal to improve performance demonstrates the utility of interfacial self-regulation for solid-state batteries.

The high specific capacity of lithium (Li) metal and its compatibility with various solid-state electrolytes (SSEs) has focused efforts on developing Li metal solid-state batteries (SSBs) (*1*–*3*). However, a critical limitation of Li metal anodes for SSBs is the loss of contact at the SSE interface during Li stripping (battery discharge) owing to void formation (*1*, *2*, *4*). The formation of voids is detrimental because they cause high interfacial impedance and current focusing during charging, resulting in Li filament growth and short circuiting (*5*–*8*).

The mechanisms that govern void formation are complex, and the process is affected by current density, stack pressure, chemo-mechanics, and other factors (*5*, *7*, *9*–*13*). During stripping, vacancies are formed in the Li metal because of Li^+ transfer into the SSE. Because Li metal exhibits relatively low self-diffusivity (~10^{-10} cm^2 s^{-1}) (*14*–*16*), the vacancies tend to accumulate to nucleate voids (Fig. 1A). Higher current densities increase the vacancy formation rate and accelerate void formation (*7*, *11*, *14*). The application of stack pressure can deform soft Li metal (bulk yield strength of 0.8 MPa) to promote contact retention during stripping, but stack pressures greatly exceeding the yield strength have been shown to be required at moderate current densities to prevent void formation (>7 MPa for 1 mA cm^{-2}) (*5*, *7*). Moreover, Li shows heightened yield strength at submicrometer length scales, which may result in needing even higher stack pressures at SSE interfaces with nanoscale roughness (*17*–*19*). Critically, stack pressures must be low for achieving high cell-level specific energy (fig. S1), ideally being less than ~1 MPa for practical applications (*17*, *20*–*22*).

Interlayers comprising various materials, such as carbon (C) or Li alloys, have been shown to enable improved SSB performance. In general, these interlayer materials enhance Li transport toward the SSE interface, homogenize current distributions, and can help maintain interfacial contact (*23*–*26*). However, these approaches have primarily used hard or brittle interlayer materials to passively control Li transport, and some of these materials undergo transformations themselves (*27*–*29*). Relatively high stack pressures are therefore usually required to maintain interfacial contact (fig. S2). Interfacial strategies are needed that feature materials that can dynamically respond to local driving forces to promote contact retention even at low stack pressures.

We developed an approach to regulate SSB interfaces that is inspired by biological morphogenesis, which is the process by which living cells self-organize to form patterns and structures through multi–length scale chemo-mechanical interactions (*30*, *31*). Our approach involves self-regulated accumulation of a secondary phase at the SSE interface in response to the evolving morphological irregularities caused by Li stripping, sustaining interfacial contact and improving behavior at low stack pressures. The approach is demonstrated by use of Li electrodes that contain distributed metallic sodium (Na) domains with <20% Na. Na is electrochemically inactive, electrically conductive, and mechanically softer than Li (the bulk yield strength of Na is 0.16 to 0.24 MPa) (table S3). Na dynamically accumulates at the interface during Li stripping and plastically deforms to create intimate electrical contact (Fig. 1B), which suppresses void formation and enhances stripping capacity at stack pressures <1 MPa without blocking Li. The accumulation and deformation of the Na enables morphogenic self-regulation at the Li-SSE interface, with Na contact spontaneously emerging without external guidance in response to electrochemical and mechanical stimuli (*30*, *31*). The electrical conductivity of Na facilitates subsequent uniform Li plating, avoiding current constrictions and enabling stable cycling at low stack pressures.

Electrochemical stripping and plating

We fabricated Li-Na foils containing between 2.5 and 20 mol % Na using accumulative roll bonding (supplementary materials, materials and methods). In fig. S3, we show cross-sectional cryogenic focused-ion beam (cryo-FIB) scanning electron microscopy (SEM) images of the binary metals, in which Na domains a few to 10 μm in size are surrounded by a continuous Li matrix. Na and Li are immiscible at room temperature, giving rise to the two-phase microstructure (*32*). The electrode potential of Na is greater than that of Li (–2.71 and –3.04 V versus the standard hydrogen electrode, respectively), suggesting that Na should remain metallic and electrochemically inactive during Li redox processes (*33*).

In Fig. 1C, we show voltage curves during electrochemical stripping of Li from various Li-Na electrodes at stack pressures between 0 and 3.2 MPa. Solid-state half cells were used with argyrodite Li_6PS_5Cl SSE (LPSC). Pure Li showed almost 30 mA·hour cm^{-2} stripping capacity up to a 0.5 V cutoff at 3.2 MPa stack pressure, but substantially less Li was accessible at lower stack pressures (2.2 mA·hour cm^{-2} at 0.8 MPa and 0.4 mA·hour cm^{-2} at 0 MPa). This is a result of uncompensated void formation during stripping at low stack pressure (*23*, *34*). The stripped capacities of the Li-Na electrodes were generally higher than pure Li at stack pressures below 1.6 MPa. For example, the 5% Na electrode delivered 16 mA·hour cm^{-2} at 0.8 MPa stack pressure, and the 20% Na electrode was able to strip 5.3 mA·hour cm^{-2} at 0 MPa. The voltage profiles of the electrodes shown in Fig. 1C had voltage variations at 0.15 to 0.25 V (fig. S4), which were absent during stripping of pure Li electrodes. This behavior likely arises from some

[1]George W. Woodruff School of Mechanical Engineering, Georgia Institute of Technology, Atlanta, GA, USA. [2]School of Mechanical Engineering, Purdue University, West Lafayette, IN, USA. [3]School of Materials Science and Engineering, Georgia Institute of Technology, Atlanta, GA, USA. [4]Department of Materials Science and Engineering, University of Illinois Urbana-Champaign, Urbana, IL, USA. [5]Materials Research Laboratory, University of Illinois Urbana-Champaign, Urbana, IL, USA. [6]Division of Engineering and Applied Sciences, California Institute of Technology, Pasadena, CA, USA. [7]Advanced Photon Source, Argonne National Laboratory, Lemont, IL, USA. [8]Department of Mechanical Science and Engineering, University of Illinois Urbana-Champaign, Urbana, IL, USA. *Corresponding author. Email: mattmcdowell@gatech.edu

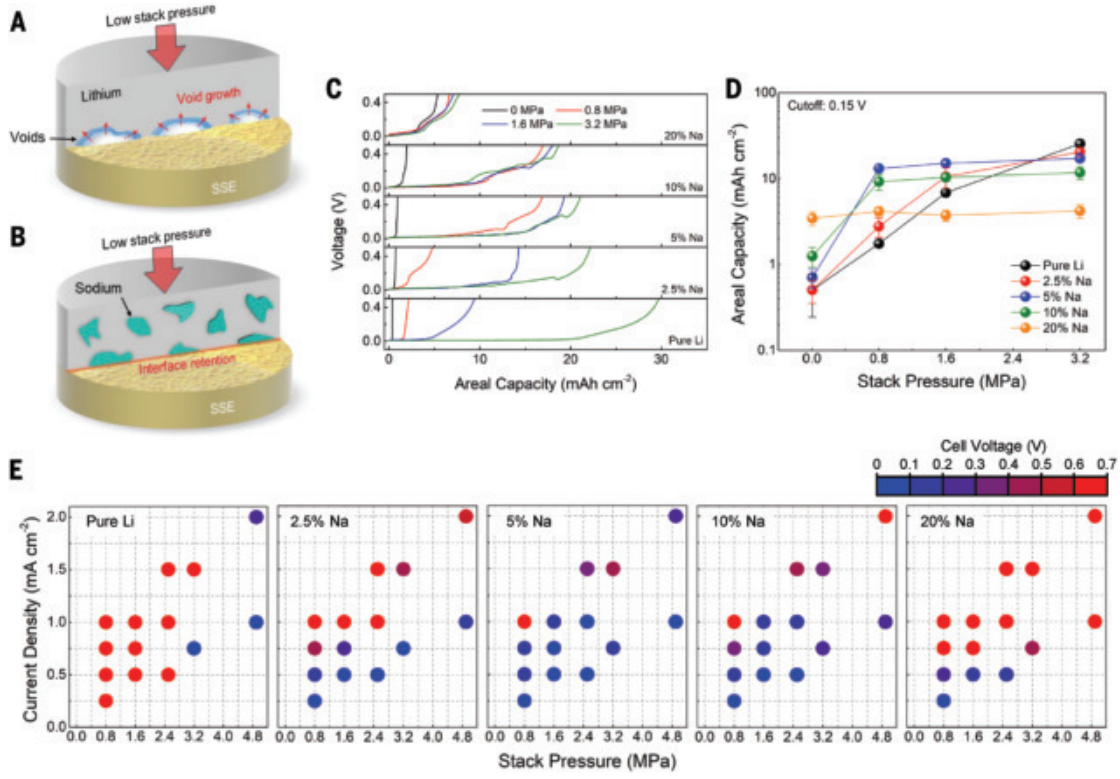

Fig. 1. Electrochemical stripping and plating tests of Li-Na electrodes. (**A** and **B**) Schematics of (A) void formation during pure Li stripping at low stack pressure and (B) Na accumulation and void mitigation during stripping of a Li-Na electrode. (**C**) Galvanostatic voltage profiles during Li stripping from various Li-Na electrodes at different stack pressures. The cells used Li_6PS_5Cl SSE, Li metal counter electrodes, and a current density of 0.25 mA cm^{-2}. (**D**) Average stripped areal capacity from different Li-Na electrodes (three experiments each) as a function of stack pressure. The stripped capacities were measured at a cutoff voltage of 0.15 V. Error bars indicate standard deviation. (**E**) Color maps showing the cell voltage after 3 mA·hour cm^{-2} of stripping or at a cutoff voltage of 0.62 V if this capacity was not reached, as a function of stack pressure (0.8 to 4.8 MPa, *x* axis) and current density (0.25 to 2.0 mA cm^{-2}, *y* axis). Working electrodes comprising pure Li, 2.5% Na, 5% Na, 10% Na, and 20% Na were used (left to right, respectively). A Li–In alloy (LiIn–In, +0.62 V versus Li/Li$^+$) electrode was used as the counter electrode to avoid short circuiting. All percentages are molar percentages.

interfacial oxidation of the Na because the potential is near the Na electrode potential.

We show in Fig. 1D statistical trends of the average stripped Li capacities for the different electrodes at varying stack pressure. Whereas the pure Li and 2.5% Na electrodes showed monotonically increasing capacity with increasing stack pressure, the other composite electrodes showed similar capacities at stack pressures between 0.8 and 3.2 MPa. The electrode with 20% Na is a limiting example, showing approximately invariant stripped capacity regardless of stack pressure, with lower capacities at higher stack pressures that may arise from early blocking of Li transport to the interface.

A comprehensive summary of the initial stripping behavior of these electrodes at various current densities and stack pressures is shown in the maps in Fig. 1E. The color of the points indicates the voltage either after 3.0 mA·hour cm^{-2} was stripped or at the cutoff voltage of 0.62 V if this capacity was not reached (fig. S5A). The pure Li electrode can only strip this capacity at stack pressures >3.2 MPa. By contrast, the electrodes with 5 and 10% Na allowed for successful stripping with <0.1 V at stack pressures down to 0.8 MPa and varying current densities. The stable stripping region for the 20% Na electrode was limited to lower current densities than composites with less Na. Further experiments were carried out at zero applied stack pressure (fig. S6 and supplementary text 1). Data at different current densities were fit to Sand's equation to extract an interfacial transport descriptor (*23*, *34*), revealing that increasing Na content in the electrodes systematically enhances the effective transport of Li to the SSE interface. This implies that the incorporated Na phase stabilizes interfacial contact at zero stack pressure.

Electrochemical behavior during further plating and stripping was also investigated (fig. S5). After initial stripping, 3 mA·hour cm^{-2} of Li was redeposited onto the electrodes, followed by a second stripping process. Pure Li electrodes short circuited under all current density/stack pressure conditions during redeposition. Many of the Li-Na electrodes, and particularly those with 5 and 10% Na, did not short circuit upon plating (fig. S5). During the second stripping, the composite electrodes tended to exhibit higher polarization than during the first, but stable stripping to 3 mA·hour cm^{-2} was achieved for the composite electrodes across a range of current densities and stack pressures. Electrodes with 10 and 20% Na showed the lowest voltage at 0.8 MPa stack pressure during the second stripping. These results show that the presence of Na contributes to stable electrodeposition and further stripping steps.

Interfacial evolution

To provide insight into interfacial evolution, we conducted potentiostatic electrochemical impedance spectroscopy (EIS) during Li stripping. We show in Fig. 2, A and B, galvanostatic stripping curves and Nyquist plots collected at increments of 0.5 mA·hour cm^{-2} capacity from pure Li and 10% Na electrodes at 1.6 MPa stack pressure. The spectral features at high frequency (~1 MHz) likely arise from bulk SSE resistance, whereas lower frequency (100 to 1 kHz) features are associated with interfacial resistance, including interphase and charge transfer resistance (*5*, *25*, *26*, *35*). At the onset of stripping, the voltages of the pure Li cell (Fig. 2A) and the 10% Na cell (Fig. 2B) were both 11 mV. The initial EIS spectra of both cells were also quite similar, showing compact spectra with a partial semicircle in the high-frequency

range (>1 kHz). Their minima along the real axis, representing interfacial resistance, were observed at 36 to 38 ohm cm^2. After stripping of the pure Li electrode to 5 mA·hour cm^{-2}, the cell voltage increased to 63 mV, and the high-frequency semicircle in the impedance spectrum expanded, representing an increase in interfacial resistance to ~200 ohm cm^2 (Fig. 2A). Additionally, the apex frequency of this semicircle shifted to lower values during stripping (fig. S7A), indicating that this feature is associated with voids at the interface (*26*, *36*, *37*). By contrast, the impedance spectrum of the 10% Na cell (Fig. 2B) showed no substantial increase in its partial semicircle and only a minor shift of interfacial resistance to ~41 ohm cm^2 during stripping, which likely includes the impact of interphase growth. This behavior was accompanied by a smaller voltage increase to 41 mV in the galvanostatic data. These EIS spectra showed the formation of a low-frequency tail (<1 kHz), which was also observed in Li-Na electrodes with other compositions (fig. S8). Higher Na concentrations typically featured earlier tail development and higher voltages in the galvanostatic profiles at the end of stripping (figs. S7, B and C, and S8).

The evolution of the Li-Na EIS spectra allows for the following conclusions. The lack of semicircle evolution indicates that the electrode-SSE interface retains low resistance with minimal void formation during stripping, and the growth of the low-frequency tails is likely due to interfacial accumulation of the ion-blocking Na phase (fig. S9 describes control experiments with Na||Na symmetric cells demonstrating blocking behavior) (*38*, *39*). This result implies that excessive Na content (20% Na and above) causes faster voltage polarization because of the more rapid interfacial accumulation of Na to block Li transport, rather than through void formation. The interfacial reaction between the accumulated Na and the SSE can be effectively controlled during operation by ensuring that the electrode potential remains below ~0.3 V versus Li/Li^+, at which Na reactions contribute to interphase formation (figs. S4 and S10). Such control maintains low interfacial impedance and minimal interphase formation (fig. S10).

Morphological evolution was investigated with cryo-FIB-SEM (Fig. 2, E and F). In the initial state, a 10% Na electrode (Fig. 2E and fig. S11A) shows Na domains distributed uniformly throughout the darker Li, without contact between Na and the SSE material. After stripping 4 mA·hour cm^{-2} in a different cell (Fig. 2F), the electrode showed a few-micrometer-thick Na layer that contacted the SSE. This indicates accumulation of Na at the interface during Li stripping, with the Na maintaining electrical contact (Fig. 2B). When Li was fully stripped from a 10% Na electrode, Na remained at the SSE interface with only minor residual Li present, supporting 74% Li utilization from the composite electrode (fig. S12).

The reversibility of this behavior was investigated to understand how the accumulated Na interfacial layer evolves upon subsequent Li plating. As displayed in Fig. 2C, stable galvanostatic Li deposition occurs without nucleation overpotential after the first stripping. We provide in Fig. 2G a cryo-FIB-SEM image that demonstrates the accumulated Na layer shifting away from the interface as Li is deposited onto it. The stripping steps during the second and third cycles showed EIS evolution and final voltage values similar to those of the first

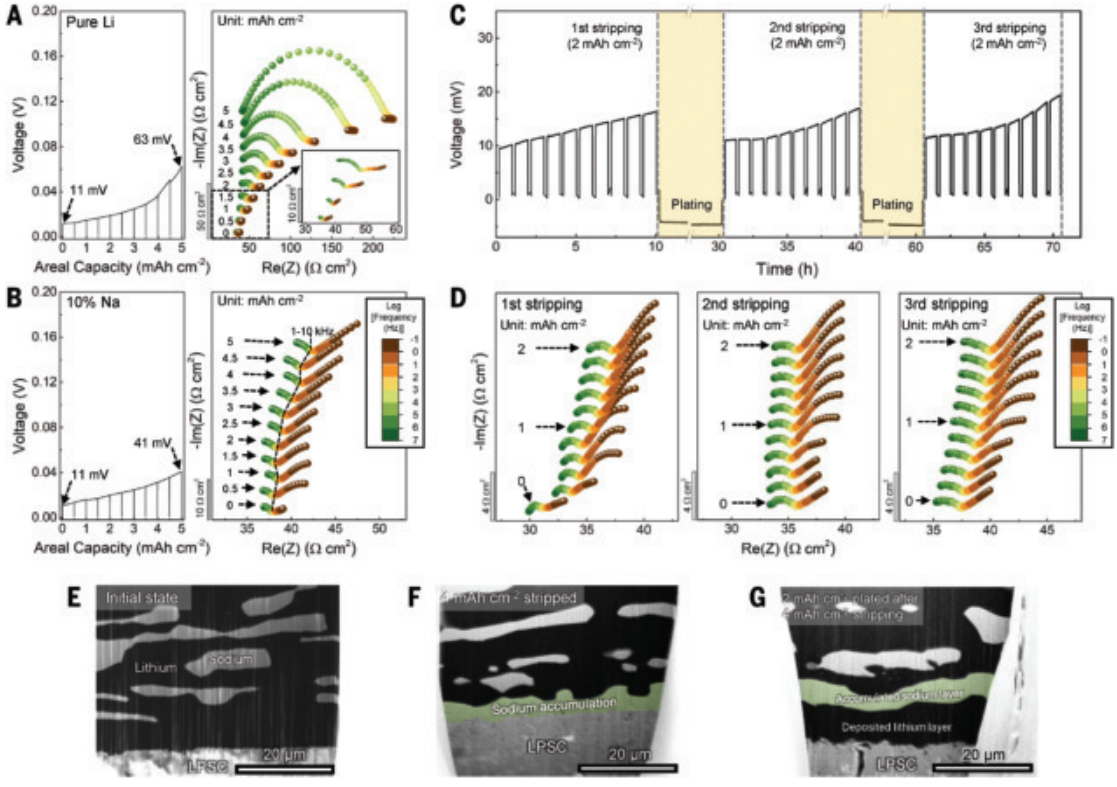

Fig. 2. Electrochemical impedance analysis of interfacial evolution. (**A** and **B**) In situ EIS analysis of (A) the pure Li and (B) 10% Na electrodes during Li stripping with Li counter electrodes at 1.6 MPa stack pressure. (Left) Voltage profiles. (Right) The associated Nyquist plots. A current density of 0.25 mA cm^{-2} was used with potentiostatic EIS spectra taken every 0.5 mA·hour cm^{-2}, as marked. Impedance spectra for other compositions are shown in fig. S7. (**C** and **D**) In situ EIS analysis of a 10% Na electrode during electrochemical cycling with a Li counter electrode at 2.5 MPa stack pressure. (C) Voltage profile and (D) associated Nyquist plots for the first, second, and third stripping steps. Current densities of 0.25 mA cm^{-2} and 0.1 mA cm^{-2} were used for stripping and plating, respectively. Potentiostatic EIS spectra were measured every 0.2 mA·hour cm^{-2} during stripping, as marked. (**E** to **G**) Cryo-FIB-SEM images of 10% Na electrodes at various stages of cycling: (E) the initial state, (F) after 4 mA·hour cm^{-2} was stripped, and (G) after 2 mA·hour cm^{-2} was plated (after initial stripping of 4 mA·hour cm^{-2}). All cells in (E) to (G) had a stack pressure of 1.6 MPa and current density of 0.25 mA cm^{-2}. In (F) and (G), an artificial green color has been overlaid on interface-accumulated Na. Images without the overlays are provided in fig. S11, B and C.

stripping step (Fig. 2, C and D). The low-frequency EIS tails appear during these stripping steps similarly to the first step. This is consistent with a cryo-FIB-SEM image in fig. S11D, which shows interfacial Na accumulation after partial stripping after multiple cycles. These results indicate that Na returns to contact the SSE interface during cyclic Li stripping without substantial void formation. Moreover, the EIS signatures suggest that Na accumulates at the interface even before the deposited Li layer is fully depleted (fig. S11D). Li deposition onto the accumulated Na layer (Fig. 2G) also implies that a Na metal layer alone could serve as an effective current collector for Li cycling. This feasibility was further validated in fig. S13, where Na metal as a current collector demonstrated extended cycling capability compared with that of a Cu current collector; however, higher Coulombic efficiency was attained with composite Li-Na electrodes.

Operando x-ray computed tomography

We investigated the dynamic evolution of a Li-Na electrode using operando synchrotron x-ray computed tomography (XCT) imaging. A half cell with a 10% Na electrode was used in a cell customized for XCT during electrochemical testing (supplementary materials, materials and methods). A cross-sectional image slice of the cell stack is shown in Fig. 3A. The grayscale contrast between both electrodes and LPSC is due to differences of the x-ray attenuation coefficients (*8*, *40*), with the electrodes appearing darker because they are primarily composed of low-Z Li metal (*8*, *41*).

Galvanostatic stripping and plating were performed sequentially by using a current density of 0.5 mA cm^{-2}, with stripping and plating capacities of 1.0 and 1.13 mA·hour cm^{-2}, respectively (fig. S14). Magnified image slices of a location at the interface between the SSE and the Li-Na electrode at various times are shown in Fig. 3B. The bright domains in the electrode are Na. To highlight Na evolution, grayscale intensity profiles across the interface are displayed below the image slices in Fig. 3B, with scanned locations indicated with red boxes. The electrode-SSE interface is indicated with a red line in each intensity plot. As shown in the profile in Fig. 3B, i, the composite electrode exhibits greater intensity variation compared with that in the SSE region. Grayscale intensity peaks and valleys in the electrode correspond to the Na domains and the Li matrix, respectively. The average grayscale pixel intensity values of the electrode and the SSE regions in this profile are 98.1 ± 65.2 and 124.3 ± 22.9, respectively, which is consistent with other locations (fig. S15 and supplementary text 3).

Three different Na domains were tracked during electrochemical cycling, with the peaks associated with these domains indicated

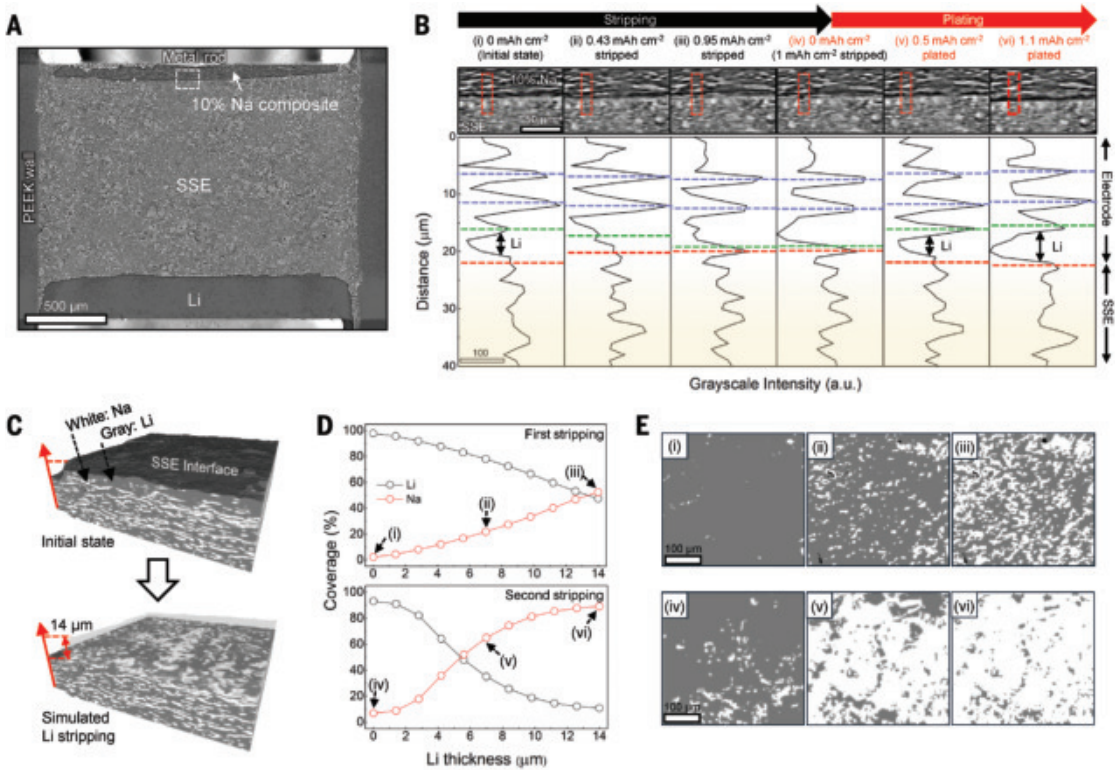

Fig. 3. Operando x-ray CT analysis of interfacial evolution. (**A** and **B**) Operando x-ray tomography imaging of a 10% Na composite electrode half cell during Li stripping and plating. (A) An image slice of the 10% Na electrode|LPSC|Li half cell. (B) Cross-sectional images of a portion of the interface between LPSC and the Li-Na electrode at different stages of cycling, along with corresponding grayscale intensity profiles from the red boxes in the images. The stages of electrochemical cycling are labeled from left to right as follows: (i) 0 mA·hour cm^{-2} stripped (initial state), (ii) 0.43 mA·hour cm^{-2} stripped, (iii) 0.95 mA·hour cm^{-2} stripped, (iv) 0 mA·hour cm^{-2} plated (equivalent to 1 mA·hour cm^{-2} stripped), (v) 0.5 mA·hour cm^{-2} plated, and (vi) 1.1 mA·hour cm^{-2} plated. The electrochemical cycling profile is shown in fig. S14. In the grayscale profiles, the SSE interface is indicated with red dashed lines. The nearest Na domain (high grayscale intensity) to the interface is indicated with a green dashed line, and other Na domains are indicated with blue dashed lines. The white box in (A) indicates the location of these cross-sectional images. (**C** to **E**) Simulated stripping analysis to determine the evolution of Li and Na coverage at the SSE interface. (C) Rendered 3D subvolumes (top) in the pristine state and (bottom) after simulated Li stripping, where Li is gray and Na is white. The reconstructed initial volume measures 420 by 420 by 131 µm. The accumulation of Na at the SSE interface was simulated by removing Li voxels from the initial state to a thickness of 14 µm (10 voxel layers), while Na remained (fig. S16 and materials and methods). (D) Interfacial coverage of Na and Li in the subvolume during the (top) first and (bottom) second stripping processes by means of simulated Li stripping. (E) 2D interfacial coverage maps at different simulated stripping states, as marked in (D). Li is gray and Na is white.

in Fig. 3B with green and blue dashed lines in the intensity profiles. The Na domain closest to the SSE interface (Fig. 3B, green dashed line) initially remained separated from the SSE interface (Fig. 3B, red dashed line) by a Li layer (Fig. 3B, i). During Li stripping, this Na peak moved closer and became conflated with the SSE interface (Fig. 3B, ii to iv). During Li plating, the Na peak again became distinct as Li deposited below it (Fig. 3B, iv to vi). This behavior is consistent with the ex situ SEM in Fig. 2G and demonstrates the accumulation and removal of Na from the interface. The other Na peaks in the profile were also displaced as Li was stripped and redeposited (Fig. 3B, blue dashed lines). This Na domain redistribution was consistent with analysis of a different location (fig. S15).

As previously discussed, the interfacial distribution of Na is different after one cycle compared with its initial state. To understand how the interfacial accumulation of Na depends on the initial distribution of Na within the microstructure, we developed an analysis to simulate Li stripping using the three-dimensional (3D) XCT data. This "simulated stripping" analysis was carried out instead of direct segmentation of Na because the Na and the SSE phases exhibited similar grayscale intensity (Fig. 3B), which precluded accurate segmentation of contacting phases. The reconstructed microstructure of the pristine composite electrode is shown in Fig. 3C. The simulated stripping process involved virtually "removing" a planar layer of Li voxels and projecting the Na voxels in the same layer onto the SSE interface, followed by identical processing of the next layers (fig. S16). The evolution of interfacial coverage of Li and Na is shown in Fig. 3D as a function of stripped Li thickness up to 14 μm (10 voxel layers, or 2.9 mA·hour cm^{-2}). Stripping was simulated for both the pristine XCT microstructure (Fig. 3B, i) and the microstructure after one cycle (Fig. 3B, vi). The corresponding 2D maps of Li and Na coverage across a region of the interface are shown in Fig. 3E. As shown in Fig. 3, D and E, i to iii, the interfacial coverage of Na during the first stripping increased steadily as Li was stripped and its coverage decreased. During the second stripping, however, a more abrupt increase of Na coverage occurred (Fig. 3, D and E, iv to vi). This more abrupt increase is due to the deposited Li layer beneath the accumulated Na being depleted to result in sudden Na-SSE contact. Thus, the microstructural distribution of Na is expected to strongly influence Na contact pattern formation at the interface and resulting electrochemical behavior.

Electrochemical cycling

We carried out galvanostatic cycling tests to investigate electrochemical reversibility. Cells with Li–In (indium) counter electrodes were cycled with 2 mA·hour cm^{-2} capacity per cycle. All the Li-Na electrodes with different compositions showed reversible cycling over 10 cycles (Fig. 4A). Because the Li-In counter electrode maintains a constant electrode potential during lithiation-delithiation (+0.62 V versus Li/Li^+) (*28*), the voltage profiles in Fig. 4A primarily reflect the behavior of the Li-Na electrodes. The overlaid stripping profiles over four cycles are shown in Fig. 4B. The voltage profiles during the first stripping generally exhibited a linear increase, with their slopes approximately proportional to Na concentration. Subsequent stripping profiles showed nonlinear increases, especially with higher Na concentrations. The Na distribution therefore affects the extent of voltage polarization because the more abrupt accumulation of the Na phase at the SSE interface observed in the second cycle in the XCT data in Fig. 3D gives rise to more rapid polarization. The 5 and 10% Na electrodes also exhibited stable cycling upon doubling the cycling capacity to 4 mA·hour cm^{-2} per cycle (fig. S17).

We also conducted longer-term galvanostatic cycling tests. We show in Fig. 4, C and D, cycling of a 5% Na electrode at a current density of 0.75 mA cm^{-2} and a stack pressure of 2.5 MPa (Fig. 4C) and a 10% Na electrode at a current density of 0.5 mA cm^{-2} and a stack pressure of 1.6 MPa (Fig. 4D). Under these conditions, pure Li electrodes typically exhibited rapid voltage polarization during stripping owing to interfacial voiding, followed by short circuiting during plating (Fig. 4, C and D, insets). By contrast, the cells with Li-Na electrodes showed substantially enhanced cyclability and low voltage. The 5% Na electrode (Fig. 4C) and the 10% Na

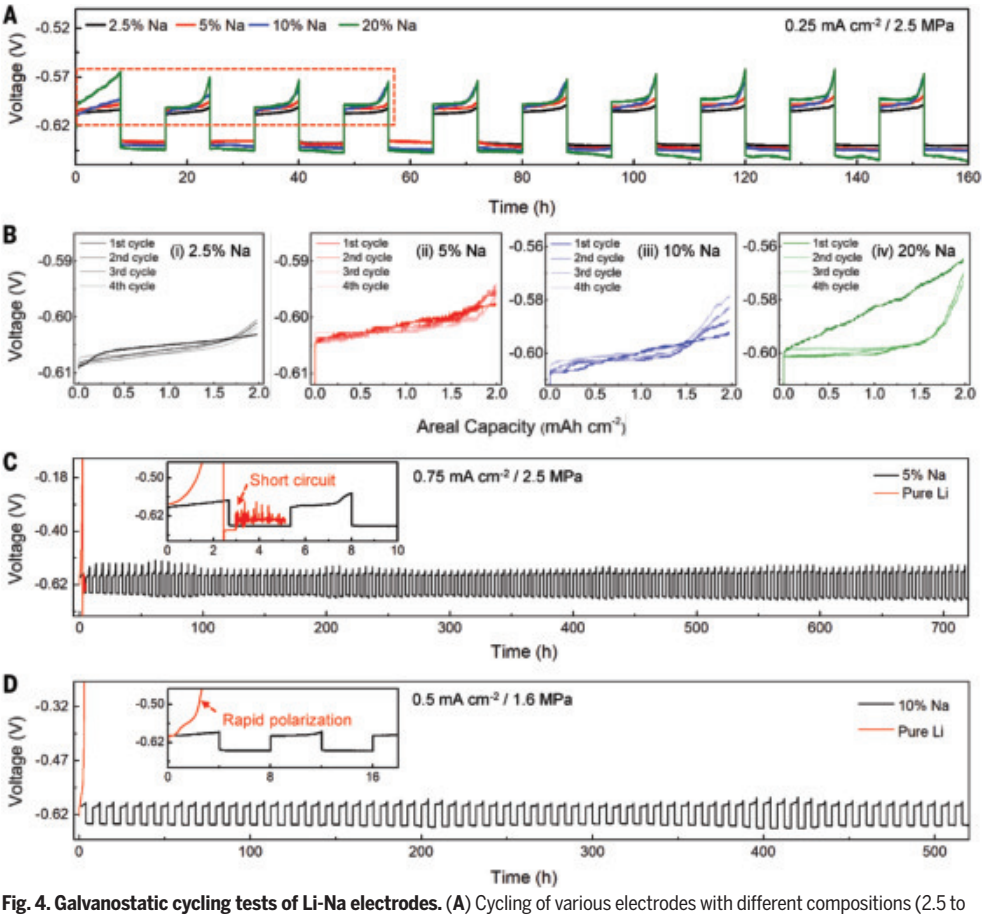

Fig. 4. Galvanostatic cycling tests of Li-Na electrodes. (**A**) Cycling of various electrodes with different compositions (2.5 to 20 atomic % Na) at a current density of 0.25 mA cm^{-2} and a stack pressure of 2.5 MPa. (**B**) Corresponding stripping voltage profiles for the first four cycles, as highlighted within the red box in (A). (**C** and **D**) Long-term cycling stability of (C) 5% Na and (D) 10% Na electrodes. For comparison, pure Li electrodes were cycled under the same conditions as in (C) and (D). The cells in (C) were cycled at a current density of 0.75 mA cm^{-2} and a stack pressure of 2.5 MPa, and those in (D) were cycled at a current density of 0.5 mA cm^{-2} and a stack pressure of 1.6 MPa. All cells used a Li–In counter electrode and were tested with an areal capacity of 2 mA·hour cm^{-2} per cycle. The measured voltage values displayed are negative because the Li–In counter electrode exhibits an electrode potential of 0.62 V versus Li/Li^+.

electrode (Fig. 4D) sustained over 100 and 50 cycles, respectively. Additionally, the 5% Na electrode demonstrated outstanding cyclability at a current density of 1 mA cm^{-2} and a stack pressure of 4.1 MPa (fig. S18). These results demonstrate that the accumulation of Na at the SSE interface not only mitigates voiding, but because of its electrochemical inactivity and deformability, it also supports stable Li plating (Fig. 2G), enabling cycling at low stack pressures.

All-solid-state full cells with Li-Na anodes and sulfur cathodes were fabricated and tested under low stack pressures between 2.5 and 0.8 MPa (figs. S19 and S20 and supplementary text 4), which is much lower than most literature demonstrations of sulfur SSBs (*42*, *43*). A cell with a 5% Na anode displayed >3 mA·hour cm^{-2} and 75% capacity retention after 100 cycles with 2.5 MPa stack pressure (fig. S19), whereas cells with pure Li anodes short circuited in approximately five cycles. A cell with a 10% Na anode exhibited 69 cycles at a stack pressure of 0.8 MPa (fig. S20A), whereas a pure Li cell short circuited in the first cycle.

In fig. S2, we compare the experimental conditions (stack pressures and current density) from the results herein with other published SSB demonstrations that used Li metal and alloy electrodes with sulfide SSEs. Alloy anodes such as Si are frequently used to overcome the challenges of Li metal (*27*–*29*). However, both Li metal and Li alloy anodes usually necessitate high stack pressures, ranging from a few megapascals to tens of megapascals (fig. S2). The required stack pressure generally rises with increased current density, with higher stack pressures needed to maintain the morphological conformity of the solid-solid interface (*29*, *44*). Our multiphase alkali metal electrodes deviate from this trend, functioning effectively at stack pressures between 0.8 and 2 MPa, with modest current densities (fig. S20). Incorporating denser Na into the Li anode reduces specific energy by only 1 to 2% (table S5 and fig. S21), allowing for mechanistic benefits to be realized with negligible impact on energy metrics.

Electro-chemo-mechanical modeling

We developed a mesoscale model to better understand how electro-chemo-mechanical interactions influence Na domain evolution at the SSE interface. The model considers electrochemical reaction kinetics, mechanical deformation of the metals, diffusivity, and ionic transport (supplementary materials). The stress distribution in a pure Li electrode near a void at the Li-SSE interface is illustrated in Fig. 5A (1 MPa stack pressure). The stresses diminish above the void because of the absence of Li/SSE contact, whereas stress concentration in the Li occurs near the void edges. Current focusing near the void edges during stripping leads to contact loss at the Li-SSE interface and void growth (Fig. 5, B and C). By contrast, a Na domain at the interface contacts both the SSE and Li, homogenizing the stress distribution with the Na domain under compressive stress (Fig. 5D). Because Na has a lower yield strength than that of Li (nanoindentation shows 54% lower hardness) (fig. S23) (*45*–*47*), the stress exerted on the Na domain by the surrounding Li can induce plastic deformation and creep along the interface as Li is stripped. The simulation shows that this causes Na to deform and extend along the SSE interface as Li is removed (Fig. 5, E and F), suppressing the formation of voids. From these results, we expect that it is the chemo-mechanical behavior of Na that enhances stripping behavior rather than a pure transport effect; density functional theory calculations showed that Li-Na interfaces exhibit lower diffusivity than do Li surfaces (fig. S24 and table S7).

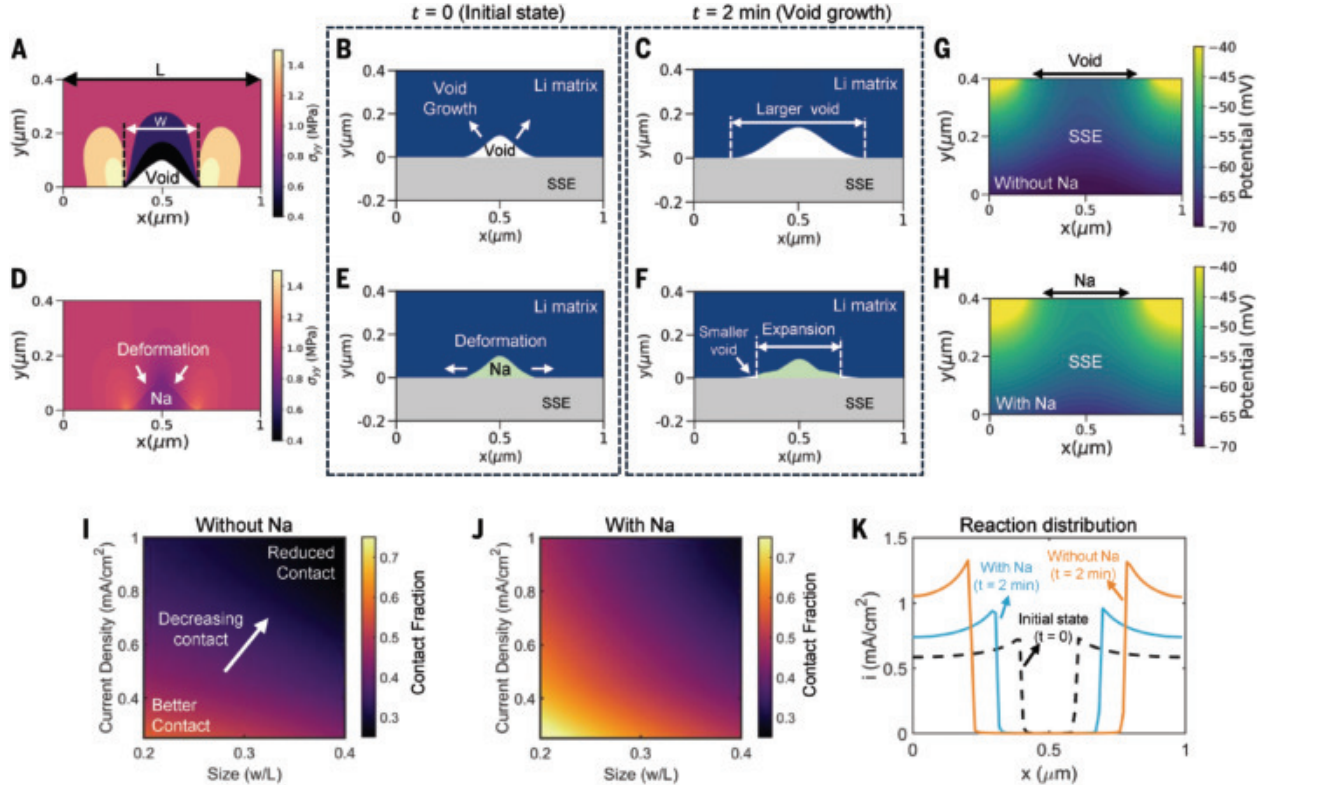

Fig. 5. Electro-chemo-mechanical modeling of the evolution of the SSE interface. (**A**) Normal stress along the *y* direction in Li metal with a void at the SSE interface. The void size $w/L = 0.3$ (where w is the void width and L is the model dimension). (**B** and **C**) Li-SSE interfacial evolution and void growth from time (B) $t = 0$ to (C) $t = 2$ min, with an applied current density (I_{App}) of 0.5 mA cm^{-2}. (**D**) Normal stress along the *y* direction in Li metal with Na at the SSE interface (Na size, $w/L = 0.3$). The other stress components are included in fig. S22. (**E** and **F**) Li-SSE interfacial evolution from time (E) $t = 0$ to (F) $t = 2$ min, when Na is present at the interface ($I_{App} = 0.5$ mA cm^{-2}). (**G** and **H**) Electric potential distribution in the SSE with (G) void and (H) Na at the Li-SSE interface. (**I** and **J**) Effects of current density and void or Na size on Li-SSE contact fraction with (I) void and (J) Na domain. (**K**) Reaction current density at the Li-SSE interface with and without Na at time $t = 0$ and $t = 2$ min. I_{App} is 0.5 mA cm^{-2}, and the void or Na domain size (w/L) is 0.2. The stack pressure applied in this model is 1 MPa. The mathematical formulation used for this model is described in supplementary text 7.

The electric potential distributions within the SSE after 2 min of stripping for both simulated cases are shown in Fig. 5, G and H, for an applied current density $I_{App} = 0.5$ mA cm^{-2}. The greater Li-SSE contact achieved with Na results in less current focusing at the interface (fig. S25) and a more uniform potential distribution in the SSE domain. The effect of void or Na domain size and applied current density on Li-SSE contact evolution at time (t) = 2 min is shown in Fig. 5, I and J. The reaction heterogeneity at the interface increases and Li-SSE contact decreases with an increase in applied current density. An increase in void or Na domain size also exacerbates current heterogeneity owing to the reduced Li-SSE interfacial contact. However, the action of Na in suppressing voids sustains higher interfacial contact fractions at higher current densities and domain sizes. The difference in Li-SSE contact evolution with and without Na is more pronounced for smaller voids because of the rapid growth of the void through Li surface diffusion. In Fig. 5K, we compare the reaction distribution for a void versus Na domain with $I_{App} = 0.5$ mA cm^{-2} in the initial state ($t = 0$ min) and after $t = 2$ min. Initially, the interfacial contact region for the void and Na are the same, resulting in an identical reaction current distribution (Fig. 5K). As the interface evolves over time, more contact loss and current focusing occurs near the void compared with Na. Overall, these simulation results show that the deformability of Na promotes dynamic interfacial contact in response to local chemo-mechanical stimuli, suppressing void formation as Na accumulates at the interface.

Conclusions

We have demonstrated the concept of interfacial morphogenesis applied to Li metal SSBs, in which interfacial properties are self-regulated across length scales in a multiphase electrode through global contact pattern formation promoted by local chemo-mechanical stimuli. Binary Li-Na electrodes show the capability to suppress void growth through accumulation of highly deformable Na domains at the SSE interface, enhancing Li stripping capacity and cycling at low stack pressures (<3.2 MPa). The electrochemical inertness of the Na phase with respect to active Li enables the Na to avoid the structural degradation often seen in Li-reactive metal alloy or carbon interlayers and composites (*25*, *29*). Additionally, binary alkali metal foils can be created and cold-rolled with simple metallurgical techniques, avoiding more complex processing (*6*, *23*, *24*, *26*). Overall, this study shows the promise of engineering Li metal electrodes with tailored chemo-mechanical properties to promote desired morphology evolution. To address the diverse demands of battery applications (such as in electric vehicles), it is essential to investigate the chemo-mechanical evolution of materials under varying conditions, such as different charging-discharging rates, temperatures, and charging modes (such as current pulsing) (*9*, *48*, *49*). Such investigations could enable multicomponent metal anodes to achieve enhanced performance metrics that would be attractive for practical applications.

REFERENCES AND NOTES

1. J. Janek, W. G. Zeier, *Nat. Energy* **8**, 230–240 (2023).
2. K. B. Hatzell *et al.*, *ACS Energy Lett.* **5**, 922–934 (2020).
3. B. S. Vishnugopi *et al.*, *ACS Energy Lett.* **6**, 3734–3749 (2021).
4. T. Krauskopf, F. H. Richter, W. G. Zeier, J. Janek, *Chem. Rev.* **120**, 7745–7794 (2020).
5. J. Kasemchainan *et al.*, *Nat. Mater.* **18**, 1105–1111 (2019).
6. V. Raj *et al.*, *Nat. Mater.* **21**, 1050–1056 (2022).
7. Y. Lu *et al.*, *Sci. Adv.* **8**, eadd0510 (2022).
8. J. A. Lewis *et al.*, *Nat. Mater.* **20**, 503–510 (2021).
9. M. J. Wang, R. Choudhury, J. Sakamoto, *Joule* **3**, 2165–2178 (2019).
10. X. Zhang, Q. J. Wang, K. L. Harrison, S. A. Roberts, S. J. Harris, *Cell Rep. Phys. Sci.* **1**, 100012 (2020).
11. H. Yan *et al.*, *Adv. Energy Mater.* **12**, 2102283 (2022).
12. B. S. Vishnugopi *et al.*, *Adv. Energy Mater.* **13**, 2203671 (2023).
13. A. Mistry, P. P. Mukherjee, *J. Electrochem. Soc.* **167**, 082510 (2020).
14. T. Krauskopf, H. Hartmann, W. G. Zeier, J. Janek, *ACS Appl. Mater. Interfaces* **11**, 14463–14477 (2019).
15. T. Jow, C. Liang, *J. Electrochem. Soc.* **130**, 737–740 (1983).
16. E. Dologlou, *Glass Phys. Chem.* **36**, 570–574 (2010).
17. M. J. Wang, E. Kazyak, N. P. Dasgupta, J. Sakamoto, *Joule* **5**, 1371–1390 (2021).
18. C. D. Fincher, D. Ojeda, Y. Zhang, G. M. Pharr, M. Pharr, *Acta Mater.* **186**, 215–222 (2020).
19. C. Xu, Z. Ahmad, A. Aryanfar, V. Viswanathan, J. R. Greer, *Proc. Natl. Acad. Sci. U.S.A.* **114**, 57–61 (2017).
20. P. Albertus *et al.*, *ACS Energy Lett.* **6**, 1399–1404 (2021).
21. J. Lee, T. Lee, K. Char, K. J. Kim, J. W. Choi, *Acc. Chem. Res.* **54**, 3390–3402 (2021).
22. T. Schmaltz *et al.*, *Adv. Energy Mater.* **13**, 2301886 (2023).
23. T. Fuchs *et al.*, *Adv. Energy Mater.* **12**, 2201125 (2022).
24. J. Aspinall *et al.*, *Nat. Commun.* **15**, 4511 (2024).
25. S. E. Sandoval *et al.*, *Joule* **7**, 2054–2073 (2023).
26. S. G. Yoon *et al.*, *ACS Nano* **18**, 20792–20805 (2024).
27. J. A. Lewis, K. A. Cavallaro, Y. Liu, M. T. McDowell, *Joule* **6**, 1418–1430 (2022).
28. W. J. Jeong *et al.*, *ACS Energy Lett.* **9**, 2554–2563 (2024).
29. S. Kim *et al.*, *ACS Energy Lett.* **8**, 9–20 (2022).
30. C. Collinet, T. Lecuit, *Nat. Rev. Mol. Cell Biol.* **22**, 245–265 (2021).
31. S. Mosleh, E. Annevelink, V. Viswanathan, L. Mahadevan, Controlling moving interfaces in solid state batteries. arXiv:2408.03175 [cond-mat.mtrl-sci] (2024).
32. C. Bale, *Bull. Alloy Phase Diagr.* **10**, 265–268 (1989).
33. S. Y. Kim, J. Li, *Energy Mater. Adv.* **2021**, 1519569 (2021).
34. Z.-X. Wang *et al.*, *Joule* **8**, 2794–2810 (2024).
35. H. Huo *et al.*, *Nat. Mater.* **23**, 543–551 (2024).
36. J. K. Eckhardt *et al.*, *Adv. Mater. Interfaces* **10**, 2202354 (2023).
37. J. K. Eckhardt *et al.*, *ACS Appl. Mater. Interfaces* **14**, 42757–42769 (2022).
38. J. Jamnik, J. Maier, S. Pejovnik, *Electrochim. Acta* **44**, 4139–4145 (1999).
39. R. A. Huggins, *Ionics* **8**, 300–313 (2002).
40. P. Pietsch, V. Wood, *Annu. Rev. Mater. Res.* **47**, 451–479 (2017).
41. Z. Ning *et al.*, *Nat. Mater.* **20**, 1121–1129 (2021).
42. J. Zhou *et al.*, *Nature* **627**, 301–305 (2024).
43. S. Ohno, C. Rosenbach, G. F. Dewald, J. Janek, W. G. Zeier, *Adv. Funct. Mater.* **31**, 2010620 (2021).
44. X. Hu *et al.*, *Nat. Rev. Mater.* **9**, 305–320 (2024).
45. C. D. Fincher, Y. Zhang, G. M. Pharr, M. Pharr, *ACS Appl. Energy Mater.* **3**, 1759–1767 (2020).
46. M. J. Wang, J.-Y. Chang, J. B. Wolfenstine, J. Sakamoto, *Materialia* **12**, 100792 (2020).
47. W. S. LePage, Y. Chen, A. Poli, M. Thouless, N. P. Dasgupta, *Extreme Mech. Lett.* **52**, 101644 (2022).
48. K. Lee, J. Sakamoto, *Adv. Energy Mater.* **14**, 2303571 (2024).
49. D. Spencer Jolly *et al.*, *ACS Appl. Mater. Interfaces* **13**, 22708–22716 (2021).

ACKNOWLEDGMENTS

Funding: Support is acknowledged from the Defense Advanced Research Projects Agency Morphogenic Interfaces (MINT) Program under cooperative agreement HR00112220028. The content of this article does not necessarily reflect the position of the policy of the government, and no official endorsement should be inferred. This work was performed in part at the Georgia Tech Institute for Matter and Systems, a member of the National Nanotechnology Coordinated Infrastructure (NNCI), which is supported by the National Science Foundation (ECCS-2025462). This research used resources of the Advanced Photon Source, a US Department of Energy (DOE) Office of Science user facility operated for the DOE Office of Science by Argonne National Laboratory under contract DE-AC02-06CH11357. V. Sundaresan is acknowledged for helpful discussions. **Author contributions:** Conceptualization: S.G.Y., M.T.M.; Methodology: S.G.Y., B.S.V., A.X.B.Y., M.T.M.; Formal analysis: S.G.Y., B.S.V., D.L.N., A.X.B.Y., S.E.S., P.S., A.S., J.R.G., E.E., P.P.M., M.T.M.; Investigation: S.G.Y., D.L.N., Y.W., S.E.S., T.A.T., K.A.C., P.S., E.P.A., C.W.; Validation: S.G.Y., J.R.G., E.E., M.T.M.; Visualization: S.G.Y., M.T.M.; Writing – original draft: S.G.Y.; Writing – review & editing: S.G.Y., J.R.G., E.E., P.P.M., M.T.M.; Supervision: M.T.M.; Funding acquisition: M.T.M.; Project administration: M.T.M. **Competing interests:** M.T.M. and S.G.Y. are inventors on US patent application 2024/0339624, which is related to the content in this article. All other authors declare no competing interests. **Data and materials availability:** All data associated with this paper can be found in the paper or the supplementary materials.

SUPPLEMENTARY MATERIALS

science.org/doi/10.1126/science.adt5229
Materials and Methods; Supplementary Text; Figs. S1 to S25; Tables S1 to S8; References (*50*–*100*); Data S1 and S2

Submitted 29 September 2024; accepted 7 April 2025

10.1126/science.adt5229

MARINE MICROBES

Oxygen intrusions sustain aerobic nitrite-oxidizing bacteria in anoxic marine zones

Pearse J. Buchanan[1,2]*, Xin Sun[1], J. L. Weissman[3,4,5], Daniel McCoy[1,6], Daniele Bianchi[6], Emily J. Zakem[1]

Anaerobic metabolisms are thought to dominate nitrogen cycling in anoxic marine zones (AMZs). However, thriving populations of aerobic nitrite-oxidizing bacteria (NOB) in AMZs challenge this assumption and remain unexplained. Using theory and modeling, we show how periodic oxygen intrusions sustain aerobic NOB in AMZs alongside more competitive aerobic heterotrophs. Ecological theory, supported by numerical simulations and genomics, frames NOB as opportunists exploiting a fleeting supply of oxygen. Consistent with in situ observations, simulated NOB contribute substantially to total oxygen consumption at AMZ boundaries, which implies that NOB may provide a major stabilizing feedback to AMZs. Fine-scale ocean currents increase the metabolic diversity in AMZs, which could stabilize AMZ volume under climate change.

Anoxic marine zones (AMZs) form in the Eastern Pacific and Northern Indian Oceans, where consumption of oxygen by respiring aerobic organisms exceeds oxygen supply. Anoxia generates a niche for anaerobic metabolisms central to nitrogen cycling and ocean-climate feedbacks. Anaerobic metabolisms remove bioavailable nitrogen, which proximally limits ocean primary productivity over half the ocean (*1*), and produce nitrous oxide (N_2O), a potent greenhouse gas and ozone depleter (*2*). As marine deoxygenation intensifies (*3*), AMZs and nitrogen loss may expand (*4*). However, our understanding of the biogeochemical consequences of this expansion remains limited, in part because recent observations have revealed ample rates of aerobic as well as anaerobic metabolisms in AMZs (*5*–*10*).

How AMZs respond to ocean deoxygenation is impacted by complex and poorly understood microbial ecology. It remains unclear how anaerobic denitrification ($NO_3^- \rightarrow NO_2^- \rightarrow NO \rightarrow N_2O \rightarrow N_2$) and anammox ($NH_4^+ + NO_2^- \rightarrow N_2$), which remove bioavailable nitrogen, co-occur alongside the aerobic metabolisms of ammonia oxidation ($NH_3 + O_2 \rightarrow NO_2^-$) and nitrite oxidation ($NO_2^- + O_2 \rightarrow NO_3^-$), the two steps of chemoautotrophic nitrification that remove oxygen (*9*–*14*). Nitrite-oxidizing bacteria (NOB) thrive in open ocean AMZs, displaying remarkably high biomass and activity in apparently anoxic waters (*12*, *15*–*20*). Ammonia-oxidizing archaea (AOA) are also active and abundant in low-oxygen waters, including the low-oxygen layers above anoxic layers, where their abundance can be 10-fold higher than that of NOB (*8*, *21*–*24*). However, AOA are typically less active than NOB in anoxic waters (*5*, *10*, *13*, *16*, *17*). The relative success of NOB in AMZs likely alters the rates of nitrogen loss and N_2O production (*8*, *10*, *25*, *26*), although the mechanism explaining their success is not yet clear. More fundamentally, the existence of thriving aerobic NOB in AMZs challenges our understanding of how diverse aerobic and anaerobic metabolisms coexist.

Multiple explanations for nitrification in AMZs have been proposed (*27*). The high oxygen affinities of both AOA and NOB suggest that these microbes can survive at nanomolar oxygen concentrations (*8*, *25*), although these chemoautotrophs are unlikely to outcompete facultatively aerobic heterotrophs for oxygen (*28*). Alternatively, certain clades of AOA and NOB may have evolved oxidation pathways by using electron acceptors other than oxygen (*11*, *12*, *27*, *29*). Others suggest that episodic oxygen supply to anoxic waters might be sufficient to sustain viable populations of nitrifiers (*8*, *9*, *14*, *30*). Although these hypotheses are not mutually exclusive, a sufficient explanation must also illuminate why AOA exhibit lower activity than NOB in anoxic waters (*5*, *10*, *13*, *16*, *17*). In this study, using ecological theory and modeling, we show that fleeting oxygen intrusions can explain the observations of active, thriving aerobic NOB in AMZs.

Results

Heterotrophs exclude aerobic nitrifiers in steady-state anoxia

A leading explanation for aerobic NOB within AMZs is their high affinity for oxygen (*8*, *25*). Previous theory has shown that aerobic and anaerobic metabolisms can coexist under steady-state anoxia with a cryptic oxygen supply, which is consistent with observations (*6*, *7*, *28*). However, empirical estimates show that chemoautotrophic nitrification demands more oxygen than aerobic heterotrophy (roughly three to four times) per mole of biomass synthesized (tables S1 and S2) (*31*, *32*). Consequently, aerobic nitrifiers are thought to be outcompeted by aerobic heterotrophs when both metabolisms are limited by oxygen (*28*). Nitrifiers could be alleviated from this competitive exclusion if heterotrophs were limited by organic substrates. Affinity, oxygen demand, other traits, and ecological factors all play a role in the competition for oxygen, together setting the subsistence concentrations of the microbial populations, which determine their competitive abilities (*32*).

We expanded a previous analysis (*28*) to assess the competitive outcomes of populations of the major microbial functional types within a virtual chemostat model representative of AMZ conditions (Fig. 1A and materials and methods). We incorporated a wider diversity of traits, accounting for differences in cell size, carbon quota, stoichiometry, maximum growth rate, biomass yields, and nutrient affinities (tables S1 and S2). We solved for the steady-state solutions across different ratios of oxygen and organic matter supply to generate an anoxic-oxic landscape (Fig. 1B).

Despite the diversity of traits considered, both nitrifying functional types (AOA and NOB) are consistently competitively excluded by facultatively aerobic heterotrophs when oxygen is limiting (Fig. 1C). The high affinity of AOA and NOB for oxygen (*8*, *9*, *25*) does enable growth at nanomolar oxygen concentrations (*10*, *17*, *18*) (table S3), but heterotrophs in general are the superior competitors across the plausible trait space because they have a lower oxygen demand for biomass synthesis (supplementary text, fig. S1, and table S2). The point at which heterotrophy transitions to perform anaerobic metabolism (denitrification in this case) occurs at oxygen concentrations that are less than the subsistence oxygen concentration required by AOA and NOB (table S3). When considering the enormous diversity of heterotrophic bacteria, we expect that nitrifiers may outcompete a subset of inefficient aerobic heterotrophs for oxygen, whereas other more efficient heterotrophs will consistently exclude nitrifiers when oxygen is limiting, at least under steady-state conditions.

Aerobic nitrifiers viable with oxygen intrusions to AMZs

The steady state can be considered as the climatological state of AMZs, set by the large-scale balance of physical supply and biological demand of oxygen. However, variability from fine-scale ocean currents sets the "weather" of the AMZs (*33*). These currents lead to

[1]Department of Global Ecology, Carnegie Institution for Science, Stanford, CA, USA. [2]CSIRO Environment, Hobart, Australia. [3]Department of Biology, The City College of New York, New York, NY, USA. [4]Department of Ecology and Evolution, Stony Brook University, Life Sciences Building, Stony Brook, NY, USA. [5]Institute for Advanced Computational Science, Stony Brook University, Stony Brook, NY, USA. [6]Department of Atmospheric and Oceanic Sciences, University of California, Los Angeles, Los Angeles, CA, USA. ***Corresponding author. Email: pearse.buchanan@csiro.au**

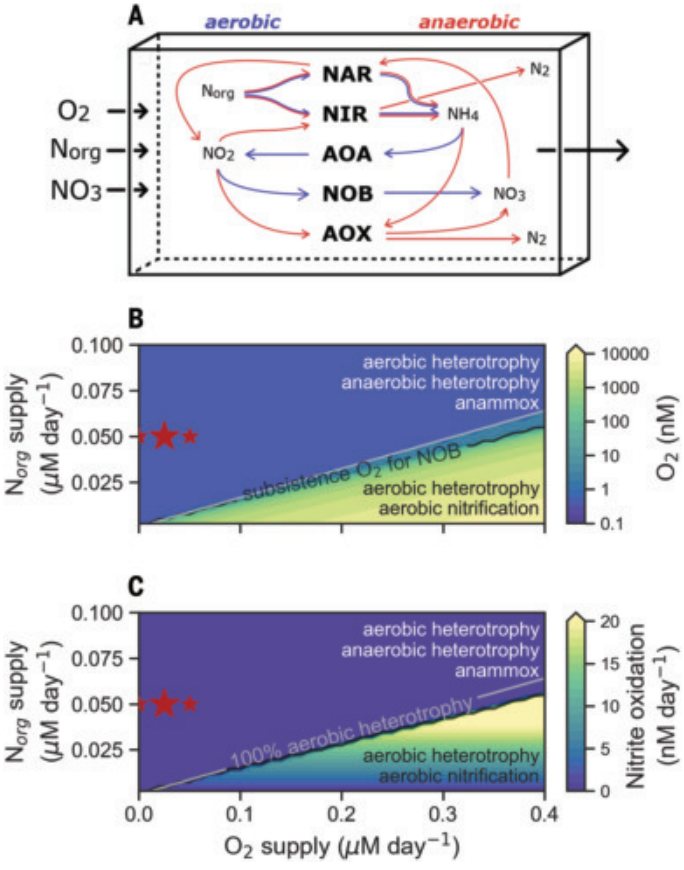

Fig. 1. Steady-state outcomes of the virtual chemostat model. (**A**) Schematic of the model. The chemostat (single-box model) contains aerobic and anaerobic metabolisms carried about by key microbes: facultative nitrate- and nitrite-reducing heterotrophs (NAR, nitrate reductase; and NIR, nitrite reductase), ammonia-oxidizing archaea (AOA), nitrite-oxidizing bacteria (NOB), and anammox bacteria (AOX). Traits and yields are detailed in tables S1 and S2. (**B**) Steady-state oxygen concentration as a function of different rates of organic nitrogen (N_{org}) and O_2 supply. (**C**) Rate of nitrite oxidation (nM day^{-1}). Silver contour marks where 100% of heterotrophy is aerobic [following Zakem *et al*. (*28*)]. Black contour is the subsistence O_2 concentration for NOB (table S3). Resulting active metabolisms in the anoxic and oxygenated regimes are listed. Red stars indicate the background (constant) N_{org} and O_2 supply rates used in the O_2 pulse experiments (large star shows the background rates for experiments presented in Fig. 2).

time-varying intrusions of oxygen (*34*). Phytoplankton in shallow AMZ waters may also supply oxygen locally (*6*). This oxygen supply results in "cryptic" oxygen cycling, inferred from nanomolar oxygen concentrations (*35*–*37*) alongside nonzero oxygen consumption rates (*7*, *9*). We next investigated how time-varying oxygen supply may allow NOB to thrive.

We modeled the biomass (B) of a microbial population as

$$\frac{dB}{dt} = (\mu - L)B \tag{1}$$

where the growth rate (μ) must balance the loss rate (L) for the population to be viable. In a time-varying environment, this balance can be achieved over time. Assuming that nitrifiers (AOA or NOB) are obligately aerobic, and neglecting limitation by micronutrients like iron (*38*), we consider oxygen intrusions to cause nitrifiers to switch from oxygen-limited growth (μ_{O_2}) to nitrogen-limited growth (μ_N) (Fig. 2A).

Following Litchman and Klausmier (*39*), we estimated the fraction of time, f, that nitrifiers must be released from oxygen-limited growth to sustain themselves in a low-oxygen environment (see derivation in materials and methods) as

$$f = \frac{L - \mu_{O_2}}{\mu_N - \mu_{O_2}} \tag{2}$$

where μ_{O_2} and μ_N are the oxygen- and nitrogen-limited growth rates, respectively, and L represents the integrated loss to predators, viral lysis, cell maintenance, and other mortality.

To simplify, we can assume μ_{O_2} is negligible when oxygen is inaccessible [ignoring potential anaerobic metabolism (*11*, *12*, *27*)]. Also, if the nitrogen resource (nitrite for NOB or ammonium for AOA) is abundant, then μ_N may approach the maximum growth rate (μ^{max}). With both assumptions,

$$f \approx \frac{L}{\mu^{max}} \tag{3}$$

and the fraction of time that oxygen does not limit growth is approximated by the ratio of the population's loss rate to maximum growth rate. If $L \ll \mu^{max}$, f approaches zero, implying viability in environments with infrequent oxygen intrusions.

This theory can explain the divergent activities of NOB and AOA in AMZs. It is typical for nitrite to accumulate and for ammonium to be depleted in AMZs (*12*, *30*). This difference in electron donor availability means that during an oxygen intrusion, AOA cannot maximize growth ($\mu_N < \mu^{max}$) and require more frequent oxygen intrusions to sustain a viable population (fig. S2). In addition, NOB may grow rapidly on the abundant nitrite pool.

Chemostat simulations with oxygen intrusions support theory

Next, we applied pulses of oxygen to the virtual chemostat model to examine whether the theory is borne out when considering the AMZ microbial ecosystem (Fig. 1A). We periodically increased the input of oxygen into the chemostat, widely varying both the intensity and the frequency of the pulses (materials and methods). We applied these pulses to background conditions (i.e., constant supply rates of organic matter and oxygen) that generate deep anoxia and exclude nitrifiers under steady state (red stars in Fig. 1). After an oxygen pulse, most experiments return to functional anoxia, containing ≈10 nM of oxygen when averaged in time (Fig. 2B, and fig. S3), roughly matching the subsistence oxygen concentration required to sustain a viable population of NOB (table S3). Even large oxygen pulses are rapidly consumed by the microbial community, returning the system to long periods of oxygen scarcity <10 nM (fig. S3).

As predicted, the episodic pulses sustain a population of obligately aerobic NOB in the model. Mean nitrite oxidation rates are substantially larger under anoxic regimes with fleeting oxygenation—reaching values as high as 500 nM day^{-1}—than they are under fully oxic or fully anoxic regimes (Fig. 2C). Peak NOB activity and biomass co-occur with f values close to the analytically derived f of Eq. 3 (dashed black line in Fig. 2, B to E), indicating that coexistence of aerobic NOB with anaerobic metabolisms is beneficial. In this case, f is an emergent property of the model (Fig. 2D), calculated as the time-averaged growth limitation by oxygen (0) or nitrogen (1). A resulting f near zero indicates persistent oxygen limitation, whereas f near one indicates fully oxygenated experiments with nitrogen limitation. This nitrogen limitation occurs because nitrite does not accumulate in the absence of heterotrophic nitrate reduction, even when ammonia oxidation is active. Thus, transient oxygenation maximizes the supply of both resources (Fig. 2E).

These results are qualitatively robust across widely varying values of maximum growth rate (μ^{max}) and conditions, including when μ^{max} of NOB is lower than that of heterotrophs and AOA (figs. S4 to S6). As Eq. 3 suggests, a lower μ^{max} for NOB increases the frequency or strength of the oxygen intrusions required to sustain the

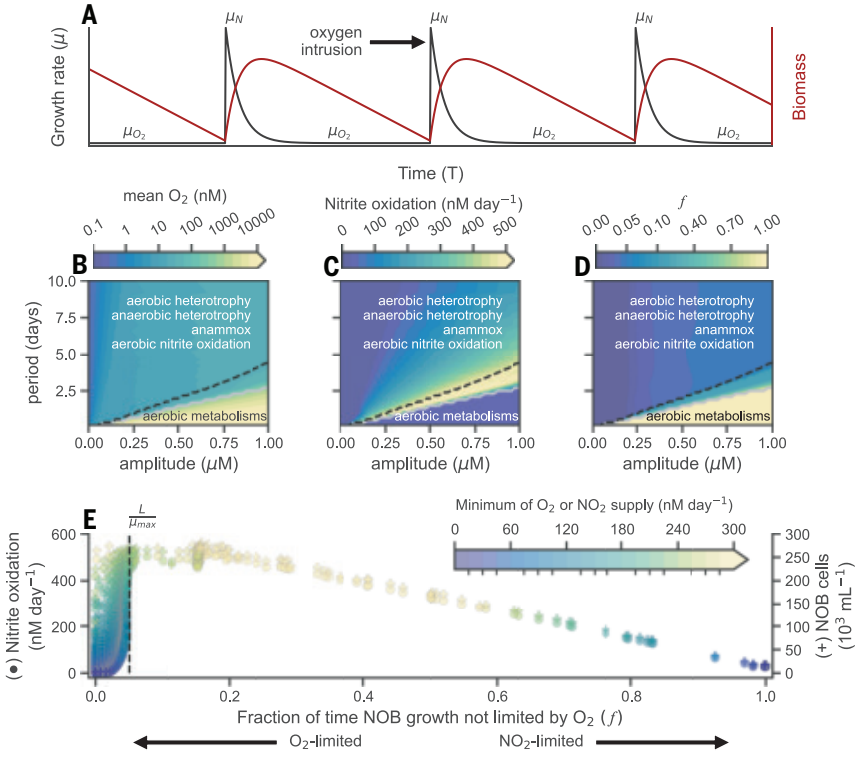

Fig. 2. Episodic oxygen pulses support aerobic nitrite oxidation in anoxic conditions. (**A**) Schematic of oxygen intrusions to an AMZ causing a shift from an oxygen-limited growth rate (μ_{O_2}) to a nitrogen-limited growth rate (μ_N) and rapid NOB biomass accumulation (red). (**B**) Average concentration of dissolved oxygen (O_2; nM) over last 100 days of chemostat experiments (run to dynamic equilibrium). O_2 pulses applied over a range of amplitudes and periods (inverse of frequency). Silver contour marks where 100% of heterotrophy is aerobic [$\phi = 1$, from Zakem *et al.* (*28*)]. Active metabolisms in the anoxic and oxygenated regimes are listed. (**C**) Average rate of nitrite oxidation in nM day^{-1}. (**D**) Fraction of time NOB released from oxygen limitation (f) in model. Black dashed line is analytically derived f, where $f \approx \frac{L}{\mu^{max}}$. (**E**) Relationship between f, the rate of nitrite oxidation (circles), and NOB abundance (pluses). Points are colored by the average rate of oxygen or nitrite supply, whichever is lowest (nM day^{-1}).

The model produces an AMZ offshore of the Peruvian upwelling, reaching a maximum vertical thickness of about 500 m, with nitrite accumulating. Because the model regularly generates mesoscale eddies of 10- to 100-km radii (*42*, *43*), oxygen intrusions are common at the boundaries of the simulated AMZ (Fig. 3A). As predicted by our theory, NOB biomass and activity peak where the supply of limiting resources—oxygen and nitrite—is maximized (Fig. 3b). NOB activity is particularly high at the upper AMZ boundary, where high rates of nitrate reduction, driven by a rich organic matter flux, coincide with more frequent oxygen intrusions (Fig. 3D). We provide animations of daily mean output in the supplementary materials.

Although AOA are active within the simulated AMZ, they do not thrive to the same extent as NOB (Fig. 3C). This captures the observed decoupling between AOA and NOB in oxygenated versus oxygen-depleted environments. In oxygenated environments, ammonia and nitrite oxidation rates are of similar magnitude, and estimated AOA:NOB abundance is of order 10:1 (*44*) (Fig. 3, E and F), as captured by the model (Fig. 3, G and H). By contrast, in oxygen-depleted waters, nitrite oxidation rates and NOB abundances are considerably higher in both data (*45*) and model.

Aerobic NOB may stabilize anoxia

NOB contribute substantially to the oxygen consumed at the boundaries of the AMZ (Fig. 4A and fig. S8). When integrated within the AMZ (oxygen <1 μM) and across simulations that vary the relative μ^{max} values of the microbial functional types (supplementary text, figs. S9 to S11, and tables S4 and S5), nitrite oxidation contributes 24 to 49% of total oxygen consumption (Fig. 4B). At individual locations, this contribution varies over a wider range (Fig. 4C): The modeled interquartile range of 0 to 66% is consistent with measured contributions of 0 to 69% (Fig. 4B and fig. S12). In the model, these location-specific contributions are low when total oxygen consumption is low (fig. S8). Because of this positive correlation, the integrated contribution exceeds the mean of the location-specific values. Thus, an empirical estimate of NOB's contribution to oxygen consumption across an AMZ likely requires weighting the mean of measured contributions at individual locations by the total oxygen consumption.

A consistent result of both the chemostat and 3D models is that aerobic NOB show increased biomass and activity when exposed to stronger and more frequent oxygen pulses, so long as anoxic conditions return. By consuming more oxygen with more biomass, NOB exert a negative feedback to increasing oxygen supply. This sustains the anaerobic niche, which also ensures nitrite supply through heterotrophic nitrate reduction (Fig. 4D). Thus, NOB may stabilize the size and intensity of AMZs and may do so in a highly responsive manner, because their growth is not typically limited by their electron donor, nitrite, which accumulates in AMZs (*12*, *30*). Heterotrophic bacteria and AOA cannot exploit an oxygen intrusion as rapidly as NOB if their growth is limited by organic matter and ammonium, respectively, which is thought to generally be the case (*46*–*48*), although this may differ in organic matter–rich environments (fig. S6). Overall, our results imply that if the oxygen supplied to AMZs declines as expected (*33*), NOB biomass and aerobic nitrite oxidation may also decline, which would in turn reduce biological oxygen demand. In this way, NOB may buffer oxygen perturbations to AMZs.

population, shifting f to higher values. Additionally, aerobic AOA is sustained at minimal rates owing to competition with anaerobic ammonium oxidation (anammox) for a limited supply of both ammonium and oxygen (fig. S7). Our sensitivity studies, however, indicate that under organic matter–rich conditions, faster-growing strains of AOA could theoretically replace slower-growing strains of NOB as the dominant oxygen consumers (fig. S6). Further experimental studies are required to determine whether this theoretical outcome is realized, perhaps nearby organic particles or in highly productive coastal areas.

Nitrite oxidizers in a three-dimensional (3D) model AMZ

We next investigated whether NOB thrive in AMZs with realistic ocean dynamics, where mesoscale eddies supply oxygen variably over space and time. We incorporated our microbial ecosystem model into an eddy-resolving, 3D model of the Eastern Tropical South Pacific, which contains one of the major AMZs of the world ocean. Specifically, we integrated the key heterotrophic and chemoautotrophic microbial functional types (Fig. 1A) into the biogeochemical elemental cycle (BEC) model (*40*), which was coupled online to the regional oceanic modeling system (ROMS) configured at an eddy-resolving (0.1° horizontal) resolution (*41*) (materials and methods). The model explicitly simulates the time-varying nature of oxygen intrusions within the emergent AMZ.

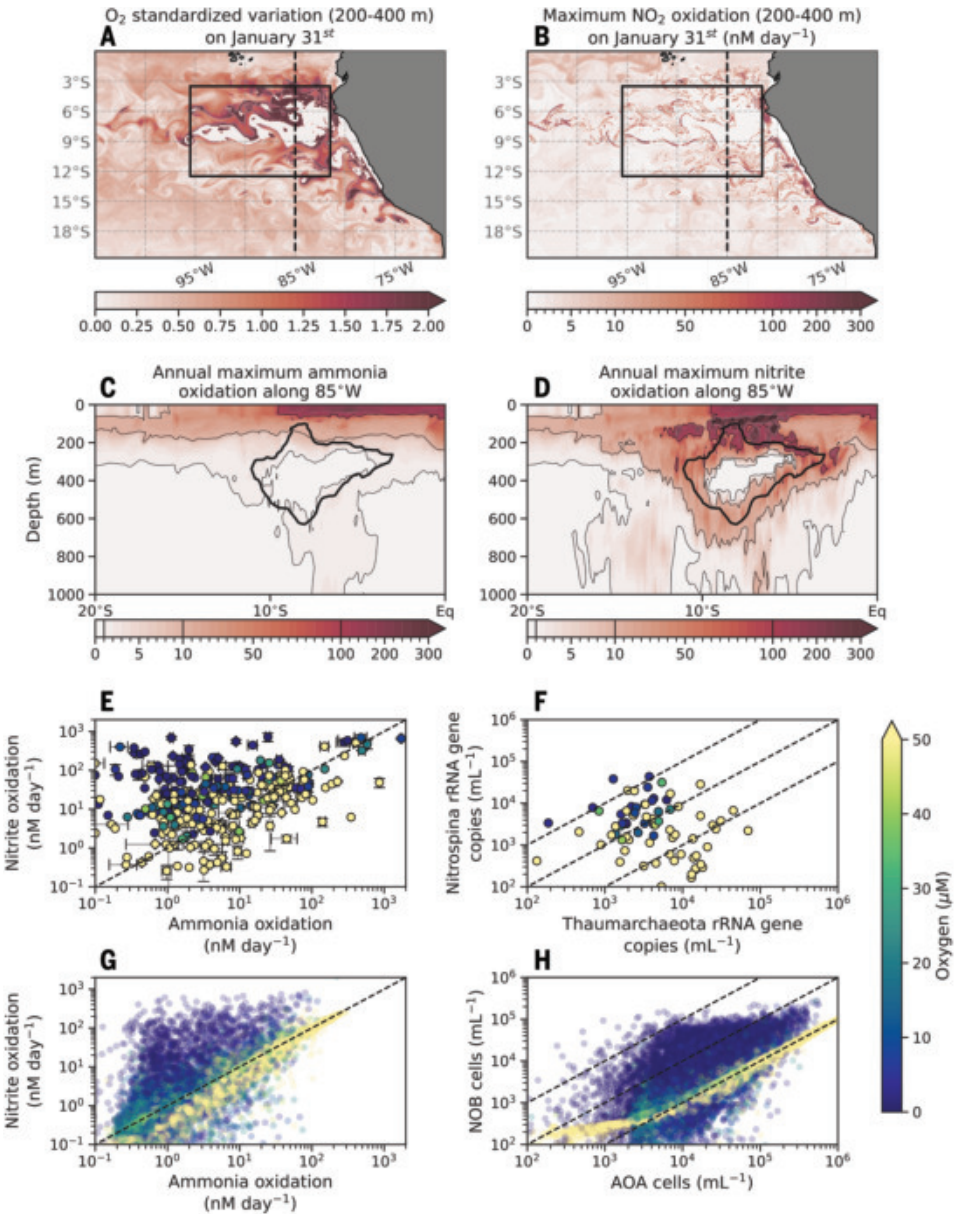

Fig. 3. AMZ nitrification dynamics in an eddy-resolving 3D ocean model. (**A**) Standardized variation (standard deviation divided by mean) in oxygen (O_2) between 200- and 400-m depth on a single day. (**B**) Maximum rate of nitrite oxidation between 200- and 400-m depth on the same day. Annual maximum values of (**C**) ammonia oxidation and (**D**) nitrite oxidation along 85°W [dashed line in (A) and (B)]. (**E**) Observed (*45*) and (**G**) modeled co-occurring rates of ammonia oxidation and nitrite oxidation, colored by in situ oxygen concentration. (**F**) Observed *Thaumarchaeota* (AOA) and *Nitrospina* (NOB) ribosomal RNA gene copies (*45*) and (**H**) modeled AOA and NOB cell-number estimates, calculated from carbon biomass by using measured cell carbon quotas of marine organisms (table S1 and materials and methods). Model data in (G) and (H) are from 2000 randomly sampled depth profiles (0 to 1000 m) within the box depicted in (A) and (B). Model statistics are generated from daily averages over the final simulation year.

Genome-based maximum growth rates support theory

Our results imply that the NOB inhabiting AMZs (*25*, *49*) survive because of an opportunistic "boom-and-bust" life-history strategy (*39*), "booming" when oxygen is available. Furthermore, Eq. 3 suggests that NOB are better adapted to AMZs when their maximum growth rates (μ^{max}) are higher. Thus, selection for faster growth to facilitate colonization deeper into AMZs, where oxygen intrusions are rarer (*50*), may leave discernable patterns of growth optimization on NOB genomes.

As a first test of this hypothesis, we applied codon usage bias statistics (*51*) to estimate μ^{max} from available metagenome-assembled genomes (MAGs) of marine NOB and other functional types (materials and methods and table S6). Codon usage bias in ribosomal proteins reflects a universal signature of optimization for rapid growth (*52*). It has been shown to accurately predict growth potential even when extrapolating across phyla (*51*). However, the limited training dataset for the algorithm is biased toward heterotrophic bacteria, so we updated the training dataset with measured μ^{max} from three AOA and six NOB species (fig. S13 and table S7) to improve the predictions.

The metagenome-based estimates of μ^{max} for NOB from AMZs, as well as from oxygenated environments, are higher than those of AOA and the available MAGs of heterotrophic bacteria extracted from AMZs (*Candidatus Pelagibacter*, a member of the ubiquitous SAR11 clade, known to grow slowly) (Fig. 5). Measurements from cultures (red markers in Fig. 5) also suggest higher μ^{max} for NOB than AOA. The genomic estimates lie at the high end of the measurements, in part because the estimates represent a theoretical maximum rate that may not be captured by laboratory conditions. That said, much uncertainty lies in the genomic estimates, although some confidence can be garnered from a previous clustering analysis (*51*) that identified a threshold delineating faster-growing copiotrophs, with more reliable estimates, from slower-growing oligotrophs (*39*). [This threshold depends on the assumed optimal growth temperature and is not subject to the 5-hour doubling time threshold presented in Weissman *et al*. (*51*) (materials and methods)]. Many NOB μ^{max} estimates appear near or above this threshold (black dashed line in Fig. 5). Acknowledging the uncertainties, we speculate that some NOB populations may be able to grow faster than AOA and *Pelagibacter* in AMZs and perhaps be considered as copiotrophs.

This analysis supports our hypothesis that opportunistic traits would benefit NOB clades in AMZs. However, we emphasize that our main conclusion—that periodic oxygen intrusions explain the success of NOB within AMZs—is not contingent on NOB having a high μ^{max} relative to other aerobic types.

Outlook and implications

Ocean-going studies have identified thriving populations of putatively aerobic NOB co-occurring with anaerobic metabolisms in all known major ocean AMZs (*10*–*14*, *19*, *20*, *49*), leading to numerous hypotheses

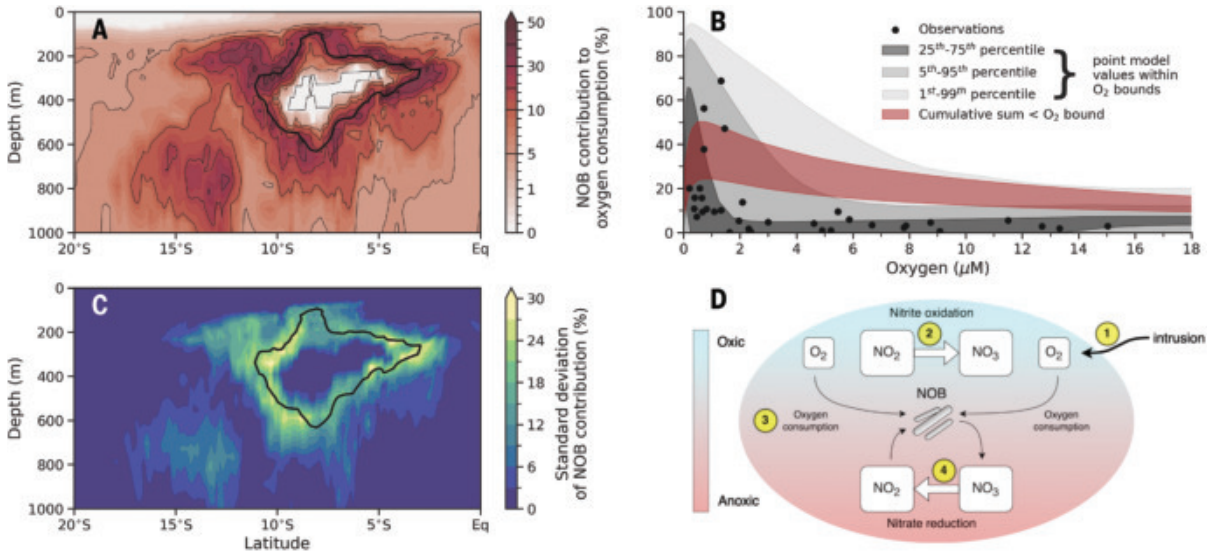

Fig. 4. NOB contribution to O_2 consumption and its stabilizing feedback to oxygen perturbations. (**A**) Annual average contribution of NOB to oxygen consumption along 85°W. The black line shows where annual mean $O_2 = 1$ μM. (**B**) Observed (*9*) and modeled NOB contribution to total O_2 consumption at different ambient O_2 concentrations. The modeled percentiles (gray shading) refer to the NOB contribution to O_2 consumption at individual locations and within discrete O_2 bounds and thus are directly comparable with the observations. The integrated contribution (red shading) is the total NOB contribution to O_2 consumption, cumulatively calculated less than an O_2 concentration. The range incorporates temporal variations and different assumptions of microbial maximum growth rates (materials and methods and supplementary text). (**C**) Temporal variability in the contribution of NOB to O_2 consumption. All model data are generated from daily averages over the final simulation year. (**D**) Schematic of the NOB feedback to perturbations in O_2 supply: O_2 intrusions (1) stimulate nitrite oxidation (2) and gains in NOB biomass, which in turn elevates O_2 consumption (3) and a more rapid return to anoxia, thereby supporting production of nitrite through anaerobic nitrate reduction (4), which maintains the ability to buffer O_2 intrusions.

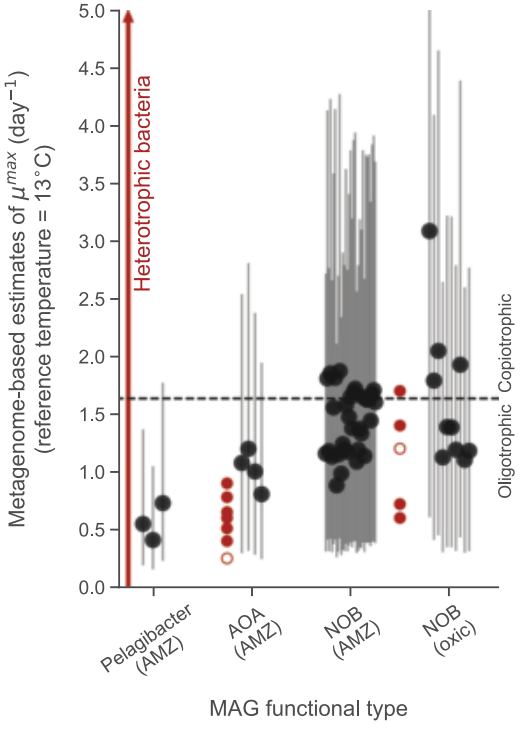

Fig. 5. Metagenome-based estimates of maximum growth rates of marine microbial functional types. Each black dot is the central μ^{max} estimate for an individual metagenome-assembled genome (MAG) obtained using codon usage bias statistics (*51*) for a reference temperature of 13°C. The vertical lines are 95% confidence intervals. MAG metadata are listed in table S6. The dashed line demarcates the threshold delineating oligotrophs from copiotrophs as well as the reliability of the estimates according to previous analysis (*51*). Filled red markers are measurements of μ^{max} from cultures of AOA and NOB (table S1). Empty red markers are in situ estimates (*24*). The vertical red arrow indicates the large range in μ^{max} for diverse heterotrophic bacteria (table S1).

to explain this counterintuitive phenomenon. Our theoretical framework suggests that AMZs prone to oxygen intrusions are ideal habitats for aerobic NOB. A "goldilocks" zone of oxygen and nitrite supply exists for NOB at the oxic-anoxic boundary (*26*), a boundary that is greatly expanded by considering the folding effect of eddies (e.g., Fig. 3A). At the shallow edge of AMZs, NOB may also access diurnally pulsed oxygen supply from phytoplankton (*6*). Whether it is biological or physical in origin, we propose that episodic oxygen supply is key to the vigorous cycling between nitrite and nitrate observed in marine AMZs (*12*, *15*–*19*). Although likely outcompeted by many heterotrophs in steady-state anoxia, NOB can sustain themselves by rapidly growing during oxygen intrusions, which offsets their losses during oxygen scarcity. We have provided initial genomic evidence that this "boom-bust" strategy has selected for opportunistic traits in marine NOB clades.

We have explained the elevated NOB activity and biomass in AMZs by assuming an obligate aerobic metabolism. Although growth through alternative electron acceptors (*11*, *12*, *27*) would be complementary, we argue that it is not essential where oxygen intrusions occur, even when rare. Anaerobic growth would, however, increase NOB viability, making NOB even less reliant on oxygen intrusions (fig. S14). Additionally, NOB may also reverse the nitrite oxidoreductase enzyme and perform heterotrophic nitrate reduction (*53*–*55*), generating the very nitrite they require for bursts of growth during an oxygen intrusion. These anaerobic metabolisms, if accessible, would further consolidate AMZs as optimal environments and allow colonization deeper into the AMZ core.

The time-varying circulation set by mesoscale eddies is critical for understanding the presence of aerobic NOB and aerobic metabolisms in general within AMZs. For the first time, we have explicitly resolved both the mesoscale and microbial populations that drive marine nitrogen cycling within a 3D simulated AMZ, allowing for the coexistence of aerobic NOB with anaerobic metabolisms. These in silico results corroborate in situ measurements of significant oxygen consumption by NOB (*9*) and also identify NOB as opportunistic stabilizers of anoxia, particularly at the AMZ boundaries. In this sense, NOB

may in fact stimulate nitrogen loss in AMZs, a view that challenges their proposed role as suppressors (*8*, *10*, *25*). However, whether NOB stimulate or suppress nitrogen loss—and whether they alter the balance of anammox to denitrification and thereby affect N_2O fluxes—will also depend on processes not well understood or resolved in this study, such as the full suite of denitrification modularity, the roles of obligately aerobic or anaerobic heterotrophic populations (*56*), and ecological interactions within particle microenvironments (*57*). These are grand challenges for our growing understanding of the nitrogen cycle. What is perhaps clearer is that the small-scale ocean circulation, the "weather" of the ocean, is essential to projections of AMZ volume and their biogeochemical implications, not only because it better represents the dynamics underpinning physical oxygen supply (*33*, *58*) but also the ecological dynamics governing oxygen demand.

REFERENCES AND NOTES

1. C. M. Moore, *Philos. Trans. R. Soc. London Ser. A* **374**, 20150290 (2016).
2. A. R. Ravishankara, J. S. Daniel, R. W. Portmann, *Science* **326**, 123–125 (2009).
3. N. L. Bindoff *et al.*, in *IPCC Special Report on the Ocean and Cryosphere in a Changing Climate*, H.-O. Portner *et al.*, Eds. (IPCC, 2019), pp. 447–588.
4. D. E. Canfield, A. N. Glazer, P. G. Falkowski, *Science* **330**, 192–196 (2010).
5. X. Peng *et al.*, *J. Geophys. Res. Oceans* **121**, 1667–1684 (2016).
6. E. Garcia-Robledo *et al.*, *Proc. Natl. Acad. Sci. U.S.A.* **114**, 8319–8324 (2017).
7. T. Kalvelage *et al.*, *PLOS ONE* **10**, e0133526 (2015).
8. L. A. Bristow *et al.*, *Proc. Natl. Acad. Sci. U.S.A.* **113**, 10601–10606 (2016).
9. J. M. Beman *et al.*, *Nat. Commun.* **12**, 7043 (2021).
10. J. Füssel *et al.*, *ISME J.* **6**, 1200–1209 (2012).
11. A. R. Babbin *et al.*, *Global Biogeochem. Cycles* **31**, 258–271 (2017).
12. A. R. Babbin, C. Buchwald, F. M. M. Morel, S. D. Wankel, B. B. Ward, *Mar. Chem.* **224**, 103814 (2020).
13. J. M. Beman, J. Leilei Shih, B. N. Popp, *ISME J.* **7**, 2192–2205 (2013).
14. C. Buchwald, A. E. Santoro, R. H. R. Stanley, K. L. Casciotti, *Global Biogeochem. Cycles* **29**, 2061–2081 (2015).
15. X. Sun, B. B. Ward, *ISME Commun.* **1**, 26 (2021).
16. X. Peng *et al.*, *Global Biogeochem. Cycles* **29**, 2034–2049 (2015).
17. A. E. Santoro *et al.*, *Global Biogeochem. Cycles* **35**, e2020GB006716 (2021).
18. C. A. Fuchsman, A. H. Devol, J. K. Saunders, C. McKay, G. Rocap, *Front. Microbiol.* **8**, 2384 (2017).
19. N. Evans, J. Tichota, J. W. Moffett, A. H. Devol, *Limnol. Oceanogr.* **68**, 1719–1733 (2023).
20. S. G. Fortin, X. Sun, A. Jayakumar, B. B. Ward, *ISME J.* **18**, wrae160 (2024).
21. S. E. Newell, A. R. Babbin, A. Jayakumar, B. B. Ward, *Global Biogeochem. Cycles* **25**, GB4016 (2011).
22. X. Peng, A. Jayakumar, B. B. Ward, *Front. Microbiol.* **4**, 177 (2013).
23. M. J. Beman, B. N. Popp, S. E. Alford, *Limnol. Oceanogr.* **57**, 711–726 (2012).
24. K. Kitzinger *et al.*, *Nat. Commun.* **11**, 767 (2020).
25. X. Sun, C. Frey, E. Garcia-Robledo, A. Jayakumar, B. B. Ward, *ISME J.* **15**, 1317–1329 (2021).
26. J. J. Anderson, A. Okubo, A. S. Robbins, F. A. Richards, *Deep-Sea Res. A: Oceanogr. Res. Pap.* **29**, 1113–1140 (1982).
27. X. Sun, C. Frey, B. B. Ward, *Global Biogeochem. Cycles* **37**, e2022GB007548 (2023).
28. E. J. Zakem, A. Mahadevan, J. M. Lauderdale, M. J. Follows, *ISME J.* **14**, 288–301 (2020).
29. B. Kraft *et al.*, *Science* **375**, 97–100 (2022).
30. T. Kalvelage *et al.*, *Nat. Geosci.* **6**, 228–234 (2013).
31. D. Tilman, S. S. Kilham, P. Kilham, *Annu. Rev. Ecol. Syst.* **13**, 349–372 (1982).
32. E. J. Zakem, M. J. Follows, *Limnol. Oceanogr.* **62**, 795–805 (2017).
33. M. Lévy, L. Resplandy, J. B. Palter, D. Couespel, Z. Lachkar, in *Ocean Mixing: Drivers, Mechanisms and Impacts*, A. C. Naveira-Garabato, M. P. Meredith, Eds. (Elsevier, 2022), pp. 329–342.
34. A. Margolskee, H. Frenzel, S. Emerson, C. Deutsch, *Global Biogeochem. Cycles* **33**, 875–890 (2019).
35. B. Thamdrup, T. Dalsgaard, N. P. Revsbech, *Deep Sea Res. Part I Oceanogr. Res. Pap.* **65**, 36–45 (2012).
36. L. Tiano *et al.*, *Deep Sea Res. Part I Oceanogr. Res. Pap.* **94**, 173–183 (2014).
37. L. A. Bristow *et al.*, *Nat. Geosci.* **10**, 24–29 (2017).
38. R. T. Shafiee, J. T. Snow, Q. Zhang, R. E. M. Rickaby, *ISME J.* **13**, 2295–2305 (2019).
39. E. Litchman, C. A. Klausmeier, *Am. Nat.* **157**, 170–187 (2001).
40. J. K. Moore, S. C. Doney, K. Lindsay, *Global Biogeochem. Cycles* **18**, GB4028 (2004).
41. D. McCoy, P. Damien, D. Clements, S. Yang, D. Bianchi, *Global Biogeochem. Cycles* **37**, e2022GB007670 (2023).
42. D. B. Chelton, M. G. Schlax, R. M. Samelson, *Prog. Oceanogr.* **91**, 167–216 (2011).
43. A. Chaigneau, M. Le Texier, G. Eldin, C. Grados, O. Pizarro, *J. Geophys. Res. Oceans* **116**, C11025 (2011).
44. E. J. Zakem *et al.*, *Biogeosciences* **19**, 5401–5418 (2022).
45. W. Tang *et al.*, *Earth Syst. Sci. Data* **15**, 5039–5077 (2023).
46. A. R. Babbin, R. G. Keil, A. H. Devol, B. B. Ward, *Science* **344**, 406–408 (2014).
47. B. B. Ward *et al.*, *Deep Sea Res. Part I Oceanogr. Res. Pap.* **55**, 1672–1683 (2008).
48. R. LaBrie *et al.*, *Sci. Adv.* **8**, eabn0035 (2022).
49. X. Sun *et al.*, *ISME J.* **13**, 2391–2402 (2019).
50. J. Kwiecinski, A. R. Babbin, *Global Biogeochem. Cycles* **35**, e2021GB007001 (2021).
51. J. L. Weissman, S. Hou, J. A. Fuhrman, *Proc. Natl. Acad. Sci. U.S.A.* **118**, e2016810118 (2021).
52. S. Vieira-Silva, E. P. C. Rocha, *PLOS Genet.* **6**, e1000808 (2010).
53. S. Lücker, B. Nowka, T. Rattei, E. Spieck, H. Daims, *Front. Microbiol.* **4**, 27 (2013).
54. J. Füssel *et al.*, *Sci. Adv.* **3**, e1700807 (2017).
55. T. M. Chicano *et al.*, *Nat. Microbiol.* **6**, 1129–1139 (2021).
56. M. M. M. Kuypers, H. K. Marchant, B. Kartal, *Nat. Rev. Microbiol.* **16**, 263–276 (2018).
57. D. Bianchi, T. S. Weber, R. Kiko, C. Deutsch, *Nat. Geosci.* **11**, 263–268 (2018).
58. J. J. M. Busecke, L. Resplandy, J. P. Dunne, *Geophys. Res. Lett.* **46**, 6716–6725 (2019).
59. P. J. Buchanan, Scripts, figures and output for "Oxygen intrusions sustain aerobic nitrite oxidation in anoxic marine zones" by Pearse J. Buchanan & colleagues, Version v2, Zenodo (2025); https://doi.org/10.5281/zenodo.15139307.
60. P. J. Buchanan, E. J. Zakem, pearseb/microbial_chemostat_model: v2022.08.0, Version v2022.08.0, Zenodo (2025); https://doi.org/10.5281/zenodo.15137671.
61. P. J. Buchanan, pearseb/BEC2-microbes: BEC2-microbes code, Version v2023.10.0, Zenodo (2025); https://doi.org/10.5281/zenodo.15137773.
62. P. J. Buchanan, pearseb/Oxygen_intrusions_NOB_ROMS_analysis: v2024.09.0, Version v2024.09.0, Zenodo (2025); https://doi.org/10.5281/zenodo.15139207.

ACKNOWLEDGMENTS

We thank C. Fuchsman, M. Beman, S. Fortin, and B. Ward for sharing data, and E. Litchman, C. Klausmier, and A. Tagliabue for discussions. Simulations with the 3D ocean model were run on the Expanse system at the San Diego Supercomputer Center. The authors wish to acknowledge use of the Ferret program (https://ferret.pmel.noaa.gov/Ferret/), Climate Data Operators (https://code.mpimet.mpg.de/projects/cdo/), NetCDF Operators (https://nco.sourceforge.net/), Python (https://www.python.org/), and GIMP (https://www.gimp.org/) for the analysis and graphics in this paper. **Funding:** This research was supported by the Simons Foundation postdoctoral fellowship in Marine Microbial Ecology (X.S.), NSF grant OCE-1847687 (D.M., D.B.), NSF grant 2125142 (E.J.Z.), Advanced Cyberinfrastructure Coordination Ecosystem: Services & Support (ACCESS) program allocations TG-OCE170017 (D.M., D.B.) and EES220053 (P.J.B., E. J. Z.), which are supported by NSF grants 2138259, 2138286, 2138307, 2137603, and 2138296. **Author contributions:** Conceptualization: P.J.B., E.J.Z.; Data curation: P.J.B., X.S.; Formal analysis: P.J.B., J.L.W.; Funding acquisition: E.J.Z., D.B.; Investigation: P.J.B., X.S., E.J.Z.; Methodology: P.J.B., E.J.Z., J.L.W., D.M.; Project administration: E.J.Z.; Resources: E.J.Z., D.B., J.L.W., X.S.; Software: P.J.B., E.J.Z., D.M., D.B., J.L.W.; Supervision: E.J.Z., D.B.; Validation: P.J.B., E.J.Z.; Visualization: P.J.B., J.L.W.; Writing – original draft: P.J.B., E.J.Z.; Writing – reviewing & editing: P.J.B., E.J.Z., X.S., D.M., D.B., J.L.W. **Competing interests:** The authors declare that they have no competing interests. **Data and materials availability:** All data and code are freely available. The chemostat model, model output, data, and scripts to reproduce the figures can be downloaded at Zenodo (*59*). The code for the chemostat model is housed at https://github.com/pearseb/microbial_chemostat_model and archived at Zenodo (*60*). The source code and the developments made to the ROMS-BEC2 ocean-biogeochemical ocean model is maintained at https://github.com/pearseb/BEC2-microbes and archived at Zenodo (*61*) and analysis of ROMS-BEC2 output is held at https://github.com/pearseb/Oxygen_intrusions_NOB_ROMS_analysis and archived at Zenodo (*62*).

SUPPLEMENTARY MATERIALS

science.org/doi/10.1126/science.ado0742
Materials and Methods; Supplementary Text; Figs. S1 to S14; Tables S1 to S8; References (*63*–*111*); Movies S1 to S9

Submitted 16 January 2024; accepted 9 April 2025

10.1126/science.ado0742

CONSERVATION

Dehorning reduces rhino poaching

Timothy Kuiper[1,2]*, Sharon Haussmann[3], Steven Whitfield[4], Daniel Polakow[5,6], Cathy Dreyer[4], Sam Ferreira[4], Markus Hofmeyr[7], Jo Shaw[8], Jed Bird[9], Mark Bourn[10], Wayne Boyd[11], Zianca Greeff[3], Zala Hartman[3], Kim Lester[12], Ian Nowak[13], Iain Olivier[12], Edwin Pierce[14], Colin Rowles[15], Sandra Snelling[4], Martin van Tonder[16], Ellery Worth[17], Hannes Zowitsky[18], E. J. Milner-Gulland[19], Res Altwegg[2]

Across 11 southern African reserves protecting the world's largest rhino population, we documented the poaching of 1985 rhinos (2017–2023, ~6.5% of the population annually) despite approximately USD 74 million spent on antipoaching. Most investment focused on reactive law enforcement—rangers, tracking dogs, access controls, and detection cameras—which helped achieve >700 poacher arrests. Yet we found no statistical evidence that these interventions reduced poaching (horn demand, wealth inequality, embedded criminal syndicates, and corruption likely combine to drive even high-risk poaching). By contrast, reducing poacher reward through dehorning (2284 rhinos across eight reserves) achieved large (~78%) and abrupt reductions in poaching using 1.2% of the budget. Some poaching of dehorned rhinos continued because poachers targeted horn stumps and regrowth, signaling the need for regular dehorning alongside judicious use of law enforcement.

Despite decades of conservation efforts, poaching for international trade continues to threaten the existence of the world's five rhinoceros species (*1*, *2*) while also reducing tourism revenues (*3*), entrenching criminal syndicates (*4*), threatening ecosystem function (*5*), and leading to loss of human life due to violent contacts between rangers and poachers (*6*). In the Greater Kruger ecosystem of southern Africa [a critical global stronghold that protected 27% of all of Africa's rhinos in 2017; (*2*)], we documented the poaching of 1985 rhinos between 2017 and 2023 (Fig. 1). This has rapidly reduced both black rhino (*Diceros bicornis*) and white rhino (*Ceratotherium simum*) populations (*1*, *7*, *8*). Poaching has persisted despite the investment of approximately USD 74 million in diverse antipoaching interventions (Figs. 2 and 3B). Political instability, local poverty, police criminality, an ineffective justice system (with poachers often let out on bail), and involvement of conservation staff with criminal syndicates have enabled wildlife crime to thrive in the region (*4*, *9*).

Rethinking strategies to tackle the poaching of high-value wildlife

In his seminal work in the 1950s, Becker argued that crime can be reduced by increasing the probability (e.g., more police patrols) or the severity (e.g., longer prison sentences) of punishment (*10*). Researchers of wildlife poaching and trade have since applied this thinking to model poacher behavior as a function of both the risks and the costs and benefits of poaching behavior (*11*, *12*). Further evidence in behavioral economics suggests that the certainty of the cost or benefit has a strong influence on human decision-making in general (*13*, *14*).

Globally, as in our study area, efforts to combat the illegal wildlife trade have for decades focused on increasing the risk of incurring a penalty, through law enforcement measures such as militarized ranger patrols and advanced surveillance technologies [(*15*–*17*); Fig. 2]. Yet consumer demand and local poverty create financial incentives for poaching despite high risk (*9*, *18*, *19*). Also, corruption allows criminal poaching syndicates to circumvent detection and arrest through inside information on ranger and camera deployments [(*4*, *20*); Fig. 2]. Furthermore, ineffective criminal justice systems dampen the deterrence value of the penalty because sentences are seldom swift, fair, and certain (*21*). Finally, raising the likelihood of detecting and arresting poachers—through measures such as additional cameras, rangers, helicopters, and dogs—may be prohibitively expensive to implement at a scale and intensity large enough to substantially deter poacher behavior across vast wildlife areas like those analyzed in our study [(*10*, *12*); Fig. 3D]. In summary, the overall expected cost to poachers (risk times penalty) achievable through law enforcement is hindered by several contingencies and extenuating factors and is therefore often too low to substantially deter poaching.

Given these complexities, rhino custodians across Africa and Asia are increasingly turning to proactive dehorning of rhinos as an entirely different approach to poaching deterrence: reducing rewards. The staggered implementation of dehorning across eight of our study reserves and over 7 years (2284 rhinos dehorned) has provided a distinctive opportunity to empirically evaluate the effectiveness of this approach. Based on the theoretical work and contextual factors referenced above, we predicted that the large, direct, and unambiguous reduction in expected reward created by dehorning would exert a stronger influence on poacher behavior in our study area than the less direct, less certain, and more contingent increases in expected penalty achievable through law enforcement interventions (Fig. 2).

Evaluating the effectiveness of antipoaching interventions

We used quarterly data collected over 7 years (2017–2023) from 11 wildlife reserves in the Greater Kruger ecosystem to measure the effectiveness of rhino dehorning alongside traditional law enforcement interventions (antipoaching rangers, fences, security control rooms, tracking dogs, detection cameras, and others; see Fig. 2). Our unit of analysis was the poaching rate and intervention intensity per reserve per year quarter (Fig. 1). Data were combined for black and white rhino species (black rhinos constituted ~8% of the total rhino population, and poaching and dehorning rates were similar by species). The interventions were applied as part of ongoing management rather than a controlled experiment. To reduce uncertainty in the attribution of changes in poaching to specific interventions in a complex system without experimental controls, we took an interdisciplinary approach that combined correlative and quasi-experimental quantitative models with structured qualitative attribution methods from policy program evaluation (*22*, *23*).

First, we built a baseline all-intervention model to test for empirical associations between poaching rates and the intensity of implementation of 11 antipoaching interventions (Fig. 1B). We used process tracing (through interviews with reserve managers and intervention experts) to map out the causal pathways for each intervention and then tested these against our quantitative data (Fig. 2 and fig. S1). We used a

[1]Department of Conservation Management, Nelson Mandela University, George, South Africa. [2]Centre for Statistics in Ecology, Environment, and Conservation, University of Cape Town, Cape Town, South Africa. [3]Greater Kruger Environmental Protection Foundation, Hoedspruit, South Africa. [4]South African National Parks, Skukuza, South Africa. [5]Departments of Statistics and Actuarial Science, University of Stellenbosch, Stellenbosch, South Africa. [6]School of Actuarial Science, University of Cape Town, Cape Town, South Africa. [7]Rhino Recovery Fund, Wildlife Conservation Network, San Francisco, CA, USA. [8]Save the Rhino International, London, UK. [9]Sabie Game Reserve, Skukuza, South Africa. [10]Manyeleti Provincial Nature Reserve, Hoedspruit, South Africa. [11]Mala Mala Game Reserve, Skukuza, South Africa. [12]Sabi Sand Nature Reserve, Skukuza, South Africa. [13]Balule Nature Reserve, Hoedspruit, South Africa. [14]Timbavati Private Nature Reserve, Hoedspruit, South Africa. [15]Klaserie Private Nature Reserve, Hoedspruit, South Africa. [16]Umbabat Private Nature Reserve, Hoedspruit, South Africa. [17]Karingani Private Nature Reserve, Chicuane, Mozambique. [18]Thornybush Private Nature Reserve, Hoedspruit, South Africa. [19]Department of Biology, University of Oxford, Oxford, UK. ***Corresponding author. Email: timothykuiper@gmail.com**

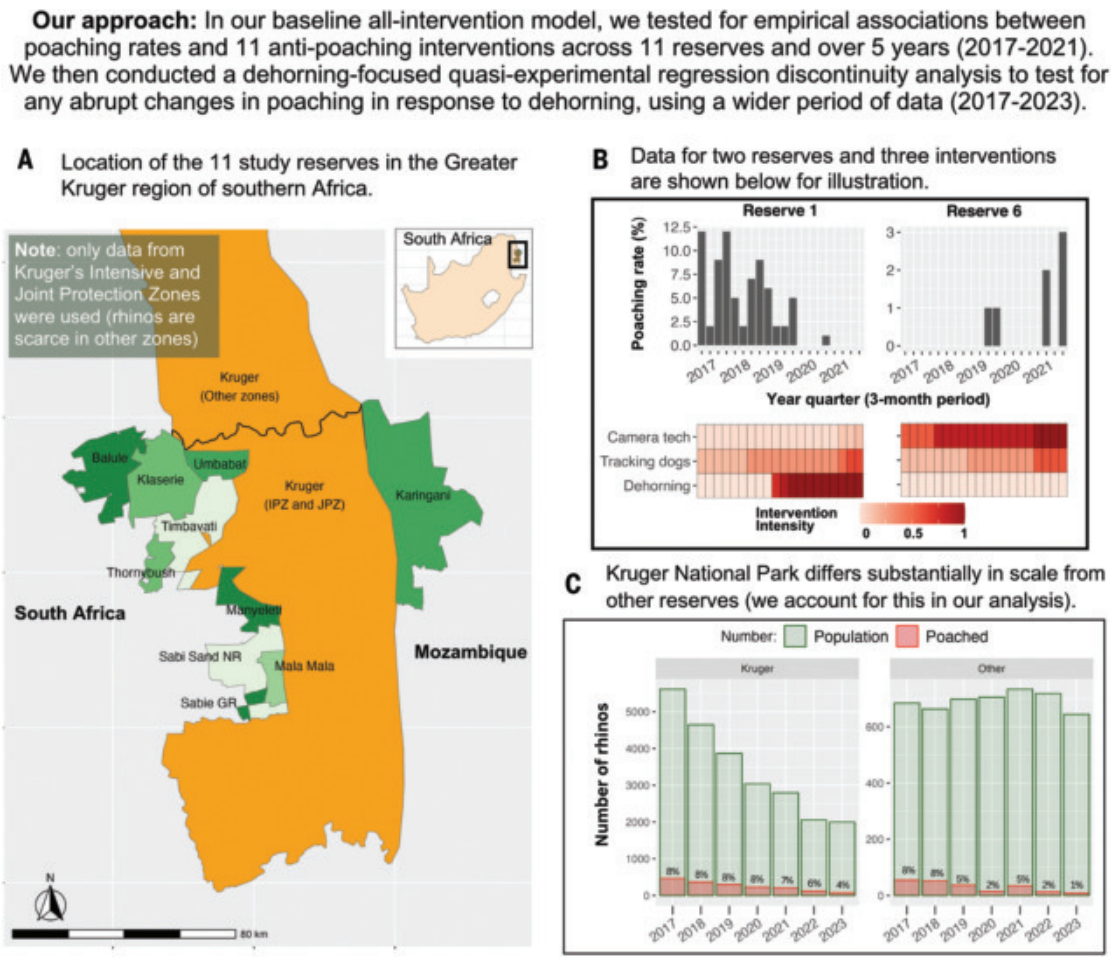

Fig. 1. Overview of study area and analysis. (**A**) We collated detailed quarterly data on poaching and interventions for 11 reserves from 2017 to 2021 (shades of green are used to distinguish the reserves visually). For Kruger NP (orange), we included data from the Intensive and Joint Protection Zones, outside of which rhinos are scarce (IPZ and JPZ, respectively). The system has outer fences, but there is free movement of rhinos between reserves. The state manages Kruger NP and Manyeleti Game Reserve (GR), whereas the other nine reserves are privately managed. Mozambique borders Kruger NP in the east. Given the distinctive size and context of Kruger NP, we conducted analyses with and without Kruger NP (see materials and methods). NR, Nature Reserve. (**B**) Poaching rates and the intensity of interventions varied across the reserves. (**C**) Kruger NP experienced large rhino population declines over the study period in contrast to stable populations on aggregate in the other 10 reserves, despite similar poaching levels in earlier years.

hierarchical Bayesian regression model with reserve and year random effects and model selection performed through regularization to account for multiple testing (see materials and methods). Next, we quantified evidence for intermediate steps along hypothesized pathways, such as the number of poachers arrested using tracking dogs. Finally, we used contribution analysis through structured results workshops to further appraise the empirical support for intervention pathways and to interrogate how and under which conditions interventions worked or did not work as intended (*23*). See materials and methods for full details.

Second, we built a dehorning-focused model to strengthen causal inference for our main intervention of interest. Although several tests confirmed no significant temporal or spatial autocorrelation in our all-intervention model residuals (figs. S3 to S8), this model was limited by the nonrandom application of multiple interventions that overlapped inconsistently in space and time. By contrast, seven reserves implemented dehorning abruptly (dehorning almost all rhinos present within 1 to 2 months; fig. S11) and in a staggered fashion (two reserves in early 2019, two in late 2019, and three in mid-2022). This provided good spatial and temporal contrast, allowing us to conduct a quasi-experimental regression discontinuity in time analysis to test for abrupt changes in poaching in response to dehorning (*24*–*26*). Staggering of dehorning by site provided multiple replicates of potential discontinuity, helping us to separate dehorning effects from potential confounders [as in (*25*)]. To account for pre-dehorning trends in poaching, our model included terms to measure immediate changes in poaching related to dehorning, as well as any change in the average poaching trend [see (*26*) and Fig. 4B]. We also confirmed that none of the other interventions changed abruptly around the point of dehorning (fig. S9).

Finally, we computed the relative risk of poaching faced by dehorned versus horned individuals at the landscape level and individual rhino level, as well as an estimate of the cost per rhino saved from poaching (see materials and methods and Fig. 5). Dehorning was conducted by a specialized veterinarian and an operational team and involved sedation of the rhino and painless removal of both horns above the growth plate using a chainsaw, followed by an antidote to sedation. Maintenance dehorning was carried out such that all rhinos were repeatedly dehorned at ~18-month intervals, owing to the rate of horn regrowth (fig. S11). Research, though nascent, suggests limited effects of dehorning on rhino ecology, behavior, and reproduction (*27*–*30*).

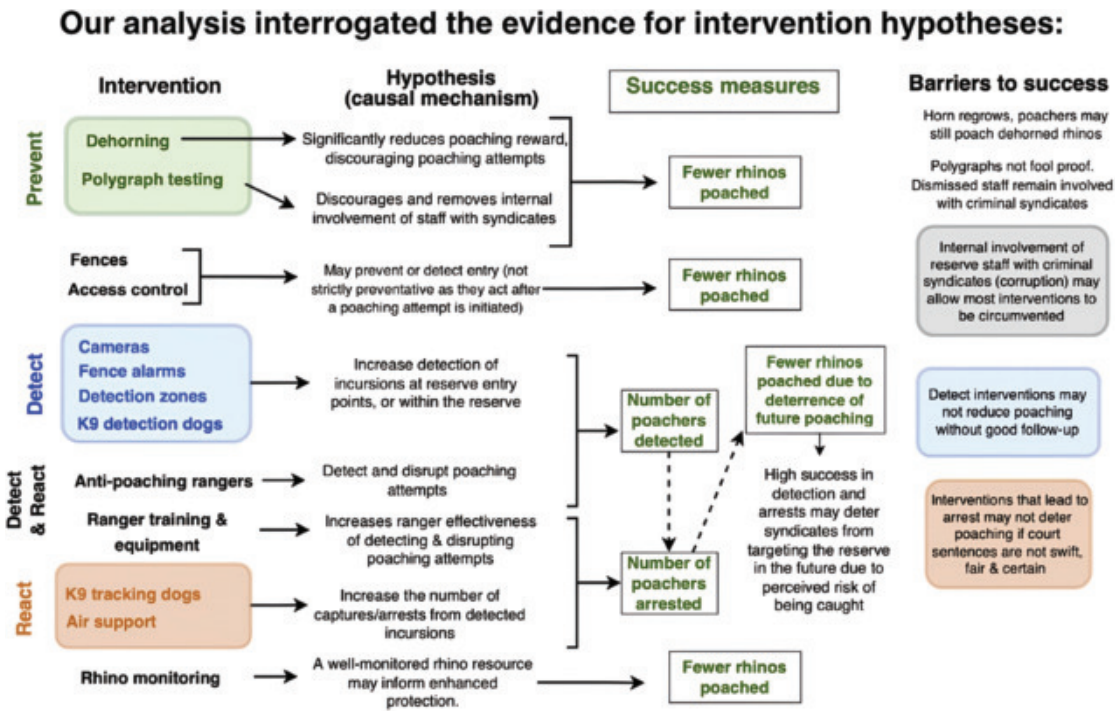

Fig. 2. Hypothesized causal pathways as to how the different categories of interventions act to reduce rhino poaching, including potential barriers to success. This conceptual model was developed from workshops and interviews with reserve managers and other experts. The statistical model served to test the strength of evidence for these hypotheses. Interventions were classed into three groups based on their approach: (i) "Preventative interventions" are designed to stop poaching incursions before they happen, (ii) "detect interventions" are designed to detect poacher incursions into a reserve, and (iii) "react interventions" are designed to react to detected incursions and help track, capture, and arrest poachers.

Results

Intervention implementation and cost

Across the 11 Greater Kruger reserves between 2017 and 2023, the horns of 2284 rhinos were proactively removed (dehorning), 671 cameras of seven different types were installed to detect poachers, 5562 polygraph tests were conducted (with 129 staff dismissed after the failure of a test), 45 detection dogs were deployed at reserve access points, 47 tracking dogs were deployed within reserves, 1150 km of detection zones were maintained and checked (roads or rivers checked for poacher footprints), and more than 500 antipoaching rangers were deployed at any given time.

To illustrate the complex environment in which interventions are implemented, and the strategies used by poachers to circumvent them, see box S1 in the supplementary materials for a description of how several interventions acted in concert to achieve the arrest of a core member of a poaching syndicate. An estimated minimum of USD 74 million (using the mid-2019 spot rate of ZAR 14.4 to USD 1) was spent on interventions related to rhino protection across all reserves in the period 2017–2021 (Fig. 3D; cost data were not available for 2022 and 2023). This equated to an estimated USD 3120 spent per resident rhino per year. Across all reserves and years, higher total expenditure on interventions was weakly correlated with lower poaching rates (fig. S20).

Dehorning was associated with large and abrupt reductions in poaching

In our baseline all-intervention model, we found strong statistical evidence that dehorning reduced poaching (Fig. 3). On average, dehorning all rhinos present on a reserve reduced poaching by ~75% from pre-dehorning levels (95% credible interval: 57 to 87% reduction), having accounted for other interventions and random effects (Fig. 3B). Poacher incursions were also significantly lower after dehorning (fig. S24), supporting the hypothesis that poachers make fewer attempts to enter reserves with dehorned rhinos because of the perception of a substantially reduced reward from poaching (Fig. 2 and fig. S1). Conclusions were the same (no significant intervention effects apart from dehorning) for supplementary models with flat Bayesian priors (fig. S2), excluding Kruger National Park (NP) data (fig. S26), using the raw number of rhinos poached instead of the poaching rate (fig. S27), using bias-corrected population estimates (fig. S28), including combinations of intervention variables (fig. S29), and including lagged intervention effects (fig. S30).

For the seven reserves that implemented abrupt dehorning, we found strong evidence for a simultaneous and abrupt reduction in poaching as well as a change in the poaching trend (Fig. 4; Bayesian regression discontinuity effects exclude zero; table S1). The estimated reduction in poaching for the regression discontinuity model was 78% (95% credible interval: 38 to 92%; table S1). Given the different times at which dehorning was introduced on each reserve (two in early 2019, two in late 2019, and three in mid-2022), it is unlikely that some unmeasured factor could have explained these effects (*29*). Furthermore, any abrupt change in the other interventions around the dehorning event was ruled out as a possible explanation for the abrupt change in poaching (fig. S9).

Using data across all reserves and years, we estimated a 13% risk of an individual horned rhino being poached in a particular year compared with a 0.6% poaching risk for a dehorned rhino, which represents a 95% reduction in relative poaching risk (Fig. 5A). Risk was also reduced at the landscape level, with higher annual levels of dehorning at this level (all 11 reserves) associated with reduced poaching rates overall (Fig. 5B and fig. S22). Thus, although dehorning on one reserve may have displaced poaching pressure to others, overall poaching rates in the system did decline. By making several simplifying assumptions,

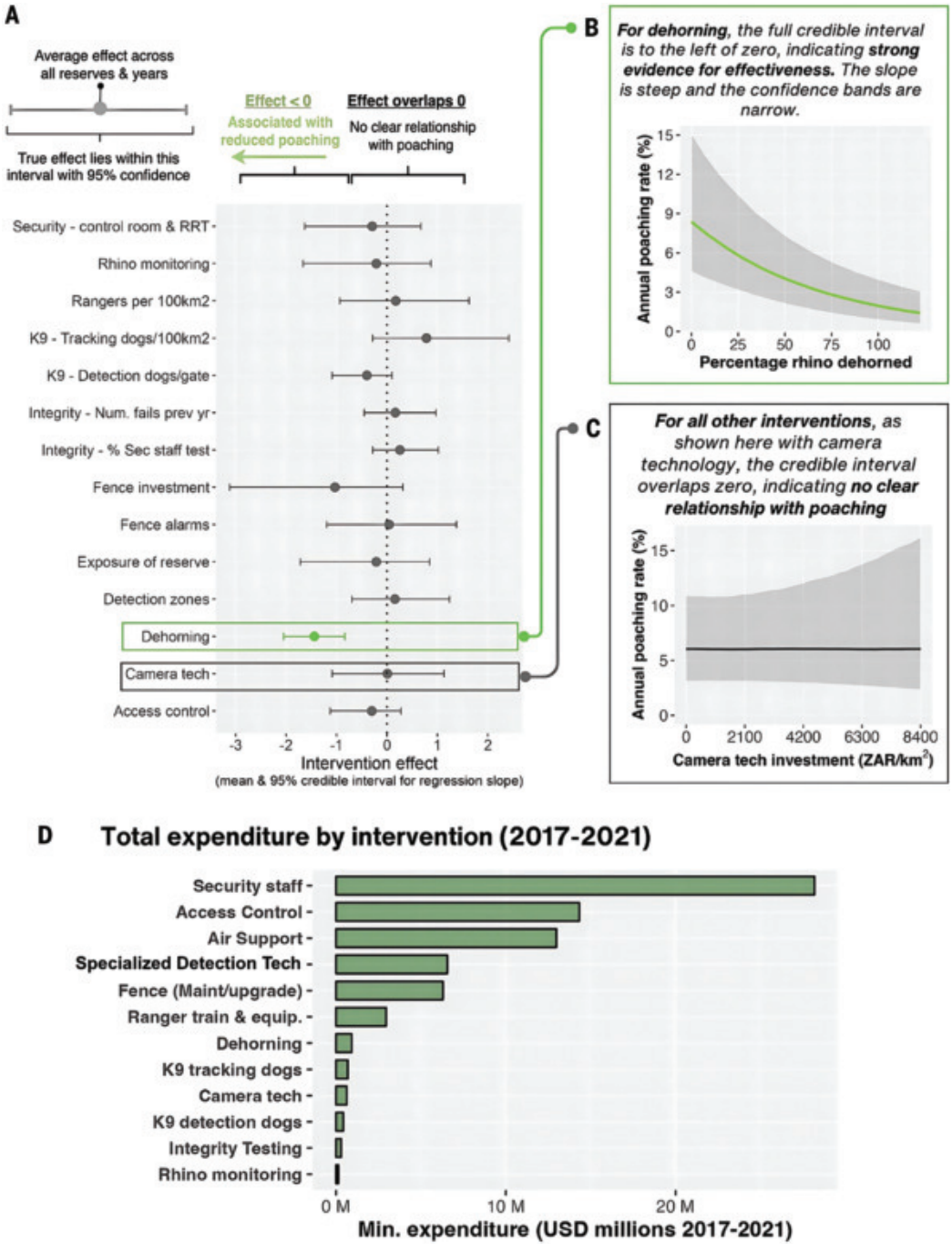

Fig. 3. The effectiveness and cost of antipoaching interventions. (**A**) Effectiveness was measured as the slope of the relationship between the intensity of each intervention and the poaching rate in a statistical model that included all interventions together and with random effects to account for unmeasured confounding factors (see materials and methods). All intervention indices are standardized to the 0 to 1 scale to allow direct comparison. Some intervention indices were correlated, so the effects of ranger training and equipment and tracking technology are shown in fig. S25. RRT, rapid response team. (**B** and **C**) Conditional effects plots for the effect of dehorning and camera technology, respectively, having accounted for all other interventions and random effects. (**D**) Total expenditure by intervention.

we estimate that a total of between 70 and 134 rhinos were saved from poaching in the 12 months after dehorning across the eight implementing reserves, at a median cost of USD 7133 per rhino saved (table S2). Dehorning was also the most cost-efficient intervention (USD 570 per rhino operation), using ~1.2% of the USD 74 million total expenditure to achieve large reductions in poaching (Fig. 3 and figs. S20 and S21).

Despite these strong effects, we recorded the poaching of 111 previously dehorned rhinos, 107 of which were poached within Kruger NP in 2022–2023 (fig. S23). During these 2 years, only 50 to 55% of rhinos on Kruger had been dehorned in the previous 18 months, on average, and horned and dehorned rhinos were poached at similar rates (fig. S23). Evidently, although the overall poaching rate within Kruger NP decreased from 7.5 to 3.4% after dehorning (see reserve 3 in Fig. 4), criminal syndicates remained willing to poach dehorned rhinos there at fairly high rates. A sizable proportion of horn mass remains on the rhino after dehorning, as veterinarians are only able to cut the horn up to the

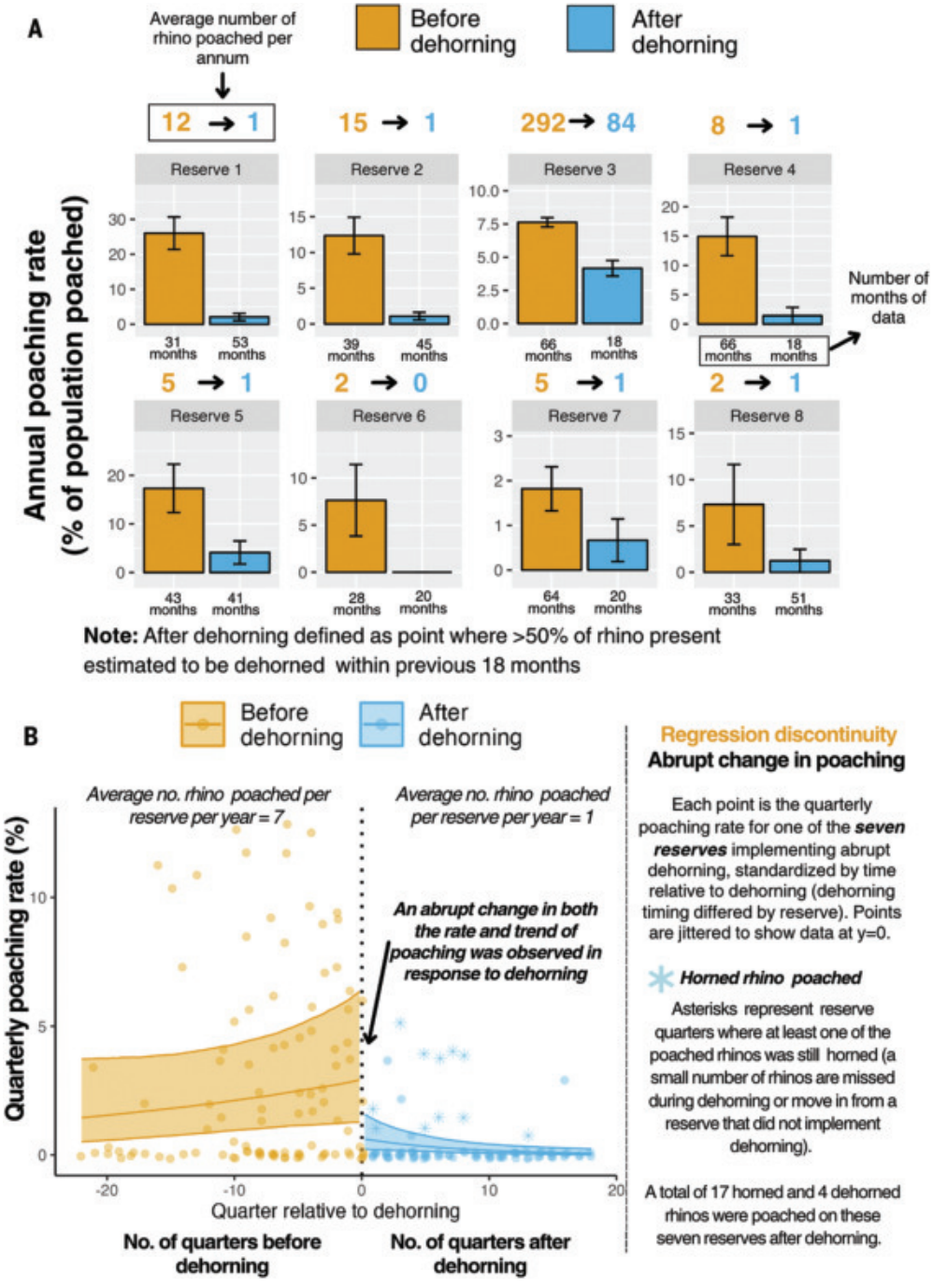

Fig. 4. Dehorning is associated with abrupt and significant reductions in poaching. (**A**) Annual poaching rates before and after dehorning for the eight reserves that implemented dehorning (mean ± SE). All these reserves implemented abrupt dehorning except Kruger NP (reserve 3). (**B**) Rhino poaching rates before and after dehorning, with data from the seven reserves that implemented abrupt dehorning standardized by the year quarter relative to dehorning (dehorning was staggered across these reserves between 2019 and 2022; see materials and methods). The blue asterisks indicate that at least one of the rhinos poached on a particular reserve in a particular quarter was still horned (either missed during dehorning or had moved in from a reserve that had not dehorned its rhinos). Trend lines and discontinuity estimates are from the Bayesian regression discontinuity-in-time model that tested for an immediate dehorning effect as well as a change in the poaching trend (see materials and methods and table S1).

growth plate, leaving 5 to 15 cm of basal horn length behind depending on the rhino's age (data are from field measurements during dehorning operations). The specific targeting of Kruger NP might be explained by lower coverage and frequency of dehorning (fig. S23) and the comparatively easy access to the reserve from Mozambique, where poaching syndicates may be more willing to poach dehorned rhinos and less able to shift operations elsewhere (compared with South African syndicates). The effective rate and frequency of dehorning was also lower in Kruger NP (fig. S23).

Law enforcement interventions show less direct success

Apart from dehorning, the credible intervals for the effects of the other 10 interventions overlapped zero, suggesting that the greater intensity of these interventions was not associated with any significant change in poaching across the study (Fig. 3, A and C). However, these results do not necessarily imply that the other interventions were ineffective. The credible intervals for all interventions are plausibly consistent with a positive effect, and the inconclusive results may reflect a low power to detect impacts from a real-world, data-sparse system in which interventions were implemented in a nonexperimental way that did follow a strong experimental design. Many interventions were successful on their own terms, as they were associated with increased rates of poacher detection and arrest, sometimes before the poaching event (fig. S31), even if this did not, on aggregate, translate to a significant effect across reserves. Detection cameras equipped with artificial intelligence detected numerous poachers, tracking dogs and air support helped track and arrest several hundred poachers, and polygraph testing led to the dismissal of 129 staff members after test failures suggested collusion with criminal syndicates (fig. S31).

Discussion

Our results bring into sharp focus the limitations of reactive approaches to rhino poaching when poachers have already entered reserves. Interventions that work to aid poacher detection and arrest, although a necessary element of the antipoaching toolkit, are compromised by several systemic factors that may dampen their effectiveness (Fig. 2). First, ongoing socioeconomic inequality incentivizes a large pool of vulnerable and motivated people to join, or poach for, criminal syndicates even when the risks are high (*4*, *9*). Second, entrenched corruption (among police and reserve staff and in the courts) allows offenders to circumvent many antipoaching efforts, greatly compromising their deterrent value (*18*, *20*). Third, ineffective criminal justice systems mean that

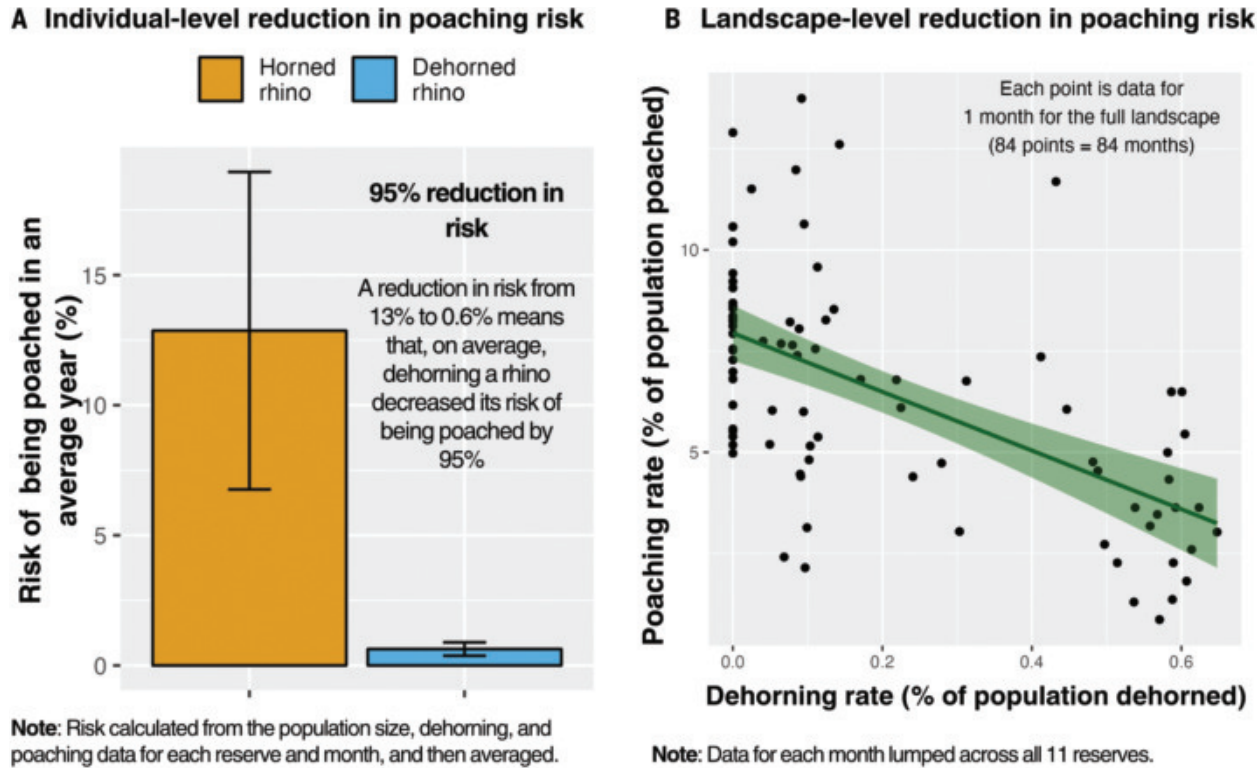

Fig. 5. Individual rhino and landscape-level reductions in poaching risk after dehorning. (**A**) Risk ratios for dehorning effectiveness. Risk ratios compare the poaching rate of horned rhino to that of dehorned rhino, using data across all reserves and months (see materials and methods). Error bars represent mean + SD. (**B**) The relationship between the monthly poaching and dehorning rate across 2017–2023 (84 months; data lumped across reserves). The shaded region represents the 95% confidence interval for the smoothed regression line.

arrested offenders often escape punishment, with evidence from our study area of multiple repeat offenders (*4*). The fact that these conditions are by no means specific to our study area broadens the importance of our work (*31*, *32*).

Reactive approaches also raise inevitable human rights concerns, as apprehending armed poachers in the field carries a high risk of either rangers or poachers losing their lives (*33*). Addressing the socioeconomic vulnerability of local communities, which allow syndicates to access a pool of poachers, is another critical strategic priority [requiring long-term collaborative efforts by government, civil society, and the private sector; (*30*)].

Dehorning was the only intervention for which we found strong evidence for effectiveness. Interventions that unambiguously reduce the revenues from poaching (such as dehorning) may be more robust to contextual complexity than interventions that act through actual or perceived costs and risks of poaching [(*9*, *12*–*14*, *20*); also see Fig. 2]. Our results align with work in behavioral economics that suggests that people respond more to outcomes that are more certain (a clear and substantial reduction in reward, such as through dehorning) than to those that are less certain (poacher detection, arrest, and sentencing are all subject to high uncertainty) (*13*, *14*). Dehorning is also an example of a more general approach in situational crime prevention—that of reducing opportunities for crime by rendering it less rewarding, an approach with many analogs in the prevention of more traditional crimes (*34*, *35*). Another likely reason for the effectiveness of dehorning is that it is less easily thwarted by internal corruption. Whereas cameras, dogs, and rangers can be avoided by poachers with internal information, dehorning cannot.

Although the removal of valuable body parts to reduce poaching is often not possible for other species threatened by the illegal wildlife trade, the broader approach of reducing opportunities for and rewards from poaching (as opposed to increasing risk) is generalizable. Researchers in Venezuela, for example, found that removing parrot nestlings from nests into safer areas at night and returning them in the morning led to large reductions in poaching (*36*). In Cape Town, South Africa, conservationists paint indigenous trees to discourage illegal debarking for medicinal trade (*37*).

Our results make a strong case for dehorning as a strategy to reduce poaching, yet there are several caveats. First, dehorned rhinos were occasionally poached (particularly those with substantial regrowth). Second, dehorning in the Greater Kruger may have displaced poaching pressure to horned populations elsewhere [with some evidence of a shift to the second largest stronghold for South African rhinos, namely, Hluhluwe-iMfolozi Park; (*38*)]. It remains to be seen whether dehorning would be as effective in the absence of horned populations that are accessible elsewhere to criminal syndicates. If dehorning had taken place in the total absence of other interventions, poaching for the stumps and regrowth would probably have continued given the lack of risk to poachers. It follows that the effective implementation of a suite of other interventions is probably necessary to ensure the ongoing effectiveness of dehorning, whether in our study system or elsewhere. Finally, the effects of dehorning on rhino biology are still unclear, with present research suggesting that dehorning may alter rhino space use but not survival and reproduction (*27*–*30*).

Our results present a challenge to governments, funders, the private sector, and nongovernmental organizations to reassess their strategic approaches to wildlife crime in general and rhino poaching in particular. Although detecting and arresting poachers is essential, strategies that focus on reducing opportunities for and rewards from poaching may be more effective. Demand reduction, by reducing the price of wildlife products, is one such strategy (*39*). Similarly, efforts to support the socioeconomic resilience of local people may help create viable

economic alternatives that render rewards from poaching less attractive (*40*). For practice and policy in global rhino conservation, our work makes a strong case for dehorning as a tool that may achieve large and immediate reductions in poaching in cases where law enforcement has not yielded the desired level of poacher deterrence. Yet the fact that poaching of dehorned rhinos continued at fairly high rates in Kruger NP suggests that horn stumps and regrowth remain attractive to criminal syndicates, pointing to the need for regular dehorning and ongoing prudent use of law enforcement.

Finally, our work is an example of both the value and difficulty of impact evaluation in conservation science and practice. We demonstrate how combining multiple lines of evidence (qualitative attribution methods through workshops and interviews, tailored statistical models, and quasi-experimental approaches) can help reduce uncertainty in the attribution of biodiversity outcomes to specific policies or interventions in messy contexts. Our work is also an example of a situation in which conservation practitioners reached out to scientists for support in addressing a perceived problem, rather than the scientists coming to an area with a question that may or may not be one of interest to local practitioners. This flipping of the scientist-practitioner relationship and the direction of knowledge exchange is still unusual [but see (*41*) for another example]. Where possible, to maximize future learning and adaptation, we suggest that scientists and conservation practitioners codesign research that seeks to actively evaluate interventions in a more explicitly experimental way, the lack of which was a limitation of this study.

REFERENCES AND NOTES

1. J. A. J. Eikelboom, H. H. T. Prins, *Sci. Adv.* **10**, eadl1482 (2024).
2. Convention on International Trade in Endangered Species of Wild Fauna and Flora (CITES), "Working document 75 for CoP19 of the Convention on the International Trade in Endangered Species: RHINOCEROSES (RHINOCEROTIDAE SPP.)" (CoP19 Doc. 19, CITES, 2022); https://cites.org/sites/default/files/documents/COP/19/agenda/E-CoP19-19.pdf.
3. B. A. Lubbe, E. A. du Preez, A. Douglas, F. Fairer-Wessels, *Curr. Issues Tour.* **22**, 8–15 (2019).
4. J. Rademeyer, "Landscape of fear: Crime, corruption and murder in greater Kruger" (Issue 36, ENACT Africa, 2023); https://enactafrica.org/research/research-papers/landscape-of-fear-crime-corruption-and-murder-in-greater-kruger.
5. J. P. G. M. Cromsigt, M. te Beest, *J. Ecol.* **102**, 566–575 (2014).
6. M. Belecky, R. Singh, W. D. Moreto, "Life on the frontline 2019: A global survey of the working conditions of rangers" (World Wildlife Fund, 2019); https://files.worldwildlife.org/wwfcmsprod/files/Publication/file/k36blpy2c_wwf_rangers_survey_report_2019.pdf.
7. S. M. Ferreira, L. Dziba, *J. Nat. Conserv.* **72**, 126359 (2023).
8. S. M. Ferreira, C. Greaver, C. Simms, L. Dziba, *Afr. J. Wildl. Res.* **51**, 100–110 (2021).
9. A. M. Hübschle, *Curr. Sociol.* **65**, 427–447 (2017).
10. G. S. Becker, *J. Polit. Econ.* **76**, 169–217 (1968).
11. E. H. Bulte, G. C. van Kooten, *Am. J. Agric. Econ.* **81**, 453–466 (1999).
12. E. J. Milner-Gulland, N. Leader-Williams, *J. Appl. Ecol.* **29**, 388–401 (1992).
13. M. Siegrist, J. Árvai, *Risk Anal.* **40**, 2191–2206 (2020).
14. D. Kahneman, A. Tversky, *Econometrica* **47**, 263 (1979).
15. D. W. S. Challender, D. C. MacMillan, *Conserv. Lett.* **7**, 484–494 (2014).
16. World Bank, "Analysis of international funding to tackle illegal wildlife trade" (Working Paper 110267, World Bank, 2016); https://documents1.worldbank.org/curated/en/695451479221164739/pdf/110267-WP-Illegal-Wildlife-Trade-OUO-9.pdf.
17. F. Massé, J. Margulies, *World Dev.* **132**, 104958 (2020).
18. T. Kuiper *et al.*, *Proc. Biol. Sci.* **290**, 20222270 (2023).
19. J. H. Liew *et al.*, *Sci. Adv.* **7**, eabf7679 (2021).
20. D. P. Van Uhm, W. D. Moreto, *Br. J. Criminol.* **58**, 864–885 (2018).
21. P. J. Cook, *Criminol. Public Policy* **15**, 1155–1161 (2016).
22. J. Zavaleta Cheek, J. Eklund, N. Merten, J. Brooks, D. C. Miller, *Conserv. Biol.* **37**, e14071 (2023).
23. J. Mayne, *Can. J. Program Eval.* **16**, 1–24 (2001).
24. C. Hausman, D. S. Rapson, *Annu. Rev. Resour. Econ.* **10**, 533–552 (2018).
25. E. G. Frank, *Science* **385**, eadg0344 (2024).
26. N. Huntington-Klein, *The Effect: An Introduction to Research Design and Causality* (CRC Press, 2022).
27. L. C. Chimes, P. Beytell, J. R. Muntifering, B. Kötting, V. Neville, *Eur. J. Wildl. Res.* **68**, 58 (2022).
28. V. Pfannerstill *et al.*, *J. Zool.* **321**, 249–259 (2023).
29. S. G. Penny *et al.*, *Afr. Zool.* **57**, 32–42 (2022).
30. V. Duthé *et al.*, *Proc. Natl. Acad. Sci. U.S.A.* **120**, e2301727120 (2023).
31. M. t'Sas-Rolfes, D. W. S. Challender, A. Hinsley, D. Veríssimo, E. J. Milner-Gulland, *Annu. Rev. Environ. Resour.* **44**, 201–228 (2019).
32. V. Felbab-Brown, *The Extinction Market: Wildlife Trafficking and How to Counter It* (Oxford Univ. Press, 2017).
33. C. Galliers *et al.*, *PARKS* **28**, 39–50 (2022).
34. A. Lemieux, Ed., *Situational Prevention of Poaching* (Taylor & Francis, 2014).
35. P. L. Brantingham, P. J. Brantingham, in *Routine Activity and Rational Choice*, vol. 5, *Advances in Criminological Theory* (Routledge, 1993), pp. 259–294.
36. J. M. Briceño-Linares *et al.*, *Biol. Conserv.* **144**, 1188–1193 (2011).
37. D. Pinnock, "A conversation with the man who paints trees to combat bark stripping," *Daily Maverick*, 25 February 2024.
38. South African Government, "Minister Barbara Creecy outlines progress in fight against rhino poaching, 1 Aug," Media Briefing, 27 July 2023; https://www.gov.za/news/media-advisories/media-briefings/minister-barbara-creecy-outlines-progress-fight-against-rhino.
39. A. Olmedo, V. Sharif, E. J. Milner-Gulland, *Conserv. Lett.* **11**, e12365 (2017).
40. R. Cooney *et al.*, *Conserv. Lett.* **10**, 367–374 (2016).
41. J. Aini *et al.*, *Oryx* **57**, 350–359 (2023).
42. T. Kuiper, TimothyKuiper/dehorning_rhinos_Science: Dehorning rhinos Science - Release for archiving code to Zenodo. Zenodo (2025); https://doi.org/10.5281/zenodo.15098035.

ACKNOWLEDGMENTS

The Greater Kruger reserve managers contributed hundreds of hours of combined time helping to design this project, consolidating the data required, and providing critical insight and experience to help interpret and contextualize the results. The steering committee provided expert oversight and much-needed direction to this project. The data collectors patiently and persistently tackled the mammoth task of gathering standardized data over countless reserve visits. We would particularly like to thank S. Hsiang for his constructive review of an earlier version of our manuscript, which resulted in substantial improvements in our methods and discussion. **Funding:** Grants from the Rhino Recovery Fund (part of the Wildlife Conservation Network) and the World Wildlife Fund South Africa Grant made this project possible. E.J.M.-G. acknowledges funding from the UK Research and Innovation's Global Challenges Research Fund (UKRI GCRF) through the Trade, Development, and the Environment Hub project (project number ES/S008160/1). T.K. is presently supported by a postdoctoral fellowship at the University of Cape Town, funded by the National Research Foundation in South Africa. **Author contributions:** Conceptualization: T.K., S.H., S.W., C.D., M.H., D.P., J.S., S.F., J.B., M.B., W.B., Z.G., I.N., I.O., E.P., R.A., C.R., M.v.T., E.W., H.Z., S.S.; Investigation: T.K., S.H., S.W., C.D., M.H., D.P., J.S., S.F., J.B., M.B., W.B., Z.H., K.L., I.N., I.O., E.P., C.R., M.v.T., E.W., H.Z., S.S., R.A.; Methodology: T.K., S.W., C.D., M.H., D.P., J.S., S.F., J.B., M.B., W.B., Z.G., Z.H., K.L., I.N., I.O., E.P., C.R., M.v.T., E.W., H.Z., S.S., R.A., E.J.M.-G.; Data curation: T.K., Z.G., Z.H., K.L.; Validation: E.J.M.-G.; Formal analysis: T.K., D.P., R.A.; Funding acquisition: S.H., S.W., J.S.; Project administration: S.H., J.S.; Resources: S.H., S.W., J.S.; Writing—original draft: T.K., R.A.; Writing—review & editing: T.K., S.H., S.W., C.D., M.H., D.P., J.S., S.F., J.B., M.B., W.B., Z.G., K.L., I.N., I.O., E.P., C.R., M.v.T., E.W., H.Z., S.S., R.A., E.J.M.-G. **Competing interests:** The authors declare that they have no competing interests **Data and materials availability:** Given the sensitivity of the rhino poaching and intervention data, it is protected by a data-sharing agreement. Queries related to data access can be directed to the Greater Kruger Environmental Protection Foundation at info@gkepf.org. The R statistical programming code for reproducing the baseline all-intervention model and the regression discontinuity model is available on Zenodo (*42*). **License information:** Copyright © 2025 the authors, some rights reserved; exclusive licensee American Association for the Advancement of Science. No claim to original US government works. https://www.science.org/about/science-licenses-journal-article-reuse

SUPPLEMENTARY MATERIALS

science.org/doi/10.1126/science.ado7490
Materials and Methods; Figs. S1 to S31; Tables S1 to S3; Box S1; References (*43*–*55*); MDAR Reproducibility Checklist

Submitted 19 February 2024; resubmitted 7 October 2024; accepted 27 March 2025

10.1126/science.ado7490

ARCHAEOLOGY

Archaeological evidence of intensive indigenous farming in Michigan's Upper Peninsula, USA

Madeleine McLeester[1]*, Carolin Ferwerda[1], Jonathan Alperstein[1], David Overstreet[2]†, David Grignon[3], Jesse Casana[1]

We describe archaeological evidence of intensive ancestral Native American agriculture in the now heavily forested Upper Peninsula of Michigan. Recent LIDAR (light detection and ranging) and excavation data have uncovered densely clustered ancient agricultural raised garden bed ridges covering an expanse far greater than previously realized. These raised agricultural fields are deeply enmeshed in the broader cultural landscape, as ceremonial and other features were also found. Our results demonstrate a rich anthropogenic landscape created by small-scale ancestral Menominee communities, located near the northern limits of maize agriculture. The excellent preservation of this site is exceptional in eastern North America and suggests that the precolonial landscape was more anthropogenically influenced than currently recognized.

Introduction

From approximately 1000 to 1600 CE, ancestral Native American communities throughout what is now the US intensely cultivated maize, a practice that coincided with extraordinary social and environmental changes. During this time, settlements became larger and more sedentary, monumental mound construction proliferated, power became increasingly concentrated and hierarchical, and vast areas of the landscape were deforested or burned (*1*–*6*). However, intensive agriculture was far from uniform across the continent (*7*–*11*), and near its northernmost margins in the northern Great Lakes, where the precolonial landscape was populated by semisedentary communities, there is no consensus on the timing, scale, and consequences of its adoption (*12*–*15*).

Michigan's Upper Peninsula, at the border between the US and Canada, seems an unlikely place for ancestral Native American communities to practice intensive agriculture. Communities had access to wild rice, a prevalent staple that was utilized in the past and remains so today (*15*–*17*). With its dense forests, cold climate, and short growing season, this is a challenging region for crops—particularly maize, a semitropical, sun-loving domesticate (*12*, *13*, *15*). Moreover, the Upper Peninsula contains no known large, urban population centers that would have required intensified agricultural production or provided the labor needed to construct and maintain intensive field systems (*14*).

To investigate past agricultural efforts in this marginal agricultural region, we conducted a drone LIDAR (light detection and ranging) survey and excavations at the precolonial, ancestral Menominee Sixty Islands archaeological site (20ME61) (Fig. 1). Previous investigations here found evidence of past agriculture preserved as raised, ridged garden beds, charred maize remains, and phytoliths of several cultigens (*18*, *19*).

Our results reveal a well-preserved agricultural landscape at a scale not previously recognized this far north, with a near-total reworking of the landscape for agriculture from 1000 to 1600 CE, the Late Woodland period (Fig. 2). Densely clustered agricultural field ridges cover almost the entire area of our survey, providing the most complete and expansive example of extant ancestral Native American farming in the eastern US. Additional findings of burial mounds and a ritual earthwork demonstrate the ways in which precolonial Native American agricultural landscapes were deeply embedded within the larger cultural landscape. Our findings reveal the massive scale of precolonial agriculture and landscape construction undertaken by ancestral Menominee, semisedentary communities during the Late Woodland period (*7*, *15*), even in the seemingly environmentally adverse, forested region of the Upper Peninsula. These results not only force a reconsideration of the cultural and environmental histories of the northern Great Lakes but also challenge conventional understandings of intensive agriculture both within the eastern US and globally.

Context

Raised, ridged field agriculture is an intensive farming technique characterized by the construction of elongate, earthen mounds that operate as the planting surface for the cultivation of maize, beans, and squash along with other plants such as melons and sunflowers. This type of agriculture is well known by archaeologists (*4*, *20*) and was practiced from at least 1000 CE through the early 19th century in eastern North America by ancestral Native American communities. Archaeological agricultural ridges typically are arranged in rows that measure on average 1 to 1.5 m in width and 20 to 50 m in length (*4*, *21*). Planting in raised, ridged beds serves several functions, including enhancing soil fertility, regulating soil temperature, and maintaining adequate soil moisture. Direct evidence of ridged field agriculture is rarely preserved today, as ancestral Native American farmlands were intensively reworked by Euro-American plowing, settlement, and industry, collectively destroying or obscuring most precolonial agricultural and other cultural features. More than 90% of ancestral Native American fields that were recorded in the Upper Midwest during the early 20th century have since been lost to industrialized agriculture and urban development (*21*). The rarity of preserved precolonial agricultural fields in eastern North America is a major stumbling block to understanding the true extent, intensity, and character of ancestral Native American farming practices.

Sixty Islands (20ME61), the focus of this study, is a ridged agricultural site and the only known archaeological site with extant evidence of precolonial agricultural fields in MI, US (Fig. 2). It is located in a densely forested region covered by a thick canopy of conifers and

Fig. 1. Locator map shows Sixty Islands (ME61) and other archaeological sites along the Menominee River as well as the LIDAR survey area. This entire area, known by its Menominee name, Anaem Omot, sits at the boundary between the states of MI and WI in the US and has recently been listed on the National Register of Historic Places.

[1]Department of Anthropology, Dartmouth College, Hanover, NH, USA. [2]Consulting Archaeologist, College of the Menominee Nation, Keshena, WI, USA. [3]Tribal Historic Preservation Officer, Menominee Indian Tribe of Wisconsin, Keshena, WI, USA. ***Corresponding author. Email: madeleine.mcleester@dartmouth.edu** †Published posthumously.

Fig. 2. Raised agricultural beds cover an estimated 70% of the LIDAR survey area. Ridges, such as those illustrated here, form a dense, quilt-like pattern across the landscape. (Inset) Photograph of the raised beds at Sixty Islands.

northern hardwoods. Sixty Islands is located along a 3-km stretch of the Menominee River. It is one of dozens of archaeological sites that collectively form the archaeological district Anaem Omot, a 1375-ha concentration of ancestral Menominee archaeological sites that was recently listed on the US' National Register of Historical Places (#100009086). Anaem Omot contains burial mound groups, village sites, and other cultural features surrounded by densely clustered raised garden bed ridges, and is a central place in Menominee oral histories and contemporary ritual practices.

Previous work at Anaem Omot includes the excavation of several burial mounds (*22*) and a village site (*23*) undertaken intermittently from the 1950s through the 1970s, before Sixty Islands was located by archaeologists. After being documented in the mid-1990s, a portion of Sixty Islands (9.5 ha) was mapped in detail, which at the time was estimated to constitute around 60% of the extant agricultural features (*18*). Limited excavations of the ridges conducted at the same time located three corn cupules, one of which provided a calibrated radiocarbon date between the 14th and 15th centuries CE (Beta-140450, supplementary text, and table S3) (*18*). More recently, Munson-Scullin and Scullin (*20*, *24*) identified maize phytoliths from one ridge, thereby additionally confirming the intensive production of maize and likely other cultigens such as beans and squash. Today, much of Sixty Islands is under threat of destruction from a planned mine (*25*). In 2023, at the request of Menominee tribal authorities and local landowners, the authors of this study undertook drone-mounted LIDAR surveys and test excavations at Sixty Islands to document the extent of the field system.

Methods

Drone-mounted LIDAR surveys

Dense ground cover and the low relief of raised garden beds in the Great Lakes region make these archaeological features notoriously difficult to recognize on the ground. Although aircraft-acquired LIDAR has been a transformative technology for documenting archaeological landscapes in forested regions (*26*, *27*), the relatively low resolution of these data makes recognition of raised garden beds difficult. Higher-resolution drone-based LIDAR offers the opportunity to document topographic features with greater precision (*28*). We conducted drone-based LIDAR surveys in early May 2023, a time of year when snow has melted and leaves have not yet emerged, to maximize penetration to the ground. LIDAR and color imagery were collected with a DJI Zenmuse L1 sensor, flown on a DJI Matrice 300 RTK "enterprise-grade" quad-copter. The survey covered a total of 134 ha, including a section of Sixty Islands (83 ha, or 42% of the known site boundaries) as well as the surrounding area that contains archaeological sites associated with Anaem Omot (Fig. 1). The collected point cloud was examined, edited, and filtered using LASTools (version 240125) and exported to ArcGIS Pro 3.0.0 for visualization and analysis (*29*) (supplementary text).

Ground-truthing

The authors undertook a pedestrian survey of archaeological features identified by LIDAR in August 2023, including the previously unrecorded dance ring and other newly identified features (see results below). Three test units placed over garden bed ridges were excavated to document internal stratigraphy, collect sediment for future analyses, and recover organic material for radiocarbon dating (Fig. 3). Excavations targeted ridges located on three different alluvial terraces, at increasing distances from the modern river channel. Ridges measured between 1.2 and 1.9 m in width and between 0.18 and 0.33 m in height (figs. S1 to S6). Raised ridges were excavated to surface level. Unit dimensions (1.5 to 2 m wide) were determined to minimize damage to the site and were established based on the size of the individual ridge being investigated as well as recovery goals. Any artifacts encountered was collected. Sediment (179 liters) was collected for flotation and processed in the field using a flotation tank, and nine charcoal samples—three from each ridge—were sent to International Chemical Analysis for radiocarbon dating. All charcoal samples were taken from the middle of each ridge (see supplementary text).

Results

Results from the LIDAR survey show densely clustered raised garden beds covering an area of 95 ha, approximately 70% of the area surveyed in this study. The density of raised, ridged beds throughout our survey area reveals a level of agricultural intensification that was not previously documented this far north. These results are 10 times greater than the area previously mapped and represent only a fraction of the known site area. Raised beds at Sixty Islands are typically constructed in a quilt-like pattern in which densely spaced parallel ridges cover small (20- to 30-m) rectilinear areas, abutting adjacent ridges in a perpendicular orientation (Figs. 2 and 3). Less commonly, some raised beds form parallel curved lines, following the natural topography. Ridges are oriented in all directions, suggesting that the site selection and ridge construction was determined by cultural rather than environmental factors such as sunlight. They are found adjacent to the Menominee River on the active floodplain as well as on higher elevation terraces, as much as 300 m from the modern river channel and on at least four distinct alluvial terraces, from 211 meters above sea level (masl) to as high as 228 masl.

Our results additionally illustrate the ways that agricultural efforts are clearly embedded into the broader cultural landscape. Although we expected this result as Sixty Islands is part of the Anaem Omot archaeological district, newly located cultural features as well as the scale of landscape construction are laid bare in new, previously unrecognized ways. Numerous burial mounds are evident (Fig. 4, D to F), including several prominent, previously investigated mounds with evident looting holes (20ME2 and 20ME108), two low, subtle mounds that are part of the excavated Backlund Mound Group (20ME2), and at least one mound on mining land (Fig. 4F). Other cultural features visible in LIDAR data include two historic logging camps (20ME23) (Fig. 4C), a square building foundation that may be the remains of a colonial trading outpost (Fig. 4B), as well as a previously unrecorded dance ring (20ME163) (Fig. 4A). The dance ring, measuring roughly 9 m by 12 m, appears to be a ditch and embankment earthwork. Dance rings are common earthwork features found throughout the region

(*30*, *31*), and several dance rings near Sixty Islands remain sacred spaces to the Menominee today.

Results additionally have significant cultural heritage management consequences, especially surrounding the documentation of extant burial mounds. The Backlund Mound Group (20ME2) once consisted of eight conical mounds associated with the late precolonial, ancestral Menominee (*22*). The mounds were thought to be completely razed through archaeological excavation, land use, and erosion; however, several mound bases, including previously undocumented ones, are visible in the LIDAR (Fig. 4, E).

Excavations of three agricultural ridges offer a cross-sectional view that suggests multiple phases of rebuilding and shows the likely addition of wetland soils and compost to enhance soil fertility (figs. S2 to S7). Excavations recovered substantial amounts of charcoal and artifacts, including sherds, flakes, faunal fragments, and fire-cracked rock (table S1). The ubiquity of charcoal and small artifactual finds located at disparate ridges, combined with the lack of a settlement site in the immediate vicinity of the beds, suggests the use of household refuse and sweepings as compost.

Charcoal and artifacts also provide dating evidence for the fields, showing that they were likely in use from ~1000 to 1600 CE. The nine wood charcoal samples recovered from flotation (table S2) all return dates in this range (table S3 and fig. S1). The earliest dates center around 1000 CE, the period when intensive maize cultivation was adopted throughout the American Midwest (*15*) (supplementary text). The earliest date for the fields is around 800 to 1000 CE, but it is difficult to establish with certainty given the potential for old wood effect (*32*). Nonetheless, we interpret the fact that all three ridges produce dates by 1000 CE to suggest that this represents an initial phase of construction. Additional dates are between 1400 and 1600 CE near the end of the Late Woodland period. Likewise, all datable artifacts recovered from excavations date to the Late Woodland period (600 to 1600 CE) and conform with a previously reported radiocarbon date of a maize cupule from Sixty Islands (1328 to 1479 CE, 2-sigma calibrated range) (*18*). Collectively, dating evidence indicates a long period of use and rebuilding of ridged fields, suggesting nearly 600 years of cultivation at Sixty Islands.

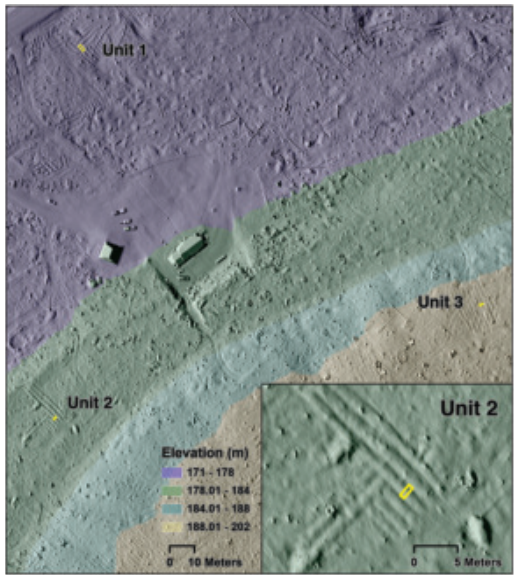

Fig. 3. Excavations were conducted at three ridges located at different elevations. Units cross-sectioned individual ridges (lower right inset).

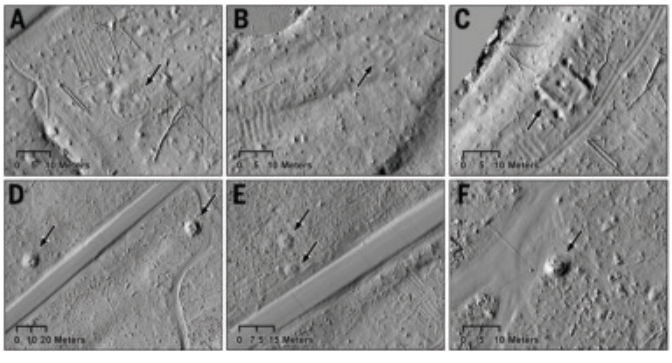

Fig. 4. Many cultural features other than agricultural field ridges are visible in LIDAR data. Examples include: (**A**) a newly documented dance ring, (**B**) a historic building foundation, (**C**) a 19th-century logging camp, (**D**) looted burial mounds, (**E**) remains of the Backlund mound group, and (**F**) a burial mound.

Discussion

The LIDAR survey at Sixty Islands reveals a vast and well-preserved landscape of raised agricultural beds interspersed with burial mounds, ritual features, and habitation sites. Results from this marginal agricultural region change how archaeologists should conceptualize intensive agriculture both within the region and globally. Although considerable scholarship has tied intensive agricultural production to emergent hierarchical state formation and inequality (*33*–*37*), efforts at Sixty Islands were undertaken by egalitarian, small-scale ancestral Menominee communities who lack any evidence of stark political hierarchies and large population centers (*38*).

Radiocarbon dates from ridged fields at Sixty Islands place them within the Late Woodland period, showing that the ridges were likely in use from 1000 to 1600 CE. This long period of intensive cultivation is surprising given the paucity of evidence for large, sedentary settlements in the immediate vicinity. The nearby Backlund Village site (1100 to 1300 CE) is the only documented settlement within our survey area that was occupied when the beds were in use, but it is interpreted as a relatively small village with a limited, likely seasonal occupation (*23*). The nearby Backlund Burial Mounds (20ME10) may similarly date from 1000 to 1300 CE; however, it is unclear when the ceramic artifacts used to date them were deposited (*22*). It is possible that other larger sites have yet to be located within the greater region of Anaem Omot, but a more parsimonious conclusion might be that the ridged fields and burial mounds at Sixty Islands were constructed by nonsedentary or semisedentary communities known to have lived in this region throughout the Late Woodland era.

Despite the absence of extensive settlement, our findings document, to our knowledge, the largest preserved archaeological field system in the eastern US, and ground-truthing shows that it extends into unmapped areas. Archaeological and historical evidence of raised bed agricultural sites from WI suggest that the largest ancestral Native American agricultural fields were up to 121 ha (*21*). However, results from this study, collected from a location even farther north, suggest that these estimates are far too conservative. Instead, our findings align more closely with field sizes recorded by Black Hawk, a Sauk leader, who in 1833 estimated that 323 ha were in cultivation at his village in northern Illinois (*39*). Our results indicate that massive field systems like these were much more common than previously recognized, a conclusion supported by our previous analysis of field systems visible in historical aerial photographs (*21*).

Excavation data provide further evidence of the effort involved in the construction and maintenance of ridged fields. Cross sections of the ridges illustrate a substantial reworking of the soils, a process that varies by ridge and probably from farmer to farmer (*24*) (supplementary text). Phytolith data from Sixty Islands has shown that nearby wetland soils were mixed into existing topsoils, likely to create a nitrogen-rich environment (*24*) and for ridge structure. Our own excavation data located abundant charcoal and small artifactual finds (table S1), best explained as the result of composted household refuse being used to

fertilize fields. The use of household compost as fertilizer has been documented as a common practice in ancient and traditional agriculture in other parts of the world (*40*–*42*) but has not been treated seriously as a practice in the context of ancestral Native American farming in eastern North America. Evidence for composting and the use of wetland soils presented herein adds to both the sophistication of past Menominee farming practices and considerably increases labor requirements.

The scale of field systems at Sixty Islands is even more surprising given that the region is unfavorable for maize, the anchoring domesticate known to be cultivated on these types of features (*4*, *18*). The short growing season at this latitude places it near the northern margins of maize agriculture, presenting major challenges to cultivation; investing so much labor into agriculture in Michigan's Upper Peninsula seems a high-risk strategy for food production (*43*). The period during which the Sixty Islands agricultural ridges were constructed bridges the Little Ice Age (1350 to 1850 CE), indicating that Indigenous farmers were successful at mitigating any potential local adverse effects of the colder climate. Findings described here demonstrate a clear commitment to intensive agriculture, despite the widespread regional availability of another staple, wild rice (*15*) that was once abundant along the Menominee River (*15*, *16*). Moreover, the limited labor reserves, the colder climate, and the lack of any evident hierarchical administrative state, all raises critical questions about why the ancestral Menominee community invested such intensive labor efforts into agriculture here.

Alongside the archaeological significance of our findings, our results have implications for understanding the ecological history of Michigan's Upper Peninsula. Today, the landscape is densely forested, conditions that help preserve these raised bed features. This forested landscape is not a pristine one as the region has seen extensive deforestation, typically thought to begin with Euro-American settlement in the mid-19th century (*44*). However, our results indicate that prior deforestation must have occurred sometime during the Late Woodland period when the beds were in use (1000 to 1600 CE), as cultivated crops require an open canopy. The scale, density, and continuity of the ridges across the study area make it unlikely that agriculture was conducted in forest hollows and imply that much of the regional landscape was likely deforested by ancestral Menominee communities sometime around 1000 CE.

Findings from this study challenge us to look for intensive agriculture in more unlikely places, particularly outside of emergent and large state societies as well as the favorable climes most associated with intensive agricultural production. Here, we see the ingenuity of past Menominee farmers to not only modify the soils and landscape, but to also organize labor and resources outside of the constraints of steep political hierarchies. This example, similar to other recent finds from the Americas (*45*–*49*), continues to challenge foundational understandings surrounding emergent hierarchies and state societies, as well as our conceptions of what is possible.

REFERENCES AND NOTES

1. R. Birmingham, L. Goldstein, *Aztalan: Mysteries of an Ancient Indian Town* (Wisconsin His. Soc. Press, 2005).
2. R. Birmingham, A. Rosebrough, *Indian Mounds of Wisconsin* (Univ. of Wisconsin Press, 2017).
3. G. Fritz, *Feeding Cahokia: Early Agriculture in the North American Heartland* (Univ. of Alabama Press, 2019).
4. W. Gartner, *Antiquity* **73**, 671–683 (1999).
5. T. Pauketat, *Cahokia: Ancient America's Great City on the Mississippi* (Penguin, 2010).
6. E. Scharf, *Veg. Hist. Archaeobot.* **19**, 159–175 (2010).
7. R. Albert, S. M. Kooiman, C. A. Clark, W. A. Lovis, *Am. Antiq.* **83**, 345–355 (2018).
8. S. Johannessen, C. Hastorf, *Corn and Culture in the Prehistoric New World* (Westview Press, 1994).
9. M. J. Schoeninger, *Curr. Anthropol.* **50**, 633–640 (2009).
10. B. D. Smith, *Science* **246**, 1566–1571 (1989).
11. B. Smith, in *Human Dispersal and Species Movement*. N. Boivin, M. Petraglia, R. Crassard, Eds. (Cambridge Univ. Press, 2017), chap. 13, pp. 332–348.
12. S. Dunham, *Wis. Archeol.* **90**, 113129 (2009).
13. R. Yarnell, *Aboriginal Relationships Between Culture and Plant Life in the Upper Great Lakes* (Museum of Anthro., Univ. of Michigan, 1964).
14. C. Cleland, *The Great Lakes Forest: An Environmental and Social History*, S. Flader, Ed. (Univ. of Minnesota Press, 1983), pp. 83–95.
15. S. Kooiman, *Ancient Pottery, Cuisine, and Society at the Northern Great Lakes* (Univ. of Notre Dame Press, 2021).
16. A. Jenks, *Bureau of Am. Eth.* **19**, 1013–1137 (1902).
17. B. Barton, *Manoomin: The Story of Wild Rice in Michigan* (St. Univ. Press, 2018).
18. M. Buckmaster, in *An Upper Great Lakes Archaeological Odyssey*. W. Lovis, Ed. (Cranbrook Institute of Science, 2004), pp. 30–42.
19. W. Munson-Scullin, M. Scullin, *Phytolith and Humic Acid Study, and Excavation of Ridged Garden Beds at 20ME61, Menominee County, Michigan* (Report #201801), prepared for the Michigan Department of Natural Resources, Michigan Historical Center, (2020).
20. M. McLeester, A. Anastasio, J. Grignon, *Ethnobiol. Lett.* **14**, 80–91 (2023).
21. M. McLeester, J. Casana, *Am. Antiq.* **86**, 283–304 (2021).
22. D. Brose, The Backlund Mound Group, *Wis. Archeol.* **49**, 34–51 (1968).
23. M. Buckmaster, *Mich. Archaeol.* **45**, 142–156 (1999).
24. W. Munson-Scullin, M. Scullin, *Wis. Archeol.* **103**, 101–125 (2022).
25. K. Hagenmaier *et al.*, "Archaeological Investigations of the Back Forty Joint Venture, Back Forty Project Area Menominee County, Michigan" (Report R0905, 2011).
26. A. Chase *et al.*, *J. Archaeol. Sci.* **38**, 387–398 (2011).
27. D. H. Evans *et al.*, *Proc. Natl. Acad. Sci. U.S.A.* **110**, 12595–12600 (2013).
28. J. Casana *et al.*, *J. Archaeol. Sci. Rep.* **39**, 103133 (2021).
29. J. Casana *et al.*, *J. Archaeol. Sci.* **157**, 105837 (2023).
30. M. Howey, M. Clark, *J. Archaeol. Sci. Rep.* **19**, 886–893 (2018).
31. M. McLeester, J. Casana, M. Schurr, A. Hill, J. Wheeler III, *J. Archaeol. Sci. Rep.* **21**, 450–459 (2018).
32. M. Schiffer, *J. Archaeol. Sci.* **13**, 13–30 (1986).
33. B. Meggers, *Am. Anthropol.* **56**, 801–824 (1954).
34. K. Flannery, J. Marcus, *The Creation of Inequality: How Our Prehistoric Ancestors Set the Stage for Monarchy, Slavery, and Empire* (Harvard Univ. Press, 2012).
35. J. Scott, *Against the Grain: A Deep History of the Earliest States* (Yale Univ. Press, 2017).
36. B. Trigger, *Understanding Early Civilizations: A Comparative Study* (Cambridge Univ. Press, 2012).
37. K. Wittfogel, in *The Prehistory of the Tehuacan Valley: Vol. 4 Chronology and Irrigation*. F. Johnson, Ed. (Univ. of Texas Press, 1972); pp. 59–80.
38. D. Overstreet, D. Grignon, *Wisc. Archeol.* **102**, 1 (2021).
39. B. Hawk, *Life of Black Hawk, or Ma-ka-tai-me-she-kia-kiak*, J. G. Kennedy, Ed. (Penguin, 1883).
40. T. Wilkinson, *J. Field Archaeol.* **9**, 323–333 (1982).
41. J. Bintliff, A. Snodgrass, *Curr. Anthropol.* **29**, 506–513 (1988).
42. R. Fraser *et al.*, *J. Archaeol. Sci.* **38**, 2790–2804 (2011).
43. M. Boyd, C. Surette, *Am. Antiq.* **75**, 117–133 (2010).
44. R. Archibald, *Upper Country: A Journal of the Lake Superior Region* **3**, 4 (2015).
45. M. Abrams, G. Nowacki, B. Hanberry, *J. Torrey Bot. Soc.* **149**, 101–121 (2022).
46. W. Balée, T. Swanson, M. Zurita-Benavides, J. Macedo, *Lat. Am. Antiq.* **34**, 842–856 (2023).
47. C. Erickson, *Amazonia: The historical ecology of a domesticated landscape. Handbook of South Am. Arch* (Springer, 2008), pp. 157–183.
48. A. Ford, *Archaeolo. Papers of the Am. Anthro. Asso.* **35**, 106–119 (2024).
49. K. Lightfoot *et al.*, *Journal of Cali and Great Basin Anthro* **41**, 187–205 (2021).
50. M. McLeester *et al.*, Data from: Archaeological Evidence of Intensive Indigenous Farming in Michigan's Upper Peninsula, USA. Zenodo (2025); https://zenodo.org/records/15106949.

ACKNOWLEDGMENTS

This project was possible because of the support of the Menominee Indian Tribe of Wisconsin, and we thank them for allowing us to share these results. We are tremendously grateful to the Boerner family for allowing us to conduct this research on their property, and especially to T. Boerner for his hospitality and assistance throughout this project. We also want to thank S. Surface-Evans, F.A. Avila, and W. Munson-Scullin for their assistance with multiple aspects of this research. We are also grateful to the anonymous reviewers whose comments strengthened this article. **Funding:** Fieldwork and data processing were supported by grants from the National Science Foundation's Archaeometry Program (#1822107), the National Endowment for the Humanities (HAA-300911-24), the Elfrida Frank Foundation, and the Clare Garber Goodman Fund for Anthropological Research. Equipment acquisition was supported by a grant from the Neukom Institute for Computational Science. **Author contributions:** Project conceptualization, field investigation, methodological development, funding acquisition, and writing: M.M. Conceptualization, field investigation, methodological development, funding acquisition, resources provision, project management, and writing: J.C. Data processing, data curation, visualization, and writing: C.F. Field investigation and writing: J.A. Field investigation, conceptualization, and writing: D.O. Field investigation, conceptualization, and writing: D.G. **Competing interests:** The authors declare no competing interests. **Data and materials availability:** Data are available online at Zenodo (*50*).

SUPPLEMENTARY MATERIALS

science.org/doi/10.1126/science.ads1643
Supplementary Text; Figs. S1 to S7; Tables S1 to S3; References (*51*–*53*);
MDAR Reproducibility Checklist

Submitted 1 August 2024; resubmitted 12 November 2024; accepted 7 April 2025
10.1126/science.ads1643

MARINE CONSERVATION

Global tracking of marine megafauna space use reveals how to achieve conservation targets

All authors with their affiliations appear at the end of this paper.

The recent Kunming-Montreal Global Biodiversity Framework (GBF) sets ambitious goals but no clear pathway for how zero loss of important biodiversity areas and halting human-induced extinction of threatened species will be achieved. We assembled a multi-taxa tracking dataset (11 million geopositions from 15,845 tracked individuals across 121 species) to provide a global assessment of space use of highly mobile marine megafauna, showing that 63% of the area that they cover is used 80% of the time as important migratory corridors or residence areas. The GBF 30% threshold (Target 3) will be insufficient for marine megafauna's effective conservation, leaving important areas exposed to major anthropogenic threats. Coupling area protection with mitigation strategies (e.g., fishing regulation, wildlife-traffic separation) will be essential to reach international goals and conserve biodiversity.

Together with the recently finalized United Nations High Seas Treaty (*1*, *2*), the Kunming-Montreal Global Biodiversity Framework (GBF) (*3*, *4*) seeks to protect, conserve, and manage at least 30% of oceans. This is a necessary step to support halting the loss of marine biodiversity (GBF Target 3), which has been particularly acute for large marine species (*5*–*7*). These include several iconic large marine vertebrates that have been driven to extinction by overexploitation [e.g., the Steller's sea cow (*Hydrodamalis gigas*), the great auk (*Pinguinus impennis*), and the Japanese sea lion (*Zalophus japonicus*)], and many others currently showing precipitous declines in abundance [e.g., the hawksbill turtle (*Eretmochelys imbricata*), shortfin mako shark (*Isurus oxyrinchus*), and North Atlantic right whale (*Eubalaena glacialis*)]. These mobile and highly migratory marine vertebrates, hereafter marine megafauna, can act as ecosystem and climate sentinels (*8*) (being good surrogates for other biodiversity) and hold key functional roles that assist in structuring and maintaining ecosystems (*9*–*11*). However, close to a third of species across marine megafauna taxa are now threatened with extinction (*5*, *12*–*18*).

Certain characteristics of marine megafauna, such as *K*-selected life-history traits, place them at priority for systematic conservation planning [i.e., high vulnerability and high irreplaceability (*19*)] and make the "effective conservation" outlined in GBF Target 3 urgently needed. Many also migrate thousands of kilometers crossing multiple exclusive economic zones (EEZs) and areas beyond national jurisdictions (ABNJs), presenting a challenge for area-based conservation approaches (*20*). Notably, such approaches are traditionally based on known geographical ranges reflecting historically known boundaries (*18*) or static maps of occurrence (*21*). However, devising a management plan that effectively conserves migratory species within Ecologically and Biologically Significant Areas (*22*) requires an understanding of how the species use space. Particularly, detecting important marine megafauna areas used for key life-history events, such as breeding or feeding and migratory behaviors, henceforth IMMegAs [to use a term similar to those recognized by the International Union for the Conservation of Nature (IUCN), such as IMMA (Important Marine Mammal Areas) or ISRA (Important Shark and Ray Areas)] is only tractable using telemetry data (*20*, *23*–*27*). Despite the challenges associated with collating such data at global scale (*28*), the detection of global IMMegAs is essential to understanding marine megafauna conservation needs to inform global treaties and should therefore be prioritized for creating the network of marine protected areas (MPAs) aimed by GBF (i.e., the planned increase to 30% of area protection).

Using telemetry data to understand global space use by marine megafauna

We assembled a telemetry dataset unparalleled in size and scope [as the result of a global effort initiated by the MegaMove project (*29*)] by accepting voluntary contributions of tracking data of highly mobile marine vertebrates—here referred to as marine megafauna, despite some (particularly flying birds) being under the 45-kg threshold (*10*). Our dataset encompasses more than three decades of tracked movements (1985 to 2018) from 15,845 individuals across 121 species, which after curation (*30*), resulted in 12,794 individual tracks from 111 species, covering 71.7% of the area of the world's oceans (Fig. 1). Species include flying birds (hereafter birds), cetaceans (mostly whales but also dolphins), fishes (mostly sharks), penguins, polar bears (*Ursus maritimus*), seals, sirenians (i.e., dugongs and manatees), and turtles. See fig. S1 for latitudinal and longitudinal coverage of the dataset, and tables S1 to S3, respectively, for lists of species tracked, tracking data details, and species-specific information. According to global assessments by the IUCN (*18*), of the 111 species considered, ~70% have decreasing (54 species) or unknown (23 species) population trends, and more than 50% (58 species) have a threatened conservation status of Critically Endangered (CR), Endangered (EN), or Vulnerable (VU) (table S4). Five main regions exhibited the highest effective number of tracked species [as calculated based on the Shannon entropy (*31*)]: the central Indian Ocean, northeast Pacific, Atlantic northeast and northwest, and around Mozambique and South Africa. A few other locations empirically known as having high animal occurrence also showed a high number of species (fig. S2). Areas where more tracking data could be made available include southeast Asia, north of Europe (e.g., Spitsbergen and Greenland), Australia, central Pacific Ocean, and western Africa (particularly the southwest Atlantic and Gulf of Guinea) (Fig. 1 and fig. S2).

Using properties of the movement detected in the tracking dataset, including speed, direction, and movement coherence (*30*) (figs. S12 and S13), we identified IMMegAs based on key behaviors reflected in residency or migratory (including nomadic or dispersive) behavior. We did this by using an approach (*30*) able to evaluate these behaviors collectively across multiple tracks without relying on interpolation across highly variable sampling intervals. This is not possible with the traditionally used state-space models that are typically designed to detect behavioral states on single tracks after interpolating position estimates [e.g., (*32*)].

We then assessed how much of the IMMegAs occurred within existing MPAs (including marine parks) (*33*) or exclusive economic zones [EEZs; (*34*)] (shown in fig. S3). We used an optimization algorithm to estimate what configuration of the area covered by our tracking dataset would yield the best selection for setting protected areas for marine megafauna, giving priority to grid cells that are used for both residency and migratory behaviors across multiple taxa (*30*). For comparison, we repeated this procedure after developing statistical models to predict areas likely to be used for residency or migration for each taxon within the areas covered by our tracking dataset (*30*). For data used as input for the models, see Table 2. After this modeling procedure, we considered the priority grid cells as those resulting in highest probabilities (i.e., >0.5 and closest to 1) of being an important area across all taxa.

Finally, we assessed the extent to which the GBF's planned increase to 30% in area protection could assist with reducing impacts from marine megafauna's exposure to anthropogenic threats with a global footprint (*35*), such as fishing (*36*–*38*), shipping (*39*–*41*), warming

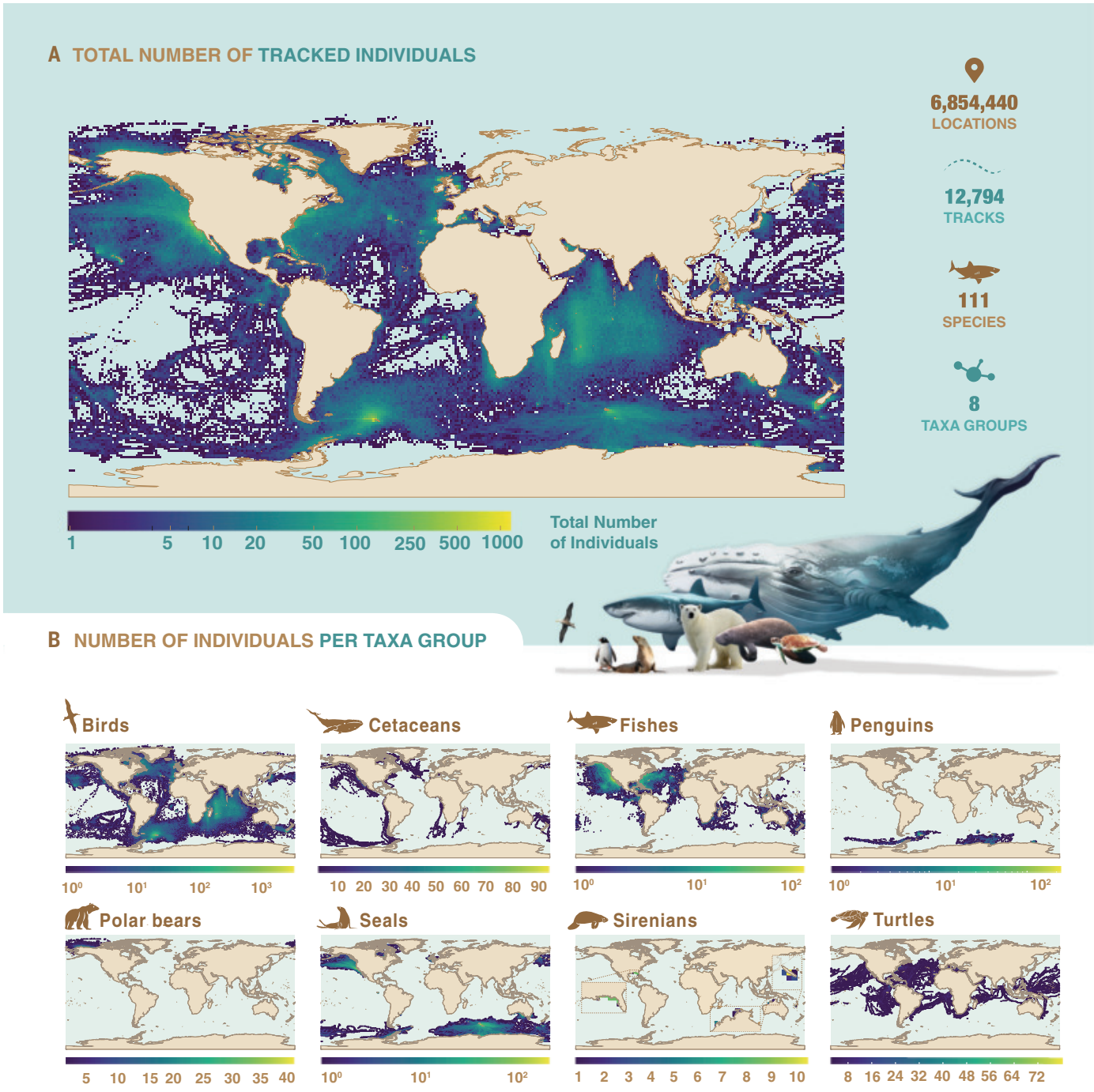

Fig. 1. Tracked movements of marine megafauna at the global scale. (**A**) Map of the total number of 12,794 individual track locations in the global dataset at 1° resolution showing the global coverage of 71.7% of the global ocean. (**B**) Maps per taxon showing the number of distinct individual track locations within each 1° grid cell. From top left to bottom right, maps per taxon show 6324 individual tracks for 39 species of flying birds; 749 for cetaceans, including 11 whales and 3 delphinid species; 1760 for fishes, including 23 shark species, 2 manta rays, and 1 ocean sunfish; 1324 for 6 species of penguins; 65 for polar bears; 1698 for 16 species of seals; 28 for sirenians, including dugongs and West Indian manatees; and 846 for all 7 sea turtles. The latitudinal and longitudinal coverage of tracked data is displayed in fig. S1. For reference, the first position obtained for each tracked individual (i.e., representing tagging locations), as well as captured and expected global biodiversity, is given in fig. S2. Maps showing the spatial extent of space use per species at 1° resolution can be seen in the data repository.

(*42*–*45*), plastic (*46*, *47*), and noise pollution (*48*, *49*). We identified these as threats on the basis of the IUCN Threats Classification Scheme (TCS) v3.3 (*50*, *51*) complemented with information from existing literature (*12*, *52*–*54*) and expert knowledge (fig. S4, and see table S4 for details). We then obtained available global threat data for fishing intensity (*55*), shipping density (*56*), plastic density (*46*, *57*), and warming (*58*, *59*) and considered noise to be ubiquitous [based on (*60*)], as no noise dataset is currently available at the resolution needed for a global analyses [but see, e.g., (*61*)].

Known biases (*23*, *62*, *63*) associated with uneven sampling and with tagging individuals in known aggregations or colonies were reduced in our analyses as far as possible by using multiple tagging sites for each species and, where applicable, by normalizing data to allow for direct comparisons across species and taxa. From specific tests to

assess the influence of (i) tagging location bias, (ii) temporal resolution of tracking data (i.e., including only one location per individual per day, in addition to all locations detected), and (iii) spatial resolution (i.e., repeating all procedures at 0.5°, 1°, and 2° grid cells), we found that these potential confounding factors had negligible effects on our main conclusions (figs. S5 to S8). Finally, randomization of tracks confirmed that animals are selectively using space for important behaviors (fig. S14).

Detected ecologically important areas for marine megafauna and extent of existing threats

We found that, on average, 66.1% of the total area covered by our tracking data was used as migratory corridors (50%) or residencies (44.8%) (Fig. 2A), with ~29% used for both behaviors (*30*); noting that for sirenians, data were insufficient to detect migratory behaviors (fig. S9). Animals spent on average 90% of their tracked time (estimated using one position per day) within areas where we detected these behaviors (Fig. 2B). Most of this time (~80%) was spent in areas used for residency (or both residency and migration) (fig. S10), with considerable overlap across both behaviors.

On average, only 7.5% of the entire area covered by our tracking dataset occurred inside MPAs (which currently cover ~8% of the global ocean), with ~5% corresponding to areas of detected residency or migratory behaviors (Fig. 2). Similarly, animals spent a greater amount of time outside, than inside, MPAs (on average >85%). The time spent inside MPAs corresponded, on average, to 13.6% of all time animals spent displaying residency or migratory behaviors (ranging between 0.3% for polar bears and 23.9% for penguins) (Fig. 2). The results indicate limited opportunity for meaningful conservation of marine megafauna within the current extent of global MPAs, which were mainly designed to protect specific habitats rather than threatened mobile marine megafauna. However, conservation efforts could be considerably improved in the future by specifically including IMMegAs in new MPA placement.

All space use and identified residency and migratory behaviors occurred with a ~40/60% split, respectively, between EEZs and the high seas, respectively (which, also respectively, cover 41.3 and 58.7% of the oceans) (Fig. 2). A similar split of space use between EEZ and high seas was obtained across each taxon, with clear exceptions for sirenians and polar bears (for which most movements occurred inside EEZs). Despite this pattern of space use slightly biased toward the high seas, most time (on average 74.1%, of which 67.1% corresponded to detected migration or residency) was spent inside, rather than outside, EEZs, and ranged from 61.5% for flying birds to 90.2% for cetaceans (Fig. 2). Although protection of high seas IMMegAs is urgently needed, the large proportion of time that animals spend conducting important behaviors within EEZs suggests that an initial focus on enhancing protection

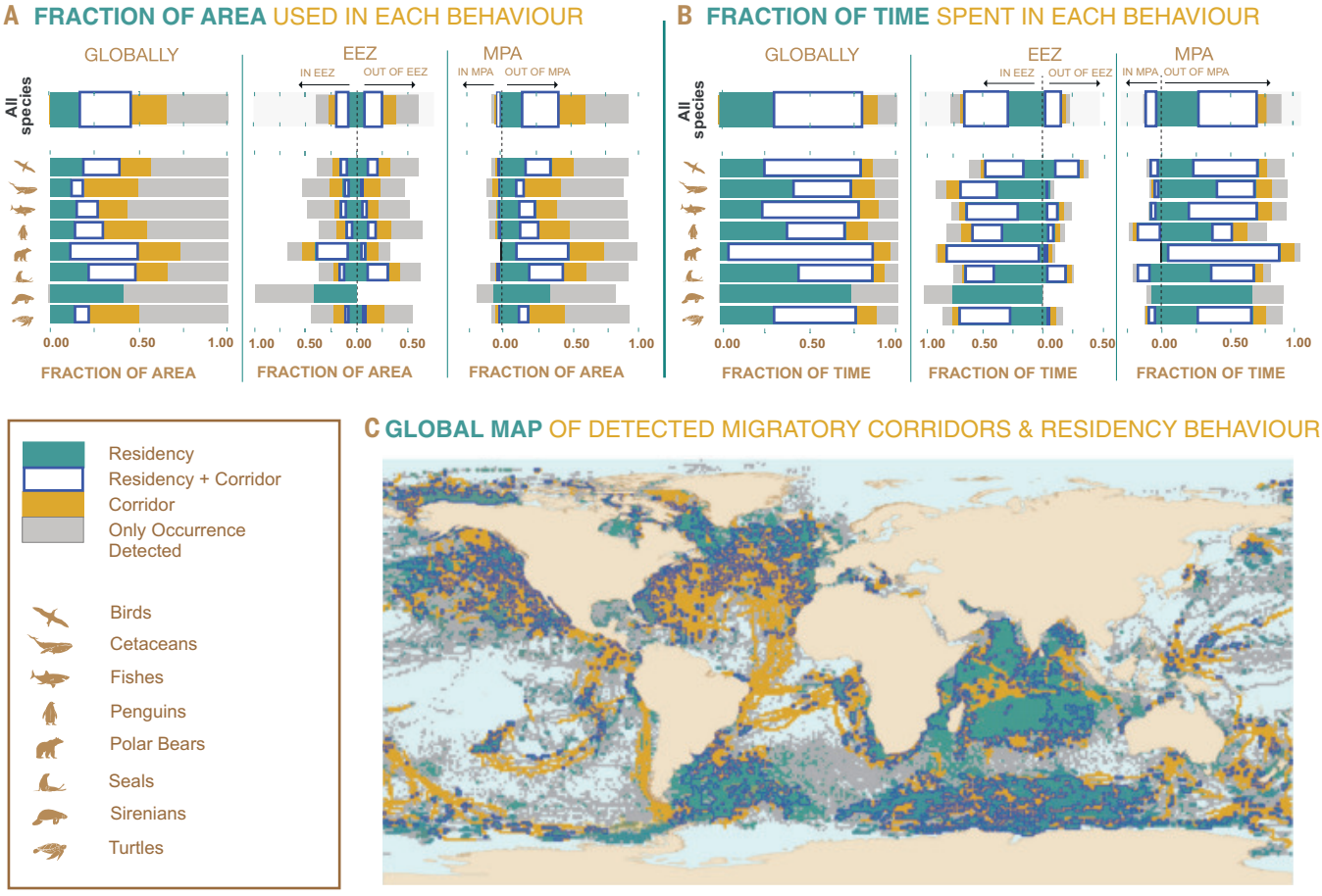

Fig. 2. Global space use of marine megafauna and time spent in different behaviors. Fractions of area (**A**) and time (**B**) used by animals globally (left plots), within and outside exclusive economic zones (EEZs) (middle plots), and within and outside existing marine protected areas (MPAs) (right plots), showing how much of the movements corresponded to detected migratory corridors or residency. Results are shown across all species together (top bar) and for each taxon (as displayed in the legend). For each taxon, the light gray portion in the bars indicates movement where no behaviors were detected. Species in each taxon group include flying birds (listed as birds), cetaceans (mostly whales but also dolphins), fishes (mostly sharks), penguins, polar bears (*Ursus maritimus*), seals, sirenians (i.e., dugongs and manatees), and turtles. (**C**) Map of detected migratory corridors, residence areas, and both corridors and residencies across taxa. Gray indicates grid cells where tracking data were available but no specific behavior was identified for any taxon. Light blue areas depict regions where we did not have tracking data. Maps of detected behaviors per taxon can be seen in fig. S9.

Table 1. Evidence of impacts from overlap of marine megafauna with anthropogenic threats. Examples of the range of impacts derived from the overlap of marine megafauna with anthropogenic threats such as climate warming, plastic pollution, shipping, noise pollution, and fishing. SST, sea surface temperature; UV, ultraviolet.

Birds (flying)	Cetaceans	Fishes	Penguins	Polar bear	Seals	Sirenians	Turtles
Climate							
Decreased survival	**UV damage**	**Habitat shift**	**Reduced prey**	**Habitat contraction**	**Habitat shift**	**Reduced food**	**Sex bias**
Affected survival and population growth rate of black-browed albatross juveniles with SST changes (*83*)	Increased skin lesions on whale related with increased UV irradiance (*84*)	Reduced counts of Scalloped hammerhead sharks *Sphyrna lewini* associated with rise in SST (*85*)	Decreased population size for penguin prey species with climate change (*86*)	Contraction of polar bear's habitat in the Arctic linked to long-term sea ice loss (*87*)	Decreased survival of southern elephant seal due to effects of sea ice dynamics on access to foraging (*88*)	Reduced dugong density by ~70% due to seagrass die-off triggered by an extreme heat wave (*89*)	Female-biased turtle populations linked to warming temperatures (*90*)
Plastic							
Ingestion	**Ingestion**	**Ingestion**	**Ingestion**	–	**Entanglement**	**Ingestion**	**Ingestion**
Death of shearwater and northern gannet due to plastic ingestion (*91*)	Stranded sperm whale stomachs with large amounts of plastic debris (*92*)	Threatened filter-feeding elasmobranchs by microplastic (*93*)	Plastic ingestion may have caused death (*94*)		Mortality of fur seals due to entanglement in marine debris (*95*)	Death of West Indian manatees from ingestion of plastic debris (*96*)	50% probability of mortality when turtles ingest pieces of plastic (*97*)
Shipping							
Habitat loss	**Ship strike**	**Ship strike**	**Noise effects**	**Ship strike**	**Propeller strike**	**Ship strike**	**Ship strike**
Habitat loss for common Eider's avoiding shipping traffic (*98*)	Increased ship strikes with humpback whales in shipping lanes (*39*)	Mortality of whale sharks correlated with risk of collision with ships (*41*)	Population collapse concomitantly with increase in noise (*99*)	Increased vulnerability of polar bears to vessel strike (*100*)	Propeller strikes affect harbor seals (*101*)	Death of manatees due to boat collisions (*102*)	Decreased survival of green turtles due to boat strikes (*103*)
Noise							
–	**Behav. change**	–	–	**Disturbance**	**Physical damage**	**Behav. change**	–
	Change in humpback whales foraging activity due to ship noise (*104*)			Disturbance of maternal dens due to seismic surveys (*105*)	Temporary hearing loss of gray and harbor seals around the British Isles (*106*)	Reduced foraging habitat for manatees due to boat noise (*107*)	
Fishing							
By-catch	**By-catch**	**Mortality**	**Reduced prey**	–	**Entanglement**	**Entanglement**	**By-catch**
High bycatch of seabirds in longline fisheries (*38*)	Higher rates of dolphin bycatch in a trawl fishery (*108*)	Greater mortality of pelagic sharks where sharks have higher exposure to longline fisheries (*23*)	Decreased population size of prey species with increased fishing of Antarctic Krill (*86*)		Increased entanglement of Cape fur seals associated with fishing (*109*)	Manatee mortalities from entanglement in fishing gear (*110*)	High levels of turtle bycatch in fishing gear hotspots (*37*)

within jurisdictions could provide the fastest benefits for marine megafauna conservation, particularly because implementation may be easier.

To identify what areas could be prioritized for protection, we used an optimization algorithm (figs. S15 and S16) to select a total of 30% of the 71.7% area covered by our tracking dataset (i.e., 21.3% of the global ocean; Fig. 3). We did this because our tracking dataset does not cover the entire ocean, and also to allow for later additions of new protected areas if other IMMegAs are identified once new tracking data are available. The optimization algorithm aims to highlight which areas could provide higher representativeness of IMMegAs, but also to indicate where the additional protected areas could be complementary to existing MPAs [sensu (*19*)], which currently fail to represent marine megafauna space use (*25*) (Fig. 3). Our results show that 30% area protection allows coverage of only less than half of the IMMegAs that we discovered (41.6 and 38.8%, respectively, based on data and model predictions; fig. S17), leaving ~60% unprotected (58.4%, and 61.2% based on data and model predictions, respectively) (Fig. 3).

Our complemented IUCN Threats Classification Scheme (*50*, *51*) (table S4) showed that commercial fishing and climate change affect more than 80% of the species included in our dataset (fig. S4). Shipping has impacts on species across all taxa, including all turtles, sirenians, polar bears, and most species of cetaceans considered, plus five birds, four fishes, five seals, and one penguin. Plastic pollution is a threat for all turtles and seals [but not yet listed on IUCN for leopard seals (*Hydrurga leptonyx*)], most cetaceans, and ~35% of birds. Some fishes are also listed as potentially being affected by this threat, including two manta rays and five sharks. Noise is listed as affecting all cetaceans, some seals, both sirenians, and also the polar bear, but for the latter this is likely due to potential disturbance of maternal dens on land.

Overlaying the identified (and predicted) areas used by marine megafauna for migration or residency behaviors at a global scale with each of the major global anthropogenic threats considered here (fig. S11), we found that >96% of IMMegAs are exposed to plastic pollution, shipping, and warming, and ~75% to fishing. This exposure includes overlaps within the areas of highest pressure observed for most threats—for example, in the North Atlantic, where we detected important areas for birds, cetaceans, fishes, and turtles (Fig. 2 and fig. S9).

Table 2. Summary of the logistic modeling inputs and results per taxon. Results of the generalized linear models relating the probability of a grid cell to be used as residence or for migratory behaviors with the set of environmental variables included in each model. Shown are the results for the highest ranked model according to the weight of the Akaike's information criteria (*wAIC*), as well as the number of parameters (*k*), the percentage of deviance explained (*pcdev*), and *Kappa*. Bold indicates the models not used to estimate the important marine megafauna areas (IMMegAs) derived from our modeling predictions (as presented in Fig. 3 and fig. S11). Species in each taxon group include flying birds (listed as birds), cetaceans (mostly whales but also dolphins), fishes (mostly sharks), penguins, polar bears (*Ursus maritimus*), seals, sirenians (i.e., dugongs and manatees), and turtles.

Taxon	Input			Results									
	Number of grid cells with:			Residence behavior					Migratory behavior				
	Presence	Residency	Migration	Model	*k*	*wAIC*	*pcdev*	*Kappa*	Model	*k*	*wAIC*	*pcdev*	*Kappa*
Birds	35,875	13,448	9,128	2	19	1.000	4.13	0.22	2	19	1.000	11.19	0.33
Cetaceans	4,397	1,501	1,758	2	19	1.000	16.52	0.44	2	19	0.980	12.62	0.29
Fishes	15,648	4,346	4,252	2	19	1.000	14.44	0.38	2	19	1.000	12.56	0.30
Penguins	1,385	446	452	1	17	1.000	13.62	0.4	2	19	1.000	40.16	0.56
Polar bear	1,124	451	803	2	14	0.995	24.78	0.33	2	14	1.000	27.78	0.48
Seals	11,358	5,510	7,175	2	19	1.000	3.12	0.22	2	19	1.000	14.91	0.30
Sirenians	114	27	0	–	–	–	–	–	–	–	–	–	–
Turtles	10,360	3,462	3,370	3	7	1.000	7.71	0.28	**2**	**19**	**1.000**	**5.18**	**0.17**

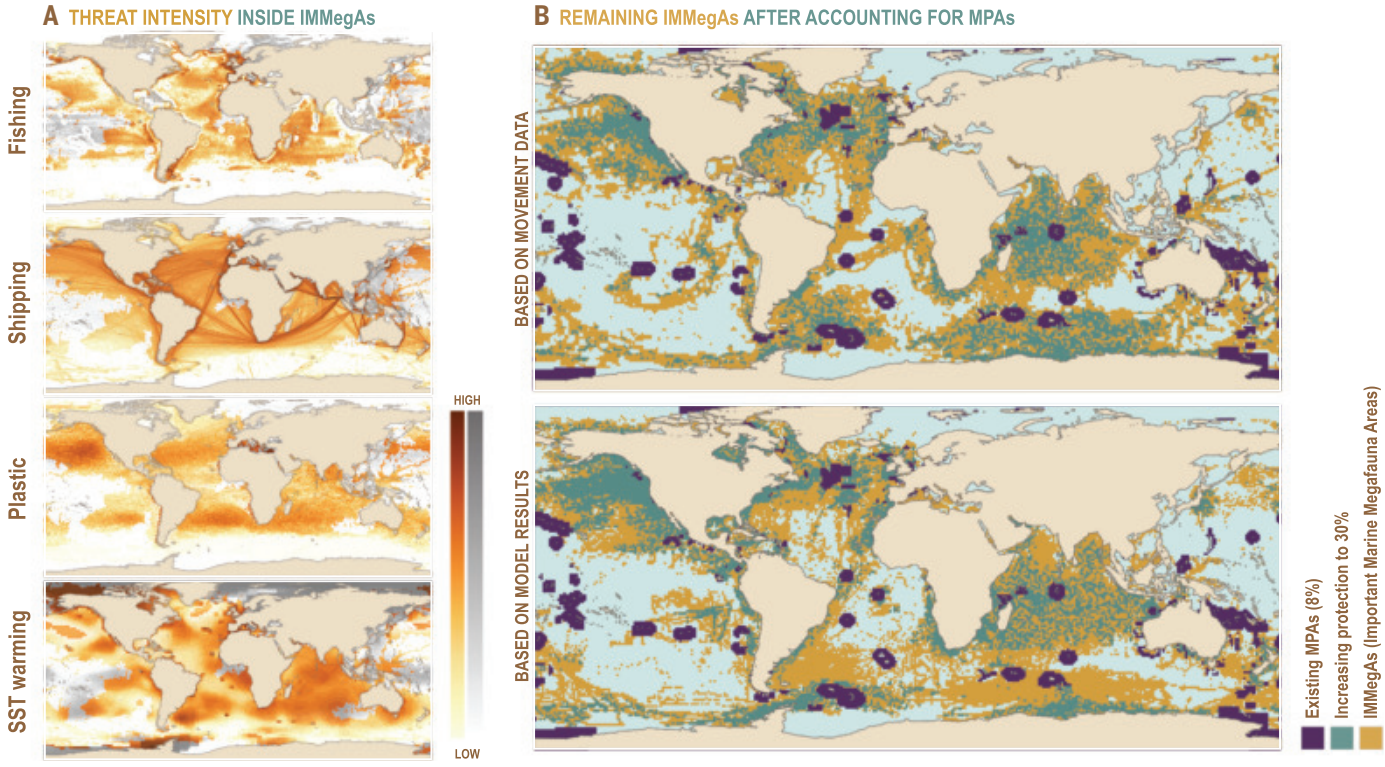

Fig. 3. Increase in area protection to 30% will leave ~60% of IMMegAs exposed to major anthropogenic threats. (**A**) Maps depicting average threat intensities for major anthropogenic threats with a global footprint: (from top to bottom) fishing, shipping, plastic pollution, and sea surface temperature (SST) warming. Displayed with an orange color palette are the threat intensities occurring inside IMMegAs, while a gray color palette is used to show the threat intensities outside IMMegAs. Note that we considered noise to be ubiquitous, as no noise dataset is currently available at the resolution needed for a global analyses. (**B**) Maps showing how much the increase in MPAs from the current 8% (purple) to 30% (green) would cover from our prioritization of IMMegAs detected from movement data (top map) and from our modeling predictions (bottom results). Note that coverage by MPAs only translates into protection from the anthropogenic threats considered if they are designated with the highest level of protection (i.e., with no activities allowed), and even then MPAs could only be effective for protection from fishing and shipping, leaving plastic and warming threats to continue to affect species. In addition to the increase in the current extent of MPAs, the introduction of mitigation strategies will assist in reducing the impact of existing threats and therefore the likelihood of human-induced extinctions.

Mitigation strategies will be needed in addition to the proposed increase in area protection to safeguard marine megafauna

Our results reveal that the 30% threshold is insufficient to encompass all IMMegAs globally (Fig. 3), leaving substantial conservation risks for marine megafauna. Considering the ubiquity of existing threats, which are pervasive in the IMMegAs that we detected (Fig. 3 and fig. S11), and the limited scope of the 30% GBF target for area protection, attaining the goal of zero loss of important biodiversity areas and halting human-induced mortality of threatened species seems unlikely (noting some management measures already in place for some species, table S5). Shipping and fishing can in part be alleviated by increasing MPAs [particularly if the highest level of protection is afforded (*64*)], which can also help reduce noise pollution. However, plastic pollution or climate change impacts will not be alleviated with the planned increase in area protection [even if MPAs can assist improving species resistance and resilience (*65*)]. Therefore, attaining the goal of zero loss of important biodiversity areas will need further action to mitigate anthropogenic pressures.

To reduce exposure of marine megafauna to existing threats and achieve the goals set out in the GBF, the introduction of additional forms of ocean management will be needed, including greater scrutiny of practices and additional direct management decisions with increased enforcement. For example, direct mortality can be reduced by applying fishing thresholds and enforcing standards in fishing operations (including modifications to gear) (*66*–*70*), and by developing wildlife-ship traffic separation schemes and slow-down areas (*71*, *72*) [e.g., to 2.16 knots (*73*)]. If applied in tandem with the increase in protected areas, such interventions will afford marine megafauna a much greater spatial protection from the major threats of industrialized fishing (*23*) and shipping (*41*) known to cause direct mortality (Table 1).

Our analyses show that animals use a large proportion of the high seas but spend the majority of their time within jurisdictions. This presents an opportunity for marine megafauna conservation because individual countries regulate and control most operations within their borders and are therefore able to implement mitigation measures to manage species that use their EEZs. Management of IMMegAs in the high seas, outside national jurisdictions, would benefit from better integration into the United Nations Convention for the Law of the Sea (UNCLOS) and should be considered in the ongoing process to better regulate biological resources in the high seas (*1*, *2*). For shipping threats specifically, International Maritime Organization regulations can reduce impacts and propel conservation success. For example, the double hull policy resulted in an average reduction of up to 62% in the size of oil spills (*74*). Engaging (and better regulating) the private sector is another timely way to advance conservation [e.g., (*75*)], as environmental damage is increasingly recognized as a threat to financial stability (*75*, *76*). Past management decisions, either involving the private sector [e.g., end of the whaling industry following the moratorium by the International Convention for Regulation on Whaling (*77*)] or by listing species on CITES [Convention on International Trade in Endangered Species (*78*)] have demonstrated success by leading to populations' recovery. However, the drivers of contrasting trajectories of similar populations or species (e.g., right whales increase in the Southern Ocean versus decrease in the North Atlantic) are not well understood and likely relate to different exposure to anthropogenic threats in the different regions.

Creating a larger network of MPAs will also greatly benefit from following a systematic conservation planning framework. Although our aim was to identify IMMegAs (rather than outlining what the final 30% of area protection should look like), we followed the initial necessary steps of that framework, including (i) using marine megafauna biodiversity data (as a surrogate for marine biodiversity); (ii) using the set targets from the GBF and UN High Seas Treaty as a goal; (iii) focusing on complementing existing MPAs; and (iv) selecting IMMegAs for potential inclusion as MPAs. We then provide a scenario for protection for up to 30% extension of MPAs to show that even if all areas selected for protection specifically included IMMegAs, the 30% protection would still be insufficient to reach set targets, and other mitigation measures will be needed. To follow a systematic conservation planning approach, the final selection of protected areas should also take into consideration aspects not considered here, such as ecosystems of high ecological importance or habitat types that are not yet well represented, as well as considerations of equity and principles of environmental justice (*79*). It is, however, likely that the final selection of areas for protection will end up being designed to minimize impacts to stakeholders (including the fishing, shipping, energy production, and tourism industries). Such a possible result further reinforces our conclusion that relying on the 30% area protection will be insufficient to reach the goal of zero loss of important biodiversity areas and halt human-induced mortality of threatened species, and that additional mitigation measures are needed before it is too late.

The work we provide here shows the power of assembling tracking datasets to answer pressing conservation concerns. The continued expansion of MegaMove through voluntary contributions will foster greater collaborations allowing researchers to fill data gaps and further reduce biases. Whereas our tracking data cover about 71% of ocean space, the tagging effort was neither random nor uniform in space and time, and 29% of the ocean space was not covered by our dataset (including the central and northwest Pacific ocean). We suggest that statistical models using existing tracking data as input could be used to develop refined global species distributions that take into account animal movements associated with short-term changes in environmental parameters to project the likelihood of encountering animals in areas underexplored by telemetry or bio-logging (*80*–*82*).

We also recognize that the available threat distribution data that we used here are incomplete and do not include, for example, illegal or artisanal fishing fleets, or discrimination across fishing gear (which affects species differently). This means that a more detailed spatio-temporal analysis of exposure to threats, as well as an assessment of the vulnerability of different species to specific threats, is required to quantify their potential impacts on species' life-history characteristics. Consideration of the phylogenetic diversity of marine megafauna by examining evolutionary drivers could also be relevant to improving spatial maps. Nevertheless, the IMMegAs that we have identified are key to informing the expansion of existing MPAs to reach the 30% target both within EEZs and in the High Seas.

REFERENCES AND NOTES

1. Editorial, *Nature* **615**, 373–374 (2023).
2. United Nations - Intergovernmental Conference on Marine Biodiversity of Areas Beyond National Jurisdiction, https://www.un.org/bbnj.
3. G. Wright, J. Rochette, K. Gjerde, I. Seeger, "The long and winding road: Negotiating a treaty for the conservation and sustainable use of marine biodiversity in areas beyond national jurisdiction," IDDRI, Studies N°08/18 82 *p.* (2018).
4. UN Convention on Biological Diversity, 15th Conference of Parties (COP15) (2022); https://www.cbd.int/cop.
5. D. J. McCauley *et al.*, *Science* **347**, 1255641 (2015).
6. C. M. Duarte *et al.*, *Nature* **580**, 39–51 (2020).
7. C. Pimiento *et al.*, *Sci. Adv.* **6**, eaay7650 (2020).
8. E. L. Hazen *et al.*, *Front. Ecol. Environ.* **17**, 565–574 (2019).
9. T. B. Atwood *et al.*, *Nat. Clim. Chang.* **5**, 1038–1045 (2015).
10. J. A. Estes, M. Heithaus, D. J. McCauley, D. B. Rasher, B. Worm, *Annu. Rev. Environ. Resour.* **41**, 83–116 (2016).
11. J. Roman *et al.*, *Front. Ecol. Environ.* **12**, 377–385 (2014).
12. M. P. Dias *et al.*, *Biol. Conserv.* **237**, 525–537 (2019).
13. G. T. Braulik *et al.*, *Conserv. Biol.* **37**, e14090 (2023).
14. N. K. Dulvy *et al.*, *Curr. Biol.* **31**, 5118–5119 (2021).
15. M. J. Juan-Jordá, I. Mosqueira, A. B. Cooper, J. Freire, N. K. Dulvy, *Proc. Natl. Acad. Sci. U.S.A.* **108**, 20650–20655 (2011).
16. A. D. Mazaris, G. Schofield, C. Gkazinou, V. Almpanidou, G. C. Hays, *Sci. Adv.* **3**, e1600730 (2017).
17. W. J. Ripple *et al.*, *Conserv. Lett.* **12**, e12627 (2019).
18. International Union for Conservation of Nature, The IUCN red list of threatened species. https://www.iucnredlist.org/en.
19. C. R. Margules, R. L. Pressey, *Nature* **405**, 243–253 (2000).
20. A. L. Harrison *et al.*, *Nat. Ecol. Evol.* **2**, 1571–1578 (2018).
21. AquaMaps, Standardised distribution maps fpr fishes, marine mammals and invertebrates; https://aquamaps.org/.

22. D. C. Dunn *et al.*, *Mar. Policy* **49**, 137–145 (2014).
23. N. Queiroz *et al.*, *Nature* **572**, 461–466 (2019).
24. M. Beal *et al.*, *Sci. Adv.* **7**, eabd7225 (2021).
25. M. G. Conners *et al.*, *Front. Mar. Sci.* **9**, 897104 (2022).
26. C. Johnson *et al.*, *Protecting Blue Corridors, Challenges and Solutions for Migratory Whales Navigating International and National Seas* (WWF International, 2022).
27. N. E. Hussey *et al.*, *Science* **348**, 1255642 (2015).
28. A. M. M. Sequeira *et al.*, *Methods Ecol. Evol.* **12**, 996–1007 (2021).
29. Marine Megafauna Movement Global Initiative, MegaMove. https://megamove.org/.
30. Materials and methods are available as supplementary materials.
31. C. E. Shannon, *Bell Syst. Tech. J.* **27**, 379–423 (1948).
32. T. A. Patterson, L. Thomas, C. Wilcox, O. Ovaskainen, J. Matthiopoulos, *Trends Ecol. Evol.* **23**, 87–94 (2008).
33. UNEP-WCMC and IUCN, U.-W. a. IUCN, Ed. (Cambridge, 2021); https://www.protectedplanet.net/.
34. Flanders Marine Institute, Maritime Boundaries Geodatabase, version 11 (2019); https://doi.org/10.14284/382
35. A. M. M. Sequeira *et al.*, *Front. Mar. Sci.* **6**, 639 (2019).
36. B. Worm, D. P. Tittensor, *Proc. Natl. Acad. Sci. U.S.A.* **108**, 11942–11947 (2011).
37. R. L. Lewison *et al.*, *Proc. Natl. Acad. Sci. U.S.A.* **111**, 5271–5276 (2014).
38. T. A. Clay, S. Oppel, J. L. Lavers, R. A. Phillips, M. L. Brooke, *Mar. Biol.* **166**, 8 (2019).
39. J. M. Aschettino *et al.*, *Front. Mar. Sci.* **7**, 121 (2020).
40. M. F. McKenna, J. Calambokidis, E. M. Oleson, D. W. Laist, J. A. Goldbogen, *Endanger. Species Res.* **27**, 219–232 (2015).
41. F. C. Womersley *et al.*, *Proc. Natl. Acad. Sci. U.S.A.* **119**, e2117440119 (2022).
42. C. A. Bost *et al.*, *Nat. Commun.* **6**, 8220 (2015).
43. L. A. Rutterford *et al.*, *Nat. Clim. Chang.* **5**, 569–574 (2015).
44. A. M. M. Sequeira, C. Mellin, D. A. Fordham, M. G. Meekan, C. J. A. Bradshaw, *Glob. Change Biol.* **20**, 778–789 (2014).
45. E. L. Hazen *et al.*, *Nat. Clim. Chang.* **3**, 234–238 (2013).
46. M. Eriksen *et al.*, *PLOS ONE* **9**, e111913 (2014).
47. M. R. Gregory, *Philos. Trans. R. Soc. Lond. B Biol. Sci.* **364**, 2013–2025 (2009).
48. S. E. Nelms, W. E. D. Piniak, C. R. Weir, B. J. Godley, *Biol. Conserv.* **193**, 49–65 (2016).
49. J. C. D. Gordon *et al.*, *Mar. Technol. Soc. J.* **37**, 14–32 (2004).
50. International Union for Conservation of Nature, The IUCN Red List of Threatened Species (2023); https://www.iucnredlist.org.
51. International Union for Conservation of Nature, Threats Classification Scheme (Version 3.3); https://www.iucnredlist.org/resources/threat-classification-scheme.
52. I. C. Avila, K. Kaschner, C. F. Dormann, *Biol. Conserv.* **221**, 44–58 (2018).
53. B. Würsig, W. F. Perrin, J. G. M. Thewissen, *Encyclopedia of Marine Mammals* (Academic Press, 2009).
54. B. P. Wallace *et al.*, *Ecosphere* **4**, 1–49 (2013).
55. Global Fishing Watch, https://globalfishingwatch.org.
56. Marine AIS Data, https://www.exactearth.com.
57. E. van Sebille *et al.*, *Environ. Res. Lett.* **10**, 124006 (2015).
58. J. Hansen, R. Ruedy, M. Sato, K. Lo, *Rev. Geophys.* **48**, 1–29 (2010).
59. NASA Goddard Institute for Space Studies, GISS Surface Temperature Analysis (GISTEMP) (2021); https://data.giss.nasa.gov/.
60. C. M. Duarte *et al.*, *Science* **371**, 583 (2021).
61. The UK Acoustics Network, https://acoustics.ac.uk/open-access-underwater-acoustics-data/.
62. B. A. Block *et al.*, *Nature* **475**, 86–90 (2011).
63. M. O'Toole, N. Queiroz, N. E. Humphries, D. W. Sims, A. M. M. Sequeira, *Methods Ecol. Evol.* **12**, 170–181 (2020).
64. K. Grorud-Colvert *et al.*, *Science* **373**, eabf0861 (2021).
65. C. M. Roberts *et al.*, *Proc. Natl. Acad. Sci. U.S.A.* **114**, 6167–6175 (2017).
66. A. C. Godin, J. K. Carlson, V. Burgener, *Bull. Mar. Sci.* **88**, 469–483 (2012).
67. E. Gilman *et al.*, *Biol. Conserv.* **139**, 19–28 (2007).
68. G. Sales *et al.*, *Aquat. Conserv.* **20**, 428–436 (2010).
69. S. D. Goldsworthy *et al.*, *Front. Mar. Sci.* **9**, 53 (2022).
70. L. D. Jenkins, *Mar. Fish. Rev.* **74**, 26–44 (2012).
71. C. Chion *et al.*, *PLOS ONE* **13**, e0202560 (2018).
72. A. S. M. Vanderlann, C. T. Taggart, *Mar. Mamm. Sci.* **23**, 144–156 (2007).
73. J. Hazel, I. Lawler, R. H. Marsh, S. Robson, *Endanger. Species Res.* **3**, 105–113 (2007).
74. T. L. Yip, W. K. Talley, D. Jin, *Mar. Pollut. Bull.* **62**, 2427–2432 (2011).
75. A. M. M. Sequeira, U. R. Sumaila, A. A. Rogers, *Npj Ocean Sustain.* **3**, 38 (2024).
76. Insight Report In partnership with Marsh & McLennan and Zurich Insurance Group, "World Economic Forum, The Global Risks Report" (2020); https://www3.weforum.org/docs/WEF_Global_Risk_Report_2020.pdf.
77. International Whaling Commission, in *ICRW Convention,* I. W. Commission, Ed. (International Whaling Commission, 1946).
78. CITES (Conference of the Parties, Washington, DC, 1973); https://cites.org.
79. M. S. Chapman *et al.*, *One Earth* **4**, 790–794 (2021).
80. G. C. Hays *et al.*, *Trends Ecol. Evol.* **34**, 459–473 (2019).
81. M. A. Hindell *et al.*, *Nature* **580**, 87–92 (2020).
82. A. M. M. Sequeira, *Nature* **580**, 34–35 (2020).
83. S. Jenouvrier *et al.*, *J. Anim. Ecol.* **87**, 906–920 (2018).
84. L. M. Martinez-Levasseur *et al.*, *Proc. Biol. Sci.* **278**, 1581–1586 (2011).
85. G. J. Osgood, E. R. White, J. K. Baum, *J. Anim. Ecol.* **90**, 2547–2559 (2021).
86. L. Krüger, M. F. Huerta, F. Santa Cruz, C. A. Cárdenas, *Ambio* **50**, 560–571 (2021).
87. K. L. Laidre *et al.*, *Ecol. Evol.* **8**, 2062–2075 (2018).
88. S. Volzke, C. R. McMahon, M. A. Hindell, H. R. Burton, S. J. Wotherspoon, *Ecol. Evol.* **11**, 11333–11344 (2021).
89. R. Nowicki *et al.*, *Ecol. Monogr.* **89**, 01365 (2019).
90. M. P. Jensen *et al.*, *Curr. Biol.* **28**, 154–159.e4 (2018).
91. K. E. Pierce, R. J. Harris, L. S. Larned, M. A. Pokras, *Mar. Ornithol.* **32**, 187–189 (2004).
92. J. K. Jacobsen, L. Massey, F. Gulland, *Mar. Pollut. Bull.* **60**, 765–767 (2010).
93. E. S. Germanov, A. D. Marshall, L. Bejder, M. C. Fossi, N. R. Loneragan, *Trends Ecol. Evol.* **33**, 227–232 (2018).
94. M. L. Brandão, K. M. Braga, J. L. Luque, *Mar. Pollut. Bull.* **62**, 2246–2249 (2011).
95. C. W. Fowler, *Mar. Pollut. Bull.* **18**, 326–335 (1987).
96. F. L. N. Attademo *et al.*, *Mar. Pollut. Bull.* **101**, 284–287 (2015).
97. C. Wilcox, M. Puckridge, Q. A. Schuyler, K. Townsend, B. D. Hardesty, *Sci. Rep.* **8**, 12536 (2018).
98. P. Schwemmer, B. Mendel, N. Sonntag, V. Dierschke, S. Garthe, *Ecol. Appl.* **21**, 1851–1860 (2011).
99. L. Pichegru *et al.*, *Sci. Total Environ.* **849**, 157878 (2022).
100. D. D. W. Hauser, K. L. Laidre, H. L. Stern, *Proc. Natl. Acad. Sci. U.S.A.* **115**, 7617–7622 (2018).
101. J. K. Olson *et al.*, *J. Wildl. Dis.* **57**, 689–693 (2021).
102. S. Aipanjiguly, S. K. Jacobson, R. Flamm, *Conserv. Biol.* **17**, 1098–1105 (2003).
103. J. Denkinger *et al.*, *Ocean Coast. Manage.* **80**, 29–35 (2013).
104. H. B. Blair, N. D. Merchant, A. S. Friedlaender, D. N. Wiley, S. E. Parks, *Biol. Lett.* **12**, 20160005 (2016).
105. R. R. Wilson, G. M. Durner, *J. Wildl. Manage.* **84**, 1022–1024 (2020).
106. E. L. Jones *et al.*, *J. Appl. Ecol.* **54**, 1930–1940 (2017).
107. J. L. Miksis-Olds, P. L. Donaghay, J. H. Miller, P. L. Tyack, J. A. Nystuen, *J. Acoust. Soc. Am.* **121**, 3011–3020 (2007).
108. S. J. Allen *et al.*, *PLOS ONE* **9**, e93178 (2014).
109. S. Curtis, S. H. Elwen, N. Dreyer, T. Gridley, *Mar. Pollut. Bull.* **171**, 112759 (2021).
110. A. Alvarez-Alemán *et al.*, *Front. Mar. Sci.* **8**, 646021 (2021).
111. A. M. M. Sequeira, J. P. Rodriguez, Dryad: Global Tracking of Marine Megafauna Space-Use Reveals How to Achieve Conservation Targets: v1 (2024); https://doi.org/ 10.5061/dryad.x95x69ptv.

ACKNOWLEDGMENTS

This research contributes to the MegaMove project endorsed by the UN Decade of Ocean Science (megamove.org). We thank M. Heupel for early discussions, L. Londoño for early assistance with formatting data, K. Goetz for earlier involvement, and all involved in fieldwork and data collection; see full details in supplementary acknowledgments. We thank Global Fishing Watch and the Global Shark Movement Project for making data available. Ethics and permits information are fully detailed in the supplementary materials. This study has been conducted using EU Copernicus Marine Service Information (https://doi.org/10.48670/moi-00021 and https://doi.org/10.48670/moi-00019); NASA Ocean Biology Distributed Active Archive Center (OB.DAAC) data (https://oceandata.sci.gsfc.nasa.gov/opendap/SeaWiFS/L3SMI/ and https://oceandata.sci.gsfc.nasa.gov/opendap/MODISA/L3SMI/contents.html); and the European Centre for Medium-Range Weather Forecasts ERA-Interim Reanalysis product (https://www.ecmwf.int/en/forecasts/dataset/ecmwf-reanalysis-interim). Any use of trade, firm, or product names is for descriptive purposes only and does not imply endorsement by the US government. **Funding:** A.M.M.S. was funded by a 2020 Fellowship in Marine Conservation by the Pew Charitable Trusts, and ARC DP DP210103091, and through support provided by the Jock Clough Marine Foundation and three other anonymous donors. G.C.H. acknowledges funding from the Bertarelli Foundation as part of the Bertarelli Programme in Marine Science (BPMS-2017-4). D.P.C. was funded by ONR and SERDP grant RC20-C2-1284. D.W.S. acknowledges funding from ERC-2019-ADG 883583 OCEAN DEOXYFISH and NERC NE/R00997X/1. V.M.E. acknowledges funding from MCIN/AEI/10.13039/501100011033 (PID2020-114324GB-C22). S.A. was supported by Ministerio de Educación, Cultura y Deporte (Spain) [FPU15/01823]. Satellite transmission fees were funded by Universitat Politècnica de València. Tag acquisitions were supported by Universitat Politécnica de València, Asociación Chelonia and Centro de Recuperación de Animales Marinos (CRAM). A.S.A. acknowledges funding granted by the National Geographic Society Conservation Trust (no. C314-15), Coordenação de Aperfeiçoamento de Pessoal de Nível Superior - CAPES (BJT/A049-2013), and Fundação para a Ciência e Tecnologia - FCT (CEEIND/02566/2021, UIDP/04292/2020, and LA/P/0069/2020). N.P.A.B. was funded by Conselho Nacional de Desenvolvimento Científico e Tecnológico (CNPq) under grant no. 482557/2011-7. R.D.A. was funded by the North Pacific Research Board and NOAA Fisheries with additional support from Texas A&M University and the Alaska SeaLife Center. M. Antonopoulou acknowledges seed funding for this work provided by the Emirates Nature –World Wild Fund for Nature office in the UAE and by the numerous private sponsors, listed here in alphabetical order: 7Days, Abu Dhabi Urban Planning Council, Bridgestone, CASP, College of the North Atlantic, Qatar, Deutsche Bank, Dubai Electricity & Water Authority, Dubai Festival City, Emirates Palace, Environment & Protected Areas Authority, Sharjah, Environment Agency–Abu Dhabi, Fairmont, Géant, Gulftainer, HSBC, Intercontinental, Dubai Festival City, Jebel Ali Golf Resort & Spa, Jumeirah Etihad Towers, Linklaters, Momentum Logistics, Mubadala, Murjan Marinas, Nokia, Sheikha Salama bint Hamdan Al Nahyan Foundation, The Club, TimeOut Dubai, and the Young Presidents Organisation. J.A.A. was funded by a scholarship from the Comisión Nacional de Investigación Científica y Tecnológica (CONICYT),

Chile, and acknowledges the Chilean Antarctic Institute, which funded the field campaign. GLS tags were provided by the British Antarctic Survey (BAS). G.A. acknowledges The Rufford Foundation. I.A. was funded by the Basque Government and the European Data Collection Programme. M. Auger-Méthé acknowledges the Canadian Research Chairs Program. R.W.B. acknowledges the US Navy (Pacific Fleet, Atlantic Fleet, Living Marine Resources and Office of Naval Research) and the NMFS (Pacific Islands Fisheries Science Center and Southwest Fisheries Science Center). A. Barnett acknowledges the Save Our Seas Foundation, Holsworth Wildlife Research Endowment, Winifred Violet Scott Charitable Trust and the Slattery Family Trust. E.J. Belda acknowledges that satellite transmission fees were supported by personal research funds made available by the Universitat Politècnica de València. Tags acquisition was funded by Ministerio de Agricultura y Medio Ambiente (16MNSV006); Ministerio de Economía, Industria y Competitividad (CGL2011-30413); Fundación CRAM, Fundación Hombre y Territorio. J. Tomás was supported by project PrometeoII (Generalitat Valenciana) and project INDICIT (EU). Funding for the transmitters came from the JM Kaplan Foundation award to the World Wildlife Fund (WWF) Canada, and from several European institutions: the Spanish International Cooperation Agency (AECI Projects A/2991/05 and A/5641/06), the Spanish Ministry of Education and Sciences (CGL2006-02936-BOS and CGL2011-30413) and the General Foundation of the University of Valencia. The project also received funding from the European Union (Marie Curie grant nos. FP6 and FP7). A. Bennison was funded by the Irish Research Council (Project ID: GOIPG/2016/503). S.R.B. acknowledges financial support and personnel provided by NMFS (Southwest Fisheries Science Center, Southwest Region, Pacific Islands Region, and Office of Protected Resources), and the Tagging of Pacific Predators (TOPP) program of the Census of Marine Life. R.B. received funding from The Wildlife Conservation Society, The Roe Foundation Inc., NABU/Shark Tracker, The National Geographic Society Explorations Council, and The Eppley Foundation. S.E.C. acknowledges funding from the International Governance Strategy of Fisheries and Oceans Canada. H.A.C. acknowledges Australia Zoo. V.G.C. was funded by the Buenos Aires Zoo, Wildlife Conservation Society, Fondo para la Conservación Ambiental from Banco Galicia, the Cleveland Metropark Zoo–Scott Neotropical Fund, the Inter-American Institute for Global Change Research (IAI) CRN 2076 sponsored by the US National Science Foundation (NSF) grant GEO-0452325, and the Agencia Nacional de Promoción Científica y Tecnológica FONCyT PICT 2013-2099 Prestamo BID. R.H.C. was funded in part by the Dauphin Island Sea Lab, University of South Alabama, Alabama Division of Wildlife and Freshwater Fisheries under traditional Section 6 of the US Fish and Wildlife Service, the Northern Gulf Institute, Mobile Bay National Estuary Program, and the Seamen's Foundation. G.C. was supported by a Macquarie University Research Excellence Scholarship. J. Charrassin acknowledges that the Weddell seals tagging study in Dumont d'Urville by LOCEAN laboratory was supported by the Program Terre-Océan-Surface Continentale-Atmosphère from Centre National d'Etudes Spatiales (TOSCA-CNES), and the Australian Animal Tracking and Monitoring System (AATAMS), a facility of Integrated Marine Observing System (IMOS). The Institut Paul Emile Victor (IPEV) programs 109 and 394, Terres Australes et Antarctiques Françaises (TAAF), and the Australian Antarctic Division provided logistical support. A. Chiaradia acknowledges funding provided by the Australian Government Research Training Program, Australian Research Council (Linkage Project; LP140100404), Monash University, Phillip Island Nature Parks, Institut Pluridisciplinaire Hubert Curien, ANR-2010-BLAN-1728-01, Australian Conservation Foundation, The Penguin Foundation, Parks Victoria, Centre d'Etudes Biologiques de Chizé and La Rochelle Université, Holsworth Wildlife Research Trust, and Coastcare Australia. C.C. was supported by the New Caledonian Dugong Technical Committee under the 2010—2015 Dugong Action Plan in New Caledonia. E.E.G.C. was supported by the Coral Reef Initiative for the South Pacific (CRISP) mostly funded by the Agence Française de Développement (AFD). R.C. acknowledges the New Zealand Ministry for Primary Industries – BRAG; Pew Charitable Trusts; Southern Ocean Research Partnership – International Whaling Commission; Australian Antarctic Division; University of Auckland; Institut de Recherche pour le Développement, France; Conservation International; Blue Planet Marine; Opération Cétacés, New Caledonia; National Marine Mammal Laboratory – NOAA; and the Scientific Committee for Antarctic Research (SCAR), UK. M.L.C. was funded by a Pew Fellowship Award in Marine Conservation and acknowledges European project FEDER Biodiversité. E. Cuevas-Flores acknowledges the Mexican National Council for Science and Technology - Mexican Ministry of Environment and Natural Resources (project 107770, CAMP-2005-C01-046), the National Fish and Wildlife Foundation (2006-0091-005), Alliance WWF- Carlos Slim Fund, Chelonia, Inc., Satellite Tracking and Analysis Tool (STAT). S. Diamant was supported by the PADI Foundation and IDEA WILD. K.L.D. acknowledges funding support from the University of New Hampshire Marine Program, Large Pelagics Research Center, NOAA grants (NA04NMF4550391 and NA10NMF4720028), National Fish and Wildlife Foundation (2008-0076-000), and the Cape Cod Commercial Fishermen's Alliance. A.D.M.D. was funded by the Georgia Aquarium, UKG Darwin Initiative St Helena Government. T.K.D. was funded by the UCC Strategic Research Fund. L.L.D. acknowledges funding provided by the North Carolina Renewable Ocean Energy Program, administered by the Coastal Studies Institute (East Carolina University Outer Banks Campus). M.V.E. warmly thanks the Indonesian Ministry of Environment and Forestry and Ministry of Marine Affairs and Fisheries, the Cenderawasih Bay National Park Authority, the Raja Ampat MPA Management Authority, and the people and government of Raja Ampat, Milne Bay, West Papua, Bali, East Kalimantan and Nusa Tenggara Timor provinces (especially those from Desa Labuhan Jambu and Desa Kwatisore) for their sponsorship and support, as well the following donors who financially supported our tagging: the Sunbridge Foundation, SEA Aquarium Singapore, MAC3 Impact Philanthropies, and the Wolcott Henry Foundation, the owners and guests of the MV True North, Asia Coating Enterprise, M.E. Mali, D. Roozen, A. and S. Wong, E. Tan, S. Argyropolous, D. Arnall, A. Hasan, R. Mambrasar, S. Heinrichs, S. Lewis. I. Syakurachman, M. Brooks, P. Rorke-Levy, and S. Neiman. N.E. acknowledges the Dutch Caribbean Nature Alliance. C.F. acknowledges that sooty tern tracking in Seychelles was funded by the Percy Sladen Foundation, James Cadbury, Robert Gaines-Cooper, Kang Nee, Amanda O'Keefe, Colin & Fiona Short, and Brian & Margaret Jasper. Funding was provided by DFO (Emerging Fisheries), Government of Nunavut, Nunavut Wildlife Research Trust Fund, Nunavut General Monitoring Program, Nunavut Wildlife Management Board (no. 3-09-04), Ocean Tracking Network, University of Windsor, University of Manitoba, ArcticNet Centre of Excellence, Natural Sciences and Engineering Research Council Canadian, Federal Program Office of International, Polar Year (MD-112), Northern Scientific Training Program (Canadian Polar Commission), Polar Continental Shelf Project, W. Garfield Weston Award for Northern Research, and the Molson Foundation. F.F. acknowledges the Bertarelli Foundation. S.F. acknowledges financial and logistical support provided by Megaptera, its members and friends, the Greenland Institute of Natural Resources, Axa Research Fund, Exagone, Sea Blue Safari, Mikkels Vaerksted, Fondation Nature et Decouverte and the National Geographic Society Waitt Grant Program. A.S.F. was funded by the Antarctic Wildlife Research Fund (ANT-0823101), NSF Office of Polar Programs (OPP) ANT-0823101, 1250208, and 1440435, IWC, and Southern Ocean Research Partnership awards. C. Garrigue was funded by New Caledonian Government, Ministère de la Transition Ecologique et Solidaire, WWF for Nature France, Greenpeace International, and Fondation d'Entreprise Total and Opération cétacés NC. B.J.G. acknowledges the Natural Environment Research Council (NERC), Darwin Initiative, Marine Turtle Conservation Fund (USFWS, US Department of the Interior). S.D.G. acknowledges the Australian Marine Mammal Centre, Fisheries Research and Development (PN 2005/031), Integrated Marine Observing System (IMOS), DEW, Professional Association of Diving Instructors (PADI) Project Advancing Wellness and Resilience in Education (AWARE), Australian Bird Environment Foundation, Holdsworth Wildlife Research Endowment, Sea World Research and Rescue Foundation Inc., Nature Foundation of South Australia, South Australian Department for Environment and Heritage Wildlife Conservation Fund, Australian Geographic Society, Norman Wettenhall Foundation, Wildlife Conservation Fund of South Australia, South Australian Research and Development Institute (SARDI) Women's Bursary 2005, MA Ingram Trust, and Lirabenda Fund (Field Naturalist Society). T.L.G. acknowledges the Save Our Seas Foundation, Swiss Shark Foundation, Watermen Project. Staff and volunteers at Bimini Biological Field Station Foundation. K.C.H. acknowledges funds provided by NERC and the Department for Business, Energy and Industrial Strategy. N.H. acknowledges support by The Batchelor Foundation, Disney Conservation Fund, Wells Fargo, Guy Harvey Ocean Foundation, Oceana, Oracle, and the West Coast Inland Navigation District. R.H. acknowledges funding provided by the Ministry for Business, Innovation and Employment Endeavour Fund C01 1710: "RAMPing-up protection of the Ross Sea," by NZARI (NZ Antarctic Research Institute) and Fisheries New Zealand (respectively), with Regina Eisert as CI, and tags and some field personnel funded by IMOS. The IMOS deployments in Prydz Bay were supported logistically by the Australian Antarctic Division through the Australian Antarctic Science Grant Scheme (AAS Projects 2794 and 4329). Work was partially funded by an Australian Research Council Linkage Grant to R.H. and David Slip (LP110200603). C.E.H. acknowledges the Earthwatch Institute, David and Lucile Packard Foundation, Wallace Research Foundation, PADI Foundation, and the Arizona-Sonora Desert Museum. Funding was also provided by the Secretaría de Educación y Posgrado – Instituto Politécnico Nacional (projects: SIP20141052; SIP20151561; SIP20161935) and the NGO Investigacion, Capacitacion y Soluciones Ambientales y Sociales A.C. C.E.H. received a Masters degree bursary from the University of Exeter and the European Social Fund and would like to thank Consejo Nacional de Ciencia y Tecnología (Mexico) for support through a PhD scholarship. L.A. Huckstadt was funded under NSF OPP grants ANT-0110687, 0840375, 0533332 and 0838937, the National Undersea Research Program, and the National Oceanographic Partnership through the Office of Naval Research (ONR). N.E. Hussey acknowledges funding from the National Sciences and Engineering Research Council of Canada. C.H. acknowledges support from the Nature Foundation SA Inc., Save Our Seas Foundation, Neiser Foundation, Humane Society International, and Mohamed bin Zayed species conservation fund. R.W.H.I. acknowledges TOPP funding (ONR, NSF, Moore, Sloan, and Packard Foundation) and US EPA GRO fellowship. A.A.K. also acknowledges the following management/advisory affiliations/paid consulting activities as part of the Top Predator Scientific Working Group of South Africa (Department of Forestry, Fisheries, and the Environment); the Global Shark Movement Project; Shark Spotters NPO (executive committee); South African Whale Disentanglement network (executive committee). D.M.P.J. acknowledges funding from the National Marine Aquarium (UK) and National Geographic. M.J. was supported by the Science Foundation Ireland Centre for Marine Renewable Energy Research (MaREI 12/RC/2302) and fieldwork supported by the Petroleum Infrastructure Programme (IS13/08) and FishKOSM project funded by the Department of Agriculture, Fisheries and the Marine (15/S/744). F.O.L. acknowledges The Pew Charitable Trusts (PEW) Ocean Science Division and Global Shark Conservation Campaign and Fundação Apolônio Salles de Desenvolvimento Educacional (FADURPE). P.H.L. thanks CENPES/PETROBRAS (Centro de Pesquisas da PETROBRAS) for supporting the 'Mamíferos e Quelônios Marinhos Conselho Nacional de Desenvolvimento Científico e Tecnológico (CNPq, PhD scholarship to T.Z.S., process number 141361/2010-7. J.L. thanks the Founder of the Save Our Seas Foundation for funding and providing all facilities for his work. G.L. was funded in part by US Fleet Forces Command and managed by Naval Facilities engineering Command Atlantic as part of the US Navy's marine species monitoring program. Additional funding was provided by the National Marine Fisheries Grant to States Program (grant NA09NMF4720033) and by private donations managed by the Virginia Aquarium & Marine Science Foundation. P.L. acknowledges the Italian Consiglio Nazionale delle Ricerche (CNR) and Ministry of Research, University of Pisa, Swedish Natural Science Research Council, NERC, the Darwin Initiative, Italian Space Agency and Accademia Nazionale dei Lincei. The work at Ascension Island was financed by grants from the Swedish Research Council and the Crafoord Foundation to S.Å. B.C.L.M. acknowledges the Secretaria da Comissão Interministerial para os Recursos do Mar (SECIRM/Brazilian Navy) and CNPq provided grant (no. 405460/2012-0) for logistics and equipment through Pró-Arquipélago/Oceanic Islands Program. The Grupo Fundação Boticário de Proteção à Natureza (0760/2007.2), Save Our Seas Foundation (66/2008) and CNPq (478070/2008-0, 482557/2011-7), provided grants for the satellite tags. A.I.M., S.D.G. and R.H. acknowledge that satellite tagging of Southern Right Whales in the Great Australian Bight, Australia was funded by a grant from the Department of the Environment Australian Marine Mammal Center, with in kind support from the South Australian Research and Development Institute (Aquatic Sciences), Blue Planet Marine, Macquarie University and Flinders University. They would like to acknowledge the support provided by M. Double and V. Andrews-Goff at the Australian Marine Mammal Centre, and all those who participated in fieldwork. M.L. Mallory acknowledges Environment Canada, Natural Resources Canada, Greenland Institute of Nature, Molson Foundation, Natural Sciences and Engineering Research Council of Canada, Canadian Wildlife Federation, and Acadia University. J.C.M. acknowledges

project funding and equipment provided by NOAA, NMFS Southwest Fisheries Science Center, and the National Fish and Wildlife Foundation. D.M. acknowledges the BBVA Foundation ("Ayudas Fundación BBVA a Equipos de Investigación Científica 2016"), Spanish Government (grant "Juan de la Cierva-Formación" FJCI-2014-20064), Fundación Reina Sofía (LIBERA 2017), and NOAA. A.M. acknowledges the Doñana Biological Station (EBD-CSIC), Consejería de Medio Ambiente y Ordenación del Territorio (CMAOT) of Junta de Andalucía, the Andalusian Marine Environment Management Center (CEGMA) and the NGO Equinac. M. Marcoux was funded by the DFO Nunavut Implementation Fund and the Strategic Program for Ecosystem-Based Research and Advice. Narwhal tagging efforts were supported from the World Wildlife Fund and the Nunavut Wildlife Management Board. L.M. was principally supported through the Australian Government's Fisheries Research and Development Corporation (FRDC) Grants Scheme (PN 2005/031), co-funded by the South Australian Sardine Fishery. We also thank the Nature Foundation South Australia for financial assistance that supported the purchase of GPS units. G.M. was principally supported by Xunta de Galicia, Spain, throught Isabel Barreto Programme (2009–2012) and FCT grants (PTDC/MARBIO/4458/2012; IF/01611/2013; NORTE-01-0145-FEDER-000031). M.M.C.M. acknowledges the MEOP-BR (Marine Mammals Exploring the Oceans Pole to Pole; Brazil), an International Polar Year (IPY) program funded by the Brazilian Science, Technology and Innovation Ministry through the Brazilian National Research Council (CNPq, grant no. 520196/2006-6). M.A.C.N. acknowledges the petrel tracking program and Malcolm Nicoll were supported by NERC (grant NE/H5081500) with in situ support from MWF and NPCS. W.J.N. was supported by a Fulbright Fellowship and a Marshall Fellowship during the period field research in Baja California was conducted. B.M.N. and S.D.R. acknowledges the many supporters, funders, donors and volunteers of ECOCEAN Inc. B.P. received a Commonwealth Scientific and Industrial Research Organisation (CSIRO) Marine Research scholarship. E.O. acknowledges funding provided by NOAA NMFS, the Institute of Marine Research in Norway, the Nordic Council of Ministers, and FCT (grants: SFRH/BD/32520/2006 and SFRH/BPD/29841/2006). S. Oppel acknowledges that work on Ascension Island was partly funded by a Darwin Grant (19026) to Ascension Island Government and the University of Exeter (A.C.B. and B.J.G.), managed on-island by N.W. and S.B.W.. The king eider study was funded by the Coastal Marine Institute (University of Alaska, Fairbanks), Minerals Management Service, US Geological Survey (Outer Continental Shelf Program), and Canadian Wildlife Service. Further financial and technical support was provided by the Sea Duck Joint Venture, USFWS, North Slope Borough, ConocoPhillips Alaska Inc., Inuvialuit Wildlife Management Advisory Council, WWF, BP Exploration Alaska, Polar Continental Shelf Project, US Geological Survey Alaska Cooperative Fish and Wildlife Research Unit, Institute of Arctic Biology (University of Alaska Fairbanks), and German Academic Exchange Service. The work on St Helena was partly funded by Enterprise St Helena and the Seabird Group. The David and Lucile Packard Foundation, Darwin Plus: Overseas Territories Environment and Climate Fund, the Sir Peter Scott Commemorative Expedition to the Pitcairn Islands, generous donors, and the Royal Society for the Protection of Birds (RSPB) helped to fund our research. A.M.P. acknowledges the US Geological Survey (USGS) Ecosystems and Climate and Land Use Change Mission Areas, the USGS Changing Arctic Ecosystems Initiative, and the Bureau of Land Management for primary funding. Additional support was provided through a National Science Foundation grant to the University of Wyoming; the United States Fish and Wildlife Service, Marine Mammals Management and the Arctic National Wildlife Refuge; Environment and Climate Change Canada; the North Slope Borough, Department of Wildlife Management; the Polar Continental Shelf Project; Polar Bears International; the University of California, Santa Cruz; the San Diego Zoo Wildlife Alliance; and the University of Alberta. V.H.P. acknowledges EU INTERREG project FAME: The Future of the Atlantic Marine Environment (2009-1/089) and by LIFE+Berlenga (LIFE13 NAT/PT/000458). Strategic program of Marine and Environmental Sciences Centre (MARE), financed by FCT (MARE – UID MAR/04292/2013). LIFE Project Marine Important Bird Areas (2004—2008) by the EU INTERREG Project FAME: The Future of the Atlantic Environment (2010—2012) founded by the EU. D.M. Palacios and B.M. acknowledge support provided by the TOPP program of the Census of Marine Life, the US Minerals Management Service, the US ONR (Grants 9610608, 0010085, 0310861, N0014-02-1-0885, N0-176A, and N00014- 09-1-0453), NSF, the Alfred P. Sloan Foundation, the Moore Foundation, the Packard Foundation, the National Geographic Society, the IWC (with funds provided by Exxon Neftegas Limited and Sakhalin Energy Investment Company), the National Research Foundation of South Africa (GUN no. 2047517), NOAA through the Northeast Consortium, based at the University of New Hampshire (grant no. NA16FL1324), the International Association of Oil and Gas Producers "Sound and Marine Life Joint Industry Programme," and private donors to the Oregon State University Endowed Marine Mammal Institute. L.R.P. was funded by the Save Our Seas Foundation and supported by the Manta Trust, the University of Western Australia, and the Australian Institute of Marine Science. Field work was supported by the SOSF-D'Arros Research Centre. N.J.P. was funded by Emirates Nature – WWF and multiple supporting agencies. M.P. acknowledges that New Zealand funding was provided by MBIE Endeavour Fund C01X1710 (Ross-RAMP), NIWA SSIF (Coasts & Ocean Centre, program 4) and NIWA Strategic CAPEX. L.P. and M. Lopez Mendilaharsu were funded by the Convention of Migratory Species, WWF as part of the Trans-Atlantic Leatherback Conservation Initiative, and Peoples Trust for Endangered Species, UK. The Coordenação de Aperfeiçoamento de Pessoal de Nivel Superior (CAPES) provided a grant to M. Lopez Mendilaharsu. N.Q. acknowledges CEECIND/02857/2018; PTDC/MAR/100345/2008 and COMPETE FCOMP-01-0124-FEDER-010580; PTDC/BIA/28855/2017 - COMPETE 1094 POCI-01-0145-FEDER-028855. F.R.C. acknowledges the transitory norm contract at the University of Coimbra (DL57/2016/CP1370/CT90) and the projects UIDB/04292/2020, UIDP/04292/2020, granted to MARE, and LA/P/0069/2020, granted to the Associate Laboratory ARNET, financed by the Foundation for Science and Technology (FCT; Portugal). J.A.R. acknowledges EU INTERREG project FAME (Future of the Atlantic Marine Environment), Fundação para a Ciência e Tecnologia (FCT; SFRH/BPD/63825/2009 and SFRH/BPD/85024/2012), EU project LIFE09 NAT/PT/000041 and by EU INTERREG project FAME 2009-1/089, as well as co-sponsorship by FCT and the European Social Fund (POPH, EU) through post-doctoral grants SFRH/BPD/95372/2013SFRH/BPD/85024/2012 and the strategic program of MARE (UID/MAR/04292/2013 and UID/MAR/04292/2020), and LIFE project "Safe Islands for Seabirds" (LIFE07 NAT/P/000649). A.J. Read acknowledges the US Navy (Atlantic Fleet Forces Command) for funding field work and analysis. A.F.R. acknowledges the TOTAL Foundation and TOTAL Muscat Branch. D.R. was supported by Save our Seas Foundation, Project Aware, Royal Geographical Society through (EXERCISE JURASSIC SHARK 2), A1 scuba, downtown aquarium, Azul Marino Restaurant, Palapas Ventana, WWF-telcel, PADI, National Geographic, and Cabo Expeditions. R.D.R. acknowledges funding from the Australian Research Council Linkage grant LP140100404 and the Holsworth Wildlife Research Endowment R.R.R. and P.J.N.B. acknowledges funding provided by the National Research Foundation Thuthuka (grant 76230) and South African National Antarctic programmes (grant nos. 93071 and 110722), through the Department of Science and Technology, Republic of South Africa, the Mohamed bin Zayed Species Conservation Fund (project no. 10251290) and the IWC Southern Ocean Research Partnership (IWC-SORP). F.G.R. acknowledges funding provided by the US Marine Mammal Commission under grant no. E4047335 and ONR grant N00014-08-1-1195, the E&P Sound and Marine Life Joint Industry Project of the International Association of Oil and Gas Producers. D.P.R. acknowledges the Qatar Ministry of Municipality and Environment (QMMOE) and Maersk Oil Research and Technology Centre (MORTC), and was supported by two small grants from the Save Our Seas Foundation. Many thanks to the Save Our Seas Foundation, Al Ghurair Foods and the Emirates Diving Association, Emirates Natural History Group and Le Meridien Al Aqah Beach Resort for providing financial support for individual satellite tags. P.W.R. acknowledges that northern elephant seal research was supported by the Moore, Packard, and Sloan Foundations with additional support from the Office of Naval Research and the E&P Sound and Marine Life Joint Industry Project of the International Association of Oil and Gas Producers, Exxon-Mobil and Shell oil. J.P.R. was supported by Juan de la Cierva Formacion program (Ref. FJC2019-040622-I) funded by MCIN/AEI/ 10.13039/501100011033. He also received additional funding from Sustainable Ocean Alliance for the Artificial Intelligence & Animal Movement (AIAM, ref. D017) project under the SOA Grants program. Funding from Vicenç Mut program of Govern de les Illes Balears. T.L.R. acknowledges the Australian Research Council Linkage Program, LP0989933; Antarctic Science Advisory Committee Program 1144, Sea World Research & Rescue Foundation Inc., Australian Research Council; and the Scott Foundation. C.A.R. and S.J.P. acknowledge two private trusts, Aqua-Firma, the Shark Foundation, Waterlust, Rufford Small Grant, and the PADI Foundation. Y.R. acknowledges the French Polar Institute Paul Emile Victor (IPEV), the WWF-UK, the PEW Foundation, the Centre National de la Recherche Scientifique (Programme Zone Atelier de Recherches sur l'Environnement Antarctique et Subantarctique, ZATA), the Agence Nationale pour la Recherche (ANR-2010-BLAN-1728-01), the Fondation Albert II de Monaco, and the Fondation des Treilles. P.M.S. was funded by New Zealand's Foundation for Research, Science & Technology under contracts CO1X0008 and CO1507. G. Schofield acknowledges Deakin University, Australia; Queen Mary University of London, UK; Swansea University, UK; National Marine Park of Zakynthos, Greece; AXA Research Fund, Boyd Lyon Sea Turtle Fund, British Chelonia Group, People's Trust for Endangered Species, Project Aware, and Thermadap. J.M.S. was funded by the Holsworth Wildlife Research Endowment. S.A.S. acknowledges TOPP funding (ONR, NSF, Moore, Sloan, and Packard Foundations). K.S. acknowledges funding received by the Centre for Ecological Sciences, Indian Institute of Science, Bangalore; the Indian Space Research Organisation/Indian Institute of Science, Bangalore Space Technology Cell; and the International Seafood Sustainability Foundation. G.L.S. acknowledges major funding from support of the TOPP program of the Census of Marine Life, and was supported by the Alfred P. Sloan Foundation, the Gordon and Betty Moore Foundation, the Packard Foundation, the National Oceanographic Partnership Program of ONR, the United Nations Educational, Scientific and Cultural Organization (UNESCO) World Heritage Program (via the United Nations Foundation and Global Conservation Fund of Conservation International), the Dr. Earl H. Myers and Ethel M. Myers Oceanographic and Marine Biology Trust, the sponsors of the 2007 Great Turtle Race, Earthwatch Institute and the National Aeronautics and Space Administration (NASA) through a grant provided by the Applied Sciences Program in the Earth Science Division. M.A. Silva and R.P. acknowledge funds provided by FCT through research grants TRACE-PTDC/MAR/74071/2006, IF/00943/2013/CP1199/CT0001, individual contracts/grants to MAS (FCT-IF/00943/2013) and RP (SFRH/BPD/108007/2015), and the strategic projects MARE (UID/MAR/04292/2019) and Okeanos (UIDB/05634/2020 and UIDP/05634/2020), co-funded by FEDER, COMPETE, QREN, POPH, FSE, and the Portuguese Ministry for Science and Education; the Regional Government of the Azores, FRCT, and the Operational Program AZORES 2020 through research grant MAPCET-M2.1.2/F/012/2011, project M1.1.A/REEQ.CIENTÍFICO UI&D/2021/010, and contracts to MAS and RP through Fund 01-0145-FEDER-000140 "MarAZ Researchers: Consolidate a body of researchers in Marine Sciences in the Azores" of the European Union. D.W.S. further acknowledges additional field research support provided by the Save Our Seas Foundation (grants 45, 87, 308) and the NERC Oceans 2025 Strategic Research Programme. G. Skomal acknowledges the Large Pelagics Research Center (grant 06-125), Federal Aid in Sport Fish Restoration, NSF (OCE-0825148), the John J. Sacco and Edith L. Sacco Charitable Foundation, the Atlantic White Shark Conservancy, the Massachusetts Environmental Trust, Discovery Communications, National Geographic, and the Woods Hole Oceanographic Institution. L.L.S. thanks G. Hays for contributing funds to purchase four Argos-GPS tags; the Oceanário de Lisboa for contributing funding to purchase two Argos-GPS tags.. Funding was provided by the FCT SFRH/BD/68717/2010. J.D. Stewart acknowledges the PADI Foundation (grant no. 7842), the New England Aquarium, MCAF, Carl F. Bucherer, the Punta Mita Foundation, David Connell, Mary O'Malley, Lupo Dion, CIMEC, and the Gulf of California Marine Program. A. Takahashi acknowledges funding provided by the North Pacific Research Board (contribution no. 1612-3), Japan Society for the Promotion of Science KAKENHI grant no. JP16H02705, and the Arctic Challenge for Sustainability program (JPMXD1300000000) of Japan Ministry of Education, Culture, Sports, Science and Technology. Work was supported by Grant-in-Aid for Scientific Research (20241001 and 24370016). JSPS research grants (19651100 and 19255001), and by a Grant-in-Aid for Scientific Research (Special Promotion) of the Ministry of Education, Culture, Sports, Science and Technology-Japan to Yamashina Institute for Ornithology. P.M.T. acknowledges funding provided by Marine Alliance for Science and Technology for Scotland, Beatrice Offshore Windfarm Ltd, Crown Estate, Highlands & Islands Enterprise, and Moray Firth Offshore Renewables Limited. J. Tomás thanks the European Union Marie Curie FP7 and the Spanish Ministry of Education and Sciences, and was also supported by project LIFE INTEMARES (LIFE18 NAT/IT/000103) F.V. acknowledges the Foundation for Science and

Technology (FCT) for individual grants (CEECIND/03469/2017, CEECIND/03426/2020) and research funds under the project UIDB/05634/2020 and UIDP/05634/2020, and support of the Regional Government of the Azores through the initiative to support Research Centers of the University of the Azores and through the project M1.1.A/REEQ.CIENTÍFICO UI&D/2021/010. M. Vedor was funded by Fundação para a Ciência e Tecnologia (FCT; PTDC/ASP-PES/2503/2020). S.V. thanks the TOPP Program supported by the Sloan, Packard and Moore Foundations, as well as the ONR, the E&P Sound and Marine Life Joint Industry Project of the IAGOP (no. JIP 2207-23), UC MEXUS, CONACYT in Mexico and Instituto Politécnico Nacional (IPN) (Project SIP-2012006) of Mexico, NSF Office of Polar Programs and Center for Remote Sensing at University of California Santa Cruz for funding and logistic support. C.V. was funded by DREAL Bretagne, FEOGA Funds (EU), DREAL Basse Normandie, Région Poitou-Charente, La Compagnie du Vent, and the Parc naturel marin d'Iroise. S. Wanless was funded by the NERC Centre for Ecology & Hydrology. R.S.W. was funded by ONR and Dolphin Quest, Inc. S.D.W. acknowledges the Department of Environment and Natural Resources, Conservation Volunteers Australia, Tiwi Land Council, Natural Heritage Trust, Charles Darwin University, and the Australian Government. B.W. acknowledges the Australian Antarctic Division. N.E.W. acknowledges that tags were part of WWF-Australia's Flatback Whereabouts Project funded by WWF, Factorie, and Winnifred Violet Scott Trust, supported by the Gudjuda Aboriginal Reference Group. D.N.W. acknowledges the Volgenau Foundation, Mudge Foundation, BOEM, Stellwagen Bank National Marine Sanctuary, and the National Marine Sanctuary Foundation. F.C.W. was funded by the UK Natural Environment Research Council (NERC) through a University of Southampton INSPIRE DTP Studentship. L.J.W. acknowledges funding by the UK Department for Energy and Climate Change (DECC). J.C.X. acknowledges the strategic program of MARE (Marine and Environmental Sciences Centre), financed by the Foundation for Science and Technology (UIDB/04292/2020), through the grants Investigator FCT program (IF/00616/2013), PTDC/BIA-BDE/64539/2006 and SFRH/BPD/28879/2006. T.Y. was partially supported by the Japan Society for the Promotion of Science research grants (19651100, 19255001) and Grant-in-Aid for Scientific Research (Special Promotion) of the Ministry of Education, Culture, Sports, Science and Technology-Japan. D.J.Y. acknowledges funding provided by Polar Continental Shelf Program, Ocean Tracking Network, Fisheries and Oceans Canada, University of Windsor, Ontario Graduate Scholarships, W. Garfield Weston Foundation and Natural Science and Engineering Research Council of Canada. P.M.Z. acknowledges the United Nations Office for Project Services, GEF Humboldt for providing tags and funding for the expedition. J.M.A. was supported by project LIFE+ INDEMARES. **Author contributions:** All authors contributed to aspects of fieldwork, animal tagging, data collection, data formatting, and/or contribution of tools (full details provided in the supplementary text: "Supplementary Author Contributions"). Conceptualization: A.M.M.S., C.M.D., V.M.E., J.P.R., D.W.S., and G.C.H. Methodology: A.M.M.S., J.P.R., M. van der Mheen, S.A.M., M. Vedor, N.Q., L.M.A., H.J.C., M. VanCompernolle, L.R.P. with input from all authors Investigation: All authors Visualization: A.M.M.S., J.P.R., N.Q., H.J.C., and M. VanCompernolle Funding acquisition: A.M.M.S. Project administration: A.M.M.S., S.A.M. Writing – original draft: A.M.M.S., D.W.S., and G.C.H Writing – review & editing: All authors. **Competing interests:** The authors declare that they have no competing interests. **Data and materials availability:** All data, code, and materials needed to reproduce this analysis are available at Dryad (*111*). Data obtained from literature review are presented in supplementary materials. Sources of environmental data collated from online databases are described in supplementary materials.

Ana M. M. Sequeira[1,2]*†, Jorge P. Rodríguez[3,4,5,6]†, Sarah A. Marley[7], Hannah J. Calich[1,8], Mirjam van der Mheen[2,9], Michelle VanCompernolle[9], Lucy M. Arrowsmith[9,10], Lauren R. Peel[11,12], Nuno Queiroz[13,14], Marisa Vedor[13,14], Ivo da Costa[13,14], Gonzalo Mucientes[13,14,15], Ana Couto[16,17], Nicolas E. Humphries[18], Sara Abalo-Morla[15,19,20], Francisco J. Abascal[21], Debra L. Abercrombie[22], Katya Abrantes[23,24], F. Alberto Abreu-Grobois[25], André S. Afonso[26], Pedro Afonso[27,28], Heidi Ahonen[29], Susanne Åkesson[30], Joanna Alfaro-Shigueto[31,32], Russel D. Andrews[33], Frédéric Angelier[34], Marina Antonopoulou[35], Javier A. Arata[36], Gonzalo Araujo[37,38], Randall Arauz[39,40], José Manuel Arcos[41], Igor Arregui[42], Haritz Arrizabalaga[42], Marie Auger-Méthé[43,44], Steffen Bach[45,46], Fred Bailleul[47,48], Robin W. Baird[49], George H. Balazs[50], Susan G. Barco[51,52], Adam Barnett[23,24], Warren Baverstock[53], Alastair M. M. Baylis[54], Annalea Beard[55], Juan Bécares[41,56], Eduardo J. Belda[19,19], Ian Bell[57], Ashley Bennison[58,59,60], Scott R. Benson[61,62], Diego Bernal[63], Michael L. Berumen[64], Sandra Bessudo[65], Natalia P. A. Bezerra[66,67], Antonin V. Blaison[68], Gabriela S. Blanco[69], Barbara A. Block[70], Mark Bolton[71], Mark E. Bond[72], Ramón Bonfil[73,74,75], Camrin D. Braun[76], Annette C. Broderick[77], Michael de L. Brooke[78], Annabelle M. L. Brooks[79], Edward J. Brooks[79,80], Ignacio M. Bruno[81], Jennifer M. Burns[82], Michael E. Byrne[83], Steven E. Campana[84], Hamish A. Campbell[85], Richard A. Campbell[86], Aaron Carlisle[87], Ruth H. Carmichael[88,89], Gemma Carroll[90], Paolo Casale[91], Filipe R. Ceia[92], Demian D. Chapman[93,94], Taylor K. Chapple[95], Jean-Benoit Charrassin[96], Andre Chiaradia[97,98], John Chisholm[99], Christopher R. Clarke[100], Thomas A. Clay[101,102], Christophe Cleguer[103], Elizabeth Clingham[104], Eric E. G. Clua[105,106,107], Jesse E. M. Cochran[64], Rochelle Constantine[108], Robert W. Cooper[109], Estelle Crochelet[110], Michelle Cronin[59]‡, Eduardo Cuevas[111,112,113,114], Kayla P. DaCosta[88,89], Laurent Dagorn[115], Ryan Daly[116,117], Randall W. Davis[118], P. J. Nico de Bruyn[119], Carlos Delgado-Trejo[120], Thomas Dellinger[13,121], Solène Derville[122,123,124], Stella Diamant[125], Andrew DiMatteo[126], Kara L. Dodge[99], Philip D. Doherty[127], Michael C. Double[128], Alistair D. M. Dove[129,130], Thomas K Doyle[58,59], Michael J. Drew[47,131], Lindsay L. Dubbs[132,133], Clinton A. J. Duffy[134], Peter H. Dutton[135], Ewan W. J. Edwards[136], Luke D. Einoder[47,137], Mark V. Erdmann[138], Eduardo Espinoza[139], Nicole Esteban[140], Ana Isabel Fagundes[141], Chris Feare[142,143], Steven H. Ferguson[144], Luciana C. Ferreira[145], Francesco Ferretti[146], John Filmalter[117], Brittany Finucci[147], G. Chris Fischer[148], Richard J. Fitzpatrick[149,150], Jorge Fontes[27], Angela Formia[151,152], Sabrina Fossette[10,153], Malcolm P. Francis[147], Ari S. Friedlaender[101], Miguel Furtado[13], Austin J. Gallagher[154], Claire Garrigue[122,124], Enrico Gennari[117,155,156], H. Grant Gilchrist[157], Brendan J. Godley[127,158], Simon D. Goldsworthy[47,48], Matthew Gollock[159], Victoria González Carman[160,161], W. James Grecian[162], Jonathan R. Green[163], Christophe Guinet[34], Johan Gustafson[164], Tristan L. Guttridge[165], Hector M. Guzman[166], Derek Hamer[167], Keith C. Hamer[168], Neil Hammerschlag[169,170], Mike O. Hammill[171], Luke Harman[58], Emma Harrison[172], Catherine E. Hart[173], A. Errol Harris[174]‡, Gordon Hastie[175], Fabio H. V. Hazin[66]‡, Matt Heard[131,176], Alex R. Hearn[40,177], Mads Peter Heide-Jørgensen[178], Leeann Henry[104], Robert William Henry III[101,179,180], Vicente Guzman Hernandez[181], Arturo E. Herrera[182], Mark A. Hindell[183], John C. Holdsworth[184], Bonnie J. Holmes[185], Lucy A. Howey[186,187,188], Edgar Mauricio Hoyos Padilla[189,190], Luis A. Huckstadt[101,127,158], Robert E. Hueter[93,148], Paulo H. Lara[191], Nigel E. Hussey[192], Charlie Huveneers[131], Kevin Hyland[53], Dylan T. Irion[193,194], David M. P. Jacoby[195], Audrey Jaeger[196], Mohammed Y. Jaidah[46], Mark Jessopp[58,59], Oliver J. D. Jewell[2,197], Ryan Johnson[198], Carl G. Jones[199,200], Ian D. Jonsen[201], Lance K. B. Jordan[187], Salvador J. Jorgensen[202], Akiko Kato[34], James T. Ketchum[40,189,203], Alexander S. Kitaysky[204], A. Peter Klimley[40,205], Alison A. Kock[117,206], Pieter Koen[207,208], Felipe Ladino Archila[65], Fernanda O. Lana[66,209], Jude V. Lane[71], Matthieu Le Corre[196], Mary-Anne Lea[183,210,211], James Lea[11,78], Eliza H. K. Leat[212], Olivia A. Lee[213], J. Jacob Levenson[109,174,214], César P. Ley-Quiñonez[215], Fiona Llewellyn[216], Gwen Lockhart[217,218], Gustave G. Lopez[219], Milagros Lopez Mendilaharsu[191,220], Andrew D. Lowther[29], Paolo Luschi[91], Molly E. Lutcavage[221,222], Warrick S. Lyon[223], Bruno C. L. Macena[27,28,66], Alice I. Mackay[47], Christine A. Madden[224], Mark L. Mallory[225], Jeffrey C. Mangel[32,127], Michael Manning[147]‡, Kate L. Mansfield[226], David March[127,227], Adolfo Marco[228], Marianne Marcoux[144], David Acuña-Marrero[229], Helene Marsh[150], Heather Marshall[63,230,231], Bruce Mate[123,232], Jaime D. McAllister[183], Rebecca L. McGuire[233], Jane McKenzie[234], Lachlan McLeay[47,48], Clive R. McMahon[183,235,236], Michelle Modest[101], John Morris[93], Mônica M. C. Muelbert[237,238], Naveen Namboothri[239], Wallace J. Nichols[240]‡, Malcolm A. C. Nicoll[216], Bradley M. Norman[241,242], Ken Norris[243], Erik Olsen[244], Steffen Oppel[245], Sabine Orlowski[196], Anthony M. Pagano[246], Brad Page[234], Vitor H. Paiva[247], Daniel M. Palacios[123,232,248], Yannis P. Papastamatiou[249], Denise M. Parker[250], Charitha Pattiaratchi[9], Hoyt Peckham[251,252], Cesar R. Peñaherrera-Palma[40], Julian G. Pepperell[253], Richard A. Phillips[60], Simon J. Pierce[185,254], Stephen K. Pikesley[127], Nicolas J. Pilcher[255], Patrick Pinet[256], Matt Pinkerton[147], Enrico Pirotta[257], Virginie Plot[196], Abby N. Powell[258], Kevin D. Powers[259], Clare E. M. Prebble[254], Tiana J. Preston[98], Rui Prieto[27,28], Laura Prosdocimi[260], John L. Quinn[58], Lina Maria Quintero[40], Thierry Raclot[261], Iván Ramirez[262], Dení Ramírez-Macías[263], Jaime A. Ramos[92], Andrew J. Read[264], Rolf Ream[265], ALan F. Rees[127,266], Richard D. Reina[98], Ryan R. Reisinger[267], Ohiana Revuelta[268], Samantha D. Reynolds[241,242,269], Anthony J. Richardson[269,270], Leena Riekkola[271], Federico G. Riet-Sapriza[272], David P. Robinson[46,53,273], Patrick W. Robinson[180], Carlos F. D. Rocha[274], Tracey L. Rogers[275], Christoph A. Rohner[254], Yan Ropert-Coudert[34], Monica Ross[276], David R. L. Rowat[277], Kevin Ruhomaun[278], Paul M. Sagar[279], Melita A. Samoilys[280], Sonia Sanchez[48], Alejandra G. Sandoval-Lugo[215,281], Erik A. P. dos Santos[282], António M. Santos[13,283], Kylie L. Scales[185], Gail Schofield[284]‡, Jayson M. Semmens[183], Edy Setyawan[285], Scott A. Shaffer[286], Kartik Shanker[239,287], Marcus Sheaves[150], George L. Shillinger[40,70,288], Mahmood S. Shivji[289], Abraham Sianipar[241,285], Janet R. D. Silk[60], Mónica A. Silva[27,28], Jolene Sim[212], Samantha J. Simpson[18], Gregory Skomal[290], David J. Slip[236,291], Malcolm J. Smale[292], German A. Soler[65,183], Marc Soria[115], Lara L. Sousa[293], Emily J. Southall[18], Jean-Claude Stahl[294], Kilian M. Stehfest[183,295], Jeremy T. Sterling[265], John D. Stevens[296], Guy M. W. Stevens[12], Joshua D. Stewart[12,123,232], Adhith Swaminathan[239], Akinori Takahashi[297,298], Vikash Tatayah[200], Jean-Baptiste Thiebot[297,299], Paul M. Thompson[136], Simon R. Thorrold[76], Michele Thums[145], Jesús Tomás[227], Leigh G. Torres[123], Alison Towner[156,300], Philip N. Trathan[60], John P. Tyminski[93,148], Ricardo Sagarminaga van Buiten[301], Robert P. Van Dam[302], Frederic Vandeperre[27], Nuria Varo-Cruz[303,304,305], Jeremy J. Vaudo[289], Michel Vely[153], Stella Villegas-Amtmann[180], Cecile Vincent[306], David Waayers[307], Sarah Wanless[308], Yuuki Y. Watanabe[309], Cortney A. Watt[144,310], Sam B. Weber[127,158,212], Nicola Weber[127,212], Michael J. Weise[311], Linda Welch[312], Randall S. Wells[313], Jonathan M. Werry[314,315], Bradley M. Wetherbee[289,316], Timothy D. White[317], Scott D. Whiting[10], Andrea U. Whiting[318], Annelise Wiebkin[234], Barbara Wienecke[128], Natalie E. Wildermann[319], David N. Wiley[320], Alexis Will[204,321], Sean Williams[79,187], Marie Windstein[177,241], Saskia Wischnewski[58,71], Matthew J. Witt[322,323], Freya C. Womersley[18,267], Andrew G. Wood[60], Lucy J. Wright[71], José C. Xavier[60,247], Takashi Yamamoto[324], David J. Yurkowski[144], Patricia M. Zarate[40,325], Alan Zavala-Norzagaray[215,326], Alexandre N. Zerbini[33,49,265], Daniel P. Costa[101], Rob Harcourt[235,236], Mark G. Meekan[327], Graeme C. Hays[329], David W. Sims[18,267]§, Carlos M. Duarte[319]§, Víctor M. Eguíluz[3,330,331]§

[1]Division of Ecology and Evolution, Research School of Biology, The Australian National University, Canberra (Australian Capital Territory), Australia. [2]UWA Oceans Institute and the School of Biological Sciences, The University of Western Australia, Perth (Western Australia), Australia. [3]Instituto de Física Interdisciplinar y Sistemas Complejos (IFISC), CSIC-UIB, Palma de Mallorca, Spain. [4]Instituto Mediterráneo de Estudios Avanzados (IMEDEA), CSIC-UIB, Esporles, Illes Balears, Spain. [5]C.A. Illes Balears, Universidad Nacional de Educación a Distancia (UNED), Palma, Spain. [6]Delegación Territorial en Illes Balears, Agencia Estatal de Meteorología (AEMET), Muelle de Poniente s/n, Palma, Spain. [7]Scotland's Rural College (SRUC), Craibstone Estate Bucksburn, Aberdeen, UK. [8]Oceans Graduate School and the UWA Oceans Institute, The University of Western Australia, Perth (Western Australia), Australia. [9]School of Engineering and the UWA Oceans Institute, The University of Western Australia, Perth (Western Australia), Australia. [10]Department of Biodiversity, Conservation and Attractions, Biodiversity and Conservation Science, Kensington (Western Australia), Australia. [11]Save Our Seas Foundation, Geneva, Switzerland. [12]The Manta Trust, Catemwood House Norwood Lane, Corscombe, Dorset, UK. [13]Centro de Investigação em Biodiversidade e Recursos Genéticos (CIBIO), InBIO Laboratório Associado, Campus de Vairão, Universidade do Porto, Vairão, Portugal. [14]BIOPOLIS Program in Genomics, Biodiversity and Land Planning, Campus de Vairao, Vairão, Portugal. [15]Instituto de Investigaciones Marinas, Consejo Superior de Investigaciones Científicas (IIM-CSIC), Vigo, Pontevedra, Spain. [16]School of Biological Sciences, University of Aberdeen, Aberdeen, UK. [17]Biomathematics and statistics Scotland, The kings building, Edinburgh, Scotland. [18]Marine Biological Association (MBA), The Laboratory Citadel Hill, Plymouth, UK. [19]Instituto de Investigación para la Gestión Integrada de Zonas Costeras, Universitat Politècnica de València, Gandia, València, Spain. [20]Instituto Español de Oceanografía. Centro Oceanográfico de Vigo (COV-IEO), CSIC, Vigo, Spain. [21]CSIC-Instituto Español de Oceanografía, Centro Oceanográfico de Canarias, Santa Cruz de Tenerife, Spain. [22]Abercrombie and Fish, Port Jefferson Station, Port Jefferson, NY, USA. [23]Marine Data Technology Hub, College of Science and Engineering, James Cook University, Townsville (Queensland), Australia. [24]Biopixel Oceans Foundation, Cairns (Queensland), Australia. [25]Unidad Académica Mazatlán, Instituto de Ciencias del Mar y Limnología, Universidad Nacional Autónoma de México, Calzada Joel Montes Camarena s/n, Mazatlán, Sinaloa, Mexico. [26]Department of Life Sciences, CFE–Centre for Functional Ecology: Science for People & Planet/TERRA Associated Laboratory, University of Coimbra, Coimbra, Portugal. [27]Instituto de Investigação em Ciências do Mar (OKEANOS), Universidade dos Açores, Horta, Portugal. [28]Instituto do Mar (IMAR), Horta, Portugal. [29]Research Department, Norwegian Polar Institute, Fram CentreTromsø, Norway. [30]Department of Biology, Lund University, Lund, Sweden. [31]Carrera de Biologia Marina, Universidad Cientifica del Sur, Lima, Peru. [32]ProDelphinus, Lima, Peru. [33]Marine Ecology and Telemetry Research, Seabeck, WA, USA. [34]Centre d'Etudes Biologiques de Chizé, UMR 7372, CNRS-La Rochelle Université, Villiers en Bois, France. [35]Emirates Nature-WWF, Dubai, JVC, United Arab Emirates. [36]Association of Responsible Krill Harvesting Companies, Toronto, Ontario, Canada. [37]Environmental Science Program, Department of Biological and Environmental Sciences, College of Arts and Sciences, Qatar University, Doha, Qatar. [38]Marine Research and Conservation Foundation, Emble Farm, Lydeard St Lawrence, Somerset, UK. [39]Marine Watch International, San Francisco, CA, USA. [40]MigraMar, Bodega Bay, CA, USA. [41]Programa Marino, SEO/BirdLife, Barcelona, Spain. [42]AZTI, Basque Research and Technology Alliance (BRTA), Pasaia, Guipúzcoa, Spain. [43]Institute for the Oceans and Fisheries, University of British Columbia, AERL, Vancouver, British Columbia, Canada. [44]Department of Statistics, University of British Columbia, Vancouver, British Columbia, Canada. [45]Impact Assessment Department, Rambøll, Copenhagen, Denmark. [46]Research Department, Qatar Whale Shark Research Project, Doha, Qatar. [47]Aquatic Sciences, South Australian Research and Development Institute (SARDI), West Beach, Adelaide (South Australia), Australia. [48]School of Biological Sciences, University of Adelaide, Adelaide (South Australia), Australia. [49]Cascadia Research Collective, Olympia, WA, USA. [50]Golden Honu Services of Oceania, Honolulu, HI, USA. [51]Research & Conservation, Virginia Aquarium & Marine Science Center, Virginia Beach, VA, USA. [52]Virginia Department of Wildlife Resources, Henrico, Richmond, VA, USA. [53]Dubai Turtle Rehabilitation Project, Dubai, United Arab Emirates. [54]South Atlantic Environmental Research Institute (SAERI), Stanley, Falkland Islands. [55]Cardiff School of Biosciences, Cardiff University, Cardiff, Wales, UK. [56]CORY'S–Investigación y Conservación de la Biodiversidad, Barcelona, Spain. [57]Queensland Department of Environment and Science, Aquatic Threatened Species, Garbutt East (Queensland), Australia. [58]School of Biological Earth and Environmental Sciences, University College Cork, Distillery Fields, North Mall, Cork, Ireland. [59]MaREI Research Centre for Energy, Climate and Marine, Environmental Research Institute, University College Cork, Cork, Ireland. [60]British Antarctic Survey (BAS), Natural Environment Research Council, High Cross Madingley Road, Cambridge, UK. [61]Southwest Fisheries Science Center, National Marine Fisheries Service, National Oceanic and Atmospheric Administration (NOAA), CA, USA. [62]Moss Landing Marine Laboratories, San Jose State University, CA, USA. [63]Biology Department, University of Massachusetts Dartmouth, Dartmouth, MA, USA. [64]Red Sea Research Center (RSRC), King Abdullah University of Science and Technology (KAUST), Thuwal, Saudi Arabia. [65]Fundación Malpelo y Otros Ecosistemas Marinos, Bogota, Cundinamarca, Colombia. [66]Departamento de Pesca e Aquicultura (DePAq), Universidade Federal Rural de Pernambuco (UFRPE), Recife, Pernambuco, Brazil. [67]Departamento de Oceanografia e Ecologia (DOE), Universidade Federal do Espírito Santo (UFES), Vitória, Espirito Santo, Brazil. [68]Observatoire Marin de La Réunion (OMAR), Saint André, La Réunion, France. [69]Centro Para el Estudio de Sistemas Marinos (CESIMAR), National Scientific and Technical Research Council (CONICET), Puerto Madryn, Chubut, Argentina. [70]Hopkins Marine Station, Stanford University, Pacific Grove, CA, USA. [71]Centre for Conservation Science, Royal Society for the Protection of Birds (RSPB), Sandy, Bedfordshire, UK. [72]Biological Sciences, Institute of Environment, Florida International University, North Miami, FL, USA. [73]Océanos Vivientes AC, Coyoacán, Mexico City, Mexico. [74]El Colegio de la Frontera Sur, Chetumal, Chetumal, Q. Roo, Mexico. [75]Consejo Nacional de Humanidades, Ciencia y Tecnología (CONAHCyT), Mexico. [76]Biology Department, Woods Hole Oceanographic Institution, Woods Hole, MA, USA. [77]Centre for Ecology and Conservation, University of Exeter, Penryn Campus, Penryn, Cornwall, UK. [78]Department of Zoology, University of Cambridge, Cambridge, UK. [79]Cape Eleuthera Institute, Rock Sound, Eleuthera, The Bahamas. [80]The Manda Projects, Manda Bay, Lamu, Kenya. [81]Independent Researcher, Mar del Plata, Argentina. [82]Department of Biological Sciences, Texas Tech University, Lubbock, TX, USA. [83]School of Natural Resources, University of Missouri, Columbia, MO, USA. [84]Life and Environmental Sciences, University of Iceland, Reykjavik, Iceland. [85]Research Institute for Environment & Livelihoods, Charles Darwin University, Darwin (Northern Territory), Australia. [86]School of Life Sciences, Curtin University, Bentley (Western Australia), Australia. [87]School of Marine Science and Policy, University of Delaware, Lewes, DE, USA. [88]University Programs, Dauphin Island Sea Lab, Dauphin Island, AL, USA. [89]School of Marine and Environmental Sciences, University of South Alabama, Mobile, AL, USA. [90]People and Nature, Environmental Defense Fund, Seattle, WA, USA. [91]Department of Biology, University of Pisa, Pisa, Italy. [92]University of Coimbra, MARE–Marine and Environmental Sciences Centre/ARNET–Aquatic Research Network, Department of Life Sciences, Calçada Martim de Freitas, Coimbra, Portugal. [93]Sharks and Rays Conservation Research Program, Mote Marine Laboratory & Aquarium, Sarasota, FL, USA. [94]Oceanic Whitetip Consortium, Sarasota, FL, USA. [95]Coastal Oregon Marine Experiment Station, Hatfield Marine Science Center, Oregon State University, Newport, OR, USA. [96]Laboratoire d'Océanographie et du Climat, Institut Pierre Simon Laplace (LOCEAN-IPSL), Sorbonne Université, Centre National de la Recherche Scientifique, Institut de Recherche pour le Développement, Muséum National d'Histoire Naturelle (Sorbonne Université/CNRS/IRD/MNHN), Paris, France. [97]Conservation Department, Phillip Island Nature Parks, Phillip Island (Victoria), Australia. [98]School of Biological Sciences, Monash University, Clayton (Victoria), Australia. [99]Anderson Cabot Center for Ocean Life, New England Aquarium, Central Wharf, Boston, MA, USA. [100]Marine Department, Marine Research Facility, Jeddah, Saudi Arabia. [101]Institute of Marine Sciences, University of California Santa Cruz, Santa Cruz, CA, USA. [102]People and Nature, Environmental Defense Fund, 93940 Monterey, CA, USA. [103]Centre for Tropical Water and Aquatic Ecosystem Research (TropWATER), James Cook University, Townsville (Queensland), Australia. [104]Environmental Management Division, Environment Natural Resources and Planning Directorate, Government of St Helena, Jamestown, St Helena Island, Saint Helena. [105]Ecole Pratique des Hautes Etudes, CRIOBE USR3278 EPHE-CNRS-UPVD, Perpignan, France. [106]Paris Science et Lettres, Papetoai, French Polynesia. [107]Labex CORAIL, Perpignan, France. [108]School of Biological Sciences & Institute of Marine Science, University of Auckland, Auckland, New Zealand. [109]Oceans Forward, Plymouth, MA, USA. [110]Agence de Recherche pour la Biodiversité à La Réunion (ARBRE), Saint Gilles les Bains, La Réunion Island, France. [111]Consejo Nacional de Ciencia y Tecnología (CONACYT)–Universidad Autónoma del Carmen, Laguna de Términos S/N Col. Renovac 2a Secc, Ciudad del Carmen, Mexico. [112]Laboratorio de Ecología Espacial y del Movimiento (LEEM), Merida, Mexico. [113]Sea Turtle Conservation Program, Pronatura Peninsula de Yucatan, Merida, Mexico. [114]Instituto de Investigaciones Oceanológicas, Universidad Autónoma de Baja CA, Ensenada, México. [115]MARBEC, Université de Montpellier, CNRS, Ifremer, IRD, Sète, France. [116]Oceanographic Research Institute, Durban, South Africa, Durban, South Africa. [117]South African Institute for Aquatic Biodiversity (SAIAB), Somerset Street, Makhanda, South Africa. [118]Department of Marine Biology, Texas A&M University, Galveston, TX, USA. [119]Mammal Research Institute, Department of Zoology and Entomology, University of Pretoria, Pretoria, South Africa. [120]Departamento de Ecología Marina, Instituto de Investigaciones sobre los Recursos Naturales, Universidad Michoacana de San Nicolás de Hidalgo, Morelia, Mexico. [121]Estação de Biologia Marinha do Funchal, Universidade da Madeira, Funchal, Portugal. [122]UMR ENTROPIE (Institut de Recherche pour le Développement–Université de La Réunion–Université de la Nouvelle-Calédonie–CNRS–IFREMER), Nouméa, New Caledonia. [123]Marine Mammal Institute, Oregon State University, Newport, OR, USA. [124]Association Opération Cétacés, Nouméa, New Caledonia. [125]Madagascar Whale Shark Project Foundation, Brussels, Belgium. [126]CheloniData LLC, Berthoud, CO, USA. [127]Centre for Ecology and Conservation, College of Life and Environmental Science, University of Exeter, Penryn, Cornwall, UK. [128]Australian Antarctic Division, 203 Channel Highway, Kingston (Tasmania), Australia. [129]Research & Conservation, Georgia Aquarium, Atlanta, GA, USA. [130]Biological Sciences, Georgia Institute of Technology, Atlanta, GA, USA. [131]College of Science and Engineering, Flinders University, Bedford Park (South Australia), Australia. [132]North Carolina Renewable Ocean Energy Program, Coastal Studies Institute, East Carolina University, Wanchese, NC, USA. [133]Institute for the Environment, University of North Carolina at Chapel Hill, Chapel Hill, NC, USA. [134]Marine Species Team, Department of Conservation, Wellington, New Zealand. [135]Southwest Fisheries Science Center, National Marine Fisheries Service, National Oceanic and Atmospheric Administration (NOAA), La Jolla, CA, USA. [136]Lighthouse Field Station, School of Biological Sciences, University of Aberdeen, George Street, Cromarty, UK. [137]Parks Australia, Kakadu National Park, Jabiru (Northern Territory), Australia. [138]Conservation International Aotearoa, University of Auckland, Auckland, New Zealand. [139]Instituto Nacional de Biodiversidad (INABIO), Quito, Ecuador. [140]Bioscience, Faculty of Science and Engineering, Swansea University, Singleton Park, Swansea, Wales, UK. [141]Sociedade Portuguesa para o Estudo das Aves (SPEA), Lisboa, Portugal. [142]WildWings Bird Management, Haslemere, Surrey, UK. [143]School of Biological, Earth and Environmental Sciences, Faculty of Science, University of New South Wales (UNSW), Sydney, Australia. [144]Fisheries and Oceans Canada, Freshwater Institute, Winnipeg, Manitoba, Canada. [145]Australian Institute of Marine Science, Indian Ocean Marine Research Centre, University of Western Australia, Crawley (Western Australia), Australia. [146]Department of Fish and Wildlife Conservation, College of Natural Resources and Environment, Virginia Tech, Blacksburg, VA, USA. [147]National Institute of Water and Atmospheric Research Ltd (NIWA), Greta PointHataitai, Wellington, New Zealand. [148]OCEARCH, Jacksonville University, Park City, UT, USA. [149]Biopixel Oceans Foundation, Fortitude Valley (Queensland), Australia. [150]College of Science and Engineering, James Cook University, Douglas (Queensland), Australia. [151]Wildlife Conservation Society–Gabon Program, Libreville, Gabon. [152]African Aquatic Conservation Fund, Chilmark, MA, USA. [153]Megaptera, Paris, France. [154]Beneath the Waves, Boston, MA, USA. [155]Oceans Research Institute, Mossel Bay, South Africa. [156]Department of Ichthyology and Fisheries Science, Rhodes University, Grahamstown, Eastern Cape, South Africa. [157]National Wildlife Research Centre, Environment Canada, Carleton University, Ottawa, Ontario, Canada. [158]Marine Science Centre, University of Khorfakkan, Sharjah, United Arab Emirates. [159]Zoological Society of London, Regent's Park, London, UK. [160]Instituto de Investigaciones Marinas y Costeras (CONICET–UNMdP), Mar del Plata, Argentina. [161]Instituto de Investigación y Desarrollo Pesquero (INIDEP), Mar del Plata, Argentina. [162]Department of Geography, Durham University, Durham, UK. [163]Galapagos Whale Shark Project, Pto. Ayora, Galapagos, Ecuador. [164]Griffith Sciences, Centre for Marine and Coastal Research, Gold Coast (Queensland), Australia. [165]Saving the Blue, Cooper City, FL, USA. [166]Smithsonian Tropical Research Institute, Panama, Panama. [167]DBMS Global Oceans, Hobart (Tasmania), Australia. [168]School of Biology, University of Leeds, Leeds, UK. [169]Environmental Science and Policy, Rosenstiel School of Marine, Atmospheric and Earth Science, University of Miami, Miami, FL, USA. [170]Shark Research Foundation Inc, Boutiliers Point, Nova Scotia, Canada. [171]Department of Fisheries and Oceans Canada, Institut Maurice

Lamontagne, Mont-Joli, Quebec, Canada. [172]Newcastle upon Tyne, UK. [173]Grupo Tortuguero de las Californias, La Paz, Baja California Sur, Mexico. [174]Dominica Sea Turtle Conservation Organization, Rosalie, Dominica. [175]Sea Mammal Research Unit (SMRU), Scottish Oceans Institute, University of St Andrews, St Andrews, Fife, UK. [176]Conservation and Wildlife Branch, South Australian Department for Environment and Water, Adelaide (South Australia), Australia. [177]School of Biological and Environmental Sciences, Galapagos Science Center, Universidad San Francisco de Quito USFQ, Diego de Robles sn y Pampite Cumbaya, Quito, Pichincha, Ecuador. [178]Birds and Mammals, Greenland Institute of Natural Resources, Strandgade 91, 2, 1401 Copenhagen K, Denmark. [179]Groundswell Ecology, Davenport, CA, USA. [180]Ecology and Evolutionary Biology, University of California Santa Cruz, Santa Cruz, CA, USA. [181]APFFLT, Comisión Nacional de Áreas Naturales Protegidas, Ciudad del Carmen, Campeche, Mexico. [182]Integrated Systems Solutions, Tysons Corner, VA, USA. [183]Institute for Marine and Antarctic Studies, University of Tasmania, Hobart (Tasmania), Australia. [184]Blue Water Marine Research, Tutukaka, New Zealand. [185]School of Science, Technology & Engineering, University of the Sunshine Coast, Sippy Downs (Queensland), Australia. [186]Biosciences, College of Life and Environmental Sciences, University of Exeter, Exeter, Devon, UK. [187]Oceanic Whitetip Consortium, Ellicott City, MD, USA. [188]Johns Hopkins University, Baltimore, MD, USA. [189]Pelagios Kakunja A. C., Sinaloa 1540, La Paz, Baja California Sur, Mexico. [190]Fins attached: Marine Research and Conservation, Colorado Springs, CO, USA. [191]Fundação Projeto Tamar, Mata de São João, Bahia, Brazil. [192]Department of Integrative Biology, Faculty of Science, University of Windsor, Windsor, Ontario, Canada. [193]Statistics in Ecology, Environment and Conservation, Department of Statistical Sciences, University of Cape Town, Rondebosch, Cape Town, South Africa. [194]Cape Research & Diver Development, Simon's Town, South Africa. [195]Lancaster Environment Centre, Lancaster University, Lancaster, UK. [196]UMR ENTROPIE (UR, IRD, CNRS, IFREMER, UNC), Université de La Réunion, Saint Denis, La Réunion Island, France. [197]Dyer Island Conservation Trust, Kleinbaai, Western Cape, South Africa. [198]Blue Wilderness Shark Research Unit, Freeland Park, Scottburgh, KwaZulu Natal, South Africa. [199]Durrell Wildlife Conservation Trust, Les Augres Manor, Trinity, Jersey, UK. [200]Mauritian Wildlife Foundation, Grannum Road, Vacoas, Mauritius. [201]StochasticQC, Halifax, Nova Scotia, Canada. [202]Marine Science Department, California State University Monterey Bay, Seaside, CA, USA. [203]Fisheries Ecology, Centro de Investigaciones Biológicas del Noroeste, La Paz, Baja California Sur, Mexico. [204]Institute of Arctic Biology, Department of Biology and Wildlife, University of Alaska Fairbanks, Fairbanks, AK, USA. [205]University of California Davis, Davis, CA, USA. [206]Cape Research Centre, South African National Parks, Cape Town, South Africa. [207]Veterinary Services, Western Cape Department of Agriculture, Elsenburg, Stellenbosch, Western Cape, South Africa. [208]Franskraal Veterinary Facility, Gansbaai, Western Cape, South Africa. [209]Instituto PROSHARK (Associação Instituto PROSHARK Ecodesenvolvimento de Tubarões e Raias), Angra dos Reis–RJ, Brazil. [210]ARC Australian Centre for Excellence in Antarctic Science, Hobart (Tasmania), Australia. [211]Centre for Marine Socioecology, Hobart (Tasmania), Australia. [212]Ascension Island Conservation & Fisheries Directorate, Ascension Island Government, Conservation & Fisheries Directorate, Conservation Centre, ASCN 1ZZ Georgetown, Ascension Island. [213]International Arctic Research Center, University of Alaska Fairbanks, Fairbanks, AK, USA. [214]School for the Environment, University of Massachusetts Boston, Boston, MA, USA. [215]Instituto Politécnico Nacional, Centro Interdisciplinario de Investigación para el Desarrollo Integral Regional Unidad Sinaloa, Departamento de Medio Ambiente, Guasave, Sinaloa, Mexico. [216]Institute of Zoology, Zoological Society of London, Regent's Park, London, UK. [217]Visualization and Data Intelligence Group, WSP, Virginia Beach, VA, USA. [218]Boston CES Group, Tetra Tech, Boston, MA, USA. [219]Fundação Florestal, Petrópolis, São Paulo, São Paulo, Brazil. [220]Karumbe, Zoo Villa Dolores, Montevideo, Uruguay. [221]Large Pelagics Research Center, School for the Environment, UMass Boston, Gloucester, MA, USA. [222]Pacific Islands Fisheries Group, Koloa, HI, USA. [223]Lyon Marine Research Limited, Karori, Wellington, New Zealand. [224]World Wide Fund for Nature, Brisbane (Queensland), Australia. [225]Biology, Acadia University, Wolfville, Nova Scotia, Canada. [226]Department of Biology, University of Central Florida, Orlando, FL, USA. [227]Marine Zoology Unit, Cavanilles Institute of Biodiversity and Evolutionary Biology, University of Valencia, Valencia, Spain. [228]Ethology and Conservation of Biodiversity, Doñana Biological Station, CSIC, Sevilla, Spain. [229]Massey University, Auckland, New Zealand. [230]Natural Science, State College of Florida, Bradenton, FL, USA. [231]Science Department, Ransom Everglades School, Coconut Grove, FL, USA. [232]Department of Fisheries, Wildlife, and Conservation Sciences, Oregon State University, Hatfield Marine Science Center, Newport, OR, USA. [233]Arctic Beringia Program, Wildlife Conservation Society, Fairbanks, AK, USA. [234]Biosecurity, Primary Industries and Regions South Australia (PIRSA), Urrbrae (South Australia), Australia. [235]IMOS Animal Tagging, Sydney Institute of Marine Science, Mosman (New South Wales), Australia. [236]School of Natural Sciences, Macquarie University, North Ryde (New South Wales), Australia. [237]Departamento de Ciências do Mar (DCMar), Instituto do Mar (IMar), Universidade Federal de São Paulo–UNIFESP, Campus Baixada Santista, Santos, São Paulo, Brazil. [238]INCT Mar COI, Instituto de Oceanografia, Universidade Federal do Rio Grande–FURG, Campus Carreiros, Rio Grande, Rio Grande do Sul, Brazil. [239]Dakshin Foundation, MCECHS Layout Sahakar Nagar, Bengaluru, India. [240]Independent researcher, Davenport, CA, USA. [241]Centre for Sustainable Aquatic Ecosystems, Harry Butler Institute, Murdoch University, Murdoch (Western Australia), Australia. [242]ECOCEAN Inc., Coogee (Western Australia), Australia. [243]Natural History Museum, London, UK. [244]Institute of Marine Research, Nordnes, Bergen, Norway. [245]Centre for Conservation Science, Royal Society for the Protection of Birds (RSPB), The David Attenborough Building, Cambridge, UK. [246]Alaska Science Center, U.S. Geological Survey, Anchorage, AK, USA. [247]University of Coimbra, CFE–Centre for Functional Ecology, Associate Laboratory TERRA, Department of Life Sciences, Calçada Martim de Freitas, Coimbra, Portugal. [248]Center for Coastal Studies, Provincetown, MA, USA. [249]Institute of Environment, Department of Biological Sciences, Florida International University, North Miami, FL, USA. [250]Golden Honu Services of Oceania, Newport, OR, USA. [251]Ocean Outcomes, Hoyo de Manzanares, Madrid, Spain. [252]Center for Ocean Solutions, Stanford University, Pacific Grove, CA, USA. [253]Pepperell Research & Consulting Pty Ltd, Noosaville (Queensland), Australia. [254]Marine Megafauna Foundation, West Palm Beach, FL, USA. [255]Marine Research Foundation, Taman Khidmat, Kota Kinabalu, Sabah, Malaysia. [256]Université de La Reunion, Saint-Denis, La Réunion Island, France. [257]Centre for Research into Ecological and Environmental Modelling (CREEM), University of St Andrews, The Observatory Buchanan Gardens, St Andrews, Fife, UK. [258]U.S. Geological Survey, Florida Cooperative Fish and Wildlife Research Unit, University of Florida, Gainesville, FL, USA. [259]Stellwagen Bank National Marine Sanctuary, Scituate, MA, USA. [260]Laboratorio de Ecología, Comportamiento y Mamíferos Marinos (LECyMM), Museo Argentino de Ciencias Naturales (MACN-CONICET), Ciudad Autónoma de Buenos Aires, Argentina. [261]CNRS, IPHC UMR 7178, Univ Strasbourg, Strasbourg, France. [262]Secretariat of the Convention on Migratory Species (CMS), Bonn, Germany. [263]Whale Shark México (WSM), Conexiones Terramar AC, Solmar L5, La Paz, B.C.S., Mexico. [264]Duke University Marine Laboratory, Duke University, Beaufort, NC, USA. [265]Alaska Fisheries Science Center, National Marine Fisheries Service, National Oceanic and Atmospheric Administration (NOAA), Seattle, WA, USA. [266]ARCHELON, The Sea Turtle Protection Society of Greece, Athens, Greece. [267]School of Ocean and Earth Science, University of Southampton, National Oceanography Centre Southampton European Way, Southampton, UK. [268]Cavanilles Institute of Biodiversity and Evolutionary Biology, Valencia, Spain. [269]School of the Environment, The University of Queensland, St Lucia, Brisbane (Queensland), Australia. [270]CSIRO Environment, Queensland Biosciences Precinct St Lucia, Brisbane (Queensland), Australia. [271]School of Biological Sciences, University of Auckland, Auckland, New Zealand. [272]Proyecto Franca Austral, Maldonado, Uruguay. [273]Sundive Research, Byron Bay (New South Wales), Australia. [274]Department of Ecology, Institute of Biology, Universidade do Estado do Rio de Janeiro, Maracanã, 20550-013 Rio de Janeiro, Rio de Janeiro, Brazil. [275]Centre for Marine Science and Innovation, School of Biological Earth and Environmental Sciences, University of New South Wales, Sydney (New South Wales), Australia. [276]Clearwater Marine Aquarium, Clearwater, FL, USA. [277]Marine Conservation Society Seychelles, Victoria, Seychelles. [278]National Parks and Conservation Service, Government of Mauritius, Reduit, Mauritius. [279]National Institute of Water and Atmospheric Research Ltd (NIWA), Riccarton, Christchurch, New Zealand. [280]CORDIO East Africa, Mombasa, Kenya. [281]Departamento de Ciencias Naturales y Exactas, Universidad Autónoma de Occidente, Unidad Regional Los Mochis, Los Mochis, Sinaloa, Mexico. [282]Centro TAMAR-ICMBio, Instituo Chico Mendes de Conservação da Biodiversidade–ICMBio, Enseada do Suá Ed. PetroTower, Enseada do Suá, Vitória, Espírito Santo, Brazil. [283]Biology, Faculty of Sciences, Universidade do Porto, Porto, Portugal. [284]School of Biological and Behavioural Sciences, Queen Mary University of London, London, UK. [285]Elasmobranch Institute Indonesia, Jl. Tukad Badung VII No.4B, Denpasar, Bali, Indonesia. [286]Department of Biological Sciences, San Jose State University, San Jose, CA, USA. [287]Centre for Ecological Sciences, Indian Institute of Science, Bengaluru, India. [288]Upwell, Monterey, CA, USA. [289]Guy Harvey Research Institute, Halmos College of Arts and Sciences, Nova Southeastern University, Dania Beach, FL, USA. [290]Shark Research Program, Massachusetts Division of Marine Fisheries, New Bedford, MA, USA. [291]Taronga Institute of Science and Learning, Taronga Conservation Society Australia, Mosman (New South Wales), Australia. [292]Zoology Department, Nelson Mandela University, Gqeberha, Eastern Cape, South Africa. [293]Wildlife Conservation Research Unit (WildCRU), Department of Zoology, University of Oxford, Recanati-Kaplan Centre Tubney House, Oxford, Oxfordshire, UK. [294]Museum of New Zealand Te Papa Tongarewa, Wellington, New Zealand. [295]Pacific Salmon Foundation, Vancouver, British Columbia, Canada. [296]CSIRO, Castray Esplanade Battery Point, Hobart (Tasmania), Australia. [297]National Institute of Polar Research, Tachikawa, Tokyo, Japan. [298]Department of Polar Science, The Graduate University for Advanced Studies, SOKENDAI, Tachikawa, Tokyo, Japan. [299]Graduate School of Fisheries Sciences, Hokkaido University, Hakodate, Japan. [300]South African International Maritime Institute (SAIMI), Gqeberha, Eastern Cape, South Africa. [301]MEDTOP programme, Alnitak, Hoyo de Manzanares, Madrid, Spain. [302]Chelonia Inc, San Juan, PR, Puerto Rico. [303]Cetacean and Marine Research Institute of the Canary Islands (CEAMAR), C/Tinasoria 5. San Bartolomé, Las Palmas, Spain. [304]Departamento de Biología, Facultad de Ciencias del Mar, University of Las Palmas de Gran Canaria, Las Palmas, Spain. [305]Observatorio Ambiental Granadilla, Santa Cruz de Tenerife, Spain. [306]Centre d'Etudes Biologiques de Chizé, La Rochelle University, CEBC–Université de La Rochelle, La Rochelle, France. [307]ERM, District I Ho Chi Minh City, Vietnam. [308]UK Centre for Ecology & Hydrology, Bush Estate, Penicuik, UK. [309]Research Center for Integrative Evolutionary Science, The Graduate University for Advanced Studies, SOKENDAI, Hayama, Kanagawa, Japan. [310]Department of Biological Sciences, University of Manitoba, Winnipeg, Manitoba, Canada. [311]Office of Naval Research, Arlington, VA, USA [312]U. S. Fish and Wildlife Service, Milbridge, ME, USA. [313]Sarasota Dolphin Research Program, Brookfield Zoo Chicago, c/o Mote Marine Laboratory, Sarasota, FL, USA. [314]Griffith Centre for Coastal Management, Griffith University, Gold Coast (Queensland), Australia. [315]GHD, L4 211 Victoria Square, Adelaide (South Australia), Australia. [316]Biological Sciences, College of Environment and Life Sciences, University of Rhode Island, Kingston, Rhode Island, USA. [317]Global Fishing Watch, Washington, DC, USA. [318]Wild Outlook Pty Ltd, Bentley DC (Western Australia), Australia. [319]Marine Science Program, Biological and Environmental Science and Engineering Division, King Abdullah University of Science and Technology (KAUST), Thuwal, Kingdom of Saudi Arabia. [320]National Oceanic and Atmospheric Administration, National Ocean Service, Stellwagen Bank National Marine Sanctuary, Scituate, MA, USA. [321]US Arctic Program, World Wildlife Fund, Anchorage, USA. [322]Faculty of Health and Life Sciences, University of Exeter, Hatherly Laboratories, Exeter, Devon, UK. [323]Environment and Sustainability Institute, University of Exeter, Penryn Campus, Penryn, County, UK. [324]Department of Animal Science and Biotechnology, School of Veterinary Medicine, Azabu University, Sagamihara, Kanagawa, Japan. [325]Departamento de Evaluación de Pesquerías, Instituto de Fomento Pesquero, Blanco, Valparaiso, Chile. [326]Grupo Tortuguero de las Californias A.C., La Paz, Baja California Sur, Mexico. [327]UWA Oceans Institute, The University of Western Australia, Crawley (Western Australia), Australia. [328]OSSARI, Neom, Saudi Arabia. [329]Deakin Marine Research and Innovation Centre, School of Life and Environmental Sciences, Deakin University, Geelong (Victoria), Australia. [330]Basque Centre for Climate Change (BC3), Scientific Campus of the University of the Basque Country, Leioa, Spain. [331]IKERBASQUE, Basque Foundation for Science, Bilbao, Spain. ***Corresponding author. Email: ana.sequeira@anu.edu.au** †These authors contributed equally to this work. ‡Deceased. §These authors contributed equally to this work.

SUPPLEMENTARY MATERIALS

science.org/doi/10.1126/science.adl0239
Materials and Methods; Supplementary Acknowledgments; Supplementary Author Contributions; Figs. S1 to S17; References (*112*–*135*)

Submitted 26 September 2023; accepted 9 April 2025

10.1126/science.adl0239

BIOCHEMICAL CYCLES

Integrated carbon and nitrogen management for cost-effective environmental policies in China

Xin Xu[1,2], Xiuming Zhang[3], Yiyang Zou[1,2,4], Tianrun Chen[5], Jingfang Zhan[1,2], Luxi Cheng[1,2,6], Wilfried Winiwarter[3,7], Shaohui Zhang[3,8], Peter M. Vitousek[9], Wim de Vries[10], Baojing Gu[1,2,11]*

Carbon and nitrogen are central elements in global biogeochemical cycles. To effectively manage carbon and nitrogen in China, we developed a comprehensive model for quantifying their fluxes, investigating their interplay across 16 human and natural subsystems. Between 1980 and 2020, nitrogen losses in China increased 2.3-fold and carbon emissions surged 6.5-fold. Integrated carbon and nitrogen management holds the potential for a 74% reduction in nitrogen losses to air and water and a 91% decrease in carbon emissions to the atmosphere by 2060. Compared with separate control of carbon or nitrogen, integrated management delivers an additional reduction of 1.8 million tons of nitrogen and 26.5 million tons of carbon by 2060, bringing out a 37% decrease in unit abatement cost and a net societal benefit of 1384 billion USD.

Carbon and nitrogen are fundamental elements in the biogeochemical cycle, playing distinctive roles in shaping both natural and human-dominated ecosystems (*1*, *2*). In natural systems, the carbon and nitrogen cycles are strongly interconnected, collectively influencing vegetation growth and biodiversity while also serving as key indicators of soil health. Within human societies, nitrogen fixation through synthetic fertilizers is indispensable for food production, but it is associated with increased emissions of ammonia (NH_3) and nitrous oxide (N_2O) into air, as well as nitrate (NO_3^-) into water. Additionally, the combustion of fossil fuels exacerbates emissions of nitrogen oxides (NO_x) and carbon dioxide (CO_2). Although carbon and nitrogen are vital for food, feed, and wood production, their excessive losses into the environment pose threats to climate, biodiversity, and air and water quality (*3*–*6*). Since the start of the preindustrial era, anthropogenic emissions of carbon and nitrogen have escalated substantially, surpassing the safe operating boundaries of our planet (*7*).

Human-induced perturbations of global carbon and nitrogen cycles are inherently linked (*8*). For example, elevated CO_2 levels have a fertilizing effect on forest ecosystems (*9*), and nitrogen normally limits vegetation growth and carbon accumulation, whereas carbon sequestration in soils may enhance N_2O emissions (*10*, *11*). Regional coordination in carbon and nitrogen management requires a comprehensive insight into the complex interactions within human and natural systems (*12*). However, the integrated management of carbon and nitrogen considering multicompartment (e.g., air, soil, or water bodies) and cross-sector (e.g., industry, agriculture, or forestry) dynamics remains largely unexplored (*13*). In China, the integrated mitigation potential is mainly explored in reducing atmospheric nitrogen pollutants and CO_2 emission across the industrial, energy, and transportation sectors (*14*, *15*). In the agricultural sector, efforts have largely targeted controlling non–point source pollution, particularly nitrate runoff and leaching. However, the interactions and trade-offs between decarbonization strategies and nitrogen reductions remain insufficiently understood. A thorough evaluation of mitigation costs and associated social benefits is crucial to ensure the feasibility of carbon and nitrogen management strategies. Therefore, a generic approach is needed to systematically model regional carbon and nitrogen cycles and to assess the mitigation potential and cost-effectiveness of different strategies, offering effective guidance for policy-making.

To address the knowledge gap, we synthesized carbon and nitrogen flows in China with the Coupled Human and Natural Systems-Carbon and Nitrogen cycles (CHANS-CN) model (fig. S1). First, we investigated carbon and nitrogen sources, fluxes, and fates from 1980 to 2020 across 16 different subsystems (fig. S2). Subsequently, leveraging subsystem-level budgets and mitigation measures, we simulated potential trajectories of carbon and nitrogen fluxes and their coupling from 2020 to 2060 under various management scenarios. Finally, we quantified the cost-effectiveness of integrated carbon and nitrogen management compared with separate strategies. This study provides valuable insights for achieving substantial environmental, climate, and economic benefits through integrated carbon and nitrogen management in China.

Results and discussion

The CHANS-CN model

We first built the CHANS-CN model to integrate carbon and nitrogen flows on a national scale, covering 16 subsystems and >6000 fluxes (see the materials and methods and supplementary text). Carbon and nitrogen inputs predominantly arise from biological fixation, chemical fixation, fossil fuel combustion, industrial processes, and geological activities, along with external imports or exports through trade and other natural sources (e.g., lightning). From 1980 to 2020, China's total carbon inputs increased from 1.5 to 6.5 Pg C $year^{-1}$, carbon input from fossil fuels increased from 0.6 to 4.6 Pg C $year^{-1}$, and carbon fixed by plant photosynthesis increased from 0.9 to 1.9 Pg C $year^{-1}$ (fig. S3a). In addition, total nitrogen inputs increased from 23.7 Tg N $year^{-1}$ in 1980 to 77.8 Tg N $year^{-1}$ in 2015, with the proportion of Haber-Bosch nitrogen fixation (*16*) rising from 46 to 77% and biological nitrogen fixation decreasing from 30 to 11%. However, from 2015 to 2020, nitrogen inputs declined slightly but remained 2.7 times higher than in 1980 (fig. S3b). These inputs circulated through subsystems, causing cascading effects, with carbon and nitrogen either stored or lost to the environment. Carbon outputs mainly involve agro-food and feed exports, along with dissolved carbon entering the ocean (*17*) (fig. S4). Nitrogen outputs primarily manifest as N_2 emissions through denitrification (*18*), along with nitrogen entering the atmospheric circulation or the ocean.

To assess the long-term trajectory and impacts of carbon and nitrogen emissions, we introduced the carbon-nitrogen impact equivalent (CNI_{eq}), an index that weighs different compounds based on their monetary value of impacts on climate, ecosystem, and human health (see the materials and methods). From 1980 to 2020, reactive nitrogen (N_r, all nitrogen species except N_2) losses initially increased, peaking around 2012 at 79.0 Tg CNI_{eq} before declining (Fig. 1A). This decline could be attributed to NO_x reductions benefiting from the

[1]State Key Laboratory of Soil Pollution Control and Safety, Zhejiang University, Hangzhou, China. [2]College of Environmental and Resource Sciences, Zhejiang University, Hangzhou, China. [3]International Institute for Applied Systems Analysis, Laxenburg, Austria. [4]Ministry of Education Key Laboratory of Environment Remediation and Ecological Health, Zhejiang University, Hangzhou, China. [5]College of Computer Science and Technology, Zhejiang University, Hangzhou, China. [6]Policy Simulation Laboratory, Zhejiang University, Hangzhou, China. [7]Institute of Environmental Engineering, University of Zielona Góra, Zielona Góra, Poland. [8]School of Economics and Management, Beihang University, Beijing, China. [9]Department of Earth System Science, Stanford University, Stanford, CA, USA. [10]Wageningen University and Research, Earth Systems and Global Change Group, Wageningen, Netherlands. [11]Zhejiang Provincial Key Laboratory of Agricultural Resources and Environment, Zhejiang University, Hangzhou, China. ***Corresponding author. Email: bjgu@zju.edu.cn**

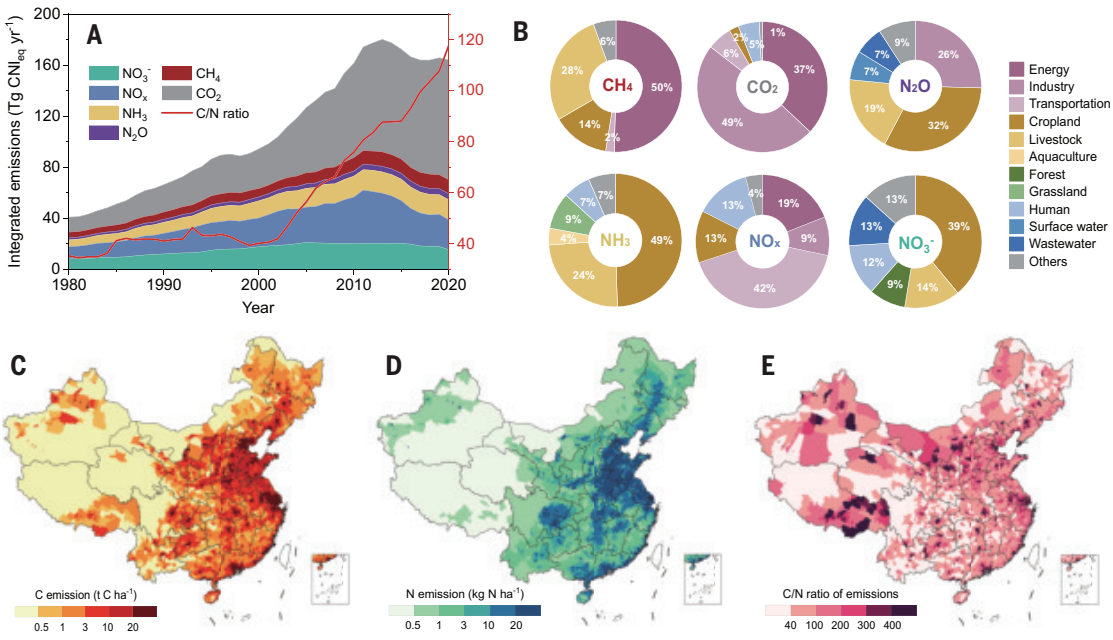

Fig. 1. Spatiotemporal characteristics of carbon and nitrogen emissions and the C/N ratio. (**A**) Carbon and nitrogen emissions, along with C/N (mass/mass) ratio of emissions in China from 1980 to 2020. Note that the carbon emissions consist of CO_2 and CH_4, and nitrogen emissions include NO_3^-, NO_x, N_2O, and NH_3 (see the materials and methods). The red line on the right vertical axis represents the C/N ratio of emissions. (**B**) Relative subsystem contributions (%) to carbon and nitrogen emissions in 2020. (**C** to **E**) Geographical distribution of carbon emission intensity (C), nitrogen emission intensity (D), and the C/N ratio of emissions (E) in 2020. The base map was derived from the Database of Global Administrative Areas (https://gadm.org/).

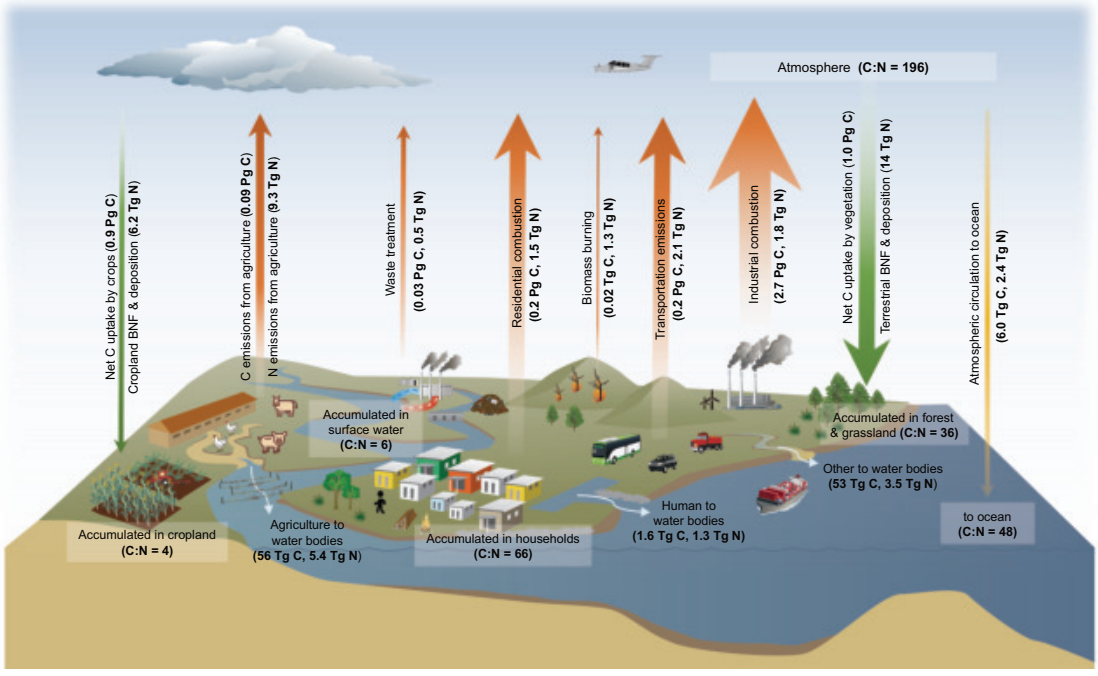

Fig. 2. Terrestrial and atmospheric carbon and nitrogen fluxes and accumulation in 2020. Shown are carbon and nitrogen fluxes and the C/N ratio of accumulation in China for 2020. Orange arrows indicate emissions to the atmosphere, blue arrows indicate emissions to the water bodies (including leaching and runoff), green arrows indicate land deposition, and yellow arrows indicate cycling quantities.

Air Pollution Control Program (*19*) and the decreased NH_3 and NO_3^- emissions due to improved synthetic fertilizer and manure management (*20*, *21*). By contrast, carbon emissions sustained an upward trend, particularly between 2000 and 2013, with an average annual growth rate of 8% (fig. S5). In recent years, the growth has been halted, reaching 105 Tg CNI_{eq} in 2020, signifying a 6.5-fold increase since 1980. Of this, industry and energy contributed >85% of CO_2 emissions and >50% of CH_4 emissions, and agriculture and livestock contributed 42% of CH_4 emissions in 2020 (Fig. 1B). Spatial variations of carbon and nitrogen emissions across China in 2020 are depicted in Fig. 1, C to E, and fig. S6. High carbon emissions were mainly concentrated in areas such as the Yangtze River Delta and the Northeast China Plain, with elevated nitrogen losses occurring in the middle and lower Yangtze Plain and the Northeast China Plain. Regions with a high C/N emissions ratio were predominantly located in densely populated or urbanized regions.

Figure 2 illustrates overall carbon and nitrogen fluxes in China's terrestrial, atmospheric, and aquatic ecosystems in 2020. The grassland and forest subsystems received inputs of 1.0 Pg C and 14 Tg N, primarily from biological fixation and atmospheric deposition. These inputs underwent transformation, recycling, and transfer through processes such as harvesting, runoff, volatilization, and denitrification, ultimately leading to an accumulation with a C/N ratio of 36 in these natural ecosystems (see the materials and methods). Similarly, 0.9 Pg C and 6.2 Tg N entered the cropland subsystem, with a lower C/N ratio of accumulation at 4. The human subsystem, as a core consumer, received 22 Tg N and 0.8 Pg C supplied from subsystems as food, fuel, and commodities (fig. S4), emitting 0.2 Pg C and 1.5 Tg N into the atmosphere, with the C/N ratio of accumulation at 66. In addition, energy and industrial production contributed 85% of carbon and 11% of nitrogen emissions; agricultural practices, including cropland, livestock, and aquaculture, contributed 56% of nitrogen and 3% of carbon emissions. The transportation sector released 2.1 Tg N and 0.2 Pg C through fuel combustion, and waste disposal, including garbage and wastewater, emitted 0.03 Pg C and 0.5 Tg N. The C/N ratio of surface water accumulation was estimated at 6, with agriculture contributing >50%, followed by domestic and industrial wastewater discharge (16%). Assuming a balanced state of emissions and distribution between the atmosphere, ocean, and inland in China, we also estimated carbon and nitrogen fluxes for air-sea circulation, revealing a C/N ratio of ~48.

Coupling between carbon and nitrogen

Based on the CHANS-CN model, we examined the historical and future trends of carbon and nitrogen emissions in China, mainly focusing on their relative magnitudes and coupling processes. Between 1980 and 2000, the C/N ratio of emissions remained stable at ~35 to 44 (Fig. 3A). Agricultural sources contributed ~35% of total emissions, and the share of industry-related sources increased from 42 to 50% (fig. S5). The stable C/N ratio suggests that appropriate carbon fertilization and adequate nitrogen supply may enhance carbon fixation in ecosystems, a trend further supported by satellite observations of the greening in China during this period (*22*, *23*). Over the past two decades, both carbon and nitrogen emissions surged, particularly from industrial sources, contributing 66% in 2020, and the share of agriculture dropped to 20% (figs. S5 and S7). The C/N ratio tripled, reaching 119 by 2020, revealing an asymmetry in carbon and nitrogen emissions. Despite enhanced carbon fertilization effects, the imbalanced

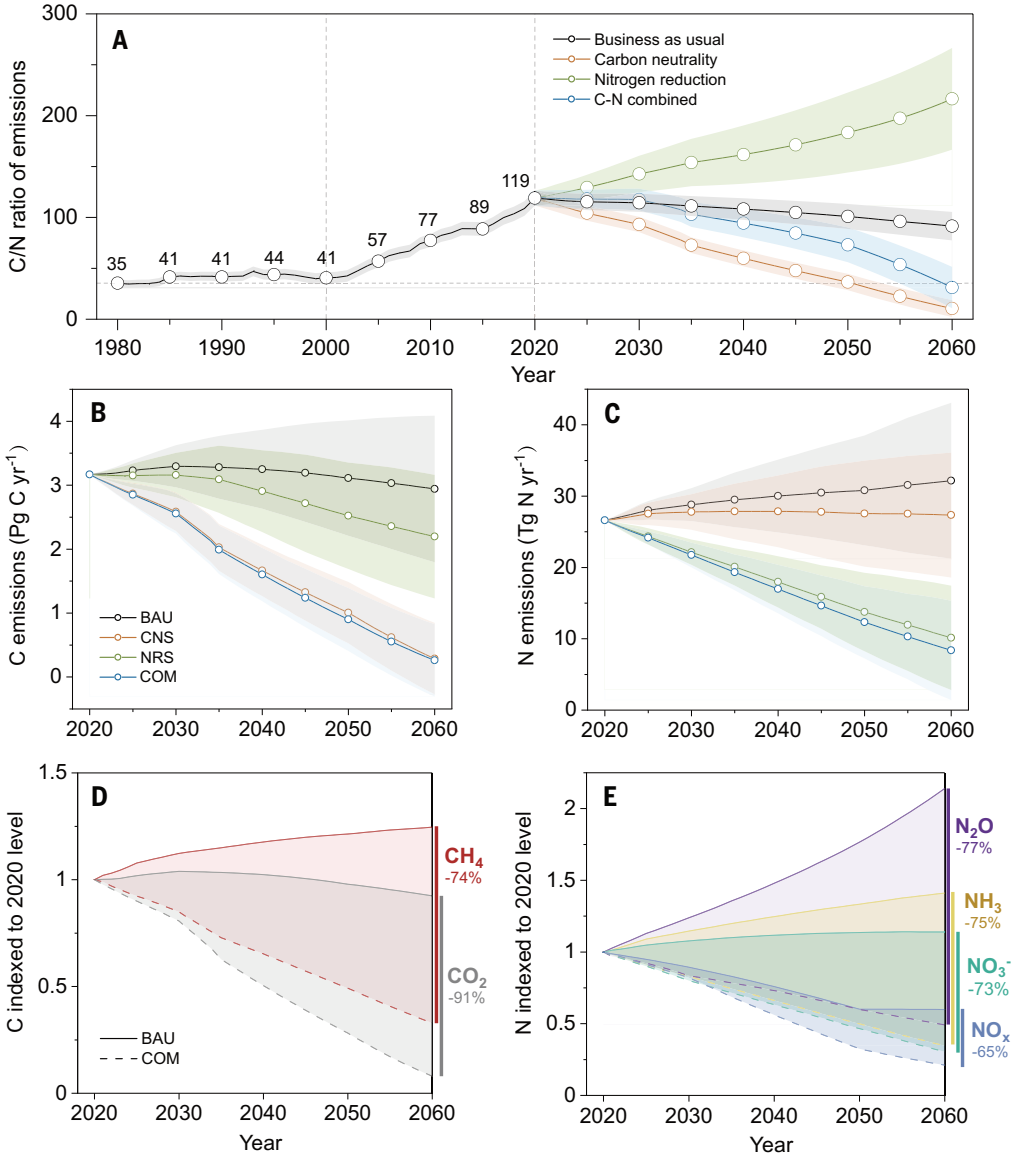

Fig. 3. Future projection of carbon and nitrogen emissions and the C/N ratio under the BAU, CNS, NRS, and COM scenarios. (**A**) C/N ratio of emissions under the BAU, CNS, NRS, and COM scenarios. (**B**) Carbon emissions from 2020 to 2060, including CH_4 and CO_2, standardized in Pg C $year^{-1}$. (**C**) Nitrogen emissions from 2020 to 2060, including NH_3, NO_3^-, N_2O, and NO_x, standardized in Tg N $year^{-1}$. (**D** and **E**) Mitigation potential of carbon (D) and nitrogen (E) emissions relative to 2020 levels under the BAU and COM scenarios, respectively.

inputs of carbon and nitrogen have restricted the potential of carbon sinks to offset excessive greenhouse gas emissions (*24*). This underscores the importance of integrated carbon and nitrogen management, which involves coordinating both carbon and nitrogen abatement across subsystems, rather than isolated controls, to safeguard food security and ecosystem carbon sequestration (*25*, *26*).

To evaluate the effects of separate versus integrated management, four management scenarios were simulated based on the CHANS-CN model: nitrogen emission reduction (NRS), carbon emission reduction (CNS), combined carbon and nitrogen emission reduction (COM), and a business-as-usual (BAU) scenario (see the materials and methods and tables S1 and S2). The NRS focuses exclusively on nitrogen management, mainly through agricultural practices and dietary transitions, and the CNS centers on carbon management, targeting fossil fuel production and consumption. By contrast, the COM emphasizes integrated management across all subsystems, aiming to mitigate the trade-offs of isolated measures. From 2020 to 2060, the C/N ratio of emissions under the BAU scenario is projected to decline slightly, with an average value of 107 (Fig. 3A). Under the NRS scenario, the C/N ratio will increase to 217 by 2060 due to inadequate control over carbon emissions. Conversely, the C/N ratio for CNS will continue to decrease, returning to historically low levels by 2050, but nitrogen losses will remain high, at ~26 Tg N $year^{-1}$ (Fig. 3C). The COM scenario demonstrates the greatest mitigation potential, reducing carbon emissions by 91% and nitrogen emissions by 74% by 2060. Specifically, emissions of CH_4 and CO_2 could decrease by 74 and 91% (Fig. 3D), and emissions of N_2O, NH_3, NO_3^-, and NO_x would decrease by 77, 75, 73, and 65%, respectively (Fig. 3E). The C/N ratio under the COM scenario in 2060 will fall between that of NRS and CNS scenarios, around the historical range of 35 to 44 observed between 1980 and 2000, when China experienced relatively good environmental quality, a stable food supply, and effective carbon sequestration (*22*, *27*, *28*).

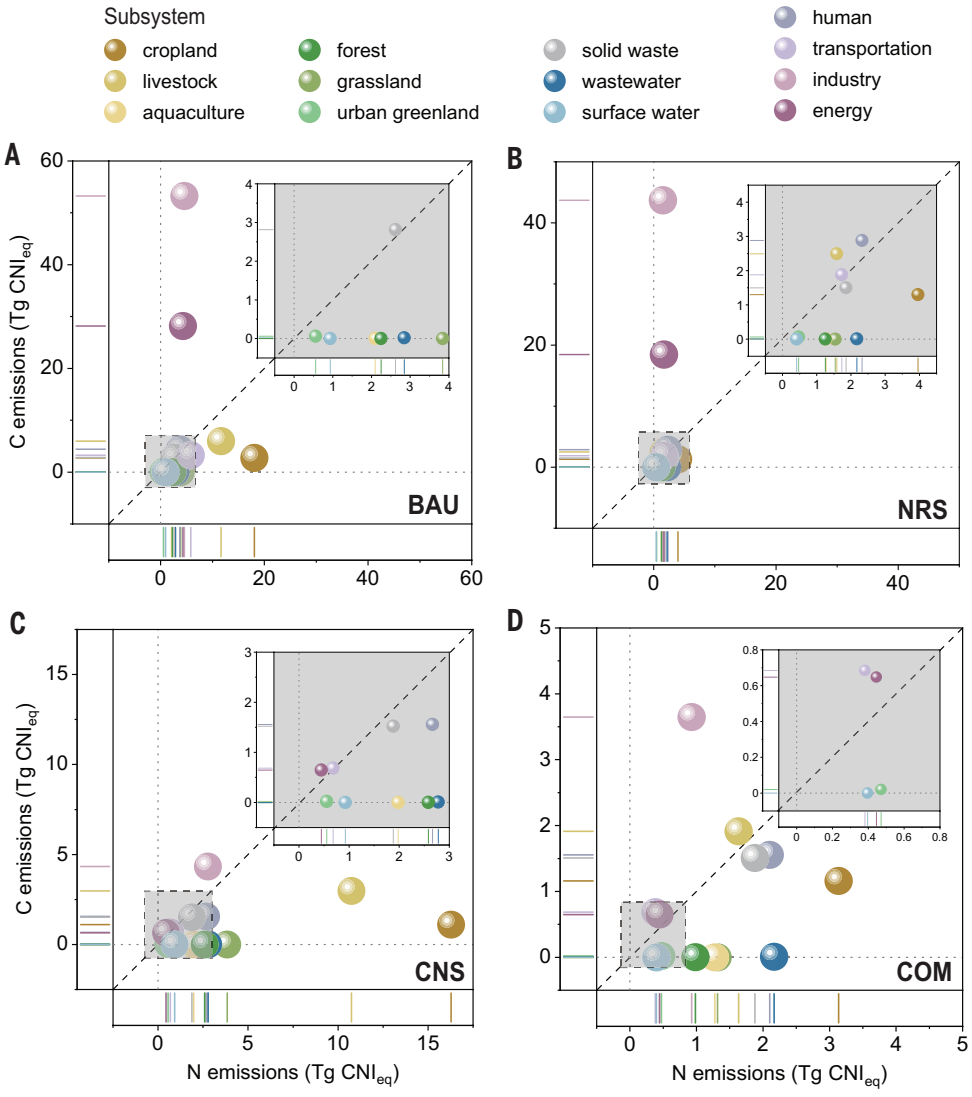

Fig. 4. Coupling degrees of carbon and nitrogen emissions for various subsystems in 2060. (**A** to **D**) Coupling degrees of carbon and nitrogen emissions under the BAU (A), NRS (B), CNS (C), and COM (D) scenarios in 2060. The horizontal coordinate represents nitrogen emissions, and the vertical coordinate represents carbon emissions, both normalized to Tg CNI_{eq} (see the materials and methods). The gray portion is an enlarged view within the small box. Note that the proximity to the dashed line indicates the degree of coupling between carbon and nitrogen emissions.

To prioritize integrated mitigation strategies at the subsystem level, we further analyzed the coupling processes in which certain carbon and nitrogen emissions share common sources or a single mitigation measure can reduce both emissions to some extent. To quantify the degree of coupling, we introduced two parameters, SE_1 and SE_2, representing the coupling degrees of emission and mitigation, respectively, within a range of 0 to 1 (see the materials and methods). A coupling degree of 1 indicates that a biogeochemical process results in equivalent carbon and nitrogen emissions (SE_1) or that a mitigation measure can reduce both emissions equally (SE_2), as defined by CNI_{eq}. A smaller coupling degree signifies weaker connections between carbon and nitrogen emissions and their mitigations. Most subsystems, especially transportation, human, and garbage subsystems, exhibited robust carbon-nitrogen coupling (fig. S8). However, this coupling pattern weakened from 2000 to 2020. Taking the industry and energy subsystems as examples, before 2000, the average coupling degree SE_1 for these subsystems was ~0.98, whereas by 2020, these coefficients had dropped to 0.52 and 0.59, respectively, as carbon emissions became dominant. Without further intervention, these coefficients are projected to be 0.54 and 0.68 by 2060, indicating persistent imbalances in carbon and nitrogen emissions along historical trajectories (Fig. 4A and fig. S9).

Nitrogen management alone will enhance the coupling of carbon and nitrogen emissions in the cropland and livestock subsystems, with coupling degree SE_1 increasing by 13% (to 0.86) and 5% (to 0.98), respectively, by 2060 (Fig. 4B). Similarly, carbon management alone will improve coupling degree SE_1 in the industry and energy subsystems by 87 and 66%, respectively (Fig. 4C). However, relying solely on carbon or nitrogen mitigation strategies reduces the overall coupling degree SE_1 by 12 and 15% across all sectors, respectively, highlighting the inherent trade-offs of singular mitigation solutions. By contrast, integrated management will elevate China's overall carbon-nitrogen coupling degree SE_1 to 0.98 by 2060. Substantial improvements will occur

in the energy, industry, livestock, and cropland subsystems, with their SE_1 increasing by 66, 54, 39, and 17%, respectively (Fig. 4D).

The coupling degree SE_2 values of carbon and nitrogen reductions under each scenario are illustrated in fig. S10. From 2020 to 2060, integrated management ensures that the coupling degree SE_2 of carbon and nitrogen reductions exceeds 0.92 across the entire system. Subsystems with higher SE_2, such as human (0.98), garbage (0.95), transportation (0.94), and livestock (0.93), suggest that their embedded abatement measures are crucial entry points for integrated management. Nevertheless, in certain subsystems where carbon or nitrogen processes dominate the overall biogeochemical dynamics, the COM strategy does not always outperform separate management. For example, in forest and grassland ecosystems, substantial nitrogen reductions may decrease nitrogen bioavailability, consequently weakening their carbon sequestration potential (*25*). Conversely, for wastewater and surface water subsystems, which are dominated by nitrogen emissions with low coupling degrees, integrated management may fail to demonstrate coupling advantages.

Co-benefits of carbon and nitrogen management

Integrated carbon and nitrogen management offers considerable economic opportunities at relatively low intervention costs, with net social benefits expected to rise continuously as mitigation measures permeate various sectors. Here, we quantified total abatement costs based on metric unit costs, baseline activity levels, and implementation rates; social benefits reflect the avoided damage costs attributed to the carbon and nitrogen emission reduction (see the materials and methods and table S3). Under the CNS scenario, the implementation cost in 2060 is estimated at 371 billion USD, yielding a net benefit of 1036 billion USD, with the highest mitigation costs in the energy (accounting for 77%) and industry (15%) subsystems (Fig. 5A). Conversely, the NRS scenario presents a lower implementation cost of 101 billion USD, with a net social benefit of 932 billion USD by 2060 (Fig. 5C), primarily benefiting the livestock (22%) and cropland (21%) subsystems. The total abatement cost across all subsystems under the COM scenario will be 424 billion USD, and the resulting social benefits will reach 1809 billion USD, surpassing the costs fourfold (Fig. 5E). In addition, the cost-benefit ratio under carbon-focused management will increase and then decrease from 2020 to 2060, peaking at 4.9 by around 2035. By contrast, the cost-benefit ratio for nitrogen-focused management will continue to increase, reaching 10.2 in 2060, driven by benefits from the transportation, livestock, and cropland subsystems (fig. S11). Thus, we suggest prioritizing carbon mitigation measures with supplementary nitrogen reduction before carbon peak to unleash the abatement potential of high-carbon-emitting industries under a progressively stricter carbon pricing market. In the long term, nitrogen mitigation options will be more cost-effective and can actively stimulate carbon co-reduction in China.

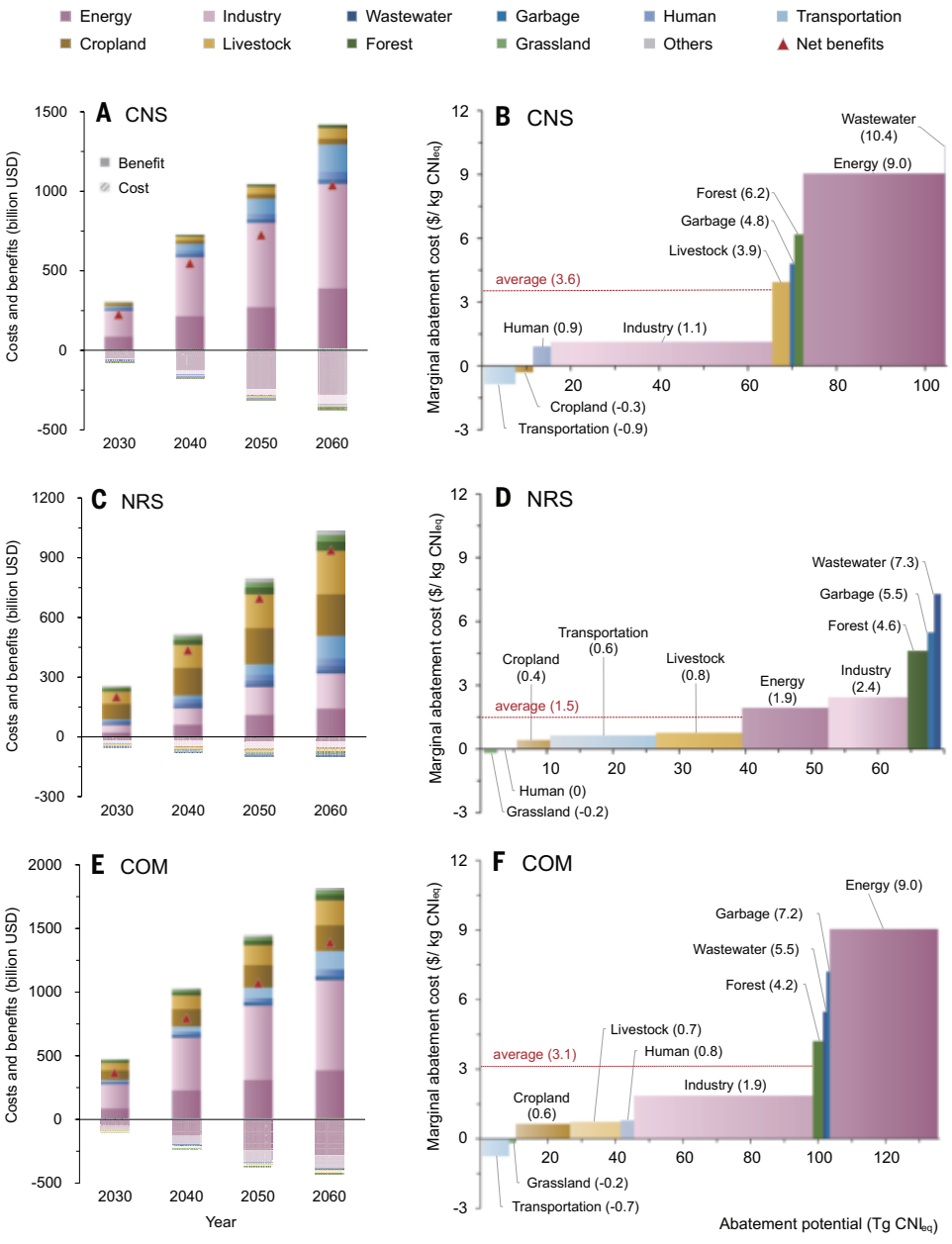

Fig. 5. Cost-benefit analysis of the subsystem abatement under the CNS, NRS, and COM scenarios. (**A** to **F**) Total implementation costs, social benefits, and net social benefits (in billions of USD) are shown for subsystem abatement in 2030, 2040, 2050, and 2060 under the CNS (A), NRS (C), and COM (E) scenarios. Marginal abatement costs (USD per kg CNI_{eq}) are shown for 10 subsystems under the CNS (B), NRS (D), and COM (F) scenarios in 2060. Note that six subsystems (aquaculture, pets, urban green land, surface water, groundwater, and atmosphere) are classified as "others" and include no specific abatement measures, so their implementation costs are not considered.

By integrating the carbon and nitrogen mitigation potential, we further analyzed the marginal abatement costs of various subsystems in 2060. Under the CNS scenario, the subsystems with the highest marginal abatement costs are wastewater treatment, energy, and forest, at 10.40, 9.00, and 6.20 USD per kg CNI_{eq}, respectively (Fig. 5B). By contrast, subsystems including transportation and cropland, despite having lower abatement potential, exhibit negative costs (i.e., cost savings), alleviating economic pressures. In the NRS scenario, the subsystems with the highest marginal costs are garbage, wastewater

treatment, and forest, at 7.30, 5.50, and 4.60 USD per kg of CNI_{eq}, respectively (Fig. 5D). The human subsystem incurs minimal additional abatement costs but contributes 2.9 Tg CNI_{eq} of the total emission reduction by 2060. Further, our findings indicate that if carbon and nitrogen emissions are managed separately, then the average unit abatement cost in 2060 would be 5.00 USD per kg of CNI_{eq}. However, under integrated carbon and nitrogen management, the average abatement cost will be 3.10 USD per kg of CNI_{eq} (Fig. 5F), representing a 37% reduction in unit costs and demonstrating a promising dual-benefit advantage for China.

Feasibility and policy implications

This study traces the spatiotemporal dynamics of China's carbon and nitrogen budgets at the human-nature interface, revealing an imbalance in carbon and nitrogen emissions. Moreover, we delve into the potential of integrated management in terms of cost-effectiveness that harmonize production processes with China's broader natural and socioeconomic conditions, facilitating an orderly reduction of carbon emission and nitrogen pollution. Recent policy developments, such as the Implementation Plan for Synergistic Pollution and Carbon Reduction, underscore the feasibility of integrated carbon and nitrogen management within China's socioeconomic and ecological development trajectory (*29*). These efforts reflect not only the theoretical viability but also the practical applicability of integrated strategies to address the dual challenges of pollution and climate change.

To fully harness the advantages of integrated management, it is crucial to prioritize measures with high cost-benefit ratios. Specifically, for the energy sector, optimizing power transmission and energy storage infrastructure to accelerate the adoption of clean energy sources such as wind and solar power should be prioritized (*30, 31*). In transportation, a focal point could be improving fuel efficiency to reduce energy consumption (*32*). In livestock management, proper feed additives can effectively reduce feeding costs by minimizing intake (*33*). The combined strategy is not always the optimal solution considering short-term urgent needs. For example, if a region is experiencing severe eutrophication and requires nitrogen-intensive actions that may increase carbon emissions, it may still be worthwhile, because local citizens might prioritize water quality during that short period. Thus, given the heterogeneity of natural resources and economic constraints, customized combinations of measures and their priorities should be tailored to different times and regions (*34*, *35*). Further, the complexity of interactions between subsystems necessitates a holistic approach to ensure that integrated actions span the entire industrial chain (*12*). For instance, manure management between the feeding and storage stages in the livestock subsystem could affect manure recycling and its application to cropland, and human consumption patterns could affect the efficiency and costs of downstream waste treatment. As a populous and pollution-intensive nation, China's adaptive and effective pathway for integrated carbon and nitrogen management can provide valuable insights for other developing countries to facilitate informed environmental policies.

Beyond technical measures, integrated carbon and nitrogen management provides a strong theoretical foundation for nature-based solutions. It is estimated that, driven by China's carbon neutrality target, by 2060, ~20% of carbon emissions will be sequestered by terrestrial ecosystems (*36*). To maximize the potential of nature-based climate solutions and to enhance the co-benefits of multiple ecosystem services (*37*), it is crucial to incorporate external factors such as climate change into the model, supporting the formulation of multilevel and resilient governance strategies (*38*). Moreover, our innovative modeling framework, applicable to carbon and nitrogen, can also be extended to other elements such as phosphorus and sulfur in the future (*39*, *40*). The multidimensional expansion will deepen our understanding of the coupling dynamics within biogeochemical cycles and clarify the diverse constraints and co-benefits engendered by human intervention. Additionally, the coupling evaluation system will evolve from a binary-element configuration to a multielement one (*41*) to facilitate the identification of optimal solutions for managing various mitigation targets, ultimately fostering holistic and cost-effective environmental policies.

REFERENCES AND NOTES

1. P. Falkowski *et al.*, *Science* **290**, 291–296 (2000).
2. X. Zhang, B. B. Ward, D. M. Sigman, *Chem. Rev.* **120**, 5308–5351 (2020).
3. J. N. Galloway *et al.*, *Science* **320**, 889–892 (2008).
4. C. Bellard, C. Bertelsmeier, P. Leadley, W. Thuiller, F. Courchamp, *Ecol. Lett.* **15**, 365–377 (2012).
5. H. D. Matthews, N. P. Gillett, P. A. Stott, K. Zickfeld, *Nature* **459**, 829–832 (2009).
6. F. Wang *et al.*, *The Innovation Geoscience* **1**, 100015 (2023).
7. K. Richardson *et al.*, *Sci. Adv.* **9**, eadh2458 (2023).
8. N. Gruber, J. N. Galloway, *Nature* **451**, 293–296 (2008).
9. J. Cui *et al.*, *Nat. Clim. Chang.* **14**, 511–517 (2024).
10. E. Du, W. de Vries, *Environ. Pollut.* **242**, 1476–1487 (2018).
11. L. F. Schulte-Uebbing, G. H. Ros, W. de Vries, *Glob. Chang. Biol.* **28**, 899–917 (2022).
12. Y. Li, S. Sang, S. Mote, J. Rivas, E. Kalnay, *Natl. Sci. Rev.* **10**, nwad054 (2023).
13. S. Niu, L. Song, J. Wang, Y. Luo, G. Yu, *Sci. China Life Sci.* **66**, 771–782 (2023).
14. H. Qian *et al.*, *Nat. Sustain.* **4**, 417–425 (2021).
15. H. Yang *et al.*, *J. Clean. Prod.* **185**, 331–341 (2018).
16. V. Smil, *Enriching the Earth: Fritz Haber, Carl Bosch, and the Transformation of World Food Production* (MIT Press, 2004).
17. P. Regnier, L. Resplandy, R. G. Najjar, P. Ciais, *Nature* **603**, 401–410 (2022).
18. D. Fowler *et al.*, *Philos. Trans. R. Soc. Lond. B Biol. Sci.* **368**, 20130164 (2013).
19. State Council of China, "The action plan on the prevention and control of air pollution" [in Chinese] (State Council of China, 2013); https://www.gov.cn/zwgk/2013-09/12/content_2486773.htm.
20. Ministry of Agricultural and Rural Affairs, "The zero increase of fertilizer and pesticides action" [in Chinese] (MOA, 2015); http://www.moa.gov.cn/govpublic/ZZYGLS/201505/t20150525_4614695.htm.
21. Ministry of Agricultural and Rural Affairs, "National plan of sustainable agricultural development 2015-2030" [in Chinese] (MOA, 2015); http://www.moa.gov.cn/nybgb/2015/liu/201712/t20171219_6103855.htm.
22. S. Piao *et al.*, *Glob. Chang. Biol.* **21**, 1601–1609 (2015).
23. H. Tian *et al.*, *Global Biogeochem. Cycles* **25**, GB1007 (2011).
24. C. Terrer *et al.*, *Nat. Clim. Chang.* **9**, 684–689 (2019).
25. F. Shang *et al.*, *Nat. Commun.* **15**, 7738 (2024).
26. X. Zhang *et al.*, *Nat. Rev. Earth Environ.* **5**, 717–731 (2024).
27. R. Yousefi *et al.*, *J. Environ. Manage.* **326**, 116847 (2023).
28. L. Xu, G. Yu, N. He, *J. Geogr. Sci.* **29**, 49–66 (2019).
29. Q. Zhang *et al.*, *Environ. Sci. Ecotechnol.* **16**, 100280 (2023).
30. F. Wang *et al.*, *Innovation* **2**, 100180 (2021).
31. Y. Wang *et al.*, *Nature* **619**, 761–767 (2023).
32. Y. Liu *et al.*, *J. Clean. Prod.* **207**, 1023–1032 (2019).
33. T. A. Woyengo, E. Beltranena, R. T. Zijlstra, *J. Anim. Sci.* **92**, 1293–1305 (2014).
34. B. Yu *et al.*, *Nat. Commun.* **14**, 8342 (2023).
35. A. Zeng *et al.*, *J. Clean. Prod.* **140**, 1226–1235 (2017).
36. Y. Huang *et al.*, *Natl. Sci. Rev.* **9**, nwac057 (2022).
37. N. Lu *et al.*, *Nat. Clim. Chang.* **12**, 847–853 (2022).
38. N. Seddon *et al.*, *Philos. Trans. R. Soc. Lond. B Biol. Sci.* **375**, 20190120 (2020).
39. Z. Luo *et al.*, *Nat. Food* **5**, 48–58 (2024).
40. M. Fakhraee *et al.*, *Nat. Rev. Earth Environ.* **6**, 106–125 (2025).
41. J. Luo *et al.*, *Ecol. Indic.* **170**, 112977 (2025).

ACKNOWLEDGMENTS

We are grateful to the anonymous reviewers for their valuable feedback. **Funding:** This work was supported by the National Natural Science Foundation of China (grants 42325707 and 42261144001 to B.G.); The National Key Research and Development Project of China (grant 2022YFE0138200 to B.G.); a Frontiers Planet Prize Award: International Champion Prize funded by the Frontiers Research to B.G.; Austria's Agency for Education and Internationalization (project CN 02/2022 to W.W.); and the European Union (grant 101149335-SynCAN-HORIZON-MSCA-2023-PF-01 to X.Z.). **Author contributions:** Conceptualization: B.G., X.Z.; Investigation: X.X., Y.Z., J.Z., L.C.; Methodology: X.Z., X.X., B.G., W.V.; Software: T.C.; Visualization: X.X.; Writing – original draft: X.X., B.G, X.Z.; Writing – review & editing: B.G., W.W., S.Z., P.V., W.V. **Competing interests:** The authors declare no competing interests. **Data and materials availability:** All data are available in the main text or the supplementary materials.

SUPPLEMENTARY MATERIALS

science.org/doi/10.1126/science.ads4105
Materials and Methods; Supplementary Text; Figs. S1 to S11; Tables S1 to S9; References (*42–291*)

Submitted 13 August 2024; accepted 28 March 2025

10.1126/science.ads4105

WELLJET dispenser stacker

INTEGRA Biosciences has expanded the capabilities of its WELLJET dispenser stacker to include automated processing of deep well plates up to 45 mm in height. This new functionality addresses key challenges in high throughput workflows, allowing labs to handle larger sample volumes more effectively in 96 or 384 well formats. Deep well plates have become indispensable in high throughput labs, where they support large-scale sample preparation, storage and processing. However, the unique design of these plates – especially their increased height – often creates mechanical constraints for standard automated liquid handlers, leading to incompatibility issues that can disrupt workflow efficiency. The updated WELLJET dispenser stacker is now optimized for rapid, accurate processing of deep well plates, making it invaluable for numerous lab applications. For instance, labs using Thermo Scientific™ KingFisher™ instruments with deep well plates prior to next generation sequencing (NGS) library preparation or quantitative PCR (qPCR) can now rely on the WELLJET dispenser stacker to automatically fill these plates, streamlining nucleic acid isolation by reducing manual handling and minimizing errors. The WELLJET dispenser stacker's compact design, low operating costs and precise liquid handling make it ideal for labs seeking cost-effective, reliable dispensing of large volumes of complex liquids, from buffers and reagents to culture media. Processing deep well plates with the WELLJET dispenser stacker instead of manual plate filling not only boosts accuracy and accelerates workflows, but also enhances the user experience, offering a walk-away solution that is simple to set up and program using a large, intuitive touchscreen interface. The WELLJET dispenser stacker is therefore a valuable addition to workflows requiring high volume liquid handling, setting a new standard for productivity and ease of use in the lab.

INTEGRA
For info: +41 (0) 81 286 95 30
www.integra-biosciences.com

Single tube decapper/recapper

Engineered to handle a wide range of large-format tubes—including centrifuge, cell culture, and glass sample tubes (11-40mm) - the IntelliXcap™ S1 from Azenta Life Sciences eliminates the inconvenience of manual adjustments by accommodating multiple tube types without requiring a cap gripper change. This seamless adaptability saves time and simplifies tube handling for low to high-throughput labs. With its ergonomic, one-handed design, the IntelliXcap S1 is built to minimize the risk of repetitive strain injuries, making it an ideal solution for daily use. Its automated system ensures consistent torque application on every cap, delivering reliable sealing without the inconsistencies of manual handling. For labs currently decapping and recapping large-format tubes by hand, a time-consuming, inconsistent task, upgrading to the IntelliXcap S1 means faster processing, increased throughput, and improved sample integrity—all in a compact footprint that fits easily in safety cabinets and tight workspaces. The small footprint of the device allows it to easily operate within safety cabinets and on space limited work benches. With an excellent cost to value ratio, the IntelliXcap S1 provides exceptional value for labs looking to improve productivity while maintaining the integrity of their valuable samples.

AZENTA Life Sciences
For info: +44 161 777 2098
www.azenta.com

InVivoSIM™ Bispecific Antibodies

Unlock the power of dual-targeting with Bio X Cell's new in vivo-grade bispecific antibodies. Bio X Cell's bispecific antibodies are engineered to simultaneously bind two distinct antigens, enhancing therapeutic precision. By redirecting immune cells, such as T-cells, to target tumor cells, these antibodies promote immune-mediated tumor cell killing, overcoming immune evasion mechanisms. They also offer dual-pathway inhibition, blocking two key signaling pathways to improve tumor growth suppression and reduce resistance. Additionally, bispecifics enable the modulation of immune checkpoints, activating immune cells while inhibiting immune-suppressive pathways. This dual-targeting mechanism enhances specificity, reduces off-target effects, and improves efficacy. Bio X Cell bispecifics are optimized for in vivo use, ensuring consistent, reproducible results from early-stage research to large-scale preclinical studies.

Bio X Cell
For info: 1-866-787-3444
www.bioxcell.com

Runge Mikron modular detectors

With a diameter of just 32 mm (1.25 inches) and measuring only 128 mm (5 inches) in length, the Mikron 71 is the smallest, commercially available fluorimeter. This detector is available with multiple interchangeable, fixed wavelength filters, light sources and flow cells enabling both simulation and emission fluorescence measurements. The flexible modularity of the Mikron 71 fluorescence detector enables it to be configured for almost any fluidic application. It is particularly ideal for instruments lacking fluorescence detection such as preparative liquid chromatography systems. Benefiting from a long-life, low power LED light source, this Mikron 71 can be used directly in a chilled environment at 4 °C (39°F) – making it perfect for bioanalytical applications such as detection of proteins down to the nanomolar level. The Mikron 71 detector reference channel ensures a high degree of accuracy and sensitivity with no need for external calibration. Runge Mikron detectors are easy to connect as they communicate through and draw power from a single USB-C port. Drivers are provided for several popular chromatography software packages, alternatively an open protocol can be used for customized implementation. The detectors conform to international standards and are CE marked.

Biotech Fluidics is a leading supplier of fluidic system solutions, liquid transfer components, degassing systems, and innovative laboratory technology to instrument developers, manufacturers, and distributors all around the world. The company's mission is to empower its customers by designing and assembling unique products, being a dependable partner, offering first-class service, in-depth knowledge, and offering advanced technical support for all the items it provides.

Biotech Fluidics
For info: + 46 300 56 91 80
www.biotechfluidics.com

Electronically submit your new product description or product literature information! Go to www.science.org/about/new-products-section for more information.

Newly offered instrumentation, apparatus, and laboratory materials of interest to researchers in all disciplines in academic, industrial, and governmental organizations are featured in this space. Emphasis is given to purpose, chief characteristics, and availability of products and materials. Endorsement by *Science* or AAAS of any products or materials mentioned is not implied. Additional information may be obtained from the manufacturer or supplier.

What's Your Next Career Move?

From networking to mentoring to evaluating your skills, find answers to your career questions on *Science* Careers

To view the complete collection, visit **ScienceCareers.org/booklets**

ScienceCareers
FROM THE JOURNAL SCIENCE AAAS

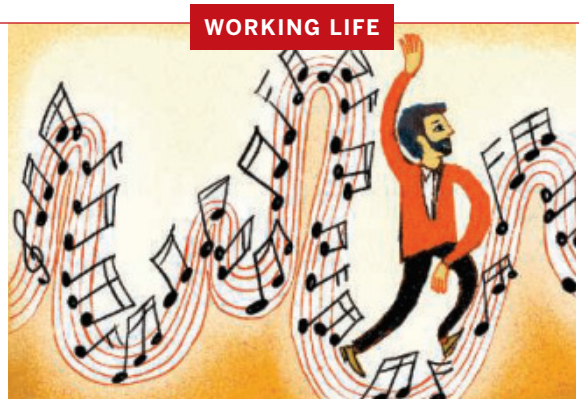

Resilience is my strength

Jary Y. Delgado

When I interviewed for my current tenure-track job, I had a stellar training background and solid publications over my 20-year career. But I was unemployed. I didn't mention that fact, but my CV had other gaps shaped by events beyond my control: shifting politics, economic crises, a mentor relationship that turned bad, and COVID-19. I had stayed on the academic path—if only barely—through sheer determination. The interviewers were friendly and I felt good about my performance, but I wasn't expecting the offer I received a month later. To my surprise, I later learned the committee had valued a factor rarely considered in an academic world obsessed with publications and impact factors: my resilience.

Growing up in Puerto Rico prepared me well for life's challenges. I witnessed my parents working hard to provide for our family, despite the ongoing economic turmoil that plagued the island. My mother, an elementary school teacher, taught me to believe in myself and offered unwavering support. The rigors of graduate school and the responsibility of becoming a father at a young age also helped build my resilience—which has turned out to be the defining feature of my career.

The first test came in 2004, when I was a graduate student in a well-funded lab, conducting research I was passionate about—until suddenly, Congress slashed the National Institutes of Health's (NIH's) budget. Our lab had to scale back, and I needed to put in a lot more hours to graduate before my adviser's grant dried up. Some days, I didn't see my 4-year-old daughter at all because I got home long after her bedtime.

My wife at the time was in school as well, and my income supported our family. But as I looked for a postdoctoral position in the midst of the NIH budget crunch, most labs told me they had no funds to take on a new trainee. With persistence, I secured a postdoc at the Neurosciences Institute, a place fueled primarily by private donations. For a while, things looked stable.

Then came the 2008 recession. The private donations dried up. Staff were laid off, and several prominent investigators left. Morale plummeted. The writing was on the wall: I had to leave.

Job hunting in 2008 was brutal. I sent out applications, knowing my family depended on me, but opportunities were scarce. Finally, a last-minute interview at a conference led to an offer for a lab in France. It meant uprooting my family and stepping away from the research path I had carefully built, but it was the only way forward. So, we packed up our lives and moved. For a while, things were good, but several years into my project, my relationship with my adviser soured, and I had to leave.

I eventually got a job as a staff scientist at the University of Chicago. I had to prioritize my new lab's research focus and could only work on my own research in spare moments, but by the end of 2018 my career was gaining traction once again. But the stress took a huge toll on my personal life, and my wife and I split up. Then COVID-19 hit. Labs shut down, slowing research and my own project. When I submitted a grant for review, it was rejected for what the reviewers said was a lack of relevant publications. I found myself once again facing unemployment.

When I finally landed my current position in 2021 it was a huge relief. A couple years later, I learned that one of the committee members had followed a path similar to mine and saw my commitment and perseverance as key factors in my favor.

But not everyone will have such an advocate. I believe we should be asking candidates for academic jobs what challenges they've overcome and how they have persevered. Applicants with CVs featuring high-profile labs and prestigious publications tend to be the ones who get jobs. But others of us have taken a slower, bumpier path, and I believe we deserve a closer look. We're the ones with the resilience to get through tough times.

Right now, I'm anxious about our nation and the future of biomedical research in the United States, but I'm not worrying for myself. If my career has taught me anything, it's that resilience alone doesn't guarantee survival. But sometimes, it gives you just enough time to catch the next opportunity before the door closes. □

Jary Y. Delgado is an assistant professor at Loyola University Chicago.

ILLUSTRATION: ROBERT NEUBECKER

Your Legacy to Science

AN ESTATE GIFT TO THE
AMERICAN ASSOCIATION FOR THE ADVANCEMENT OF SCIENCE



Since 1848, our founding year, the American Association for the Advancement of Science (AAAS) has been deeply committed to advancing science, engineering and innovation around the world for the benefit of all people.

By making AAAS a beneficiary of your will, trust, retirement plan or life insurance policy, you become a member of our 1848 Society, joining Thomas Edison, Alexander Graham Bell and the many distinguished individuals whose vision led to the creation of AAAS and our world-renowned journal, *Science*, so many years ago.

Unlike many of its peers, *Science* is not for-profit. Your estate gift would provide long-term financial stability and durable annual income that will support operations and competitive innovation for years to come. **This support is vital.**

"As a teacher and instructor, I bear responsibility for the younger generations. If you have extra resources, concentrate them on organizations, like AAAS, that are doing work for all."

—Prof. Elisabeth Ervin-Blankenheim, 1848 Society member

If you intend to include AAAS in your estate plans, provide this information to your lawyer or financial adviser:

Legal Name: American Association for the Advancement of Science
Federal Tax ID Number: 53-0196568
Address: 1200 New York Avenue, NW, Washington, DC 20005

If you would like more information on making an estate gift to AAAS, cut out and return the form below or send an email to philanthropy@aaas.org. Additional details are also available online at **www.aaas.org/1848Society**.

1848 SOCIETY
AAAS

cut here ✂

Yes, I would like more information about joining the AAAS 1848 Society.

PLEASE CONTACT ME AT:

Name: _____

Address: _____

City: _____ State: _____ Zip code: _____ Country: _____

Email: _____ Phone: _____

RETURN THIS FORM TO:
AAAS Office of Philanthropy and Strategic Partnerships • 1200 New York Avenue, NW • Washington, DC 20005 USA

NOSTER

Connecting life & gut microbiome

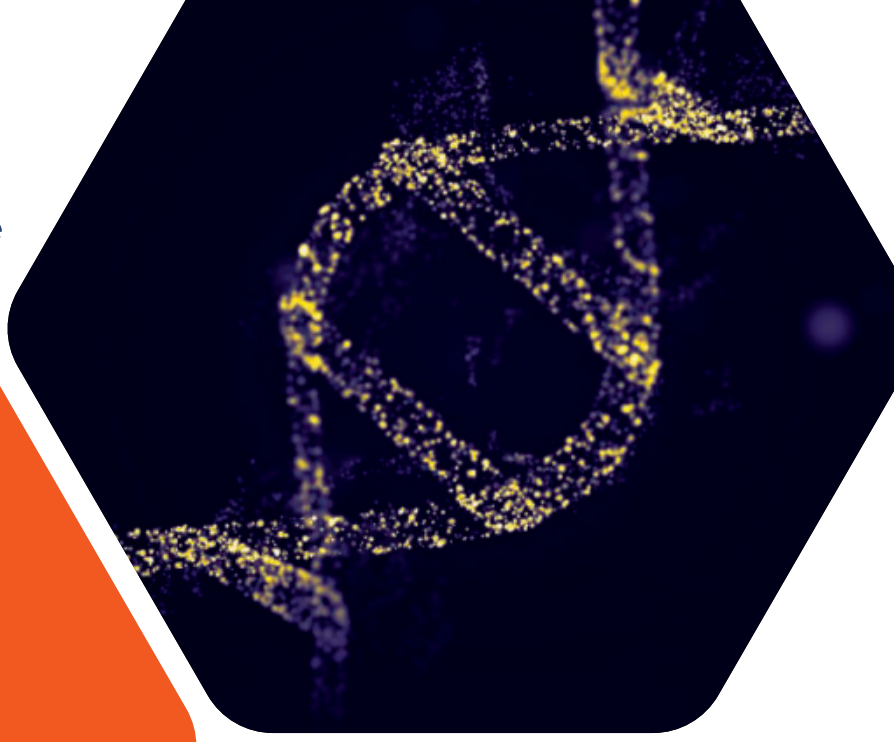

Utilizing NOSTER's
original lipid metabolite database

Postbiotics Scan Metabolome Analysis Service

By conducting a thorough analysis of lipid metabolites produced by gut bacteria, you can gain valuable insights into the metabolic mechanisms of the microorganisms, discover novel biomarkers and therapeutic targets, and uncover new functional properties of food products.

Whole Genome Sequencing

Analysis Service Gut Microbiota

By employing cutting-edge next-generation sequencing technology, we are able to conduct a comprehensive assessment of the diversity and distribution of microorganisms within samples. Moreover, by merging NOSTER's advanced cultivation techniques with real-time PCR analysis, we have developed the capability to quantitatively analyze gut bacteria that were previously challenging to culture and evaluate.

Application areas

Wide range of areas related to lipids and microorganisms such as gut bacteria as described below.

Food sector

Development of supplements and exploration of new functions of fats and oils and fermented foods.

Basic research

Analysis of metabolic mechanisms of gut bacteria.

Medical fields

Elucidation of pathological mechanisms / Search and development of diagnostic markers / Evaluation of therapeutic effects

Others

Studies related to gut microbiota and disease.

Noster Inc., Kyoto, Japan

https://www.noster.inc/

Email : contact@noster.inc